Electronic-structure insights into aqueous redox chemistry: permanganate and manganate ions studied using liquid jet photoelectron spectroscopy

Dissertation
zur Erlangung des Grades eines
Doktors der Naturwissenschaften (Dr. rer. nat.)

am Fachbereich Physik
der Freien Universität Berlin

vorgelegt von
Karen Denise Mudryk

Berlin
2021

Abstract

This thesis presents a combined study of the (microscopic) electronic structure and (macroscopic) redox properties of permanganate (MnO_4^-) and manganate (MnO_4^{2-}) ions in aqueous solution using liquid jet soft X-ray photoelectron spectroscopy (XPS). $MnO_{4\ (aq.)}^-$ is a versatile, strong oxidizing agent and redox precursor of manganese species with a range of oxidation states. $MnO_{4\ (aq.)}^{2-}$ is a transient species that acts both as an oxidizing or reducing agent, forming a highly-reversible redox pair with $MnO_{4\ (aq.)}^-$ in alkaline environments. Such redox properties make these transition metal complexes (TMCs) attractive for sustainable (electro-)chemical applications. The goal of this work was to gain insight into the absolute energetics and redox behavior of $MnO_{4\ (aq.)}^-$ and $MnO_{4\ (aq.)}^{2-}$ from electronic structure information. Alternative sample sources – a micro-mixing scheme and an electrolysis cell liquid jet – were developed to generate and study $MnO_{4\ (aq.)}^{2}$ transient ions.

Within a single-configuration and single-active-electron electronic structure picture, binding energy-scaled molecular orbital (MO) diagrams were produced from $MnO_{4\ (aq.)}^-$ and $MnO_{4\ (aq.)}^{2-}$ XPS data. Mn 2p and O 1s resonantly-enhanced photoelectron spectroscopy (RPES) measurements revealed intramolecular Auger processes and valence electron binding energies that were not accessible from the XPS experiments, as well as hybridization of and electronic coupling between the valence electrons. In addition, the O 1s RPES experiments revealed intermolecular coulombic decay (ICD) processes, signatures of electronic coupling between solute and solvent molecules in the first solvation shell.

For $MnO_{4\ (aq.)}^-$ at 0.2 M concentration, similar electronic energetics were observed at the gas-solution interface and in the solution bulk, independently of the nature of the counter ion ($Na_{(aq.)}^+$ or $K_{(aq.)}^+$). Depth profiling experiments at 0.2 M and 1.0 M concentration highlighted a tendency of $MnO_{4\ (aq.)}^-$ to accumulate in the solution bulk and away from the interface, with non-linear accumulation behavior occurring for the higher concentration. Through comparison to the gas-phase ionization energetics, the Gibbs free energy of hydration (ΔG_{hyd}) for isolated MnO_4^- was also calculated. For $MnO_{4\ (aq.)}^{2-}$, valence band features could only be isolated in surface-sensitive XPS experiments and RPES experiments were relied on to study bulk-solution energetics. These results were applied to infer thermodynamic parameters of half redox reactions involving the $MnO_{4\ (aq.)}^-$ / $MnO_{4\ (aq.)}^{\bullet}$ and $MnO_{4\ (aq.)}^{2-}$ / $MnO_{4\ (aq.)}^-$ redox pairs, including oxidative reorganization energies (λ_{ox}), adiabatic ionization energies / Gibbs free energy of oxidation (ΔG_{ox}) and vertical electron affinities. For the $MnO_{4\ (aq.)}^{2-}$ / $MnO_{4\ (aq.)}^-$ redox pair, the ΔG_{ox} value purely extracted from spectroscopic data was shown to match the reported electrochemical value. Overall, the extracted redox parameters demonstrate how insights into the macroscopic (redox) properties of chemical systems can be built up from microscopically (molecularly) sensitive measurements. The methodology can be extended to aqueous redox-active species that cannot be probed by conventional electrochemical methods.

Zusammenfassung

Diese Arbeit stellt eine kombinierte Untersuchung der (mikroskopischen) elektronischen Struktur und der (makroskopischen) Redox-Eigenschaften von Permanganat- (MnO_4^-) und Manganat- (MnO_4^{2-}) Ionen in wässriger Lösung mittels Flüssigkeitsstrahl-Soft-Röntgen-Photoelektronenspektroskopie (XPS) dar. $MnO_{4\ (aq.)}^-$ ist ein vielseitiges, starkes Oxidationsmittel und Redox-Vorläufer von Mangan-Spezies mit einer Reihe von Oxidationsstufen. $MnO_{4\ (aq.)}^{2-}$ ist eine transiente Spezies, die sowohl als Oxidations- als auch als Reduktionsmittel wirkt und in alkalischen Umgebungen ein hochreversibles Redoxpaar mit $MnO_{4\ (aq.)}^-$ bildet. Solche Redox-Eigenschaften machen diese Übergangsmetallkomplexe (TMCs) attraktiv für nachhaltige (elektro-)chemische Anwendungen. Das Ziel dieser Arbeit war es, Einblicke in die absolute Energetik und das Redoxverhalten von $MnO_{4\ (aq.)}^-$ und $MnO_{4\ (aq.)}^{2-}$ aus der Information der elektronischen Struktur zu gewinnen. Alternative Flüssigkeitsstrahl-Probenquellen – ein Mikro-Mischsystem und eine Elektrolysezelle – wurden entwickelt, um $MnO_{4\ (aq.)}^{2-}$ transiente Ionen zu erzeugen und zu untersuchen.

Innerhalb eines elektronischen Strukturbildes mit einer einzigen Konfiguration und einem einzigen aktiven Elektron wurden aus XPS-Daten von $MnO_{4\ (aq.)}^-$ und $MnO_{4\ (aq.)}^{2-}$ Molekülorbitaldiagramme mit Bindungsenergieskala erstellt. Mn 2p und O 1s resonanzverstärkte Photoelektronenspektroskopie (RPES) Messungen zeigten intramolekulare Auger-Prozesse und Valenzelektronen-Bindungsenergien, die aus den XPS-Experimenten nicht zugänglich waren, sowie Hybridisierung und elektronische Kopplung zwischen den Valenzelektronen. Darüber hinaus zeigten die O 1s RPES-Experimente intermolekularer coulombischer Zerfallsprozesse (ICD): Signaturen der elektronischen Kopplung zwischen gelösten und Lösungsmittelmolekülen in der ersten Solvatationsschale.

Für $MnO_{4\ (aq.)}^-$ bei 0,2 M Konzentration wurden ähnliche elektronische Energetiken an der Gas-Lösungs-Grenzfläche und innerhalb der Lösung beobachtet, unabhängig von der Art des Gegenions ($Na_{(aq.)}^+$ oder $K_{(aq.)}^+$). Tiefenprofilierungsexperimente bei 0,2 M und 1,0 M Konzentration zeigten eine Tendenz zur Akkumulation von $MnO_{4\ (aq.)}^-$ innerhalb der Lösung und weg von der Grenzfläche, wobei bei der höheren Konzentration ein nichtlineares Akkumulationsverhalten auftrat. Durch Vergleich mit der Ionisierungsenergetik in der Gasphase wurde auch die Gibbs-Energie der Hydratation (ΔG_{hyd}) für isoliertes MnO_4^- berechnet. Für $MnO_{4\ (aq.)}^{2-}$ konnten Valenzbandeigenschaften nur in oberflächensensitiven XPS-Experimenten isoliert werden und RPES-Experimente wurden zur Untersuchung der Energetik innerhalb der Lösung herangezogen. Aus diesen Ergebnissen wurden thermodynamische Parameter von halben Redoxreaktionen mit den Redoxpaaren $MnO_{4\ (aq.)}^-$ / $MnO_{4\ (aq.)}^{\bullet}$ und $MnO_{4\ (aq.)}^{2-}$ / $MnO_{4\ (aq.)}^-$ abgeleitet, einschließlich oxidativer Reorganisationsenergien (ox), adiabatischer Ionisierungsenergien / Gibbs-Energie der Oxidation (ΔG_{ox}) und vertikaler Elektronenaffinitäten. Für das Redoxpaar $MnO_{4\ (aq.)}^{2-}$ / $MnO_{4\ (aq.)}^-$ wurde gezeigt, dass der rein aus den spektroskopischen Daten extrahierte ΔG_{ox}-Wert mit dem berichteten elektrochemischen Wert übereinstimmt. Insgesamt zeigen die extrahierten Redox-Parameter, wie Einblicke in die makroskopischen (Redox-)Eigenschaften chemischer Systeme aus mikroskopisch (molekular) sensitiven Messungen aufgebaut werden können. Die Methodik kann auf wässrige redoxaktive Spezies erwitert werden, die mit konventionellen elektrochemischen Methoden nicht untersucht werden können.

Acknowledgements

I would like to thank everyone who ever shared a beam time with me, stood by the experiment in the middle of the night when nothing was working, and still believed it was a good idea to try again. Completing these experiments would not have been possible without you.

I would first like to thank my supervisor, Iain Wilkinson, for giving me the opportunity to come to Berlin to do my PhD. The work presented here is the result of joint, everyday efforts over several years during which we discussed ideas, experiments, and technological developments to expand on the capabilities of liquid jet photoelectron spectroscopy to study chemical systems. I feel very lucky to have had the chance to work with him, and will always be grateful for his constant dedication and support.

I would also like to thank Prof. Holger Dau for being a second reviewer of this thesis and for his prompt advice and support.

A very big thank you to Robert Seidel, whose interest and enthusiasm in performing experiments with aqueous manganese species in every oxidation state that nature can offer made the realization of many of the experiments presented here possible. I am also very thankful to Bernd Winter, who introduced us to the liquid jet technique and the synchrotron radiation beam times. Very special thanks to Garlef Wartner, Dennis Hein, Sebastian Malerz and Florian Trinter for their dedicated support during the experiments. I would also like to thank Ronny Golnak, Jie Xiao, Stephan Thürmer, Uwe Hergenhahn and Prof. Gerard Meijer for their very kind support.

I would also like to specially thank Florian Gores for working with us on the development of the electrolysis cell liquid jet, and for his constant guidance and cheerful support, which had a very positive impact on my everyday work. I am also very grateful to the workshops at Helmholtz-Zentrum Berlin and Freie Universität Berlin for their incredible support to meet very tight deadlines!

Special thanks also to Catalina Jimenez, whose help at the beginning of my PhD made a huge difference on my stay here.

I am also happy and grateful to have had the chance of meeting and working with everyone in my group, especially the PS-ALTS team, who shared everyday life with me over the years. Special thanks to Lili, Nataliia, and Heba (my closest fellow women in science at HZB), who made facing many everyday challenges easier – thank you for sharing your strength with me! And a very big thank you to Daniel, for long conversations about the ideas presented here, and for asking all of the right questions.

Finally, I would like to thank my family, especially my mom, Romi, Jime, and Nair – we are always together in everything we do.

Contents

List of Abbreviations

2D	Two Dimensional
AIE	Adiabatic Ionization Energy
BE	Binding Energy
EAL	Effective Attenuation Length
EMFP	Elastic Mean Free Path
ETMD	Energy Transfer Mediated Decay
HOMO	Highest Occupied Molecular Orbital
HPLC	High-Performance Liquid Chromatography
ICD	Inter Coulombic Decay
IMFP	Inelastic Mean Free Path
LRA	Linear response approximation
LUMO	Lowest Unoccupied Molecular Orbital
MO	Molecular Orbital
PEEK	Polyether Ether Ketone
PES	Photoelectron Spectroscopy
PEY	Partial Electron Yield
PTFE	Polytetrafluoroethylene
RHE	Reversible Hydrogen Electrode
RPES	Resonantly-Enhanced Photoelectron Spectroscopy
SHE	Standard Hydrogen Electrode
TMC	Transition Metal Complex
VEA	Vertical Electron Affinity
VIE	Vertical Ionization Energy
XAS	X-ray Absorption Spectroscopy
XPS	X-ray Photoelectron Spectroscopy

List of Figures

List of Tables

1   Introduction

The study of the relationship between electronic structure and function in molecules in their natural or applied environments has been central to the understanding of natural processes – such as enzyme catalysis [1] and oxygenic photosynthesis [2] – and the development of sustainable technologies – for example, in environmentally-friendly, non-toxic materials (so called green chemistry [3]) and energy conversion and storage [4, 5]. Experimentally, spectroscopic techniques form the basis of these studies, allowing molecular electronic structure to be probed via light-matter interactions [6-8]. By combining spectroscopic data with quantum mechanical and thermodynamic descriptions of matter [9], chemical system energetics can be mapped and their macroscopic properties may be understood from a microscopic (molecular) point of view [10-12].

The phenomenon of chemical change driven by the transfer of electric charge – for example, *aqueous redox chemistry* – is ubiquitous in the aforementioned applications. Photosynthesis, cellular respiration, and protein-mediated processes in living organisms [13], as well as terrestrial biogeochemical element cycling [14] are facilitated by electron transfer reactions in the aqueous phase. Similarly, redox reactions are the basis of electrochemical energy storage devices – such as redox flow batteries [15] – and sustainable innovations in synthetic chemistry and catalysis [16]. The direct investigation of the aqueous phase electronic structure of the chemical species involved in those processes provides insight into the molecular properties and energetics that underpin both natural and artificially-engineered redox cycles [17].

In an aqueous solution, the electronic structure of the solute (redox reagent) and the solvent (water molecules) are intrinsically correlated. Consequently, an understanding of redox (charge transfer) events in the aqueous phase requires consideration of the solute-solvent polarization interactions as well as the relative molecular structures adopted by reactants and reaction products [18-20]. An experimental technique that allows aqueous phase electronic structure information to be directly accessed is liquid jet photoelectron spectroscopy [8, 21, 22]. The work presented here aims to apply this technique to the study of aqueous redox synthetic species suitable for sustainable chemical and electrochemical applications.

Within that context, chemical species of relevance are transition metal complexes (TMCs) [16, 23, 24]. TMCs are compounds that consist of several atomic or molecular groups (ligands) bound to a common atomic or molecular transition metal center. The property of transition metals to adopt different oxidation states results in TMCs having the ability to act as versatile electron transfer reagents [25]. In addition, the diverse nature of the ligands – including both inorganic and organic species – confers selectivity to their redox activity [26, 27]. The experiments and results described in this thesis focused on investigating the electronic structure and redox energetics of two manganese (Mn)-based TMCs in aqueous solution: permanganate ($MnO_4^-{}_{(aq.)}$) and manganate ($MnO_4^{2-}{}_{(aq.)}$) ions. Part of the work presented here (in particular, the results associated with $MnO_4^-{}_{(aq.)}$) has led to publication of the following article: "**The electronic structure of the aqueous permanganate ion: aqueous-phase energetics and molecular bonding studied using liquid jet photoelectron spectroscopy**" (K. D. Mudryk, R. Seidel, B. Winter, I. Wilkinson, *Phys. Chem. Chem. Phys.*, 2020, 22, 20311. DOI: 10.1039/D0CP04033A).

This chapter is divided into three sections. Section 1.1 describes the Mn-water redox system and the redox properties and general relevance of $MnO_4^-{}_{(aq.)}$ and $MnO_4^{2-}{}_{(aq.)}$ ions. Section 1.2 provides a general introduction to the application of liquid jet photoelectron spectroscopy to the study of the electronic structure and properties of redox reactants in the aqueous phase. An overview of the capabilities of the technique, how electronic structure and redox energetics can be linked, and technical challenges that needed to be overcome to enable the study of transient redox species (such $MnO_4^{2-}{}_{(aq.)}$ ions) are briefly outlined. Finally, Section 1.3 presents the objectives and outline of the thesis.

1.1 The Mn-water redox system
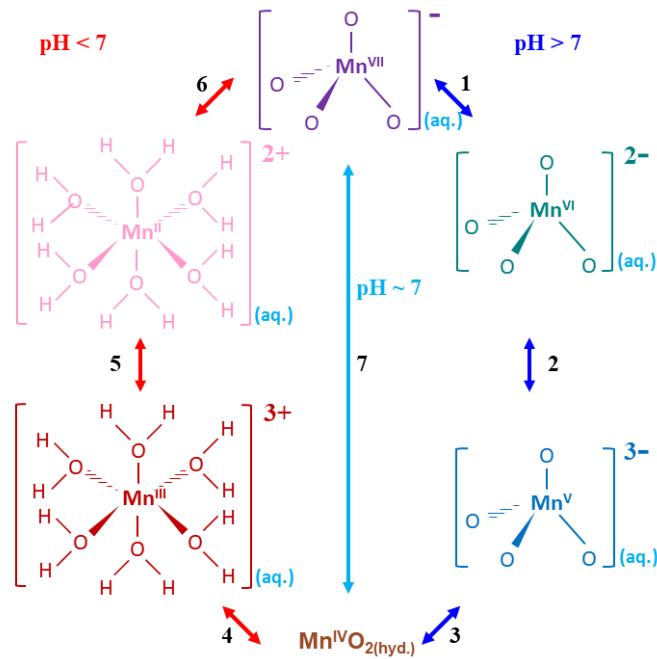
Figure 1.1. Aqueous Mn compounds and redox equilibria

Chemical configurations adopted by aqueous Mn compounds with different oxidation states (indicated by a superscript using Roman numerals) [28]. Different colors are used for each oxidation state, according to the colors of the aqueous solutions of the associated compounds. The arrows represent the main redox equilibria between species. Red arrows are used to indicate redox equilibria taking place at acidic pHs and blue arrows indicate equilibria occurring at alkaline pHs. The light blue arrow connecting $MnO_4^-{}_{(aq.)}$ and $MnO_{2(s)}$ represents the most thermodynamically favorable route of $MnO_4^-{}_{(aq.)}$ reduction at neutral pH, which results in the formation of hydrated $MnO_{2(hyd.)}$ in nanoparticle form [29].

Mn is one of the twelve most abundant elements forming the Earth´s crust [30, 31]. As such, it is considered to be in abundant supply for applications [32], with approximately 2% of the total reserves of Mn in the world being exploited every year [33]. However, it is a non-renewable resource and the development of sustainable methods for Mn metal recovery and recycling has been increasingly investigated over the last years [34].

Mn is predominantly found in minerals and as part of polymetallic nodules in the seafloor [31, 32, 35]. Its most thermodynamically stable form, manganese dioxide ($MnO_{2(s)}$) [23, 36] is a solid that

crystallizes in several structures, such as α-MnO$_2$, β-MnO$_2$ and γ-MnO$_2$ [37]. This oxide can also exist in a hydrated form [29], which originates upon reduction of manganese species with higher oxidation states, as will be described below. Overall, the presence of Mn compounds in the aqueous phase is enabled by redox processes that produce soluble ionic Mn species from solid phase precursors [30, 38]. As a transition metal with an [Ar]3d^{5}4s^2 electronic configuration, Mn forms TMCs in which it exists with a variety of oxidation states ranging from II+ to VII+ in the aqueous phase. Given that the redox potential required to drive the formation of different charged states depends on the H$^+_{(aq.)}$ and OH$^-_{(aq.)}$ concentrations in solution, these chemical species are correlated between one another by numerous pH-dependent redox reactions and equilibria, as illustrated in Figure 1.1 [28]. The lower oxidation states (II+ – IV+) form species that facilitate electron transfer between organic reaction centers in biological systems [23]. The higher oxidation states (V+ – VII+) are strong oxidizing agents applied in industry as green alternatives to more toxic and less abundant compounds [39]. In addition, the reversible character displayed by redox pairs formed by the VI+/VII+ (redox equilibrium labelled as '**1**' in Figure 1.1) and II+/III+ (redox equilibrium labelled as '**5**' in Figure 1.1) oxidation states has led to the investigation of their potential application as electrolytes in redox flow batteries [40, 41]. The equilibrium labelled '**7**' in Figure 1.1 highlights the most thermodynamically favorable route of MnO$_4^-_{(aq.)}$ reduction at neutral pH, which results in the formation of hydrated manganese dioxide in the form of nanoparticles [29].

The occurrence of predominant Mn species with different oxidation states at equilibrium is described by the Pourbaix diagram for the Mn-water system [36] shown in Figure 1.2. Mn complexes relevant to this work have been highlighted in color in the figure: MnO$_4^-_{(aq.)}$ (with Mn in the VII+ oxidation state), MnO$_4^{2-}_{(aq.)}$ (with Mn in the VI+ oxidation state) and MnO$_{2(s)}$ (with Mn in the IV+ oxidation state).
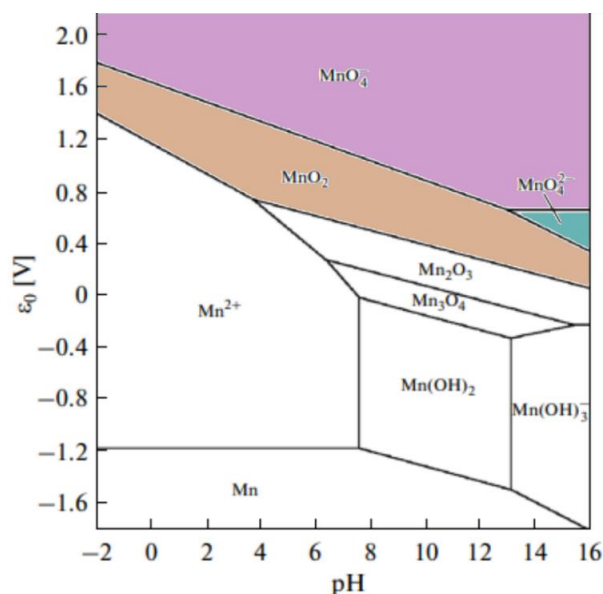
Figure 1.2. Pourbaix diagram of the Mn-H$_2$O system

Pourbaix diagram of the Mn-H$_2$O system at 25°C. Species relevant to this work are highlighted in color: MnO$_4^-_{(aq.)}$ (purple), MnO$_4^{2-}_{(aq.)}$ (green) and MnO$_{2(s)}$ (brown). Adapted with permission from Springer Nature Customer Service Centre GmbH: Springer Nature [36], Copyright © 2015, Pleiades Publishing, Ltd.

While Figure 1.1 summarizes (all) the chemical identities adopted by Mn TMCs with different oxidations states in the aqueous phase, the Pourbaix diagram shows the most prevalent (or stable) species under equilibrated conditions. As a result, transient intermediates shown in Figure 1.1 – such as $Mn[(H_2O)_6]^{3+}_{(aq.)}$ and $MnO_4^{3-}_{(aq.)}$ – are not present in Figure 1.2. However, those species can be stabilized under certain conditions and, for example, a Pourbaix diagram including $Mn^{3+}_{(aq.)}$ can be found in Reference [42].

$MnO_4^-_{(aq.)}$ is a strong oxidizing agent at acidic, neutral, and alkaline pH and redox precursor of Mn TMCs with other oxidation states, as can be seen from the redox equilibria illustrated in Figure 1.1. As a result, it has been applied as a versatile oxidizer in green chemistry and sustainable industrial processes [39, 43]. Due to its relatively low toxicity, it is also widely applied in the oxidation of micro-pollutants [44], the detection of organic compounds [45] and water disinfection processes [46-48]. It has also proven to be an effective electron acceptor in microbial fuel cells [49]. In the aforementioned applications, $MnO_4^-_{(aq.)}$ reacts to form $MnO_{2(s)}$ (redox equilibrium number **7** in Figure 1.1). This is highly beneficial in the design of sustainable chemical processes, given that $MnO_{2(s)}$ can be recycled and converted into any of the other Mn compounds shown in Figure 1.1 (by following the redox equilibria **4-6** at acidic pH or **1-3** at alkaline pH as shown in the figure). For example, it has been found that recycling of $MnO_{2(s)}$ can take place under industrial conditions to form $MnO_4^{2-}_{(aq.)}$ and $MnO_4^-_{(aq.)}$ [43].

$MnO_4^{2-}_{(aq.)}$ ions act both as reducing and oxidizing agents at alkaline pH [50-53]. This species is unstable towards disproportionation, that is, their stability in aqueous solution is relatively limited and these compounds convert to $MnO_{2(s)}$ over time [54]. This is represented by redox equilibria **2** and **3** in Figure 1.1. Consequently, $MnO_4^{2-}_{(aq.)}$ ions are generally formed as transient intermediates during the reduction of $MnO_4^-_{(aq.)}$ in alkaline media, with relevance for the oxidation and degradation of organic compounds [51, 55-58]. In addition, as previously mentioned, $MnO_4^{2-}_{(aq.)}$ forms a highly reversible redox pair with $MnO_4^-_{(aq.)}$ that has found to be applicable as a catholyte in redox-flow batteries [40]. This redox pair has a redox potential within the water electrochemical potential window and a relatively high solubility in water, properties that facilitate large electrochemical energy storage capacities [40].

1.2 Photoelectron spectroscopy and redox chemistry

1.2.1 Liquid jet photoelectron spectroscopy

Photoelectron spectroscopy (PES) allows the electronic structure of atoms, molecules, and materials to be probed under (nearly) isolated (gas phase) or condensed conditions (solid phase, liquid phase and interfaces) [59-63]. A PES experiment involves irradiation of a sample by a monochromatic ionizing radiation source and measurement of the kinetic energy (KE) of the emitted electrons [63]. With a known photon energy and a KE calibration of the spectrometer, the associated electron binding energies (BEs) can then be determined from those measurements on an absolute energy scale [64, 65]. When (soft) X-rays are used as the irradiation source – as in the work presented here – PES is referred to as (soft) X-ray photoelectron spectroscopy (XPS) [64, 65]. The high photon energy of X-rays (as will be described in Chapter 3) allows valence and core electrons of a sample to be ionized, hence allowing the overall electronic structure to be probed.

During a XPS experiment, the sample is placed inside a vacuum chamber in order to propagate the ionizing light to the sample, to operate the high-voltage electron detector, and to minimize extrinsic changes in the nascent electron KEs due to collisional events prior to measurement [62]. This requirement poses a challenge for volatile liquid phase samples, since such liquids would normally freeze under vacuum conditions. Furthermore, the vapor pressure surrounding the liquid provides a source of gas phase molecules that will also be ionized and can scatter outgoing electrons [66, 67].

The above-mentioned challenges were overcome with the realization of in-vacuum liquid beams in 1973 [68] and the subsequent development of the liquid micro-jet technique in 1988, allowing XPS studies to be performed on aqueous solutions [69]. Previous pioneering XPS experiments in liquids had implemented wetted rotating wires and rotating metal or quartz disks to produce clean liquid surfaces in vacuum [21, 70, 71]. With the liquid jet sample delivery methodology, pure liquids and aqueous solutions are generally introduced into the vacuum experimental chamber by means of a (Pt) disk or (glass) capillary nozzle with a $5 - 50$ µm orifice [21, 69]. In this way, a fast-flowing laminar liquid stream is created, with a surrounding gas phase sheath with low enough molecular density to allow electrons to reach the detector with negligible gas phase scattering, as long as differential pumping is provided in sufficient proximity (*i.e.* within the mean free path) [69].

The combination of the liquid jet technique with XPS allows the determination of valence band and core level electron binding energies of aqueous solutes [72]. In the latter case, XPS provides atomic-site and charge-state sensitivity to the environment of the solute or solvent molecule under study. Hence, liquid jet XPS enables the detection of changes in oxidation state (via chemical shifts) and chemical bonding (and, indirectly, geometric structural changes) [8, 22] and highlights the effects of solvents on aqueous phase species. In that way, the technique offers the possibility to probe changes in electronic structure as a function of oxidation state in coordinated complexes, such as Mn TMCs. In addition, the probing depth into the liquid jet can be varied to selectively sample photoelectrons from the aqueous solution interface or both interfacial and bulk-solution contributions [22, 73, 74], thus accessing spectroscopic information from different hydration environments. The aforementioned capabilities of liquid jet XPS relate to information that can be extracted by performing so called *direct* XPS experiments, where electrons are directly ionized with a photon energy in excess of the considered BEs [8, 22]. In addition, chemical bonding can be further studied by performing *resonantly enhanced* photoelectron spectroscopy (RPES) experiments.

RPES consists of detecting photoelectrons following resonant photoexcitation and the subsequent relaxation that leads to secondary electron emission, thus revealing information about electronic coupling [8]. In that way, RPES enables the atomic parentage of *intramolecular* bonding interactions to be probed [8]. Moreover, where present, non-local relaxation pathways involving solvent molecules can also be detected, providing insight into solute-solvent *intermolecular* interactions [75]. Finally, due to the constructive interference between direct and resonantly-enhanced photoemission channels, RPES often permits the isolation of signals from solutes with relatively low ionization cross sections or those that are more generally buried under predominant solvent contributions [76].

The theoretical and experimental aspects of liquid jet XPS, RPES, and non-local relaxation are described in more detail in Chapters 2 and 3, respectively.

1.2.2 Application to redox chemistry

During a homogenous aqueous phase redox reaction, one or more electrons are transferred from a reduced (or donor) species to an oxidized (or acceptor) atom or molecule. Overall, a redox reaction is enabled by a difference in redox potential (*i.e.* the tendency of a chemical species to gain or lose electrons) between the donor and the acceptor. During this process, the molecular structure of both the donor and the acceptor are changed in order to accommodate the transfer of charge [19]. When a redox reaction takes place in aqueous solution, the polarization of the water molecules also needs to change [77].

In aqueous solutions of TMCs, the oxidation state of the metal center has a direct effect on the polarization of the surrounding solvent molecules [77]. In addition, the redox potential is dependent on the oxidation state of the metal center and the changes in metal-ligand bonding interactions [78, 79]. As a result, the overall charge distribution in solution and within the solute has a direct influence on electron transfer events – the reaction energetics, pathways and kinetics [19] – especially given the interdependence of the electronic structure of both the solute and the solvent due to solute-solvent interactions [80, 81]. Consequently, the study of the solution phase electron BEs and intra- and inter-molecular bonding properties of chemical compounds – by performing XPS and RPES experiments as described in the previous section – is a particularly useful approach to the development of a better understanding of their redox activity [82-84].

Furthermore, a parallel can be drawn between ionization in XPS and electron transfer reactions between donor and acceptor molecules [85, 86]. A redox reaction is enabled by a difference in redox potential and facilitated by polarization-induced changes in the nuclear framework and electronic structure of solute and solvent molecules [77]. Ionization can be considered as electron transfer driven by light absorption, in which the photo-absorbed energy facilitates the removal of an electron from the sample into the ionization continuum. During ionization, an electron is removed from the chemical system in its ground state (reduced) configuration to produce a charge-separated excited state (oxidized) configuration. The transition from initial to final state occurs instantaneously compared with the timescale required for the solvent dipoles to re-orient around the oxidized configuration [77]. After relaxation and solvent reorganization, the oxidized state is equivalent to that produced during a redox reaction. Consequently, ionization energies and redox potentials are linked and their relationship can be used to derive redox energetics and kinetic parameters from spectroscopic information, under certain approximations [19]. The theoretical foundations of the correlation between electronic structure and thermodynamic redox information are described in detail in Chapter 2.

1.2.3 Challenges in sample delivery for unstable ions

The liquid micro-jet technique relies on samples being stable for a period of time long enough to enable continuous delivery into the experimental chamber through a high-performance liquid chromatography (HPLC) transfer line and a micro-jet capillary ($25 - 35$ µm open orifice diameter) [87]. Relatively unstable (transient) chemical species – such as $MnO_4^{2-}{}_{(aq.)}$ ions, prone to disproportionation [54] – generally do not meet this requirement. Furthermore, the formation of micrometer-sized solids – such as $MnO_{2(s)}$ from the disproportionation reaction – blocks the micro-jet capillary, impeding continuation of the experiment. In order to circumvent those difficulties, a

mechanism to generate the solute of interest as close to the light-sample interaction region as possible is required.

The microfluidic generation of solutes is an attractive option in that regard. It allows higher control over reaction conditions and conversion efficiencies while benefiting from the inherent characteristics of working within laminar flow regimes [88-90], as required to produce stable liquid jets. With that in mind, this thesis proposes the incorporation of chemical and electrochemical microfluidic-based solutions as expansions of the liquid micro-jet technique. A micro-mixing scheme and an electrolysis cell liquid jet were designed and implemented for the generation of $MnO_4^{2-}{}_{(aq.)}$ transient ions. These sample source developments are presented in Chapter 3.

1.3 Objectives and outline of the thesis

The main goal of the work described within this thesis was the application of the liquid jet photoelectron spectroscopy technique to investigate the electronic structure and aqueous redox chemistry of $MnO_4^{-}{}_{(aq.)}$ and $MnO_4^{2-}{}_{(aq.)}$ ions. Direct XPS and RPES experiments were performed with the aim of addressing the following points:

1. To map the electronic structure of $MnO_4^{-}{}_{(aq.)}$ and $MnO_4^{2-}{}_{(aq.)}$ by determining valence band and core level electron binding energies in the aqueous phase;

2. To compare the aqueous phase electronic structure at different liquid jet probing depths – *i.e.* at the solution-gas interface and in the solution bulk – and to infer the existence of interfacial or bulk preferential solute distributions for the above-mentioned species;

3. To investigate the changes in the atomic parentage of the relevant bonding interactions, the nature of the Mn-ligand bonding interactions, and ligand-solvent interactions in the above-mentioned complexes;

4. To correlate electronic structure information with redox properties by considering the thermodynamics of ionization and electron transfer in order to estimate aqueous phase redox energetics from the acquired spectroscopic data;

5. To incorporate micro-mixing and electrolysis flow cell devices into liquid jet photoelectron spectroscopy experiments as sample delivery methodologies and to facilitate the investigation of unstable (transient) $MnO_4^{2-}{}_{(aq.)}$ ions.

The study of the electronic structure, chemical bonding, and solute-water interactions provides insight into the microscopic effects responsible for electron transfer reactions that facilitate green chemistry and energy conversion applications involving $MnO_4^{-}{}_{(aq.)}$ and $MnO_4^{2-}{}_{(aq.)}$. The spectroscopic information on the electronic structure of these aqueous manganese species also provides benchmark data for future theoretical calculations and steady-state and time-resolved photoelectron spectroscopy experiments with those ions. Finally, the incorporation of microfluidic devices to the liquid micro jet technique constitutes a novel and general approach to realize photoelectron spectroscopy experiments with unstable, transient species (with lifetimes on the order of seconds) that drive redox chemistry in aqueous solution.

This thesis is organized into seven chapters. Chapter 2 describes the theoretical and experimental background that forms the basis of the results and discussions presented throughout the thesis. Chapter 3 focuses on the experimental setups and methods implemented to perform the liquid jet XPS and RPES experiments reported here, including the design and optimization of a micro-mixing scheme and an electrolysis cell liquid jet for sample delivery of unstable ions. Chapters 4 – 7 present

and discuss the main findings derived from this work. A comprehensive study of the electronic structure, molecular bonding and solution phase behavior of $MnO_4^-{}_{(aq.)}$ and $MnO_4^{2-}{}_{(aq.)}$ ions are presented in Chapters 4 and 5, respectively. The redox energetics and thermodynamic information derived from the spectroscopic data reported in Chapters 4 and 5 is presented in Chapter 6, with a focus on the $MnO_4^{2-}{}_{(aq.)}$ / $MnO_4^-{}_{(aq.)}$ and $MnO_4^-{}_{(aq.)}$ / $MnO_4^{\bullet}{}_{(aq.)}$ redox pairs. Finally, a summary of the main conclusions and an outlook for future work are presented in Chapter 7.

2 Theoretical and experimental background

This chapter describes the theoretical and experimental background that forms the basis of the experimental methods and the interpretation of the results presented in this thesis. Such theoretical concepts allowed the recorded spectroscopic data to be used to map the electronic structure and redox energetics of MnO_4^- $_{(aq.)}$ and MnO_4^{2-} $_{(aq.)}$ ions. In addition, data treatment methodologies and the overall interpretation of the aqueous phase data relied on previous investigations of water and aqueous solutions using liquid jet X-ray spectroscopy, as will be described here.

The chapter is divided into three sections. Section 2.1 introduces an overview on the description of the electronic structure of water and the MnO_4^- and MnO_4^{2-} ions. Section 2.2 presents the thermodynamic relations that allow redox energetics to be derived from electronic structure information. Section 2.3 focuses on the underlying physical phenomena and theoretical concepts related to the XPS technique, starting from a broader perspective and then focusing on aqueous phase photoemission. Section 2.3.1 presents the general characteristics of the liquid water photoelectron spectrum. Section 2.3.2 describes the phenomenon of photoemission in the condensed phase, including the probing depth / electron KE dependence that allows different hydration environments to be studied. Second order electron emission and the RPES technique – which facilitates the element-specific study of both intramolecular and intermolecular electronic interactions – are described in Sections 2.3.3 and 2.3.4, respectively. Finally, Section 2.3.5 introduces an overview on (photoelectron) spectroscopy experiments with MnO_4^- and MnO_4^{2-} solid-, aqueous-, and gas-phase samples.

2.1 Electronic structure

2.1.1 Water and aqueous solutions

The structure and properties of matter are governed by its fundamental components, electrons and nuclei in atoms and molecules [91]. Their (correlated) dynamics underpin chemical bonding transformations and energy transfer processes. Electronic spectroscopy experiments allow the determination of electron energetics by monitoring the response of the interrogated system to light-matter interactions. The postulates of quantum mechanics and some necessary assumptions allow such energetic (spectroscopic) information to be associated with the distribution of electrons (or electronic structure) in, for example, a molecular system [91].

The first aqueous solution electron spectroscopy experiments were performed by Paul Delahay and his group using a rotating wheel approach as the sample source [70]. Manfred Faubel and Bernd Winter later built on this work by recording KE-dispersed photoelectron spectra in the aqueous phase [21, 92]. The energetic information obtained from these experiments has been interpreted based on the electronic structure of gas phase water, appending the gas phase water molecular orbital (MO) labels to the experimentally determined liquid phase BEs [21, 92, 93]. Within this framework, the ground state electronic structure of water can be described by a $(1a_1)^2(2a_1)^2(1b_2)^2(3a_1)^2(1b_1)^2$ electronic configuration, considering a molecular geometry belonging to the C_{2v} symmetry point
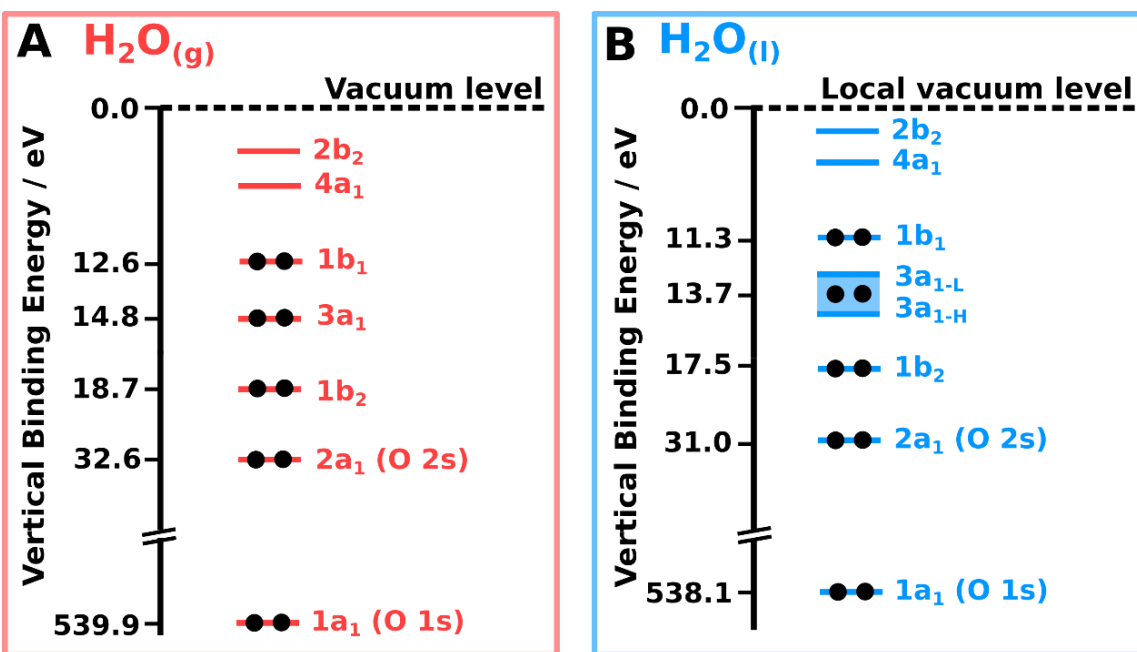
Figure 2.1. MO diagram of water

(A) MO diagram of gas phase water. **(B)** MO diagram of liquid phase water. The values indicated on the BE axis were appended based on References [92, 94]. The light blue fill in panel B highlights a splitting of the $3a_1$ MOs from intermolecular anti-bonding ($3a_{1-L}$) and bonding ($3a_{1-H}$) contributions, respectively (see Reference [95] for details). The meanings of the vacuum level in panel A (also referred to as *vacuum level at infinity*) and local vacuum level in panel B will be explained in Section 2.3.

group [92, 95]. MO diagrams of gas phase and liquid water are shown in Figure 2.1 (panels A and B, respectively). The energy scales in the diagrams have been scaled according to experimentally determined BE values from the literature [92, 94]. The different gas phase and liquid phase energetics observed in Figure 2.1 highlight the effects of condensation on the electronic structure of isolated (gas phase) molecules. The *gas phase versus liquid phase* shifts in BE primarily originate due to [92]:

- Electronic polarization effects across the aqueous phase: the relative permittivity of liquid water results in differential screening of the electrons with respect to the gas phase. The magnitude of this effect is reflected in the Gibbs free energy of hydration [92], as will be discussed for the MnO_4^- ion in Chapter 6;
- The presence of surface dipoles at the gas-solution interface: partial hydration results in a re-orientation of molecules near the surface and an additional (surface) potential affecting the magnitude of the electron BEs [92];
- The existence of the hydrogen bonding network in liquid water: differential, orbital-specific gas versus liquid BE shifts reflect hydrogen-bonding-induced charge delocalization, *i.e.* different degrees of intermolecular covalency [8, 92].

In addition, the existence of a continuum of different and constantly evolving hydration configurations in liquid water results in broader photoelectron spectral distributions [95]. Overall, intermolecular interactions are responsible for the differences in the electronic structure between gas-phase and liquid water, as highlighted, for example, by the splitting in the $3a_1$ MOs in the latter (see Figure 2.1 and figure caption) [95].

When considering aqueous solutions, the electronic structure of the solute is influenced by the polar environment of liquid water and, similarly, water molecules are influenced by the polarizability of the solute [80, 95], with different solute-solvent configurations being adopted in the bulk of the solution or in the presence of interfaces [20, 96]. Nuclear geometric structural changes also arise due to solute-solvent interactions, such as solute-solvent spin interactions [97], solvent effects on the nuclear magnetic shielding of the solute [98], and breaking of the solvent structure due to hydration of the solute [99]. For TMCs – particularly for the $MnO_4^-{}_{(aq.)}$ and $MnO_4^{2-}{}_{(aq)}$ *tetra-oxo* complexes considered in this work – the BE values associated with the electron distributions in the solute overlap with those of the water solvent molecules [87, 100].

Theoretical models of the electronic structure of water and aqueous solutions have focused on simulating the valence photoelectron spectra of liquid water and solvated ions [95, 101]. The combination of XPS and theoretical calculations allowed solute-solvent and gas-liquid solvent energetic shifts to be attributed to intermolecular interactions between specific solute and solvent MOs [95]. Experimental results and ab initio calculations have also investigated hydrogen bonding effects and the existence of different hydration configurations, associated polarization screening, surface potentials and charge delocalization, with fingerprints in the spectra of water clusters [102]. In addition, similar studies have investigated the effect of thermal fluctuations and intermolecular coupling on the electronic density of states, which is responsible for spectral broadening in liquid water with respect to the gas phase [103].

The existence of intermolecular interactions renders the application of MO electronic-structure representations (a single-configuration electronic structure picture) for isolated molecules inadequate for a true representation of the electronic structure of aqueous solutions. Such descriptions originate in the gas-phase-based analysis of the liquid PES spectra of water (as discussed above and in Section 2.3.1) and are generally adopted [8, 95] to facilitate comparison of the energetics of the solute species across phases. However, the condensed phase nature of aqueous solutions needs to be taken into account in order to interpret the physical processes responsible for XPS and RPES experiments, as will be described across Sections 2.3.2 – 2.3.4.

2.1.2 Permanganate and manganate ions

The distribution of the chemically-active (*outer valence*) electrons in MnO_4^- is qualitatively described by a $(3t_2)^2(1e)^2(6a_1)^2(4t_2)^2(1t_1)^2(2e)^0(5t_2)^0$ ground state electronic configuration, which considers a molecular geometry belonging to the T_d symmetry point group [104, 105]. The $3t_2$ and $1e$ MOs are linear combinations of the Mn 3d and O 2p atomic orbitals and represent metal-ligand bonding interactions. The $6a_1$ MO is primarily associated with Mn 4s, 3p and O 2pσ bonding interactions. The $4t_2$ and $1t_1$ orbitals are O-localized, Mn-O non-bonding orbitals, with respective degrees of O-O bonding and anti-bonding character. The $2e$ and $5t_2$ unoccupied (*virtual valence* [106]) orbitals are the Mn-O anti-bonding analogues of the $3t_2$ and $1e$ bonding features. The electronic structure of

MnO_4^- is illustrated in Figure 2.2 (left panel). The $4a_1$ (Mn 3s), $2t_2$ (Mn 3p), and $5a_1$ (O 2s) MOs associated with *inner valence* electrons, as well as the O-centered $3a_1$ and the Mn-centered, spin-orbit split, $1t_2$ MOs associated with the *core level* electrons are also shown in the figure.
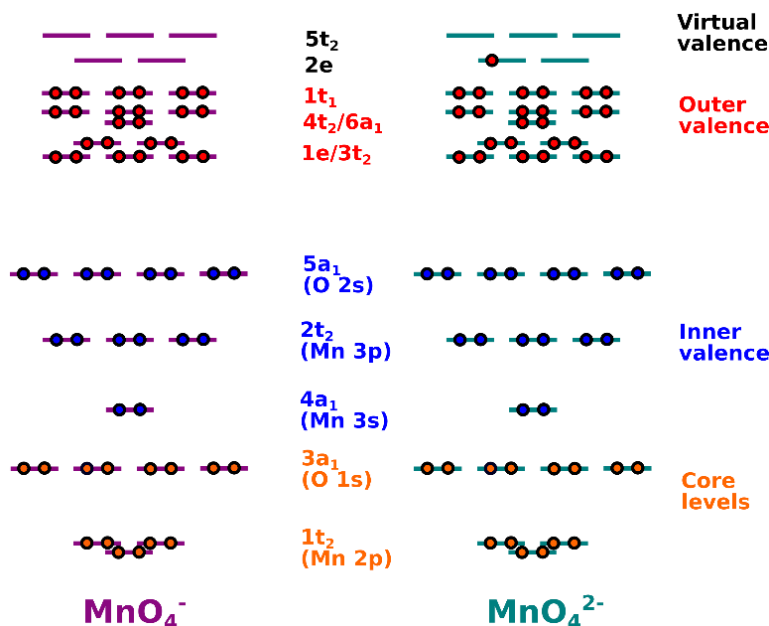
Figure 2.2. MO diagrams of MnO_4^- and MnO_4^{2-}

MO diagrams of MnO_4^- and MnO_4^{2-} based on the isolated molecule calculations from References [105, 107-110]. The core levels (Mn 2p, O 1s), inner valence (Mn 3s, Mn 3p, O 2s), outer valence and virtual (unoccupied) valence are highlighted in color and labelled according to a T_d molecular symmetry, as explained in the text. For MnO_4^-, the virtual valence is described by the 2e and $5t_2$ MOs. For MnO_4^{2-}, the 2e orbital is partially occupied in the ground state of the ion, and hence only the $5t_2$ orbital is described as part of the virtual valence.

Theoretical calculations show a retention of an average tetrahedral ion symmetry in moving from the gas [108] to the (bulk) aqueous phase. The latter was concluded after comparison of the isolated molecule geometries in Reference [108] with aqueous phase nuclear geometries associated with Reference [111] and provided by Jógvan Magnus Haugaard Olsen [112]. In addition, the $MnO_4^-{}_{(aq.)}$ (from $KMnO_{4(aq.)}$ solutions) and $KMnO_{4(s)}$ average Mn–O bond lengths (162 pm and 163 pm, respectively) [113] and MnO_4^- breathing vibrational mode frequencies ($\nu_1 \sim 104$ meV) and anharmonicity constants [114] were found to be near identical in the aqueous solution and the crystalline solid. These results imply that MnO_4^- retains a tetrahedral geometry in vacuum, as a component of a solid, and in bulk aqueous solution. Consequently, a T_d point group and existing (isolated-molecule) MO diagrams [105, 107, 108] were utilized to assign and label the $MnO_4^-{}_{(aq.)}$ XPS and RPES signals reported in this thesis.

The ground state electronic structure of isolated MnO_4^{2-} ions has been described following the same MO considerations as for MnO_4^- [109, 110]. The main difference in the electron distribution between MnO_4^- and MnO_4^{2-} ions is the occupancy of the 2e MO in the latter, as illustrated in the right panel of Figure 2.2. To highlight the different occupancy of the 2e MO in both ions, MnO_4^- and MnO_4^{2-} are generally respectively referred to as d^0 (closed shell) and d^1 (open shell) configurations, given the Mn 3d atomic-character of the 2e MO [109]. In addition, similar average Mn-O bond lengths were

reported for $K_2MnO_{4(aq.)}$ [113] and $K_2MnO_{4(s)}$ [115] (167 pm and 166 pm, respectively), suggesting similar ion symmetries in both phases. With this information in mind, the XPS and RPES results reported for MnO_4^{2-} $_{(aq.)}$ in this thesis were assigned considering a T_d group symmetry and the MO diagram presented in Figure 2.2 (right), which was adapted from Reference [109].

In addition, interpretation and assignments of the UV-visible absorption bands in MnO_4^- $_{(aq.)}$ and MnO_4^{2-} $_{(aq.)}$ solutions were considered when reporting the aqueous energetics and RPES results. Figure 2.3, panel A shows UV-visible absorption spectra recorded from $NaMnO_{4(aq.)}$ (top) and $KMnO_{4(aq.)}$ (bottom) solutions at 0.25 M concentrations. The electronic state and associated predominant MO transitions are labelled in accordance with Reference [104]. At such concentrations, the spectra show similar optical transitions despite the presence of different cations. Panel B in Figure 2.3 shows a UV-visible absorption spectrum recorded from a 0.2 M MnO_4^{2-} $_{(aq.)}$ in 4 M $NaOH_{(aq.)}$ solution over a narrower spectral range (see Section 3.2.1 for details about sample preparation). The spectra were fit using a set of Gaussian functions in order to extract the energies associated with different spectral bands, particularly of those attributed to transitions between the $1t_1$, $2e$, and $5t_2$ MOs, as will be discussed in Chapters 4 and 5. The results of these fits are summarized in Table 2.1.
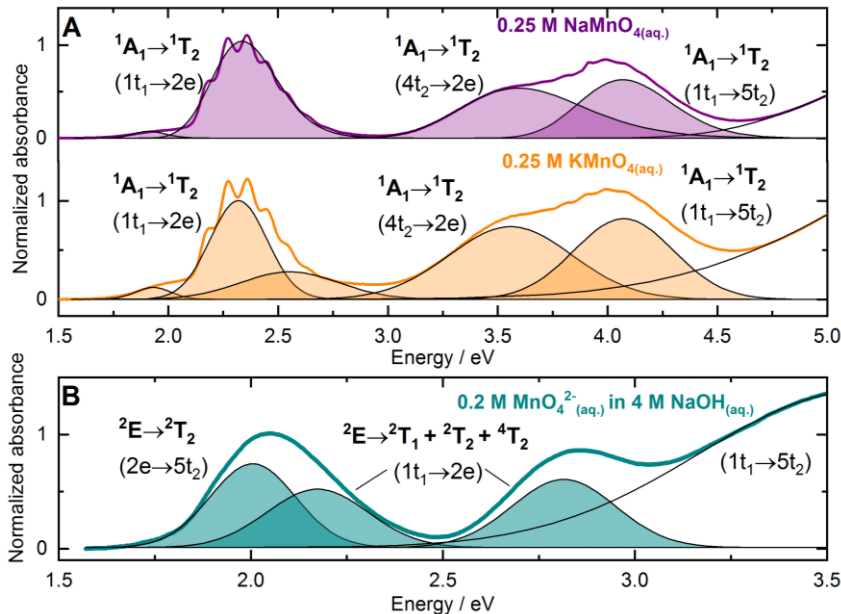
Figure 2.3. UV-visible absorption spectra of MnO$_4^-$$_{(aq.)}$ and MnO$_4^{2-}$$_{(aq.)}$

UV-visible absorption spectra and cumulative Gaussian fits (see Table 2.1 for the associated fit results) to the MnO_4^- $_{(aq.)}$ and MnO_4^{2-} $_{(aq.)}$ electronic absorption bands. **(A)** $NaMnO_{4(aq.)}$ (top) and $KMnO_{4(aq.)}$ (bottom) solution spectra, labelled according to Reference [104]. The lower-intensity band at ~1.9 eV is associated with spin and / or orbital-angular-momentum forbidden transitions to the $^3T_2$ and $^1T_1$ states [111]. **(B)** 0.2 M MnO_4^{2-} $_{(aq.)}$ in 4 M $NaOH_{(aq.)}$ solution spectrum, labelled according to References [109, 116].

Table 2.1. Bands in the UV-visible absorption spectra of MnO$_4^-$$_{(aq.)}$ and MnO$_4^{2-}$$_{(aq.)}$

Fit results and assignments based on References [104, 109, 116] (see the text for details) to the optical bands in the UV-visible absorption spectra of $MnO_4^-$$_{(aq.)}$ and $MnO_4^{2-}$$_{(aq.)}$ shown in Figure 2.3.

$MnO_4^-$$_{(aq.)}$ ($^1A_1 \rightarrow ^1T_2$)	Peak center / eV	$MnO_4^{2-}$$_{(aq.)}$ ($^2E \rightarrow ^2T_2$)	Peak center / eV
$1t_1 \rightarrow 2e$	2.3 ± 0.1 eV	$2e \rightarrow 5t_2$	2.0 ± 0.1 eV
$4t_2 \rightarrow 2e$	3.6 ± 0.1 eV	$1t_1 \rightarrow 2e$	2.2 ± 0.1 eV
$1t_1 \rightarrow 5t_2$	4.1 ± 0.1 eV	$1t_1 \rightarrow 2e$ or $1t_1 \rightarrow 5t_2$	2.8 ± 0.1 eV

MnO_4^- is characterized by a $^1A_1$ ground state, with optical transitions in its UV-visible-absorption spectrum being described as $^1A_1 - ^2T_2$ transitions [104]. The first three main optical bands are predominantly associated with the following MO occupation changes: $1t_1 \rightarrow 2e$, $4t_2 \rightarrow 2e$ and $1t_1 \rightarrow 5t_2$, involving the ligand-based, highest occupied MO (HOMO, $1t_1$), the HOMO-1 ($4t_2$) and the antibonding $2e$ (the lowest unoccupied MO, LUMO) and $5t_2$ orbitals (LUMO +1), respectively [104].

MnO_4^{2-} is described by a ^2E ground state, and the electric dipole allowed transitions are $^2E \rightarrow ^2T_2$ and $^2E \rightarrow ^2T_1$ [109]. With the exception of the $2e \rightarrow 5t_2$ optical band, electron excitations in MnO_4^{2-} are characterized by producing more than one excited state transition that results in multiplet structures in the absorption spectrum [109]. For example, the $1t_1 \rightarrow 2e$ electron excitation results in the $2^2T_1 + 2^2T_2 + ^4T_2$ excited states [109]. Similarly, three bands in the UV-visible absorption spectrum have been associated to the $1t_1 \rightarrow 5t_2$ transition [116, 117]. In the UV-visible absorption spectrum shown in Figure 2.3 (panel B), the first optical band has been labelled as a $2e$ (HOMO) $\rightarrow 5t_2$ (LUMO+1), based on References [109, 116]. The second and third band have been assigned as $1t_1$ (HOMO-1) $\rightarrow 2e$ (HOMO), based on Reference [109]. However, for the third band, a $1t_1$ (HOMO-1) $\rightarrow 5t_2$ (LUMO+1) assignment has also been suggested [116]. The shoulder observed in Figure 2.3, panel B around 3.5 eV belongs to one of the other multiplets associated with this transition (the third one occurring at ~4.2 eV) [116].

2.2 Redox energetics

Aqueous phase electronic structure information can be used to infer energetic parameters that underpin electron transfer reactions in aqueous solution.

From a thermodynamic point of view, redox reactions are driven by a difference in redox potential between the reactant partners – *i.e.* the electron donor and acceptor species. Provided that coupling between the donor and the acceptor is weak, a *full* redox reaction can be studied in terms of two *half* reactions, each one corresponding to oxidation of the electron donor and reduction of the electron acceptor. An oxidation half reaction can be described as

$$D_{(aq.)} \rightarrow D_{(aq.)}^+ + e^-$$
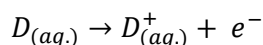
where $D_{(aq.)}$ represents the *reduced* (or *donor*) species and $D_{(aq.)}^+$ represents the *oxidized* product. Similarly, a reduction half reaction can be represented as

$$A_{(aq.)} + e^- \rightarrow A_{(aq.)}^-$$
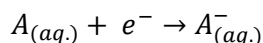
where $A_{(aq.)}$ represents the *oxidized* (or *acceptor*) species and $A_{(aq.)}^-$ represents the *reduced* product. The full electron transfer reaction between the donor and the acceptor is then expressed as

$$D_{(aq.)} + A_{(aq.)} \rightarrow D_{(aq.)}^+ + A_{(aq.)}^-$$
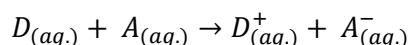
Being dependent on the energetics of the outer valence electrons that are directly involved in the reaction, the redox potential associated with each half reaction is intrinsically correlated with the electronic structure of the reactants [118]. In this way, this redox parameter is specifically dependent on two key reactant electronic properties: ionization energies (particularly for the electron donor) and electron affinities (particularly for the electron acceptor) [119]. Within that context, as described in Section 1.2.2, a parallel can be drawn between electron transfer and ionization events [85, 86].

During a (full, ground adiabatic state) redox reaction, reduced and oxidized species are initially produced in a geometrically excited state. The energy required for the solvated reactants to adopt the electronic structure and nuclear configuration of the reaction products is termed the *reorganization energy* (λ), which can be individually considered for the reduction and oxidation half reactions (λ_{red} and λ_{ox}, respectively) [120]. There are two terms contributing to the reorganization energy: a vibrational component, and a solvational component, the latter specifically highlighting the effect of solvation on the electron transfer event [85].

Similarly, during ionization, an electron is removed from the chemical system in its ground state (*reduced*) configuration to produce an excited state (*oxidized*) configuration with an excess energy that is eventually transferred to the aqueous solution in the form of thermal energy [120]. The transitions associated with the aforementioned initial and final states are termed *vertical* ionizing transitions, given that the time scale in which the molecule transitions from the ground state to the excited state during ionization is fast compared to the timescale of nuclear motion, which can be neglected [77, 100]. The energies associated with such transitions are termed *vertical ionization energies* (VIEs) and are equivalent to the BEs determined during XPS experiments, as will be explained in Section 2.3. The term *vertical* indicates that promotion of an electron into the vacuum occurs without nuclear rearrangement. Similarly, *vertical electron affinities* (VEAs) are associated with the most probable energy required for *electron attachment – i.e.* as opposed to the electron promotion event considered for VIEs [121].

In the case of oxidation processes, which are the focus of the work presented here, the half reaction can be viewed as a combination of vertical ionization and reorganization in which electron transfer occurs on a faster timescale compared to nuclear rearrangement [85]. As a result, the initially reduced solute loses an electron to produce its *oxidized* form, which relaxes to equilibrium after solute and solvent thermal-induced rearrangements to accommodate the transfer of charge. These rearrangements are quantified by the associated reorganization energy, λ_{ox} [85]. The energetic relations between VIE, VEA and λ_{ox} are illustrated in Figure 2.4.

As can be seen from Figure 2.4, the difference between VIE and λ_{ox} corresponds to the adiabatic ionization energy, AIE, a characteristic minimum energy threshold for liberating electrons to vacuum. AIE can be linked to the Gibbs free energy of oxidation, ΔG_{ox}, and its associated enthalpic and entropic components [122]. The enthalpic component is related to the energy gap between the equilibrium geometries of the initially reduced solute and the oxidized product. However, the VIEs recorded in XPS measurements refer to the non-relaxed oxidized state. Furthermore, as described in Section 2.3, such experimental VIEs are referenced to the local vacuum level. VIEs should be referenced to the vacuum level at infinity in order to relate their values to ΔG_{ox} via the electrochemical potential (see Figure 2.5 in Section 2.3 for details). A theoretical treatment of the entropic component of electron transfer in aqueous condensed-phase media can be found in Reference [122].
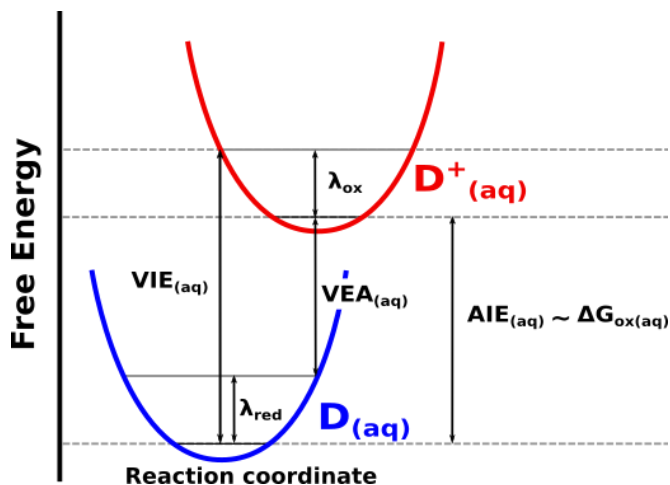
Figure 2.4. Energetic relations between ionization energies and redox parameters

Schematic (harmonic) potential energy curves depicting ionization or electron transfer from a ground state, reduced, donor species (D $_{(aq.)}$) to its corresponding excited state, oxidized configuration (D$^+_{(aq.)}$). The processes can be described by the D $_{(aq.)}$ → D$^+_{(aq.)}$ + e$^-$ half redox reaction, as discussed in the text. The diagram highlights the energetic relations between VIE (vertical ionization energy), VEA (vertical electron affinity), AIE (adiabatic ionization energy), ΔG_{ox} (Gibbs free energy of oxidation), and λ_{ox} and λ_{red} (oxidation and reduction reorganization energies, respectively).

VIEs have been previously applied to the study of the energetics of oxidation half reactions, both from purely theoretical [85, 123-125] and combined theoretical and experimental approaches [83, 126-129]. In the latter, VIEs were determined from liquid jet XPS experiments and redox parameters were obtained using Expressions 1 – 6 presented below. As described in Chapter 6, the work presented in this thesis will apply a similar approach, expanding on initial theoretical work on the MnO$_4^-$$_{(aq.)}$ / MnO$_4^{2-}$$_{(aq.)}$ redox pair [85] based on experimental VIEs determined from XPS and RPES experiments performed with MnO$_4^-$$_{(aq.)}$ and MnO$_4^{2-}$$_{(aq.)}$ solutions.

AIE and ΔG_{ox} will be considered to be equivalent as in previous liquid jet XPS determinations of redox parameters, assuming the differences in local vacuum level and vacuum level at infinity to be relatively small [83, 126, 127] and ignoring entropic effects in the first solvation shell – *i.e.* solvent molecules directly interacting with the reactant [122]:

$$AIE = VIE - \lambda_{ox} \sim \Delta G_{ox} \ (1)$$

Hence, λ_{ox} can be inferred from VIEs by combining experimentally determined BEs with thermodynamic information from electrochemistry. In that case, the redox potential (E^0) referenced to the standard hydrogen electrode (SHE) is related ΔG_{ox} (AIE) via the following expression [17, 128, 130, 131]:

$$\Delta G_{ox} = -E^0 + E_{SHE} \ (2)$$

where E_{SHE} is the absolute potential of the SHE (4.44 ± 0.02 V at 298 K [132]). Redox potentials can also be referenced against the reversible hydrogen electrode (RHE), which takes into account the pH of the solution [133], in situations where the redox processes are pH-dependent

$$E^0_{RHE} = E^0 - 0.059 \ pH \ (3)$$

Alternatively, within the LRA, λ_{ox} can be inferred purely from spectroscopic information – *i.e.* independently from electrochemical (ΔG_{ox}) data – using the following equation [83, 85, 126, 128, 134]:

$$\lambda_{ox} = \frac{\left(FWHM_{IB}/2\sqrt{2ln2}\right)^2}{2k_B T} \quad (4)$$

where $FWHM_{IB}$ characterizes the inhomogeneously broadened width of the photoelectron peak, which is assumed to take on a Gaussian form, k_B is the Boltzmann constant, and T is the solution temperature. The overall ionization peak width is only partially determined by its nascent linewidth and inhomogeneous broadening term, being further widened by experimental resolution limitations and potential lifetime broadening effects. As explained in Section 3.4, analysis of the XPS data presented here confirmed that lifetime broadening effects are negligible in the valence spectral region. $FWHM_{IB}$ can therefore be determined as follows:

$$FWHM_{IB} = \sqrt{FWHM_G^2 - FWHM_{IR}^2} \quad (5)$$

Where $FWHM_G$ is the Gaussian component of the peak width and $FWHM_{IR}$ represents the broadening contribution from the overall instrumental resolution (see Section 3.3. for details).

Finally, within the limits of the LRA [85, 128] – which considers changes in the polarization of the solvent to be linearly dependent on the charge of the solute – *i.e.* the donor and acceptor species [135] – VEA values can be estimated using the following expression:

$$VEA = 2AIE - VIE \quad (6)$$

2.3 X-ray photoelectron spectroscopy

This section describes the fundamental concepts required for the interpretation of PES (and XPS) experiments. As described in Section 2.1.1, the interpretation of liquid water PES experiments in the literature has been based on the electronic structure assignments of gas phase water. However, the condensed phase nature of liquid samples requires consideration of the principles of PES from dense, strongly interacting subunits, as applied to the PES of solids. Hence, this section will present elements concerned with both gas phase and solid phase PES.

During a PES experiment, BEs are determined from the measured KEs of electrons produced after ionization of the sample in a vacuum environment (see Section 1.2 for details). The energy of an electron in a chemical system is ideally defined with respect to the energy of an electron at rest at a point in vacuum and at an infinite distance from the sample – *i.e.* the vacuum level at infinity, E_∞ [136, 137].

E_∞ is the common energetic reference in PES experiments with gases [137]. Figure 2.5 illustrates the energetic relations between the incident photon energy ($\hbar\omega$), and the measured KE – with respect to E_∞ – in a gas phase PES experiment.
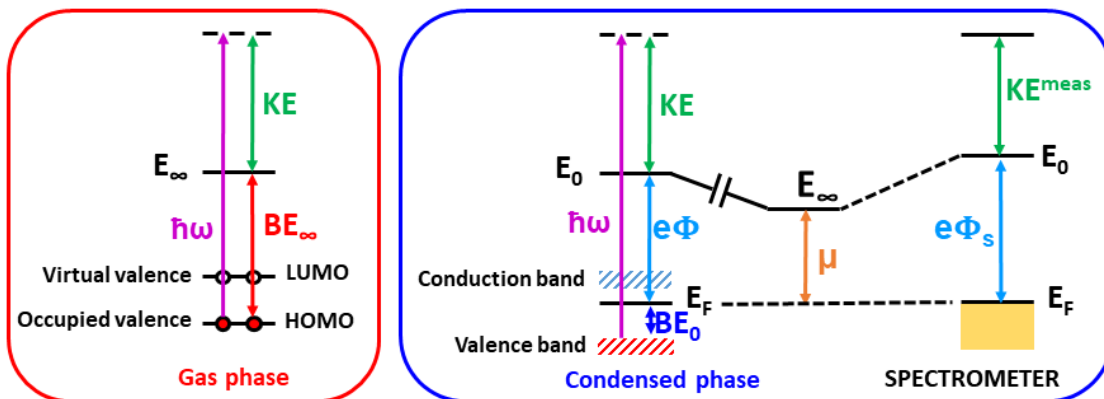
Figure 2.5. Energetics in photoelectron spectroscopy

Diagram illustrating the energetics of a photoemission process in PES, showing the relationships between photon energy ($\hbar\omega$), electron kinetic energy (KE) and binding energy (BE) for gas phase (left) and condensed phase (right) samples, as described in the text. For the condensed phase, the Fermi level (E_F), work function of the sample ($e\Phi$) and the spectrometer ($e\Phi_s$), and electrochemical potential ($\bar{\mu}$) of the sample are shown. The different vacuum levels as defined in the text are also indicated: local vacuum level (E_0) and vacuum level at infinity (E_∞). HOMO: highest occupied molecular orbital; LUMO: lowest occupied molecular orbital.

The schematic shows that the BE of an electron with respect to E_∞ (BE_∞) – in this case from the occupied valence – is given by [62]:

$$KE = \hbar\omega - BE_\infty \text{ (9)}$$

The energetics of condensed phase PES are explained by the photoelectric effect, as first observed by Heinrich R. Hertz in 1887 and explained and described by Albert Einstein in 1905 [63], by the following equation [63, 138]

$$KE^{max} = \hbar\omega - e\Phi \text{ (10)}$$

where KE^{max} is the maximum electron KE, $\hbar\omega$ the photon energy and $e\Phi$ the work function of the sample, which is both sample- and detection geometry-dependent [138]. $e\Phi$ is the minimum energy required to remove an electron from a given point inside the sample and place it (at rest) at the closest point outside of the material where the electron is no longer affected by image forces [138, 139]. When an electron is emitted into vacuum – such as during a PES experiment – the latter point is defined as the *local vacuum level, E_0* [136]. As a result, $e\Phi$ can be defined as [140]

$$e\Phi = E_0 - E_F \text{ (11)}$$

where E_F is the so-called Fermi level. For an electron with a BE below the Fermi level (and measured with respect to it, BE_F)

$$KE = \hbar\omega - BE_F - e\Phi \text{ (12)}$$

As opposed to the case for gas samples, E_∞ cannot generally be accessed experimentally for condensed phase samples [137, 141]. In this case, electrons are subject to the sample's work function, which constitutes the sum of the electrochemical potential ($\bar{\mu}$) and outer (Volta) potential [138]. Figure 2.5 illustrates the relationship between $\bar{\mu}$, E_F, and E_∞ [137]. During a condensed phase PES

experiment, the sample is held in electrical contact with the spectrometer, with both most often being grounded to Earth, which results in a contact potential difference ($\Delta\phi$) that is required to equilibrate E_F [137]. $\Delta\phi$ can be expressed as [138]:

$$\Delta\phi = e\Phi - e\Phi_S \ (13)$$

where $e\Phi_S$ is the work function of the spectrometer. As a result, KEs are measured with respect to E_0 of the spectrometer, whose value is generally unknown relative to E_∞ (or E_0 of the sample) [137]. Then, as illustrated on the right panel of Figure 2.5 [138]:

$$KE_{meas} = \hbar\omega - BE_F - e\Phi_S \ (14)$$

Consequently, solid phase PES data is usually referenced to E_F, which can be linked to E_0 of the sample via $e\Phi$, as described above. A more in-depth discussion can be found in References [138, 142].

For aqueous samples, E_F lies in the band gap of liquid water (within the wide band gap semiconductor model) and has no associated electron density. Although E_F [143] and $e\Phi$ [144] values for aqueous solutions have been reported in the literature, PES spectra in the aqueous phase have thus far been referenced to E_0 and using predetermined reference energies for neat liquid water's lowest ionization energy, *i.e.* the 1b$_1$ photoelectron peak, as will be described in the next section [92, 94, 95]. Consequently, a BE_0 referencing scale is generally adopted for aqueous phase samples, as is utilized here.

2.3.1 The liquid water XPS spectrum

Exemplary photoemission spectra of liquid water are shown in Figure 2.6, highlighting its full electronic structure and ionization behavior – i.e. the outer and inner valence (panel A) and core-level (panel B) spectral regions. As can be seen in Figure 2.6, the first ionizing transition in liquid water – (termed $1b_{1(l)}^{-1}$ within a MO framework) has been determined to have an associated BE of 11.31 ± 0.04 eV [94] which is generally adopted as an energetic reference to calibrate the BE scale in aqueous solution PES spectra [95].
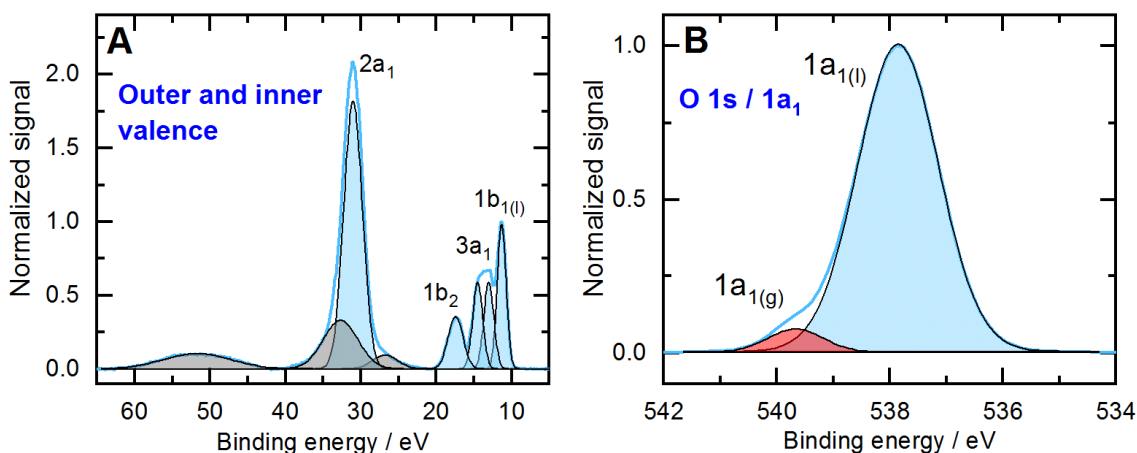
Figure 2.6. Photoelectron spectra of liquid water

(A) Outer and inner valence spectrum recorded at a photon energy of 635 eV. **(B)** O 1s / 1a$_1$ spectrum recorded at a photon energy of 1135 eV. Cumulative Gaussian (A) and Voigt profile (B) fits to the background-corrected water (0.05 M NaCl$_{(aq.)}$) background-corrected spectra (see Section 3.4.1 for details) are shown by light blue fills (liquid phase water signals), red fill (gas phase water signals), and grey fills. The latter are primarily associated with electron energy-loss background signals [92]. Ionization features are labelled within a MO framework and according to the ground state MOs of water that are deemed to be involved in the ionization process, as described in the text.

The valence photoelectron spectrum of liquid water spans the ~10 eV – 38 eV BE range, including both liquid and gas phase contributions. The data shown in Figure 2.6 was recorded at the P04 beamline at PETRA III (see Section 3.1.2 for details) using a photon energy of 635 eV. As will be explained in more detail in Section 3.2.1, liquid jet experiments require the sample to be sufficiently electrically conductive to mitigate streaming potentials [94] and photoionization-induced sample charging. Consequently, nearly-pure water spectra are measured from water samples with a low concentration of salt – usually ~0.05 M of NaCl or NaI. The spectra shown in Figure 2.6 have been baseline corrected and the signals were cumulatively fit using a set of Gaussian (panel A) or Voigt profile (panel B) functions (see Section 3.4.1 for details).

2.3.2 Photoemission in the condensed phase

Photoemission consists of an incoming photon interacting with the system (being absorbed by the sample), with a photoelectron subsequently being created and emitted [62]. It is a many body problem where photon, photoelectron, and remaining particles in the system (remaining electrons and nuclei) are correlated and collectively interact during the light-matter interaction and electron scape processes. The term photoemission includes both photoionization (as it occurs during a PES / XPS experiment, as described in the previous section) as well as second order electron emission (as it occurs during an RPES experiment and will be described in Sections 2.3.2 and 2.3.3). This section presents the basis of photoemission in condensed media with a specific focus on the aqueous phase.

A simplified model to explain photoemission in the condensed phase is the three-step model [145]. The three-step model artificially separates and describes the overall process in terms of the probabilities associated with three independent, consecutive processes: (1) photon absorption (electronic excitation), (2) propagation of the generated photoelectron through the sample, and (3)

transmission of the photoelectron through the sample's surface into vacuum [62, 146]. A more refined quantum mechanical approach, the one-step model, considers condensed-phase photoemission as a single event. During this event, a photon is absorbed by the multi-electron system to reach a final (photoionized) state when certain boundaries conditions are met – *i.e.* when the electron has travelled through the sample and through the sample´s surface to reach vacuum [62, 146].

In the next paragraphs, the processes of photo-absorption, photoelectron propagation through the sample and exiting through its surface will be discussed for aqueous solutions, considering the three-step model proposed by William Spicer in 1958 [147-149].

1. *Photo-absorption:* absorption of photons by solute and solvent molecules in the liquid sample results in the generation of "delocalized" photoelectrons inside the aqueous phase medium [148]. The light-matter interaction process is described by the ionization quantum yield, that is, the emitted photoelectron / absorbed photon ratio per unit area and time [148]. This ratio is dependent on the reflectivity and attenuation length of the ionizing radiation as it passes into and through the sample medium, respectively, and the ionization cross section. For soft X-rays in liquid water, the penetration depth is 330 nm [74]. As a result, given that photoelectrons are sampled from nanometer depths into the liquid (as will be explained in the next paragraph), there is almost no attenuation of photons by absorption by water molecules on the relevant length scale of photoemisison spectroscopy [148].

2. *Scattering in liquids:* the probability of an electron to escape the liquid phase depends on the inelastic mean free path. After the electrons are ejected from the photoabsorber (e.g. a solute or a solvent molecule), there will be a probability for scattering events to occur that will affect both their kinetic energy and / or their orientation towards the detector. Depending on the kinetic energy values, the electrons can encounter elastic scattering, inelastic scattering, or both [73, 74]. For the liquid phase, if focusing on the inelastic scattering processes that affect the photoemission spectrum, the liquid region from where the produced electrons can reach the detector can be approximated to be equal to the effective attenuation length (EAL), the distance over which there is a probability of 1/e for an electron to be inelastically scattered. This approximation is valid at electron KEs higher than 200 eV, in which case electron scattering in liquid water occurs primarily due to inelastic collisions, and EAL values are thus similar to the inelastic mean free path (IMFP) [73, 74]. At lower KEs, both elastic and inelastic scattering become important and have an effect on the EAL [73, 74]. Figure 2.7 shows the dependence of EAL with electron KE for liquid water [150]. By tuning the photon energy during XPS experiments, photoelectrons with KEs corresponding to different probing depths into the liquid can be sampled. In this way, aqueous–gas interfaces or (predominantly) bulk-liquid environments can be probed [151, 152].

3. *Transmission through the solution-gas interface:* photoelectrons that reach the interface have to overcome the surface dipole potential to cross the sample-vacuum barrier [148]. The surface potential at the water-vapor interface originates from the net dipole moment of the water ensemble and establishment of a net molecular orientation close to the interface [96]; the value of this quantity has been calculated but not yet experimentally measured [96, 153] due to the complexity in disentangling this effect from other potentials affecting the gas-solution interface – for example, streaming potentials in liquid jets [94].
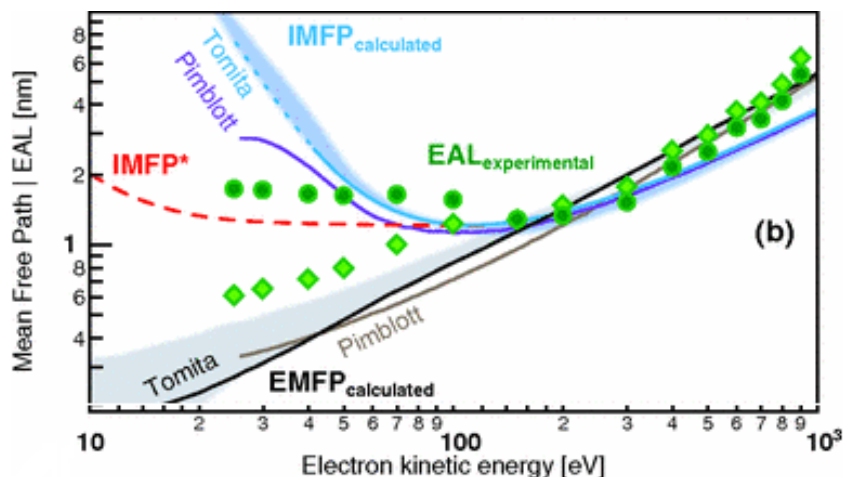
Figure 2.7. Electron attenuation length as a function of kinetic energy

EAL values and IMFP dependence as a function of KE in liquid water (see Reference [150] for details). Reprinted Figure with permission from [150] Copyright 2013 by the American Physical Society. 10.1103/PHYSREVLETT.111.173005

2.3.3 Second order emission (autoionization)

This section explains the second-order electron emission processes that can take place after initial photoionization or, alternatively, (resonant) photoexcitation of an electron into the virtual valence manifold. In line with the objectives of this thesis, these autoionization phenomena will be described for aqueous molecular solutes in an aqueous environment.

After an electron has been removed from or excited within the solute, the overall molecular system is left in an excited state characterized as having a vacancy or hole associated with photoelectron removal. If an electronically core-excited ion state is formed upon photoionization, the excited state, will relax on a (sub) femtosecond timescale. In light atoms, this most often occurs by re-filling the vacancy with a lower-energy electron – usually from the valence manifold – with energy being liberated as a result. The excess energy can be released either via radiative decay (that is, via X-ray emission [154]) or non-radiative decay. The latter can take place via second order electron emission [155] (be it intramolecular or intermolecular) or vibronic relaxation (that is, conversion of electronic to vibrational energy [156]).

Non-radiative decay after inner-shell often results in autoionization and is based on the Auger effect [157], in which the core hole left behind after photo-excitation (or photoionization) is refilled by a higher-lying electron and, simultaneously, a partner electron is emitted. The emission of Auger electrons is governed by Coulombic interactions, given its dependence on the overlap between the wave functions associated with the core and valence electrons involved in the process [158]. Relaxation via Auger electron emission predominates over radiative decay for elements with relatively low atomic number [158]. The phenomenon was named after Pierre Auger, who described the effect in 1925 [159]. However, it was originally reported by Lise Meitner in 1922 [160].
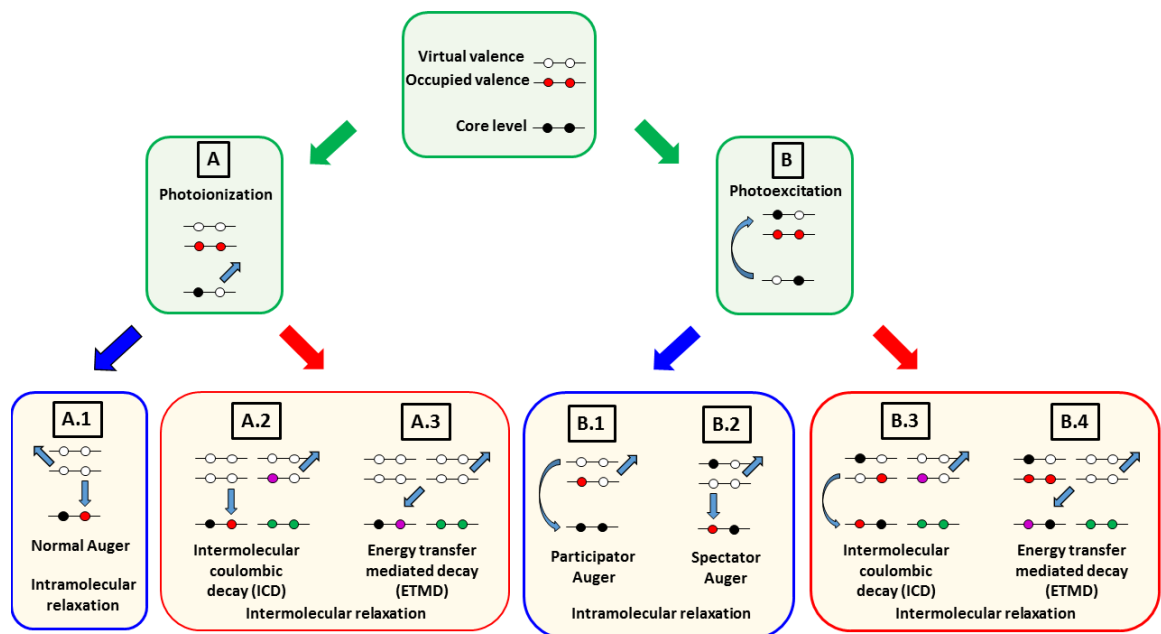
Figure 2.8. Overview of auotionization processes

Overview of non-resonant (following photoionization) and resonant (following photoexcitation) intramolecular and intermolecular autoionization processes. The labels refer to the description of each process as presented in the text. This Figure was produced considering the content of a similar figure in Reference [161].

Spectrally, Auger electrons are distinguished from direct photoemission by having approximately constant KE, independent of the photon excitation energy. Auger emission takes place on a few- to sub-femtosecond timescale, and can be intramolecular (non-radiative *local* decay) or intermolecular (non-radiative *non-local* decay) in nature. Figure 2.8 shows an overview of such autoionization processes in aqueous solution. Panels A and B show the initial electronic excitation processes: photoionization (non-resonant photo-excitation) and resonant photo-excitation, respectively. Relaxation after photoionization results in emission of an Auger electron, a process known as *normal Auger* emission (panel A.1). When electrons from neighbouring solute or solvent molecules are involved in the de-excitation, the Auger-like pathways are termed intermolecular Coulombic decay (ICD, panel A.2) [75, 162] or electron transfer mediated decay (ETMD, panel A.3) [163].

Relaxation after resonant photo-excitation can lead to *intramolecular Auger* (panels B.1 and B.2) or *intermolecular (non-local) decay* (*resonant* ICD and ETMD in panels B.3 and B.4, respectively). In the case of intramolecular, local decay, when the initially photo-excited electron is directly involved in the de-excitation, the process is referred to as participator Auger emission (panel B.1). Otherwise, it is referred to as spectator Auger emission (panel B.2). In the first case, the final state is equivalent to that achieved through direct ionization, with the binding energy of the emitted electron being mostly independent of the photon energy and equal to that extracted from a regular direct photoemission spectrum. In the second case, the binding energy of the emitted electron varies with photon energy. Its kinetic energy remains approximately constant at all resonances and it is predominantly dependent on the orbital energy of the electrons involved in the de-excitation process.

2.3.4 Resonantly-enhanced photoelectron spectroscopy (RPES)

RPES consists of (resonantly) photo-exciting core-level or valence electrons into the virtual valence (or partially filled valence) and recording the photoelectrons produced through autoionization (*i.e.* secondary electron emission, as explained in the previous section) [8]. Consequently, RPES allows participator and spectator Auger processes – as well as signatures of non-local relaxation phenomena, where present – to be detected [8, 72, 75, 164].

The application of the RPES technique to the study of the electronic structure of solutes provides the following specific advantages [8, 151]:

- Resonant enhancement of signals from valence electronic states with relatively low off-resonant absorption cross-sections, photoelectron features that overlap with dominant solvent signals, and/or samples with relatively low local concentrations [76] – via analysis of participator Auger features, due to constructive interference between direct (non-resonant) photoemission and participator Auger channels with equivalent final states [8].
- Access to solution-bulk electronic structure information of surface-active solutes – given that the relatively high photon energies associated with the excitation of core-level electrons generally, and specifically in the case of O K- and Mn L-edge excitation primarily considered here, results in photoelectron KEs that correspond to solution-bulk spectral sensitivities (see Section 2.3).
- Interrogation of the atomic parentage of different electronic states, MOs, or bonding interactions as well as the couplings between those states or MOs, revealed through the photoexcitation energy dependence of the photoelectron signals as a function of the excitation energy and probed absorption edge [22].

During a typical RPES experiment, the sample is ionized over a photon energy range near an absorption edge and photoelectron spectra are collected over a particular (often valence) energy range. Hence, a photon energy versus BE (or KE) two-dimensional (2D) map is produced. As an example, an RPES map of liquid water [165] is shown in Figure 2.9 (left panel). Integration of the RPES map over the BE range is performed to produce partial electron yield (PEY) X-ray absorption spectroscopy (XAS) proxies of true transmission-based XAS spectra (as displayed on the right panel in Figure 2.9). These spectra can be used to identify resonant photon energies [166].

The data shown in Figure 2.9 spans O K-pre-edge, main edge, and post edge, thus including both resonant photo-excitation (pre-edge) and non-resonant photoionization (main edge and post-edge), as indicated in the right panel by a dashed line. Auger electrons (with constant KE) and direct photoemission signals (labelled as 'direct PE' in the figure) are highlighted in the RPES map on the left panel.

In this thesis, the Mn $L_{II,III}$- and O K-pre-edges were scanned over the outer and inner valence energy range in order to produce RPES maps and PEX-XAS spectra similar to the ones described above (see Section 3.4.2 for details). Additional higher signal-to-noise ratio data was recorded at the resonant photon energies extracted from the PEY-XAS data, allowing participator and spectator Auger, as well as non-local decay (ICD), processes to be identified. Fortunately, the O K-pre-edge of the aqueous Mn tetra-oxo-complexes studied here did not overlap with the water (solvent background) features shown in Figure 2.9.
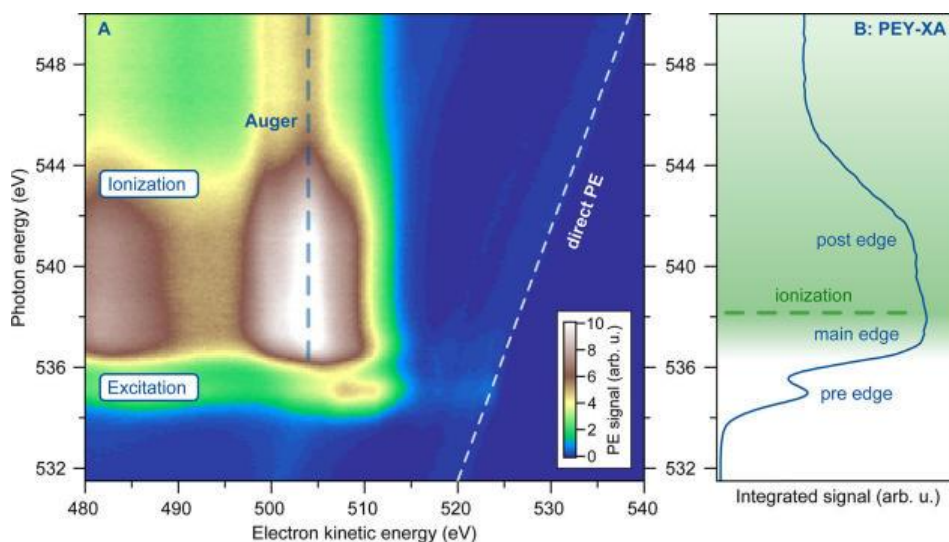
Figure 2.9. RPES data of liquid water

(Left) RPES map highlighting the photon energy ranges associated with excitation and ionization in liquid water. Dashed lines are used to highlight Auger signals (displaying constant KE as a function of photon energy) and direct photoemission ('direct PE') signals (with varying KE as a function of photon energy). **(Right)** PEY-XAS spectra produced from the data shown in the left panel, highlighting the pre-edge, main edge, and post-edge absorption regions. Reprinted with permission from [165]. Copyright (2013) American Chemical Society.

2.3.5 Permanganate and manganate ions

Previously, photoemission techniques have been adopted to study solid $KMnO_4$ and gas phase MnO_4^- samples. Crystalline $KMnO_4$ valence band [167-169], Mn 3p [168-170], Mn 3s [167, 168, 170], O 1s [167, 168, 170], and Mn $2p_{3/2}/2p_{1/2}$ [167, 168, 171, 172] BEs have been determined using He-I, He-II, Al-K_α, and synchrotron radiation sources. Solid state Mn 3p, O 1s, and Mn $2p_{3/2}/2p_{1/2}$ $KMnO_{4(s)}$ RPES experiments have also been performed, revealing partial d-orbital occupation for this formally d^0 compound [173, 174]. The associated O 1s and Mn $2p_{3/2}/2p_{1/2}$ (solid state) $KMnO_{4(s)}$ total electron yield (TEY), X-ray absorption spectra (XAS) have also been reported. In the case of gas phase MnO_4^-, the two lowest VIEs – as well as their corresponding AIEs – were determined from photo-detachment experiments performed at a 6.42 eV photon energy [175]. Similarly, the MnO_4^{2-} ion has been studied by means of solid state XPS on $K_2MnO_{4(s)}$ samples, probing valence band, Mn 3p, Mn 3s, O 1s [168], and Mn $2p_{3/2}/2p_{1/2}$ [168, 171, 172] ionizing transitions.

In the aqueous phase, Mn 1s near-edge XAS [176] and extended X-ray absorption fine structure spectroscopy (EXAFS) experiments on $MnO_4^-{}_{(aq.)}$ and $MnO_4^{2-}{}_{(aq.)}$ solutions have been reported and compared with similar $KMnO_{4(s)}$ and $K_2MnO_{4(s)}$ measurements, extracting the (average) Mn-O bond lengths in both phases [113] (as discussed in Section 2.1.2). All of the aforementioned work sets the stage for the novel aqueous phase experiments reported and discussed throughout this thesis.

3 Liquid jet photoelectron spectroscopy methodology and instrumentation

This chapter describes the methods and instrumentation required to perform the liquid jet photoelectron spectroscopy experiments reported in this thesis. The chapter is divided in four sections. Section 3.1 presents an overview of X-ray light sources and describes synchrotron radiation facilities and beamlines. In most of the work reported here, liquid jet soft X-ray photoelectron spectroscopy experiments were carried out at the U49/2 PGM-1 beamline [177] at the BESSY II (*Berliner Elektronenspeicherring-Gesellschaft für Synchrotronstrahlung II*) synchrotron radiation facility (Helmholtz-Zentrum Berlin für Materialien und Energie, Berlin, Germany) using the SOL³PES (*Solid, Solution and Solar Photoelectron Spectroscopy*) end-station [178]. Additional, complementary experiments were performed at the P04 beamline [179] at the PETRA III (*Positron-Electron Tandem Ring Accelerator III*) synchrotron facility (Deutsches Elektronen-Synchrotron, Hamburg, Germany) using the EASI (*Electronic Structure from Aqueous Solution and Interfaces*) end-station [180]. Section 3.2 focuses on sample preparation and delivery methodologies. It describes the liquid micro-jet technique and two complementary sample source developments – a micro-mixing scheme and an electrolysis cell liquid jet – to enable liquid jet photoelectron spectroscopy experiments with unstable, transient $MnO_4^{2-}{}_{(aq)}$ ions. Section 3.3 describes the main components of the SOL³PES and EASI experimental end-stations. Section 3.4 outlines XPS and RPES experimental protocols and describes the data treatment methodology adopted during the course of this work.

3.1 X-ray light sources

X-rays were first discovered by Wilhelm Conrad Röntgen in 1895 [181]. The term refers to electromagnetic radiation with wavelength in the $0.01 - 10$ nm range – or, equivalently, the $0.1 - 100$ keV energy range. Of interest for the aqueous Mn complexes investigated as part of this thesis are the so called *soft* X-rays, with energies in the $100 - 1000$ eV range [182]. Soft X-rays are capable of probing (outer and inner) valence as well as O 1s and Mn 2p core-electrons in surface- and bulk-sensitive liquid jet photoelectron spectroscopy experiments, as will be explained in more detail in Section 3.4.

The BESSY II and PETRA III third generation synchrotron radiation facilities used in this work provide high photon flux, relatively low peak intensity, photon energy tunable, and high repetition rate soft X-ray beams. Correspondingly, these sources allow data collection efficiencies to be maximized while minimizing non-linear effects and, ideally, sample damage. With the aforementioned properties of synchrotron radiation in mind, the properties of alternative soft X-ray sources, such as discharge lamps (X-ray tubes) [183], liquid metal jets [184], and laser-based upconversion methods [185] will be considered, as will be outlined below. X-ray sources are best characterized by their brilliance, which is defined as the photon flux, per unit solid angle and area over a 0.1% bandwidth centered at the source central frequency. Peak and average brilliances are generally quoted with units of photon s^{-1} $mrad^2$ mm^{-2} (0.1 % bandwidth)$^{-1}$. Different X-ray sources and their peak brilliance are listed in Table 3.1.

Starting with discharge lamps, these sources generate X-rays by applying a voltage between a heated filament (cathode) and a metallic target (anode) in a vacuum-sealed environment [183]. More compact sources are *liquid-metal-jet anodes*, in which an electron beam is focused onto a metal jet with micrometer diameter, with the advantage of minimizing thermal effects at the anode that tend to reduce the source brilliance [184]. Laser-based techniques to generate X-rays include inverse Compton scattering (incoherent hard X-rays) and high harmonic generation (coherent soft X-rays), with the advantage of providing ultra-short pulses for time-resolved experiments [185-187]. Finally, superior in peak brilliance to synchrotron radiation are free-electron lasers, providing high photon flux, coherent radiation, and potentially (sub-) femtosecond pulse duration [188].

Table 3.1. Brilliance of different X-ray sources

X-ray source	Average brilliance / (photons/s mm^2 mrad^2 0.1%BW)	Peak brilliance / (photons/s mm^2 mrad^2 0.1%BW)
X-ray tubes	10^7 [189]	10^7 [190]
Metal jets		$10^9 - 10^{10}$ [191]
Inverse Compton scattering	10^{14} [192]	10^{16} [193]
High harmonic generation	$10^7 - 10^{17}$ [194]	$10^{25} - 10^{30}$ [195]
Synchrotron radiation facilities (third generation)	$10^{18} - 10^{21}$ [189]	10^{24} [190]
Free-electron lasers	10^{26} [189]	10^{34} [190]

3.1.1 Synchrotron radiation sources

This section focuses on describing synchrotron radiation phenomena and the main components of synchrotron radiation facilities, as well as the general specifications of BESSY II and PETRA III.

Synchrotron radiation is produced when charged particles (in this case electrons) are guided along a curved path – under the influence of applied magnetic fields – at speeds close to the speed of light [196, 197]. Generally, free electrons emit radiation when their velocities are changed by electromagnetic fields. When electrons are moving at relativistic speeds, the emitted radiation has the properties of being broad-band (spanning frequencies from the infrared to the X-ray region) and potentially highly collimated and polarized [196, 198]. These properties are afforded by synchrotron light which allow states of matter to be probed at the molecular level in spectroscopic, diffraction, scattering, and imaging experiments [199, 200].

A synchrotron radiation light source is most often formed by a storage ring designed to circulate electrons at relativistic speeds. Figure 3.1 shows a generic schematic of a synchrotron radiation facility and its main components.

Electrons are typically generated by an electron gun and pre-accelerated in a cyclotron, microtron, or linear accelerator (LINAC), reaching energies of several MeV [196]. After that, a booster ring further increases their acceleration [196]. At that point, with energies of several GeV, they are injected into the storage ring [196]. Once there, bending, quadrupole, and sextupole magnets guide and focus the electrons so as to form a guided electron beam [196, 198]. As electrons circulate in the storage ring and emit synchrotron radiation, they lose energy that is replenished by radiofrequency (RF) cavities [196, 198].
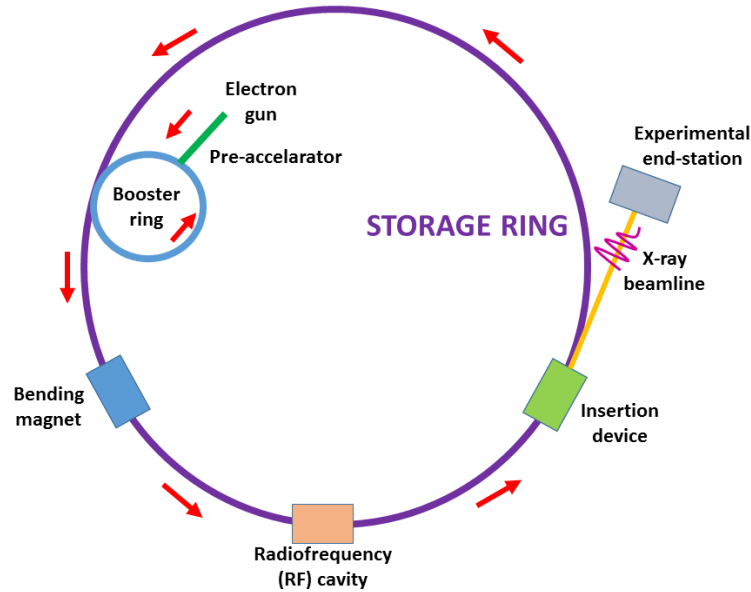
Figure 3.1. Schematic of a synchrotron radiation facility

Generic diagram of a synchrotron radiation facility illustrating its main components, as described in the text. The red arrows indicate the path travelled by the electrons.

The number density, spatial distribution and temporal characteristics of the electron beam are defined by the *ring current* and the *electron bunch* distribution. The latter refers to the longitudinal distribution of the electrons that have been injected into the storage ring – for example, modelled as a Gaussian bunch [201]. The *ring current*, the *circumference of the storage ring* and the *wavelength of the RF cavities* determine the number and length of electron bunches and their temporal distribution, which in turn determines the pulse duration of the emitted synchrotron radiation light (usually on the order of picoseconds) [201]. In addition, synchrotron facilities can operate in different *filling modes of the storage ring*, such as multi-bunch or single-bunch modes (a more detailed overview of the BESSY II and PETRA III operation modes can be found in References [202] and [203], respectively). The experiments reported here were performed under multi-bunch filling mode operation of the storage rings.

Third generation storage rings – such as BESSY II and PETRA III – are characterized by incorporating insertion devices, of which two types exist: wigglers and undulators [204]. These structures consist of an array of magnets where electrons are forced to oscillate and emit partially coherent, polarized, broad-band (wigglers) or narrow-band (undulators) synchrotron radiation [198]. Both the U49/2 PGM-1 and P04 beamlines incorporate soft X-ray undulators, as will be described in Section 3.1.2. The main characteristics and specifications of BESSY II and PETRA III are summarized in Table 3.2.

Table 3.2. Characteristics and parameters of BESSY II and PETRA III

Facility	BESSY II [205]	PETRA III [206]
Circumference / m	240	2300
Electron energy / GeV	1.7	6
Current (multi bunch mode) / mA	300	100
Emittance / nm rad	$4 - 6$ nm	1.2 nm
Average brilliance /(photons/s mm^2 mrad^2 0.1%BW)	$10^{16} - 10^{17}$ [194]	10^{21} [207]

3.1.2 Soft X-ray beamlines

This section describes the main characteristics of the soft X- ray beamlines at which experiments were performed during the course of the work presented here: the U49/2 PGM-1 beamline at BESSY II and the P04 beamline at PETRA III.

As mentioned in the previous section, both beamlines incorporate undulators [198] as their sources. An undulator consists of a row of dipole magnets with alternating polarity where the electron beam is forced to adopt a sinusoidal trajectory. As a result, electrons emit X-ray radiation that can be tuned to different photon energies by changing the gap in the dipole structure. The U49/2 PGM-1 beamline incorporates the U49/2 planar hybrid undulator, which is composed by 84 periods with a 49.4 mm period length [177]. The minimal photon energy at 1.7 GeV is 84.4 eV with a minimal gap of 16 mm [177]. The undulator at the P04 beamline is the APPLE-2 (Advanced Planar Polarized Light Emitter), with 72 periods, a period length of 65.6 mm, and a minimum gap of 11 mm [179].

Figure 3.2 shows the layouts of the U49/2 PGM-1 (top) and P04 (bottom) beamlines. At both beamlines, undulator radiation is monochromatized with a combination of a pre-mirror (M2 in Figure 3.2) and exchangeable gratings (600 l/mm and 1200 l/mm at U49/2 PGM-1 and 400 l/mm and 1200 l/mm at P04), forming a collimated, plane-grating monochromator configuration [208]. The 1200 l/mm grating at the U49/2 PGM-1 beamline was not operable during the course of the work reported here. The main parameters of the U49/2 PGM-1 and P04 beamlines are summarized in Table 3.3, and the experimental conditions during the course of this work are outlined below.

The U49/2 PGM-1 beamline provides linearly, horizontally polarized light in the $85 - 1600$ eV photon energy range. The photon flux and energy resolution vary depending on the exit slit size and the photon energy. During the experiments presented throughout this thesis, ~340 meV beamline resolution was achieved at a 635 eV photon energy when adopting a 100 µm exit slit. The photon flux (measured after the last focusing mirror in the beamline) was of the order of 10^{13} photons s^{-1} at photon energies below 500 eV and 10^{12} photons s^{-1} at photon energies above 500 eV. The focal spot size was approximately 100×80 µm^2 (horizontal $\times$ vertical) when using the aforementioned exit slit size.

The P04 beamline provided circularly-polarized light in the $250 - 3000$ eV range, with a photon flux higher than 10^{12} photons s^{-1} at photon energies higher than 500 eV. The energy resolution at 635 eV photon energy was ~90 meV when using a 100 µm exit slit. The focal spot size was 180×33 µm^2 during the experiments. The reduced vertical dimension of the P04 focus with respect to the U49/2 PGM-1 experiments allowed spectra to be recorded with reduced gas phase contributions.
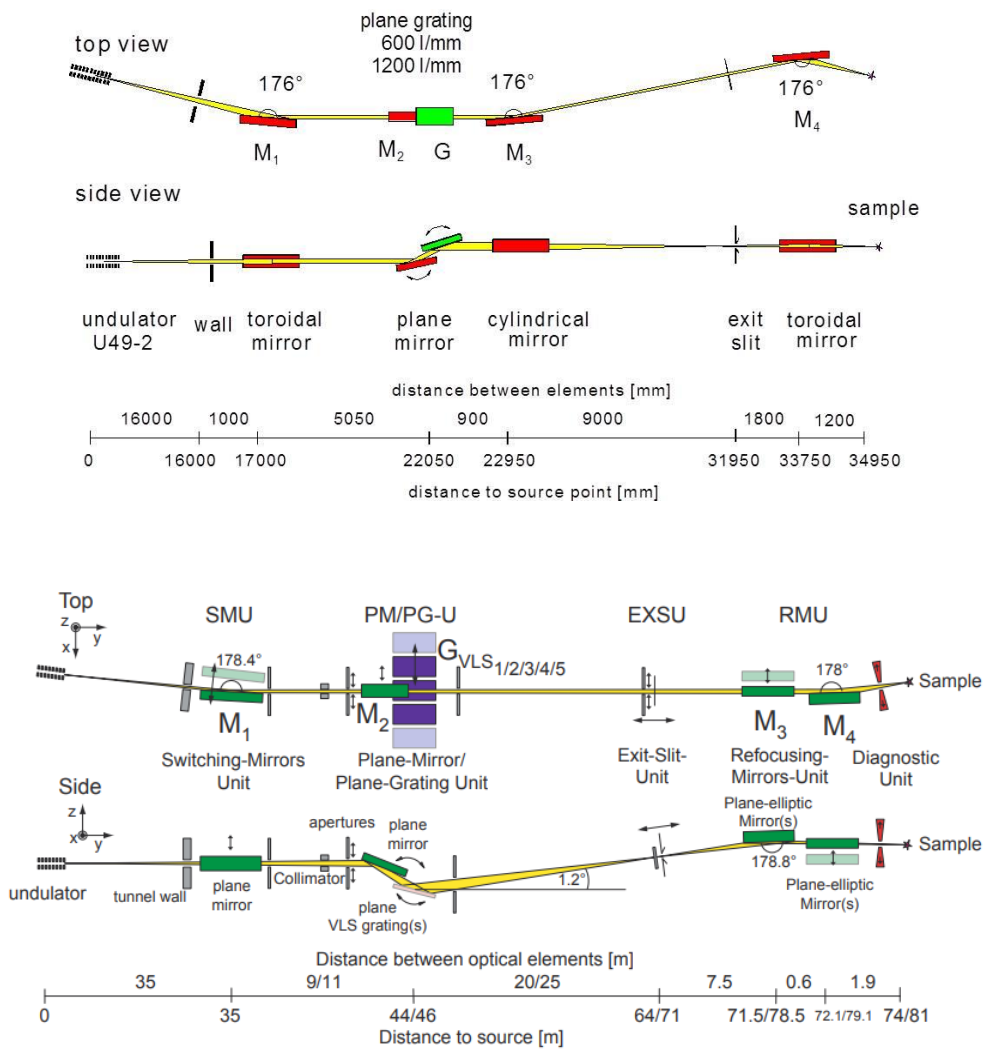
Figure 3.2. Beamline layouts

(Top) Layout of the U49/2 PGM-1 beamline at BESSY II. **(Bottom)** Layout of the P04 beamline at PETRA III. The main components of the beamlines – the undulator, the plane-grating monochromator, and the guiding and focusing optics – are illustrated. The top panel of this Figure has been reproduced from Reference [177], licensed under a Creative Commons Attribution 4.0 International License. The bottom panel of this Figure has been reprinted from [179], Copyright 2013, with permission from Elsevier.

.

Table 3.3. Parameters of the U49/2 PGM-1 and P04 beamlines

Beam line	U49/2 PGM-1	P04
Insertion device	U49/2 undulator	APPLE-2 undulator
Monochromator	PGM-1 plane-grating	Plane-grating
Photon energy range	85 – 1600 eV	250 – 2200 eV
Energy resolution	90 meV at 400 eV (20 µm slit)	<10 meV at 335 eV, <40 meV at 1 keV
Maximum flux	10^{13} photons s^{-1} (150 eV photon energy, 50 µm slit)	10^{15} photons s^{-1} (1 keV photon energy)
Polarization	Linear, horizontal	Circular
Minimum spot size (H x V)	85 x 25 µm^2 (10 µm slit)	10 × 10 µm^2

3.2 Sample delivery

3.2.1 Sample preparation

Millipure water (with 18.2 MΩ cm resistivity at 25°C, from a ELGA PURELAB Plus water purification system with a 0.2 µm point-of-use filter) was used to prepare all of the aqueous solutions described here.

MnO_4^-(aq) solutions were prepared by diluting aliquots of a commercial $NaMnO_4$ solution (Aldrich, 40 wt. % in water) or by dissolving $KMnO_4$ crystals (Roth, ≥99 % p.a., ACS, and Fluka, puriss. p.a., ACS, Ph. Eur., ≥99 %) using Millipure water. 0.05 M $NaCl_{(aq.)}$ solutions (Aldrich, ACS, ≥99 % NaCl crystals dissolved in Millipure water) were used to record nearly-pure water (solvent only) reference spectra. The relatively low concentration of NaCl in solution provided sufficient conductivity to compensate liquid jet streaming potentials [8, 94] and X-ray-pulse-induced charging effects [209]. All sample and reference solutions were ultrasonically degassed before the start of the experiments. Reservoirs and sample solution loops (see Section 3.2.2) containing MnO_4^-(aq) solutions were covered in aluminum foil to prevent ambient light-induced photochemical reactions [210].

MnO_4^{2-}(aq.) solutions were prepared by mixing stoichiometric amounts of $NaMnO_{4(aq.)}$ (as described above) in $NaOH_{(aq.)}$ (Honeywell Fluka, 98% NaOH pellets dissolved in Millipure water) with $NaI_{(aq.)}$ (Sigma Aldrich, 99% NaI crystals dissolved in Millipure water) in $NaOH_{(aq.)}$. During the MnO_4^{2-}(aq.) experiments, $NaOH_{(aq.)}$ – or $NaI_{(aq.)}$ in $NaOH_{(aq.)}$ – were adopted as solvent media reference solutions. The generation of solutions of MnO_4^{2-}(aq.) ions for liquid jet XPS and RPES experiments required the development of alternative sample delivery methodologies. The details of the micro-mixing scheme and electrolysis cell liquid jet device – and associated sample preparation procedure – developed to generate MnO_4^{2-}(aq.) ions are presented in Sections 3.2.3 and 3.2.4, respectively.

3.2.2 The liquid micro-jet technique

This section describes the principles of the liquid micro-jet technique and the components of the liquid jet setup used to perform the experiments reported here.

As briefly introduced in Section 1.2, the liquid-micro-jet technique [69] consists of pushing a liquid through a glass capillary nozzle with a micrometer-size open orifice diameter. The diameter of the liquid jets produced with such capillaries ranges between 5 – 50 µm [69], and typical jet velocities ranging between 30 – 120 m s^{-1} are achieved [21]. The liquid jet's relatively small diameter and high speed enable the following characteristics of the liquid micro-jet technique, which facilitate the study of liquids with relatively high vapor pressure – such as aqueous solutions – under the vacuum conditions required by PES experiments [69, 211]:

- Formation of a millimeter-long laminar-flow liquid filament [67, 72] from which measurements can be performed (*i.e.* placement of the light-sample interaction area within this region);
- Free-flowing sample, without freezing due to evaporative cooling under vacuum in the laminar region of the jet. Notably, the jet breaks down into droplets after a cm or so of propagation, which are subsequently collected by a liquid nitrogen cooled cryo trap;
- Continuously replenished sample volume, resulting in a sample that is essentially unaffected by surface contamination or radiation damage;
- Development of a gas phase sheath around the liquid filament into a collision-free, molecular flow regime gas, ensuring the probability of scattering events of the emitted photoelectrons is negligible, (given that the liquid jet's diameter is comparable to the mean free path of electrons in the surrounding vapor, Knudsen condition);
- Minimized gas phase load that can be handled inside the vacuum experimental chamber by implementing turbo molecular pumps and cryo traps (see Section 3.3).

Figure 3.3 shows a schematic of the liquid jet illustrating the different liquid phase and gas phase flow regimes.
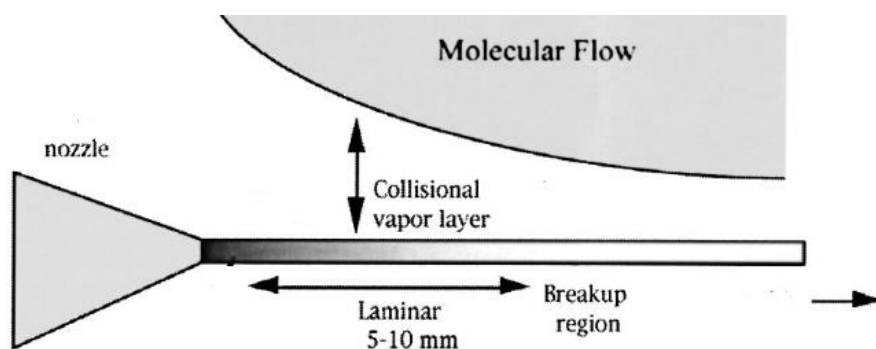
Figure 3.3. Liquid jet flow regimes

Schematic of a liquid micro-jet produced from a capillary or nozzle, illustrating the different liquid phase and gas phase flow regimes. Reprinted from [211] with the permission of AIP Publishing.

A schematic of the liquid jet system used during the MnO_4^-(aq.) experiments performed at BESSY II is shown in Figure 3.4. A slightly different layout – which followed the same principle – was used at PETRA III. The setup primarily consisted of two HPLC pumps and two polytetrafluoroethylene (PTFE) tubing loops (for sample and reference solution). Pre-filtered millipure water pushed through the HPLC pump and fed to these tubing loops, which were pre-filled with sample, so as to protect the pumps from chemical damage and to prevent contact reaction of the samples with metal parts inside the pumps. A polyether ether ketone (PEEK) tubing system was used to interface the sample loops with a metallic rod (liquid jet holder) that held the micro-jet capillary in place (the sample circulated through PEEK tubing inside the liquid jet holder as well). The micro-jet capillary was made of quartz and had an orifice diameter of 25 µm or 35 µm. A peristaltic pump was used to fill the PTFE tubing loops. The pre-filtered, millipure water (or 0.05 M $NaCl$(aq.) solution) was run through the HPLC pumps behind the solutions in order to deliver the sample or reference solution to the glass capillary nozzle, with flow rates ranging between $0.7 – 1.1$ ml min^{-1}. A system of switching valves allowed one of the sample loops to be simultaneously re-filled while running sample to the liquid jet from the

other. A filter assembly with a 10 µm frit was placed before the liquid jet holder in order to prevent micro solids in the solution reaching the injection nozzle and potentially blocking the capillary. After the filtering stage, a gold wire was immersed in the solution and electrically connected to the electron analyzer. The low concentration ionic solutions used in this work provided sufficient conductivity for the gold wire to act as a solution electrical grounding mechanism. The liquid jet holder was mounted on a custom flange and 3D manipulator forming an air-vacuum interface with the experimental end-station (see Section 3.3) and was connected to a cooling system to regulate the temperature of the solution prior to injection. Both the temperature and sample flow rate were optimized to maximize jet stability during measurements. In addition, specific sample temperatures were adopted in situations where photoelectron features and spectral widths were expected to be compared or used to derive additional (temperature-sensitive) parameters [151].
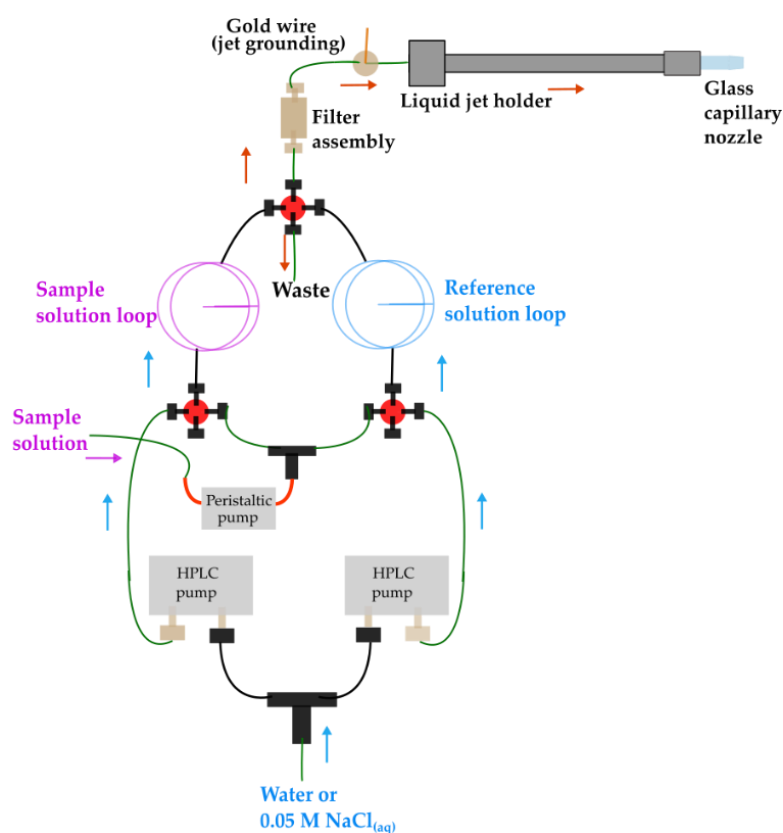
Figure 3.4. Liquid jet sample delivery setup at BESSY II

Liquid micro-jet sample delivery setup used to perform experiments at BESSY II, as described in the text.

3.2.3 Micro-mixing scheme

As described in Section 1.2.3, $MnO_4^{2-}{}_{(aq.)}$ ions undergo disproportionation within tens to hundreds of seconds [54, 212] which complicates the study of its electronic structure by means of the liquid micro-jet setup described in the previous section. The micro-mixing scheme facilitated the $MnO_4^{2-}{}_{(aq.)}$ XPS and RPES experiments presented in Chapter 5.

During a disproportionation reaction, a chemical species is simultaneously reduced and oxidized, producing two compounds with lower and higher oxidation state, respectively. MnO_4^{2-}(aq.) ions disproportionate according to the following chemical equilibrium [54]:

$$3MnO_{4(aq.)}^{2-} + 4H_{(aq.)}^+ \leftrightarrow 2MnO_{4(aq.)}^- + MnO_{2(s)} + H_2O$$
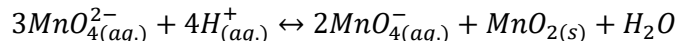
The kinetics of this equilibrium are pH-, concentration-, and temperature-dependent. In addition, $MnO_{2(s)}$ formed during the reaction acts as a heterogeneous catalyst for the forward reaction, further accelerating the disproportionation [54].

As shown in the Mn-H$_2$O Pourbaix diagram (Figure 1.2), MnO_4^{-2-}(aq.) ions can be stabilized in alkaline environments. A chemical route to the generation of MnO_4^{-2-}(aq.) is [213, 214]:

$$6MnO_{4(aq.)}^- + I_{(aq.)}^- + 6OH_{(aq.)}^- \rightarrow 6MnO_{4(aq.)}^{2-} + IO_{3(aq.)}^- + 3H_2O$$
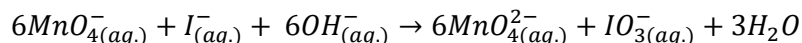
With that in mind, as an initial step, ~0.2 M MnO_4^{2-}(aq.) solutions were prepared at pH ~14.6 by mixing 0.2 M NaMnO$_{4(aq.)}$ and 0.033 M NaI$_{(aq.)}$ in 4 M NaOH$_{(aq.)}$. 0.2 M concentrations were chosen so as to ensure high XPS solute-to-solvent signal contrast ratio and allow solute photoelectron spectroscopic signatures of interest to be distinguished from those of the predominant water solvent. In addition, the solution should be stable for at least 40 minutes in order to be able to record XPS data [87]. Sample stability was studied by recording UV-visible absorption spectra as a function of time and monitoring the formation of colloidal $MnO_{2(s)}$ (with an absorption band at a wavelength of ~425 nm [214, 215]), as shown in Figure 3.5. Given that disproportionation at 0.2 M concentration was evident at ambient temperature (usually below 19°C) the MnO_4^{-2-}(aq.) solutions were kept in an ice bath during those experiments.
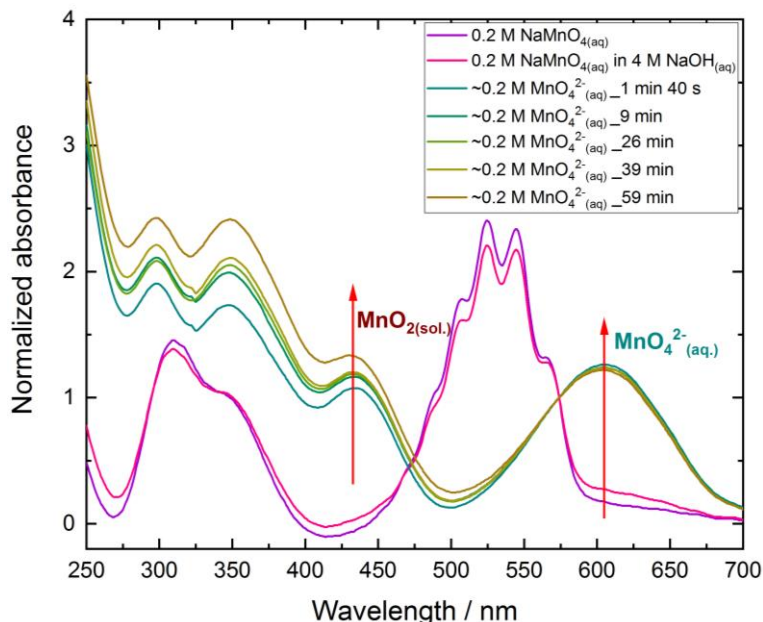
Figure 3.5. UV-visible absorption spectra of MnO$_4^{2-}$(aq.) as a function of time

The arrows highlight the changes in the MnO$_4^{2-}$(aq.) and MnO$_{2(s)}$ concentrations at their signature absorption wavelengths of ~600 nm and ~425 nm, respectively [58, 214, 215]. 0.2 M NaMnO$_{4(aq.)}$ spectra in the presence and absence of 4 M OH$^-$(aq.) are shown for comparison. The spectra were normalized to the isosbestic point close to 555 nm [216].

XPS experiments performed using the (regular) liquid jet setup described in Section 3.2.2 and the sample preparation methodology described above allowed the (first) valence band signatures of $MnO_4^{2-}{}_{(aq.)}$ to be recorded, revealing a ~6.9 eV lowest BE spectroscopic signature, which is unique to $MnO_4^{2-}{}_{(aq.)}$, as shown in Figure 3.6 (panel B.1). Despite keeping the sample loop inside an ice bath to reduce the rate of disproportionation, residues of $MnO_4^{2-}{}_{(aq.)}$ accumulated in the sample loop and delivery paths, with disproportionation occurring over time. As a result, $MnO_{2(s)}$ accumulated through the delivery system, generally obstructing the circulation of liquid and completely blocking the filter frit and / or glass capillary nozzle after ~20 minutes. In addition, contact of the $MnO_4^{2-}{}_{(aq.)}$ solution in the sample loops with water circulating through the HPLC pumps had to be avoided by ensuring the presence of $NaOH_{(aq.)}$ in the delivery path between the HPLC pump and the sample loop. Otherwise, dilution of the $OH^-{}_{(aq.)}$ ion concentration at the water-sample interaction point resulted in a decrease in the pH, thus driving the disproportionation reaction.

The micro-mixing scheme was designed to overcome the aforementioned difficulties, by facilitating longer acquisition times and reducing the required amount of $NaOH_{(aq.)}$ stabilizing agent. The scheme was based on the idea of incorporating microfluidic devices into the liquid micro-jet technique as in-line micro-reactors to generate transient species.

The concept developed for the generation of $MnO_4^{2-}{}_{(aq.)}$ ions is illustrated in Figure 3.6 (top). A 0.57 µl T micro-mixer was connected to two streams, combining the following reagents to generate and deliver $MnO_4^{2-}{}_{(aq.)}$ ions to the experiment in short succession: a *$MnO_4^-{}_{(aq.)}$ reagent stream* (0.4 M $NaMnO_{4(aq.)}$ in 0.5 M $NaOH_{(aq.)}$) with a *$I^-{}_{(aq)}$ reagent stream* (0.066 M $NaI_{(aq.)}$ in 0.5 M $NaOH_{(aq.)}$) to produce a 0.2 M $MnO_4^{2-}{}_{(aq.)}$ in 0.3 M $NaOH_{(aq.)}$ sample stream (pH~13.5). The third arm was connected to the gold wire connector assembly and the liquid jet holder (see Figure 3.4 in the previous section). The liquid jet temperature was set to 5°C, to minimize disproportionation. The flow dynamics and chemical conversion efficiency – under laminar flow regime conditions, as required for liquid jets – using T-shaped micro-mixers has been described in the literature [217]. The mixing efficiency was tested by recording $MnO_4^{2-}{}_{(aq.)}$ valence band spectra at 150 eV as a function of the angular alignment of the mixer, mixing length, and flow rate. The mixing was found to be independent of its angular alignment relative to the electron spectrometer, indicating that complete mixing was achieved at the synchrotron-liquid-jet interaction point.

Efficient, full-mixing conditions were achieved with the developed setup, as illustrated in panels B – D in Figure 3.6. The $MnO_4^{2-}{}_{(aq.)}$ valence spectra recorded using the liquid jet setup described in Section 3.2.1 and using the micro-mixing scheme are shown in panel panels B.1 and B.2, respectively. Panel C shows $MnO_4^{2-}{}_{(aq.)}$ Mn 2p spectra recorded at 1251 eV photon energy under optimized (only $MnO_4^{2-}{}_{(aq.)}$ present) and partial mixing conditions (both $MnO_4^{2-}{}_{(aq.)}$ and $MnO_4^-{}_{(aq.)}$ present). A $MnO_4^-{}_{(aq.)}$ spectrum is shown for comparison. The mixing time required to chemically produce $MnO_4^{2-}{}_{(aq.)}$ liquid jet samples was optimized by recording PEY-XAS spectra recorded at different flow rates, as shown in panel D. This allowed the identification of the experimental conditions required to record $MnO_4^{2-}{}_{(aq.)}$ XPS and RPES data without the interference from $MnO_4^-{}_{(aq.)}$ signals. Details of the micro-mixing setup are described in Figure 3.7.
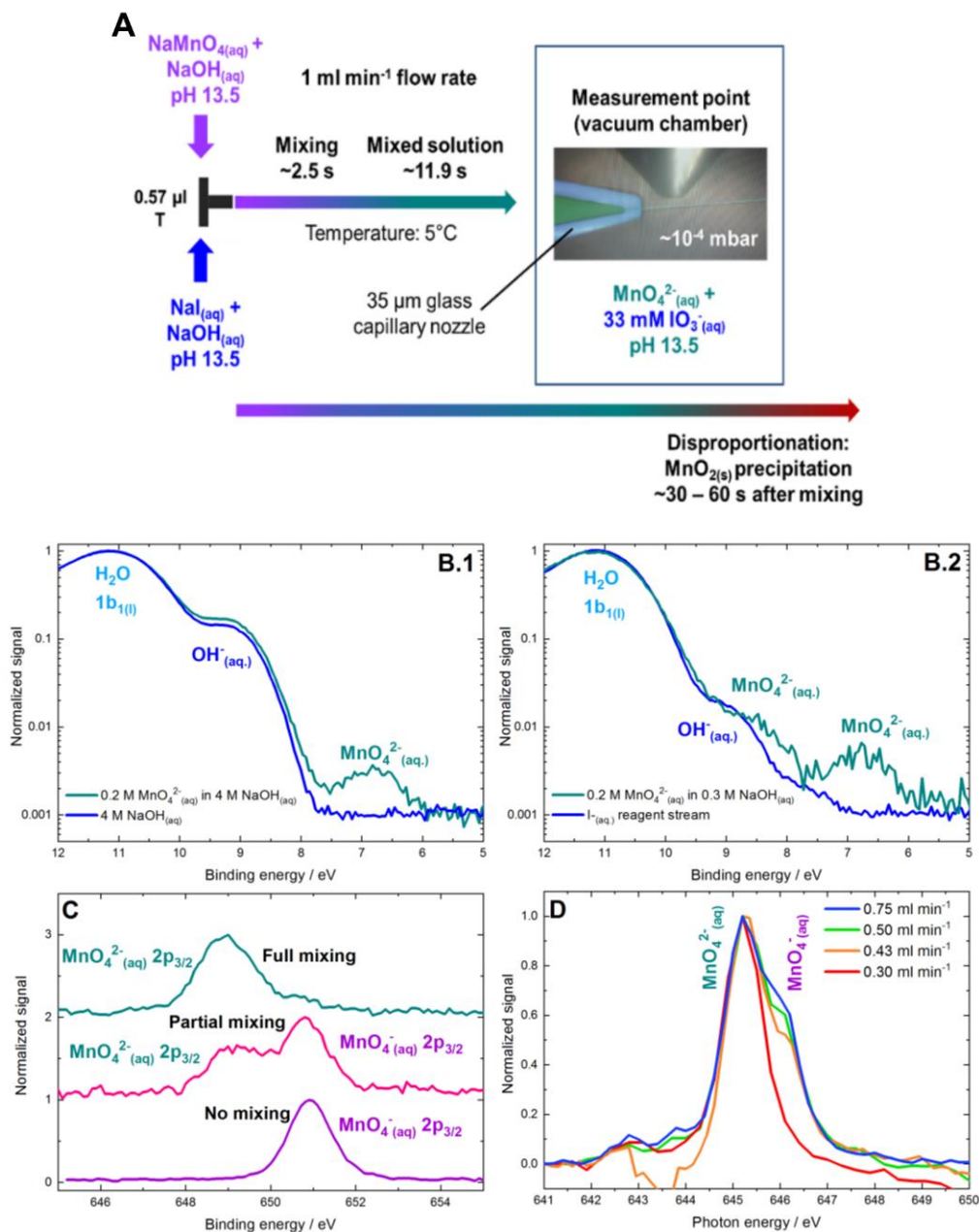
Figure 3.6. Spectra of MnO$_4^{2-}$(aq.) generated using the micro-mixing scheme

(A) Schematic of the micro-mixing scheme, highlighting the reagent streams and time scales for the generation of MnO$_4^{2-}$(aq.) estimated by considering the description of flow dynamics and mixing conditions for T-shaped micro-mixers previously adopted in the literature [217]. **(B)** MnO$_4^{2-}$(aq.) valence spectra recorded at a 150 eV photon energy using the liquid jet setup described in Section 3.2.1 (1) and using the micro-mixing scheme (2). Spectra from NaOH(aq.) solutions are shown for comparison. The micro-mixing scheme offers two primary benefits over the regular LJ scheme, the micro-mixing scheme allows MnO$_4^{2-}$ to be produced with similar yields to the regular liquid jet technique but at significantly lower OH$^-$(aq.) concentrations (and pHs) and (most importantly) a stable MnO$_4^{2-}$(aq.) sample stream can be maintained over a significantly longer timescale (>1 hour) **(C)** MnO$_4^{2-}$(aq.) Mn 2p spectra recorded at 1251 eV photon energy under optimized and partial mixing conditions. A MnO$_4^-$(aq.) spectrum is shown for comparison (purple curve). **(D)** PEY-XAS spectra recorded as a function of flow rate.
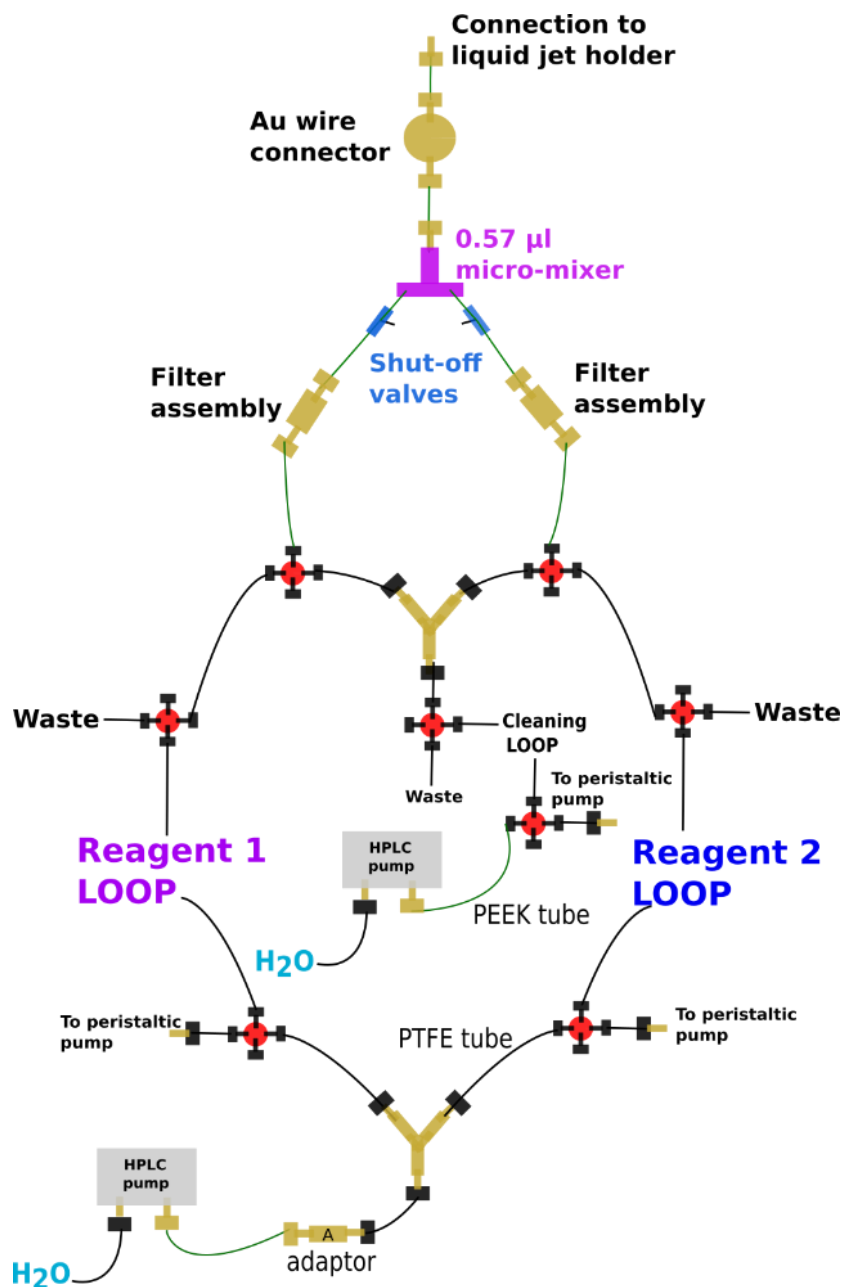
Figure 3.7. Micro-mixing scheme

Diagram showing the HPLC and switching valve sample delivery system associated with the micro-mixing scheme, as detailed in the text. The setup consisted of a T-shaped micro-mixer (0.57 µL volume) that combined two laminar chemical reagent streams into a unique, initially turbulent stream. The streams mixed as they travelled along the PEEK tube (0.57 mm internal diameter) before promptly re-establishing laminar flow, exiting the liquid micro-jet nozzle and reaching the measurement point. Two loops were used for each reagent stream, while a third loop was implemented to circulate $NaOH_{(aq.)}$ in order to clean $MnO_{2(s)}$ residues. Both HPLC pumps were set at the same flow rate. The flow was divided at the Y-connector and then unified again at the T-connector micro-mixer. Isolation valves were implemented to prevent the solution from flowing backwards through either of the reagent lines and mixing taking place outside of the mixer, which would block the lines.

3.2.4 Electrolysis cell liquid jet

As a more compact alternative to the micro-mixing scheme presented in the previous section, and a potential means to study transient species with even shorter lifetimes, an in-vacuum electrolysis-based sample source assembly was produced and tested. The primary advantage of this sample source with respect to the micro-mixing scheme is the possibility of incorporating this device inside the vacuum chamber (*i.e.* closer to the synchrotron-liquid-jet interaction point). The device was designed according to the working principles of flow electrolysis cells for organic electro-synthesis [89, 218-220]. However, it was tailored towards having the capability of producing stable liquid jet samples at applied voltages within the water electrochemical window (0-1.23 V) [221], so as to avoid competitive reactions with the solvent. As a result, it should allow shorter lived species and ions (transient intermediates) to be probed in their nascent form (*i.e.* with lower concentration of stabilizing agents).

Figure 3.8 (top) shows a schematic of the developed electrolytic cell liquid jet assembly. Its main components (numbered from **1 – 8** in the figure) are: (**1**) ambient pressure-vacuum chamber interface; (**2**) air-vacuum seal, (**3**) PEEK liquid delivery interface; (**4**) platinum (Pt) disc pair anode and cathode or working electrode and counter electrode; (**5**) glass capillary ferrule; (**6**) glass capillary retaining nut; (**7**) electrolytic chamber holder; (**8**) PTFE spacer.

The electrolysis chamber consisted of pure Pt working and counter electrodes (1.2 mm^2 area each) and a PTFE electrode spacer (~250 µm thickness). Given that the electrochemical setup implies coupling of an electrolysis cell assembly to a liquid jet in vacuum, adequate flow rate conditions for both redox conversion and a stable liquid jet needed to be met. The slowest possible flow rate to maintain stable liquid jet conditions is close to 0.5 ml min^{-1}. The residence time between the working electrode and counter electrode was optimized by varying the liquid sample flow rate. When using flowrates in the $0.5 – 1$ ml min^{-1} range, the chemical species generated in the electrolysis chamber reached the synchrotron-liquid-jet interaction point within $3.0 – 6.0 \pm 0.1$ s. As a result, the setup facilitated the study of species with lifetimes of $4 – 7$ s or longer.

The capability of the proposed design to generate aqueous ions via electrolysis was tested in MnO_4^{2-} $_{(aq)}$ proof-of-principle experiments [222]. The applied voltage and flow rate conditions were explored to achieve maximum redox conversion efficiency considering the following redox reaction for the generation of MnO_4^{2-} $_{(aq)}$ ions:

$$4MnO_{4(aq.)}^{-} + 4OH_{(aq.)}^{-} \rightarrow 4MnO_{4(aq.)}^{2-} + O_{2(g)} + 2H_2O$$
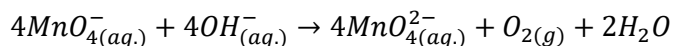
With the reaction corresponding to the following half reactions:

$$MnO_{4(aq.)}^{-} + e^{-} \rightarrow MnO_{4(aq.)}^{2-}$$

$$4OH_{(aq.)}^{-} \rightarrow O_{2(g)} + 2H_2O + 4e^{-}$$
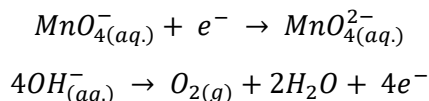
Valence band spectra from 0.2 M $NaMnO_{4(aq.)}$ in 4 M $NaOH_{(aq.)}$ solutions were recorded under different applied voltage and flow rate conditions at a 150 eV photon energy, as shown in Figure 3.8 (bottom). The MnO_4^{2-} $_{(aq)}$ signal increased with applied voltage and decreased with increasing flow rate. A conversion efficiency of ~10% was estimated at 0.9 V and 0.5 ml min^{-1}, based on the recorded data, an example of which is shown in Figure 3.8.
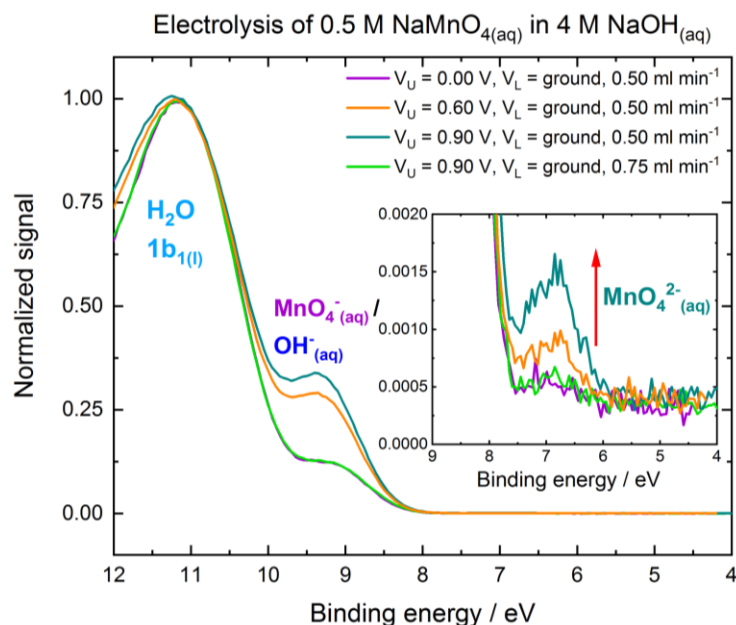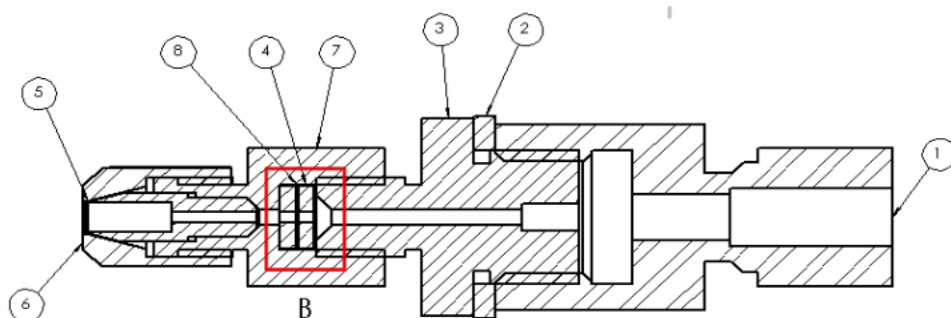
Figure 3.8. Electrolysis cell liquid jet for the generation of $MnO_4^{2-}{}_{(aq.)}$ ions

(Top) Schematic of the electrochemical cell liquid jet assembly. Parts 1-7 highlight the ambient pressure-vacuum chamber interface, liquid-delivery interface, working electrode holder and seal, counter electrode holder and seal, liquid microjet capillary ferrule, and LJ capillary retaining nut. **(Bottom)** Valence-band spectra from 0.5 M $NaMnO_{4(aq.)}$ in 4 M $NaOH_{(aq.)}$ solutions recorded as a function of applied voltage and flow rate at 150 eV photon energy. The intensity of the $MnO_4^{2-}{}_{(aq.)}$ signature at a 6.9 eV binding energy increased with applied voltage.

Larger electrode areas and reduced electrode separation are required to increase the conversion efficiency. The former would result in increased dimensions of the device, hence providing larger residence times. Consequently, an additional challenge is the dimensioning of the device, so as to make it fit in the liquid-soft-X-ray-beam interaction region inside the vacuum chamber.

In order to address the aforementioned requirements, a different prototype was developed, as illustrated in Figure 3.9. The revised electrolysis cell assembly incorporated a set of concentric electrodes and exchangeable spacers of different lengths. Such electrode geometry facilitated larger electrode areas (higher electrode area / reaction volume ratio) within the flow rate limitations to run stable liquid jets. Such limitations are associated with a minimum flow rate of $0.3 - 0.5$ ml min^{-1} required to ensure a sufficiently large (of the order of a few millimeters) laminar liquid jet region is produced from where photoelectrons can be efficiently sampled from the liquid jet. These limitations

have an impact on the residence times and, consequently, on the electrochemical conversion efficiency. The residence time in the electrolysis compartment can be tuned by changing the flow rate, and should be long enough to achieve higher conversion efficiency. An optimum compromise between those parameters can be found by further increasing the electrode area in the electrolysis cell flow channels while simultaneously maintaining high electrode area / reaction volume form factors.
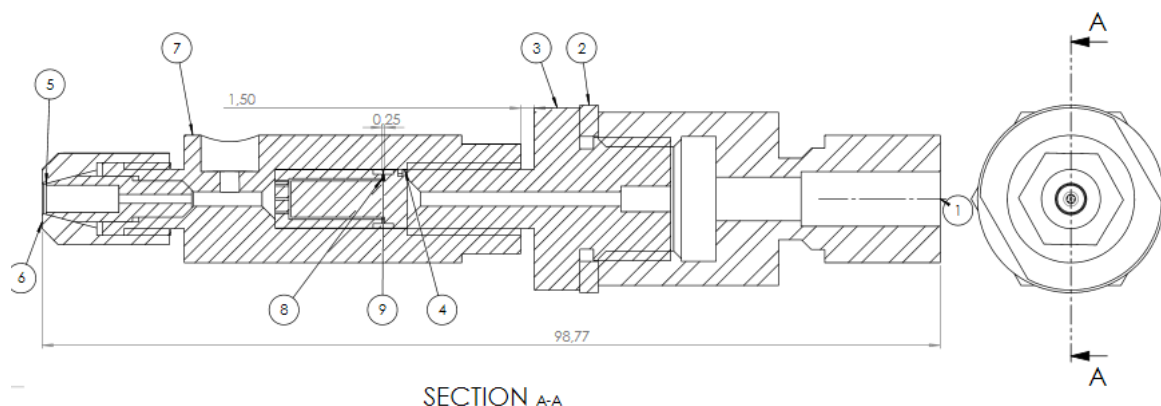
Figure 3.9. Electrolysis cell liquid jet – concentric electrodes

Schematic of the assembly. All dimensions are in millimetres. Parts 1-9 highlight the ambient pressure-vacuum chamber interface (**1**), air-vacuum seal (**2**), PEEK liquid-delivery interface (**3**), concentric electrodes and spacer (**4**, **8**, **9**), liquid microjet capillary ferrule (**5**), and LJ capillary retaining nut (**6**).

In the prototype presented in Figure 3.8, the direction of the field produced by the applied difference potential between the electrode plates was parallel to the direction of flow of liquid inside the electrolysis cell liquid jet. In the design presented in Figure 3.9, the incorporation of concentric electrodes resulted in two different *applied potential versus flow rate* regimes: parallel orientation towards the end of the electrolysis compartment, and perpendicular orientation along the cell. Similar experiments to those performed with the initial prototype showed no further improvements in redox conversion efficiency. These results seem to indicate that the perpendicular orientation geometry did not contribute to an improvement in the overall conversion efficiency, despite the similar sample volume flow rate and higher electrode area.

Consequently, future improvements of the electrolysis cell liquid jet assembly should focus on maximizing electrode areas while favoring a parallel orientation between applied potential and sample flow rate directions.

3.3 X-ray photoelectron spectroscopy end-stations

This section describes the main components of the SOL³PES [178] and EASI [180] end-stations that were used to perform liquid jet soft X-ray photoelectron spectroscopy experiments at the U49/2 PGM-1 and P04 beamlines, respectively. The central component of the experimental end-stations is their interaction chambers, where the liquid jet sample is aligned onto the soft X-ray beam delivered by the beamline. Figure 3.10 shows a schematic illustrating its main components.

The interaction chambers are equipped with several ports that connect to:

- The *end-station-beamline differential pumping unit* – devised to protect the beamline from the liquid samples introduced into the experimental chamber;

- The *hemispherical electron analyzer* – used to sample and measure the kinetic energy of photoelectrons emitted from the liquid jet sample. Both the SOL^3PES and EASI end-stations are equipped with differentially-pumped Scienta Omicron R4000 analyzers (HiPP-2 model in SOL^3PES [178] and HiPP-3 model in EASI [180]). The electron analyzer pre-lens axes were aligned either at 90° or at magic angle with respect to the soft X-ray beam polarization during the experiments reported here. The liquid jet orientation was orthogonal to the soft X-ray beam propagation direction.

- A *micrometer precision XYZ manipulator* – attached to the liquid jet holder (see Section 3.2.2), which facilitated precise (micrometer-scale) alignment of the liquid jet at the light-sample interaction region in front of the entrance to the electron analyzer (see Figure 3.10, top). The liquid jet position was optimized by maximizing the photoelectron count rate from the liquid water $1b_1^{-1}$ ionizing transition (see Section 2.3.1) – in experiments performed at photon energies lower than 540 eV – or of the liquid water Auger electron signal – in experiments performed at photon energies higher than 540 eV – thus reducing gas-phase spectral contributions [151];

- The main *turbo molecular pump* and several *cryogenic traps* – used to maintain a 5×10^{-4} – 1×10^{-3} mbar pressure inside the interaction chamber, as required to perform photoelectron spectroscopy experiments. The turbo molecular pump had a ~2000 L s^{-1} (SOL^3PES) or ~2700 L s^{-1} (EASI) pumping speed for water vapour. The liquid nitrogen-filled cryo traps (two in the SOL^3PES instrument or three in the EASI end-station) provided ~4.5×10^4 L s^{-1} pumping speed for water vapour per trap. In addition, one of the cryogenic traps was used as a catcher onto which the droplet train produced at extended distances by the liquid jet were cooled, frozen, and collected.
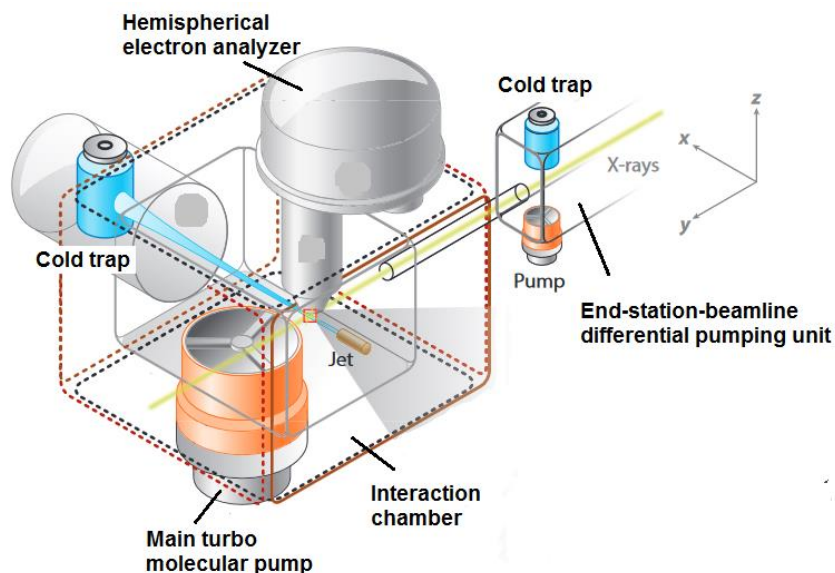
Figure 3.10. Experimental chamber

Schematic of the light-sample interaction region in front of the entrance to the electron analyzer. Republished with permission of Annual Reviews, Inc., from [8]; permission conveyed through Copyright Clearance Center, Inc.

As mentioned above, photoelectrons were detected using differentially-pumped Scienta Omicron R4000 hemispherical electron analyzers [223]. With appropriate magnetic shielding, these analyzers are respectively capable of detecting electron energies in the $5 - 6000$ eV and $2 - 1500$ eV ranges, respectively [224]. Figure 3.11 shows schematics of this type of analyzer. Its main components are:

- Exchangeable entrance skimmers, where 500 µm and 800 µm apertures were respectively implemented in the SOL^{3}PES and EASI experiments, used to sample photoelectrons from the liquid jet at the measurement point;
- Differentially-pumped, electrostatic pre-lens and lens systems that guide the sampled photoelectrons towards the entrance of the hemisphere and accelerate or decelerate them according to the implemented analyzer settings [223];
- A pair of concentric, inner and outer (200 mm nominal radius, r_o) hemispheres with entrance and exit slits. Only electrons with a specific KE range around a defined central energy (referred to as the *pass energy, E_p*) are able to reach the exit slit and be detected;
- A detection unit, consisting of two 40 mm diameter micro-channel plates (MCPs) and an associated phosphor screen [178]. The MCPs amplify the photoelectron signals while the phosphor screen produces an energy versus position and angle 2D image. A charge-coupled device (CCD) mounted outside vacuum is used to record the images, synchronously with the analyzer field sweeps and potential beamline monochromator changes [178].
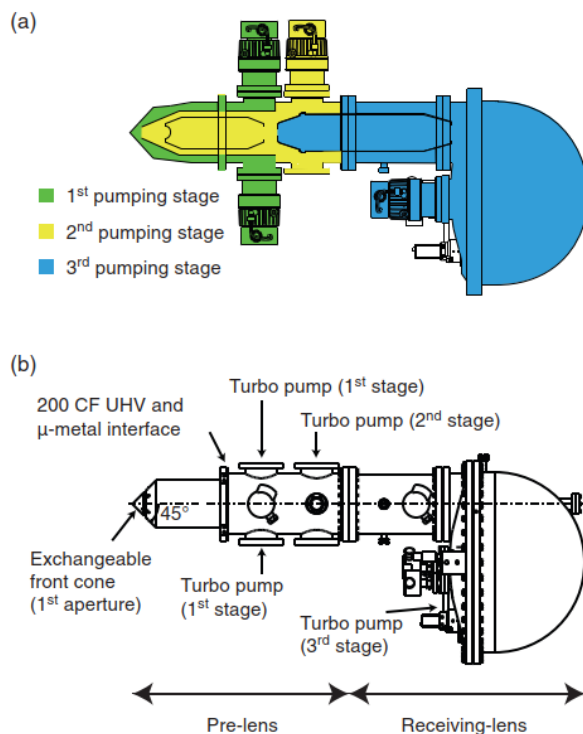
Figure 3.11. Hemispherical electron analyzer

Schematics of the Scienta Omicron R4000 HiPP 2 hemispherical electron analyzer, highlighting the different pumping stages (top) and the electrostatic pre-lens and receiving-lens areas (bottom). Reprinted from [223] with the permission of AIP Publishing.

For a given experiment, E_p is selected so as to be approximately a third of the center KE in the spectrum. The experiments reported here were performed in transmission mode, with the hemispherical analyzer entrance slit being set to maximize electron collection.

The analyzer slit size, E_p, and r_o as well as the beamline slit size determined the total instrumental resolution for the experiments. For the U49/2 PGM-1 beamline and SOL³PES end-station setup, the instrumental resolution was determined by recording Argon 3p and 2p XPS spectra under beamline and analyzer conditions matching those adopted when performing the liquid jet experiments [151]. Voigt profile fits to the Ar spectra allowed instrumental resolutions of ~53 meV, ~310 meV, and ~400 meV to be determined at 150 eV, 530 eV, and 638 eV photon energies, respectively [151]. For the P04 beamline and EASI end-station, the instrumental resolution was estimated from data provided by P04 beamline scientists [225] and the group at the Fritz-Haber Institut Berlin who constructed the EASI setup [226], with total energy resolutions of ~410 meV, ~460 meV, and ~480 meV at 635 eV, 1135 eV, and 1251 eV photon energies, respectively.

3.4 Experimental protocols and data treatment

3.4.1 Non-resonant photoemission experiments

With the aim of fully characterizing the electronic structure of MnO_4^- (aq.) and MnO_4^{2-} (aq.) ions, non-resonant photoelectron spectroscopy experiments were performed to determine the aqueous phase BEs of (outer and inner) valence and core level electrons. In addition, ionizing photon energies were tuned to selectively probe gas-solution interfacial or solution-bulk environments. Correspondingly, for the valence region, experiments were performed at photon energies of 150 eV and 635 eV, thus producing photoelectrons with KEs of ~130 eV and ~600 eV, respectively. As explained in Section 2.3, KE values of those magnitudes respectively correspond to ~1 nm (surface sensitive) and ~4 nm (bulk sensitive) EALs [150]. With a similar purpose, O 1s and Mn $2p_{3/2,1/2}$ core-level spectra were recorded at photon energies of 688 eV / 1135 eV (O 1s) and ~800 eV / 1251 eV (Mn $2p_{3/2,1/2}$) in order to sample photoelectrons from ~1 nm / ~4 nm probing depths, respectively. Valence and O 1s spectra were recorded for both the sample of interest (MnO_4^- (aq.) and MnO_4^{2-} (aq.) solutions) as well as from reference solutions (see Section 3.2.1) facilitating a direct comparison between solution and solvent-only data as well as the identification and isolation of solute spectral features.

The secondary electron background in the data was treated by fitting and sequentially subtracting a series of Shirley baselines to the 5 – 20 eV, 20 – 40 eV, and 40 – 90 eV BE spectral regions. The background-corrected spectra were fit using a set of Voigt profile functions. The mathematical expression of a Voigt profile allows for an appropriate representation of inhomogenous broadening, instrumental resolution and life-time broadening contributions to the photoelectron signals (assuming the photoemission peaks are inherently symmetric). For valence band spectra, where contributions from life-time broadening effects proved to be negligible, more robust Gaussian fits were adopted instead. The BE scale was calibrated using the water $1b_{1(l)}$ (in valence band spectra) and O $1s_{(l)}$ (in O 1s and Mn 2p spectra) BE values of 11.31 ± 0.04 eV [94] and 538.1 ± 0.1 eV [227], as respectively reported and generally adopted in the existing literature (see Section 2.3). BEs and peak widths at FWHM were determined from average values extracted from fits to different data sets, with the associated errors corresponding to standard deviations. Fitting errors and the uncertainty in the water $1b_{1(l)}$ BE value used to calibrate the BE scale were considered individually for each data set to determine the reported errors.

Solution-solvent (reference) difference spectra were produced for the valence band and O 1s data. The spectra were smoothed (3-point adjacent-averaging smoothing) before subtraction. This methodology was applied as an alternative and complementary BE and peak width extraction approach to the cumulative fit treatment described above. Consequently, the peak widths reported throughout this thesis reflect inhomogeneous broadening due to the aqueous environment and the beamline / analyzer combined instrumental resolution (see Section 3.3), excluding lifetime broadening effects.

3.4.2 Resonant photoemission experiments

RPES experiments were performed at photon energies in the vicinity of the Mn $L_{II,III}$- and O K-pre-edges, recording 2-dimensional (2 D) photon energy versus BE maps. Integration over the photon energy scale in those maps produced PEY-XAS spectra proxies of the transmission-based XAS spectra [166] (see Section 2.4.1). The PEY-XAS spectra were used to determine resonant photon energies corresponding to different core-to-virtual-valence and core-to-partially-occupied-valence transitions (as in the case of MnO_4^{2-}, see Figure 2.2) involving Mn $2p_{3/2,1/2}$ and O 1s core-level electrons and the HOMO (in the $MnO_4^{2-}$$_{(aq.)}$ case), LUMO, and LUMO + 1 valence electrons. The Mn $L_{II,III}$- and O K-pre-edge PEY-XAS spectra were fit using a set of Gaussian functions in order to extract the resonant photon energies (for the Mn $L_{II,III}$-pre-edge data, a cubic baseline was fit and subtracted as a preliminary step). In the Mn $L_{II,III}$-pre-edge experiments, the photon energy scale was calibrated using Voigt fits to the water O $1s_{(l)}$ spectra recorded using the fundamental and residual second harmonic signal of the monochromatized beamline. The difference between the central KEs extracted from those measurements defined the experimental photon energies. In the O K-pre-edge PEY-XAS experiments, the water O $1s_{(l)} - 4a_1$ resonance at 535.0 eV [228] was used to calibrate the photon energy scale.

In order to isolate participator and spectator Auger features – as well as signatures of non-local autoionization involving solute and solvent molecules, as explained in Section 2.4 – higher signal-to-noise ratio spectra were recorded at each core-virtual-valence resonant photon energy. The resonant photoelectron spectra were compared with photoelectron spectra recorded at lower, off-resonant photon energies (which were devoid of resonant signal enhancements). The off-resonant spectra were subtracted from the corresponding resonant spectra, with the data being BE smoothed (5-point adjacent-averaging) as a preliminary step. The resulting difference spectra were fit using sets of Gaussian or Voigt functions in order to extract the energetic information associated with the different resonant signal enhancements. The BE scale was calibrated using the water $1b_{1(l)}$ photoemission peak from the off-resonant spectra in both the RPES maps and higher-signal-to-noise spectra.

4 Electronic structure of permanganate ions in aqueous solution ($MnO_4^-{}_{(aq.)}$)

This chapter presents and discusses results obtained from XPS and RPES experiments performed with $MnO_4^-{}_{(aq.)}$ solutions. As described in Chapter 1 (and illustrated in Figure 1.1), $MnO_4^-{}_{(aq.)}$ ions are redox precursors of aqueous Mn species with other oxidation states. These ions are strong oxidizing agents at alkaline, neutral, and acidic pH and constitute a benchmark case for electronic structure calculations of transitions metal complexes [105, 108, 229]. The relatively high stability of MnO_4^- in aqueous solution [36] allowed a comprehensive set of liquid jet photoelectron spectroscopy experiments to be performed, from probing its electronic structure in relatively dilute solutions, to investigating counter-ion, probing-depth, and concentration effects. Primary attention was given to bulk-sensitive spectra recorded from 0.2 M $NaMnO_4{}_{(aq.)}$ and $KMnO_4{}_{(aq.)}$ solutions, a concentration at which $MnO_4^-{}_{(aq.)}$ ions are expected to behave as hydrated, separated ions – *i.e.* without ion-pairing with other $MnO_4^-{}_{(aq.)}$ ions or $Na^+{}_{(aq.)}$ or $K^+{}_{(aq.)}$ counter cations – as confirmed by the experimental data presented here. The electron collection axis of the analyzer was set orthogonal or at magic angle to the light propagation and light polarization axes in all the direct XPS and RPES experiments. While the use of different polarization geometries is generally adopted to probe photoelectron angular distributions [150], favoring perpendicular or magic angle electron analyzer orientations yielded equivalent results (*i.e.* system energetics) in the work described here, with the exception of the depth profiling experiments. In that case, experiments were performed using the magic angle configuration, given the dependence of the probing depths on the photoelectron angular distributions [150].

The chapter is organized in three sections. Section 4.1 reports the BEs extracted from the direct XPS experiments, as well as the results and discussions regarding the depth- and counter-ion dependence of the BEs (Sections 4.1.1 and 4.1.2). A more involved depth profiling study from 0.2 M and 1.0 M $NaMnO_4{}_{(aq.)}$ solutions is presented and discussed in Section 4.1.3. A comparison between the aqueous phase BE values reported here with those associated with solid [167] and gas phase samples [175] reported in the literature is presented in Section 4.1.4. Sections 4.2 focuses on the Mn $2p_{3/2}$ / $2p_{1/2}$ and O 1s RPES results, discussing electronic structure, Mn(VII)-O molecular bonding, and solute-solvent interaction information extracted from intramolecular Auger and non-local autoionization processes. A summary of the key findings reported in this chapter is presented in Section 4.3.

Figure 4.1 shows a MO diagram for a NaMnO$_{4(aq.)}$ solution, showing the electronic structure of the fully hydrated MnO$_4^-$$_{(aq.)}$ ion and Na$^+$$_{(aq.)}$ counter ion, as well as that of the water solvent. This MO diagram will be used as a reference when presenting the experimental data throughout this chapter. Spectral features associated with different MOs will be labelled as follows: (**1**) 1t$_1$, (**2**) 4t$_2$/6a$_1$, (**3**) 1e/3t$_2$, (**4**) 5a$_1$, (**5**) 2t$_2$, (**6**) 4a$_1$, (**7**) 3a$_1$, and (**8, 9**) 1t$_2$ (see Section 2.1.2 for details). The vertical energy scale displays the BEs extracted from the bulk-sensitive direct XPS and RPES experiments recorded at 0.2 M concentration. The BEs associated with the 2e and 5t$_2$ virtual valence orbitals (5.15 ± 0.08 eV and 6.88 ± 0.08 eV, respectively) were estimated by considering the experimentally determined BE of the (1t$_1$)$^{-1}$ ionizing transition and the excitation energies extracted from fits to the first and third optical UV/visible absorption bands (as reported in Section 2.1.2), neglecting electron correlation effects.

Figure 4.1. MO diagram of NaMnO$_{4(aq.)}$ solutions

MO diagram of a NaMnO$_{4(aq.)}$ solution. The MnO$_4^-$$_{(aq.)}$ MO diagram was adapted from the isolated molecule diagram presented in References [104] and [108] (see Section 2.1.2 for details) and scaled according to the experimental BEs determined from the liquid jet XPS and RPES bulk-sensitive experiments with 0.2 M NaMnO$_{4(aq.)}$ solutions and from UV-visible absorption measurements, as explained in the text. MO diagrams for H$_2$O (center) and Na$^+$$_{(aq.)}$ ions (right) are shown for comparison, based on the data reported in this chapter and in References [21, 92, 94]. The energetic information is referenced to the local vacuum level.

4.1 Direct (non-resonant) photoelectron spectroscopy

4.1.1 Bulk-sensitive spectra

Figure 4.2 shows 0.2 M NaMnO$_{4(aq.)}$ bulk-sensitive data (purple curves) recorded at the outer valence (panel A), inner valence (panel B), O 1s (panel C), and Mn 2p$_{3/2}$/2p$_{1/2}$ (panel D) spectral regions at a

regulated liquid jet temperature of 280 ± 3 K. The spectra shown in panels A, C, and D were recorded at the P04 beamline at PETRA III, while the spectrum shown in panel B was recorded at the U49/2 PGM-1 beamline at BESSY II. As described in Section 3.4.1, photon energies of 635 eV (panels A and B), 1135 eV (panel C), and 1251 eV (panel D) were used in order to sample photoelectrons from the solution bulk, *i.e.* from fully hydrated solute molecules. 0.05 M NaCl$_{(aq.)}$ solvent reference spectra (light blue curves) and the associated solution-solvent difference spectra (red curves) are additionally shown in panels A – C. The MnO$_4^-$$_{(aq.)}$ solute peaks are numbered from $\mathbf{1-9}$, and water and Na$^+$$_{(aq.)}$ peaks are labelled using Roman numerals. Fits to the MnO$_4^-$$_{(aq.)}$ and Na$^+$$_{(aq.)}$ ionization features in the difference spectra are highlighted with purple and black fills, respectively.

Figure 4.2. Solution bulk-sensitive spectra of NaMnO$_{4(aq.)}$

Bulk-sensitive XPS spectra (purple curves) recorded from 0.2 M NaMnO$_{4(aq.)}$ solutions in a magic angle polarization configuration. 0.05 M NaCl$_{(aq.)}$ solvent reference spectra are shown for comparison (light blue curves). Solution-solvent difference spectra are shown in red. MnO$_4^-$$_{(aq.)}$ solute ionization signals are labelled with numbers ($\mathbf{1-9}$). Signals associated with the water solvent and the Na$^+$$_{(aq.)}$ counter ion are labelled with Roman numerals. In Panel C, the 'g' next to the leftmost peak VII is used to denote gas phase signals. Purple fills are used for Gaussian or Voigt profile fits (see Section 3.4 and explanation in the text) of solute signals. Counter ion fits are shown in grey. **(A)** Outer valence spectrum. The insets highlight valence band signal contributions extracted from the solution-solvent difference spectrum (peaks **1-4**). **(B)** Inner valence spectrum. **(C)** O 1s spectrum. The inset highlights the solute O 1s signal extracted from the solution-solvent difference spectrum. **(D)** Mn 2p$_{3/2}$ / 2p$_{1/2}$ spectrum.

As discussed in Section 3.4.1, Gaussian curves were adopted to model the data where Voigt profile and Gaussian fits yielded equivalent peak widths. That was the case for the inner and outer valence

features shown in panels A and B in Figure 4.2, with the exception of peak **6**. The $MnO_4^-{}_{(aq.)}$ core-level solute features shown in Panels C and D were fit using Voigt profiles.

Fits to peaks **1 – 4** (panel A, outer valence region) allowed the following BEs to be determined: 9.22 ± 0.08 eV (peak **1**), 10.67 ± 0.04 eV (peak **2**), 12.84 ± 0.09 eV (peak **3**), and 26.82 ± 0.04 eV (peak **4**). Similarly, BEs of 59.6 ± 0.1 eV (peak **5**) and 94.1 ± 0.1 eV (peak **6**) were extracted from the inner valence data shown in panel B. Peak **1** was assigned to a $(1t_1)^{-1}$ ionization process, corresponding to ionization of an electron from the HOMO and the first VIE of $MnO_4^-{}_{(aq.)}$. The assignment of peaks **2** and **3** was not as straightforward as for peak **1**. The relatively large peak widths extracted for peaks **2** and **3** with respect to that extracted for peak **1** suggests the presence of more than one ionizing transition contributing to those signals – *i.e.* the presence of two underlying signal components. With the MO diagram shown in Figure 4.1 in mind, peak **2** can be ascribed to a $(4t_2)^{-1}$ or $(6a_1)^{-1}$ ionization process. Similarly, peak **3** can be assigned to a $(1e)^{-1}$ or $(3t_2)^{-1}$ ionization process. Hence, the features associated with peak **2** and **3** cannot be assigned unequivocally. However, the RPES experiments provided additional information to elucidate the nature of those spectral features, as will be shown in Section 4.2. While peaks **1** and **2** were reproducibly extracted from fits to the solution-solvent difference spectra, peak **3** – underlying the gas phase water $1b_1$ (HOMO) ionization vibronic peaks – could only be isolated from data recorded under tight focus conditions at the P04 beamline at PETRA III. The reduced spot size afforded at that beamline allowed spectra to be recorded with minimal gas phase signal contributions.

The $MnO_4^-{}_{(aq.)}$ peaks **4 – 6** were respectively assigned to $(5a_1)^{-1}$, $(2t_2)^{-1}$, and $(4a_1)^{-1}$ ionization processes. The aforementioned features correspond to ionization from the O 2s $(5a_1)$ ligand-based orbitals and the Mn 3p $(2t_2)$ and Mn 3s $(4a_1)$ Mn metal-center-based orbitals. However, these orbitals are hybridized, as will be shown and discussed in Section 4.2.

Peaks **7 – 9** are associated with ionization from the O 1s $(3a_1)$ and Mn $2p_{3/2} / 2p_{1/2}$ $(1t_2)$ core-levels in $MnO_4^-{}_{(aq.)}$, as shown in Figure 4.1. A BE of 536.0 ± 0.1 eV was determined for peak **7**, which was assigned to a $(3a_1)^{-1}$ ionization process. This value is 2.1 eV lower than that associated with the O 1s $(1a_1)$ feature of liquid water (peak vii in panel C in Figure 4.2). The negative chemical shift is indicative of a higher $MnO_4^-{}_{(aq.)}$ O-ligand charge density that may be attributed to intramolecular (ligand-ligand) and potential intermolecular (ligand-water) O-O covalent bonding interactions. The differential shifts observed between the O 1s solvent gas phase signals – peak vii-g – in the sample solution and aqueous reference spectra occurs due to changes in electrokinetic and ionization-induced charging effects with the liquid jet samples. BEs of 650.9 ± 0.1 eV and 661.9 ± 0.1 eV were respectively extracted for peaks **8** (Mn $2p_{3/2}$) and **9** (Mn $2p_{1/2}$), with BE values ~12 eV larger than in metallic Mn [167, 172, 230]. Here, the positive chemical shift reflects the formal Mn^{7+} oxidation state of the $MnO_4^-{}_{(aq.)}$ metal centre and its covalent bonding to the O ligands.

The BEs and peak FWHMs associated with the aforementioned $MnO_4^-{}_{(aq.)}$ signals (**1 – 9**) are summarized in Table 4.1. The values shown there correspond to the average results extracted from fits to multiple data sets recorded at liquid jet temperatures of 280 ± 3 K, with the reported errors corresponding to the standard deviations of the results from different measurements. Water and $Na^+{}_{(aq.)}$ BEs and peak widths are reported in Table 4.2. The results associated with the water signals were extracted from cumulative fits to baseline-corrected 0.2 M $NaMnO_4{}_{(aq.)}$ valence spectra recorded at a 635 eV photon energy and a regulated liquid jet temperature of 280 ± 3 K, shown in Figure 4.3. The results are in full agreement with those reported in References [21, 92, 94].

Table 4.1. MnO$_4^-$$_{(aq.)}$ bulk-sensitive BEs and FWHM peak widths

MnO$_4^-$$_{(aq.)}$ BEs and Gaussian peak width components, FWHM$_G$, extracted from direct XPS experiments performed at a regulated liquid jet temperature of 280 ± 3 K. FWHM$_G$ values were directly extracted from Gaussian fits for peaks **1 – 5**, while for peaks **6 – 9** Voigt profile fits were adopted instead. For peak **6**, given its low intensity and spectral breadth, the FWHM$_G$ extracted from 0.2 M solutions is supplemented with the peak width from fits to higher signal-to-noise ratio, 0.75 M NaMnO$_4$$_{(aq)}$ solution data (reported in parenthesis).

Label	Peak Origin	BE / eV	FWHM$_G$ / eV
1	$(1t_1)^{-1}$	9.22 ± 0.08	0.8 ± 0.1
2	$(4t_2/6a_1)^{-1}$	10.67 ± 0.04	1.2 ± 0.1
3	$(1e/3t_2)^{-1}$	12.84 ± 0.09	1.9 ± 0.2
4	$(5a_1)^{-1}$	26.82 ± 0.04	2.1 ± 0.6
5	$(2t_2)^{-1}$	59.6 ± 0.1	2.3 ± 0.2
6	$(4a_1)^{-1}$	94.1 ± 0.1	2 ± 4 (2.70 ± 0.07)*
7	$(3a_1)^{-1}$	536.0 ± 0.1	0.9 ± 0.3
8	$(1t_2)^{-1}$	650.9 ± 0.1	0.93 ± 0.06
9	$(1t_2)^{-1}$	661.9 ± 0.1	1.0 ± 0.9

Table 4.2. H$_2$O$_{(l)}$ and Na$^+$$_{(aq.)}$ bulk-sensitive BEs and FWHM peak widths

H$_2$O$_{(l)}$ and Na$^+$$_{(aq.)}$ BEs and FWHM peak widths extracted from cumulative Gaussian (valence-band) and Voigt profile (O 1s) fits to the direct XPS spectra. The Na$^+$$_{(aq.)}$ 2p BE was extracted from solution-solvent difference spectra. Entries in bold font highlight the BE reference values used to calibrate the PES and RPES data BEs (See Secion 3.4.1).

Label	Peak Origin	BE / eV	FWHM$_G$ / eV
i	$(1b_1)^{-1}$	**11.31 ±0.04** [94]	1.42 ± 0.03
ii-a	$(3a_{1-L})^{-1}$	13.02 ± 0.05	1.6 ± 0.1
ii-b	$(3a_{1-H})^{-1}$	14.46 ± 0.06	1.6 ± 0.1
iii	$(1b_2)^{-1}$	17.42 ± 0.04	2.32 ± 0.06
iv	$(2a_1)^{-1}$	31.04 ± 0.04	2.97 ± 0.02
v	2p	35.65 ± 0.04	1.25 ± 0.08
vi	2s	68.46 ± 0.04	1.6 ± 0 .1
vii	$(1a_1)^{-1}$	**538.1 ± 0.1** [227]	1.65 ± 0.03

Figure 4.3. Cumulative Gaussian fit to a NaMnO$_{4(aq.)}$ solution XPS spectrum

Cumulative Gaussian fit to a baseline-corrected outer and inner valence spectrum recorded from 0.2 M NaMnO$_{4(aq.)}$ at a 635 eV photon energy in a magic angle polarization configuration. Spectral features corresponding to MnO$_4^-$$_{(aq.)}$ (purple), Na$^+$$_{(aq.)}$ (grey), and water (light blue) are labelled following the assignments explained in the text and shown in Tables 4.1 and 4.2. The fit associated with peak **4** was highlighted in purple and striped to indicate an overlap between photoelectron signals corresponding to the solute (5a$_1$)$^{-1}$ ionizing transition and electron energy-loss peaks associated with water (1b$_1$)$^{-1}$ and (3a$_1$)$^{-1}$ photoelectrons. The additional striped signals at nominal BEs of 33 eV and 51 eV are similar energy-loss peaks primarily associated with water (1b$_2$)$^{-1}$ and (2a$_1$)$^{-1}$ photoelectrons, respectively [92].

4.1.2 Solution-gas interface and counter-ion effects

Surface-sensitive experiments were performed in order to ascertain whether incomplete interfacial hydration has any discernible effects on the electronic structure of MnO$_4^-$$_{(aq.)}$. Figure 4.4 shows surface-sensitive spectra recorded from 0.2 M MnO$_4^-$$_{(aq.)}$ solutions using 150 eV (outer and inner valence, panel A), 688 eV (3a$_1$/O 1s, panel B), and 800 eV (1t$_2$/Mn 2p, panel C) photon energies. Peaks were labelled consistently with the bulk-sensitive data presented in the previous section. The spectra shown in panels A and B were recorded at the U49/2 PGM-1 beamline at BESSY II under ambient temperature conditions, while the spectrum shown in panel C was recorded at the P04 beamline at PETRA III at a regulated liquid jet temperature of 277 K. Comparison between data sets recorded at temperatures in the ~ 2 – 20°C range confirmed that variations in sample temperature have no detectable effect on the extracted BEs under the applied experimental conditions. In panel A, the drop in the spectrometer transmission efficiency at low KEs (<100eV) and the relatively high secondary electron background yield prevented resolution of peaks **4** and **5**. Hence, outer (panel D) and inner (panel E) valence spectra were additionally recorded at a photon energy of 225 eV achieving more uniform collection efficiency over the spectrum, which facilitated the determination of the MnO$_4^-$$_{(aq.)}$ 5a$_1^{-1}$ (peak **4**) and 2t$_2^{-1}$ (peak **5**) BEs. It was not possible, however, to extract the MnO$_4^-$$_{(aq.)}$ 4a$_1^{-1}$ (peak **6**) BE from any of the surface-sensitive XPS measurements.

Figure 4.4. Surface-sensitive spectra of NaMnO$_{4(aq.)}$

(A) Outer and inner valence spectrum recorded at a 150 eV photon energy in a magic angle polarization configuration. **(B)** O 1s solute and solvent reference spectra recorded at a 688 eV photon energy. The † peak label denotes an apparent solute signal that exclusively arises in the surface-sensitive direct XPS data and is ascribed to the slight increase of the liquid water O 1s peak (peak vii) width in the solution versus the aqueous-solvent reference spectra. **(C)** Mn 2p spectrum recorded at a 800 eV photon energy. **(D)** Outer valence spectra recorded at 225 eV photon energy. **(E)** Inner valence spectrum, displaying the 2t$_2$$^{-2}$ solute ionizing transition (peak **5**) recorded at a 225 eV photon energy. The 4a$_1$$^{-1}$ signal (peak **6** in Fig. 3 in the main text) could not be isolated in the surface-sensitive spectra. The signal at ~87 eV is present in both the solution and solvent spectra and appears to be an artefact associated with the analyzer lens table.

The increased gas-phase signals at 150 eV with respect to 635 eV photon energies and the differential sample charging that occurs between the solution and solvent jet samples lead to numerous gas phase background subtraction artefacts in the 150 eV photon energy difference spectra. This, for example, prevented the determination of a peak **3** BE. In the O 1s solution-solvent difference spectrum an

53

additional peak arises with respect to the bulk-sensitive data at a BE of ~538 eV (peak marked by a † in the inset of the Figure). This apparent solute ionization feature likely originates from a slightly larger liquid water peak vii (O 1s) width in the surface-sensitive $MnO_4^-{}_{(aq.)}$ spectrum with respect to the corresponding water reference (50 mM $NaCl_{(aq.)}$) spectrum. Another explanation would be the presence of an additional solute peak. However, in contrast with fitting the difference spectra, cumulative Voigt profile fits to O 1s spectra revealed a single contribution for the solute's O 1s BE (peak **7**). Both of these interpretations can be associated with a broader range of hydration environments being sampled at the aqueous-gas interface and/or a reduction of the solute molecular symmetry at the interface [231]. The first explanation seems more likely given that no solution-gas interfacial effects were discerned in the valence-band surface-sensitive spectra.

Overall, the surface-sensitive data was found to be very similar to the bulk-sensitive data, except for the different relative intensities of most of the peaks. This largely reflects the changes of relative ionization cross sections at the different photon energies, although smaller effects due to photoelectron elastic scattering occur as well. Analysis of the surface-sensitive spectra revealed similar results to those reported from bulk-sensitive measurements in Table 4.1, showing that potential incomplete hydration at the interface has too small an effect to be detected in the experiments performed here. This suggests that (on average) $MnO_4^-{}_{(aq)}$ presents a similar molecular structure both in the aqueous bulk and at the solution–gas interface, at least at 0.2 M concentration. The $MnO_4^-{}_{(aq)}$ BEs extracted from fits to the data presented in Figure 4.4 are summarized in Table AI.1 in Appendix I.

Figure 4.5 shows outer valence (panel A), O 1s (panel B) and Mn 2p (panel C) surface-sensitive spectra recorded from 0.22 ± 0.02 M $KMnO_{4(aq.)}$ solutions. Given the relatively low solubility limit of $KMnO_4$ [232], the liquid jet temperature needed to be set to temperatures in the 287 – 303 K range in order to achieve stable liquid jet conditions during the acquisition time. This was required to achieve sufficient signal-to-noise ratio over a 5 – 45 eV BE range. The lone extractable $K^+{}_{(aq.)}$ counter-ion feature, $3p^{-1}$, is highlighted in the left inset of panel A, labelled as peak viii, and identified by a green Gaussian profile associated with a fit to the solution-solvent difference spectrum.

The $KMnO_{4(aq.)}$ spectra are comparable to the $NaMnO_{4(aq.)}$ data shown in panels A-C in Figure 4.4. BEs extracted from data such as that shown in Figure 4.5 are reported in Table 4.3. Comparison of the $KMnO_{4(aq.)}$ and $NaMnO_{4(aq.)}$ results showed that a change in counter-ion has no discernible effect on the extracted electron BEs. This result highlights that $MnO_4^-{}_{(aq.)}$, and $Na^+{}_{(aq.)}$ or $K^+{}_{(aq.)}$ counter-ions similarly (and likely fully) dissociate in ~0.2 M aqueous solutions and that the anions and cations are, on average, similarly well-separated at the aqueous-gas phase interface.

As discussed in Section 2.3.4, the high photon energies associated with the core-to-virtual valence energy gaps in the RPES experiments ensures bulk-solution sensitivity in those experiments. Consequently, bulk-sensitive RPES results from 0.15 M $KMnO_{4(aq.)}$ solutions can be compared to the $NaMnO_{4(aq.)}$ bulk-sensitive BE information reported in Section 4.1.1 in order to assess the effects of the counter-ion on the bulk electron energetics. The results from such experiments are shown in Figure AI.4 (and reported in Table AI.3, with the peaks labelled with numbers) in Appendix I. The aforementioned $KMnO_{4(aq.)}$ RPES and $NaMnO_{4(aq.)}$ bulk-sensitive XPS data comparison indicates that the different counter ions ($Na^+{}_{(aq.)}$ / $K^+{}_{(aq.)}$ cations) are inconsequential for the $MnO_4^-{}_{(aq.)}$ solute BEs extracted at 0.2 M concentration in the bulk of the solution. This highlights that (like at the aqueous-vacuum interface) $MnO_4^-{}_{(aq.)}$ and $Na^+{}_{(aq.)}$ or $K^+{}_{(aq.)}$ counter-ions fully dissociate in bulk ~0.2 M aqueous

solutions and that the anions and cations are on average well-separated in the aqueous-bulk (in contrast to previous reports regarding partial aqueous dissociation of permanganate salts [233]).

Figure 4.5. Surface-sensitive spectra of KMnO$_{4(aq.)}$

(A) Outer valence spectrum recorded at 150 eV photon energy in a perpendicular angle polarization configuration. **(B)** O 1s MnO$_{4-(aq.)}$ and water reference spectra recorded at 688 eV photon energy. **(C)** Mn 2p spectrum recorded at 793 eV photon energy. The † peak label in the inset of panel B denotes an apparent solute signal that exclusively arises in the surface-sensitive direct XPS data and is ascribed to the slight increase of the liquid water O 1s peak (peak vii) width in the solution versus the aqueous solvent reference spectrum. The solute anion and cation (peak viii) signals are illustrated by brown and green fills, respectively.

Table 4.3. KMnO$_{4(aq.)}$ surface-sensitive BEs and and FWHM peak widths

MnO$_4^-$$_{(aq.)}$ solute BEs and associated Gaussian peak width components, FWHM$_G$, extracted from KMnO$_{4(aq.)}$ surface-sensitive direct XPS experiments. The values associated with features 7 and 8, were extracted from Voigt profile fits.
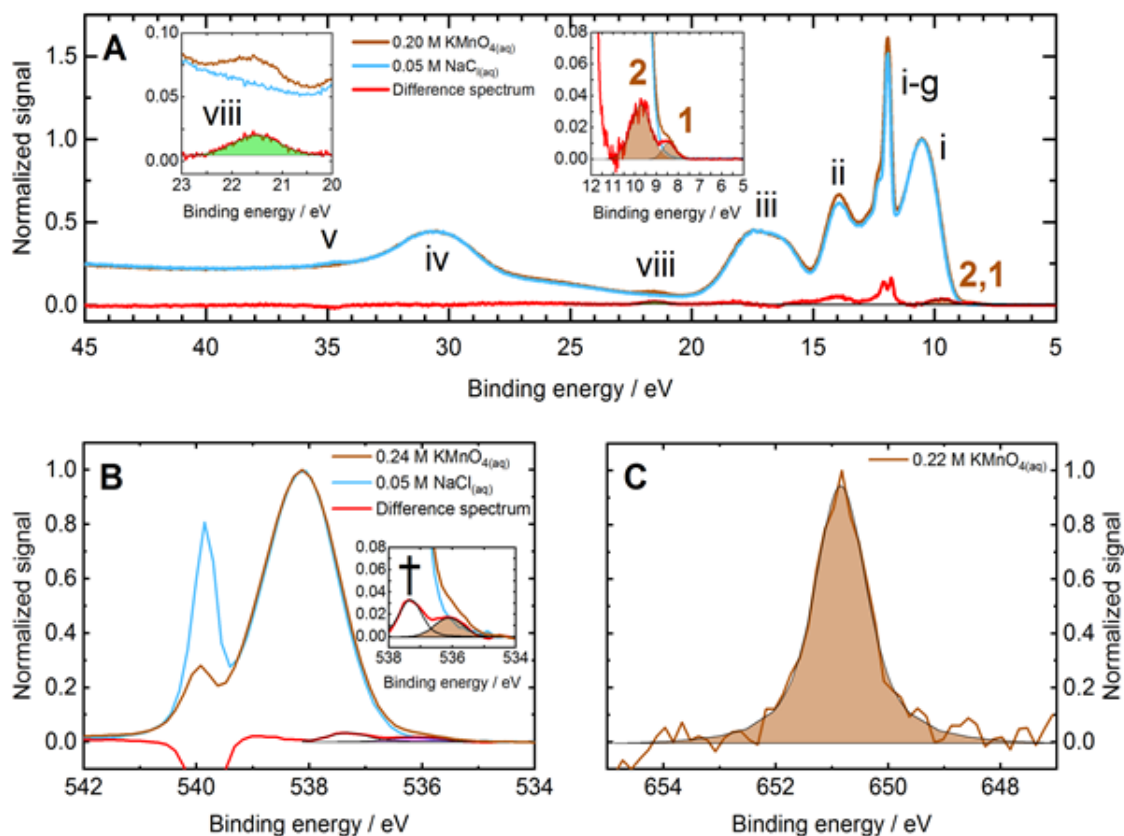
Label	Peak Origin	BE / eV	FWHM$_G$ / eV
1	$(1t_1)^{-1}$	9.29 ± 0.07	0.75 ± 0.06
7	$(3a_1)^{-1}$	536.2 ± 0.1	1.59 ± 0.01
8	$(1t_2)^{-1}$	650.8 ± 0.1	1.11 ± 0.04

4.1.3 Depth profiling and concentration effects

In order to assess whether $MnO_4^-{}_{(aq)}$ ions have a tendency to remain in the bulk of the solution, at the gas-solution interface, or whether they are homogeneously distributed, O 1s spectra were recorded from 0.2 M and 1.0 M $NaMnO_{4(aq.)}$ solutions as a function of photon energy and, hence, probing depth. Spectra were recorded at the P04 beamline at PETRA III in near magic angle polarization configuration [150], using five different photon energies: 688 eV, 838 eV, 988 eV, 1138 eV, and 1288 eV. Considering the $MnO_4^-{}_{(aq)}$ O 1s BE (peak **7**) value reported in Table 4.1, the aforementioned photon energies respectively correspond to ~150 eV, ~300 eV, ~450 eV, ~600 eV, ~750 eV KEs. The lower and highest KEs correspond to estimated probing depths of 1 nm and 5 nm, respectively [150] (see Figure 2.7 for details).

The spectra are shown in Figure 4.6 in panels A (0.2 M concentration) and B (1.0 M concentration). The insets in the Figures highlight Voigt profile fits to the $MnO_4^-{}_{(aq)}$ O 1s signals extracted from cumulative fits to the spectra. The $MnO_4^-{}_{(aq)}$ O 1s BE extracted from the 0.2 M and 1.0 M spectra did not change within the experimental uncertainties and uncertainty in the calibration of the BE scale. The data was intensity normalized to the water O $1s_{(l)}$ ionization feature at 538.1 eV [227], assuming that the probed concentration of water is constant at all photon energies and probing depths. The gas phase signal is observed to decrease with increasing photon energy (and condensed phase probing depth).

Within the experimental uncertainties, at 0.2 M concentration, the intensity of the $MnO_4^-{}_{(aq)}$ O 1s signal seems to remain constant as a function of photon energy (*i.e.* as the probing depth increases from ~1 nm to ~5 nm). Panel C shows that at 1.0 M concentration, the $MnO_4^-{}_{(aq)}$ O 1s signal intensity significantly increases in the 988 – 1288 eV photon energy range – that is, for probing depths in the ~2 – 4 nm range – suggesting non-linear anion accumulation in the bulk of the solution (*i.e.* away from the gas-solution interface). At 0.2 M concentration, the existence of a similar behavior to that observed at 1.0 M concentration can not be confirmed due to the large errors asssociated with the determination of the peak areas. Consequently, the results presented in this section seem to suggest that $MnO_4^-{}_{(aq)}$ ions tend to accumulate in the bulk of the solution and away from the gas-solution interface, potentially in both dilute and concentrated solutions. Alternatively, $MnO_4^-{}_{(aq)}$ ions could be homogeneously distributed in solution at 0.2 M concentration, with non-linear accumulation behavior in the bulk of the solution occurring at a higher concentration only.

Depth profiling studies can provide insight into the effect of solute ions on the surface tension of water. In general, the presence of inorganic ions in aqueous solution increases the surface tension of water, while organic ions have the opposite effect [234]. The increase in surface tension due to the presence of inorganic solutes can be explained by the presence of solute-solvent polarization interactions and hydration effects that result in a 'repulsion' of the solute from the gas-solution interface [235]. In dilute solutions, the surface tension of water increases linearly with the ion concentration in the bulk of the solution, with non-linear effects being present at higher concentrations [234]. The trend observed in the 'signal intensity versus photon energy / probing depth' plots shown in panel C are consistent with these phenomena.
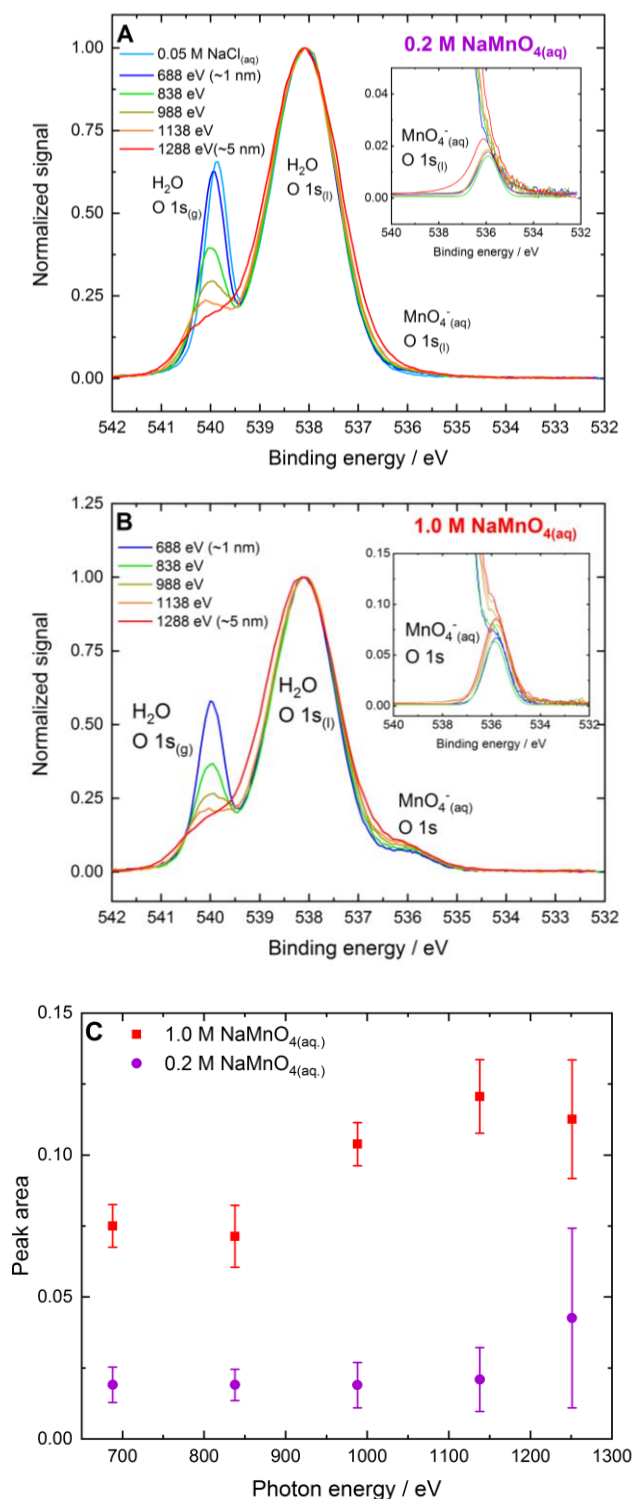
Figure 4.6. Depth profiling of 0.2 M and 1.0 M NaMnO$_{4(aq.)}$ solutions

O 1s spectra recorded from 0.2 M **(A)** and 1.0 M **(B)** NaMnO$_{4(aq.)}$ solutions as a function of photon energy in a magic angle polarization configuration. The insets highlight Voigt profile fits to the MnO$_4^-{}_{(aq.)}$ O 1s signals from cumulative fits performed to the spectra. **(C)** Plot of MnO$_4^-{}_{(aq.)}$ O 1s signal peak area extracted from the aforementioned fits as a function of photon energy for 0.2 M (purple) and 1.0 M (red) NaMnO$_{4(aq.)}$. Fitting errors are indicated by vertical lines.

Overall, the depth profiling experiments explored the ion distribution in solution, potentially providing insight into the effect of $MnO_4^-(aq.)$ in the surface tension of water, both at moderately dilute and relatively high concentrations. An understanding of such effects is relevant for the degradation of organic compounds, where $MnO_4^-(aq.)$ ions are used as oxidizing agents in combination with anionic surfactants [236].

4.1.4 Electronic energetic comparison across phases

Starting with the aqueous / solid phase comparison, the BEs respectively extracted from $MnO_4^-(aq)$ (Table 4.1) and crystalline $KMnO_4$ [167] samples need to be brought onto a common local vacuum reference level to be properly compared. With that aim, a solid-state work function of 5.3 eV [167] (assumed to be a $KMnO_4$ crystal-face-independent value [142]) was considered and added to the Fermi-level-references solid state BEs. As a result, the inner and outer valence BEs are found to be 0.0-0.4 eV larger in the solid phase compared to the aqueous phase. Following similar energetic reference considerations, the Mn 2p and O 1s core-level BEs are found to be shifted by -0.1 ± 0.1 eV and $+0.2 \pm 0.1$ eV in the solid phase with respect to the aqueous phase. The shifts observed for the valence band spectral region can be interpreted as the result of a lower degree of dielectric screening in aqueous solution compared to that provided by a crystalline environment. In addition, the almost negligible shifts observed for the core levels are an indication of similarly net-screened local charge distributions across the two phases.

For the aqueous / gas phase comparison, the $(1t_1)^{-1}$ / $HOMO^{-1}$ VIE of isolated MnO_4^- reported in Reference [175] relative to vacuum is considered, being ~4.3 eV lower compared to that determined for the aqueous phase ion (peak **1** in Table 4.1). This comparison highlights that the gas phase MnO_4^- ion is sigificantly less stable with respect to ionization than the aqueous and solid phase species, likely as a result of the ion being stabilized by the aqueous solvent or crystal lattice.

4.2 Resonantly-enhanced photoelectron spectroscopy

This section presents results from Mn $2p_{3/2}$, Mn $2p_{1/2}$ and O 1s RPES experiments performed with 0.2 M $NaMnO_4(aq.)$ solutions. These experiments allowed intramolecular Auger processes to be identified and applied to complement the bulk-sensitive electronic structure information reported in Section 4.1.1. Furthermore, they provided insight into the hybridized nature of the valence electronic distributions in $MnO_4^-(aq)$. In addition, the O 1s RPES data revealed the occurrence of non-local autoionization (particularly, ICD processes following soft X-ray excitation of the $MnO_4^-(aq.)$ ion). The data was recorded at a regulated liquid jet temperature of 280 ± 3 K.

4.2.1 Mn $2p_{3/2}$ intramolecular Auger processes

Figure 4.7 shows a Mn $2p_{3/2}$ RPES map (panel A, left) and the associated PEY-XAS spectrum (panel A, right) recorded at the U49/2 PGM-1 beamline at BESSY II. The dashed lines indicate the (resonant) photon energies at which two Mn $2p_{3/2}$ core-to-virtual valence transitions occur. The peak photon energies were determined to be 643.4 ± 0.1 eV (Resonance I, red dashed lines) and 645.7 ± 0.1 eV (Resonance II, blue dashed lines) from a cumulative Gaussian fit to the PEY-XAS spectrum (see Figure AI.1, left panel in Appendix I).
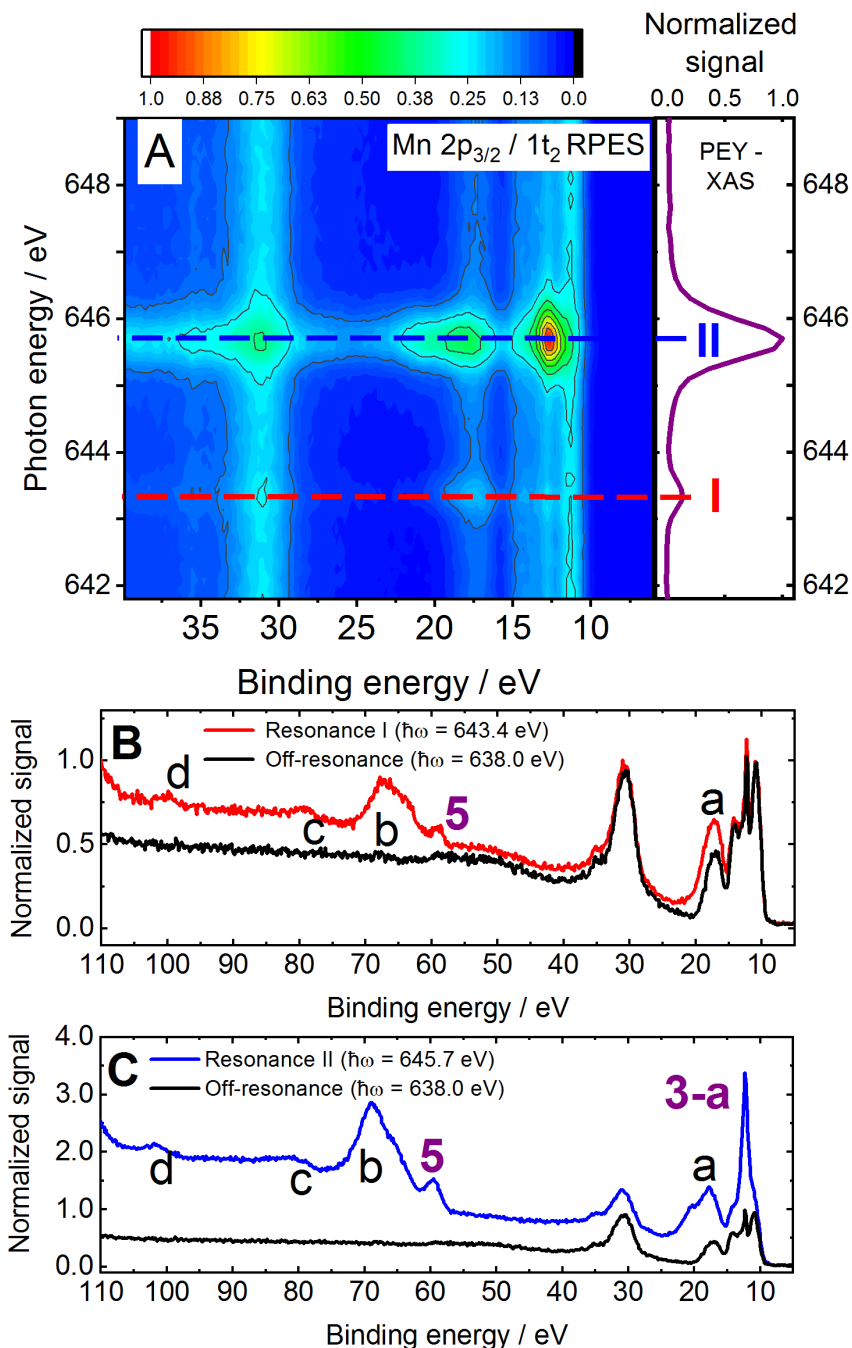
Figure 4.7. Mn 2p$_{3/2}$ RPES spectra from MnO$_4^-$$_{(aq.)}$ solutions

Mn 2p$_{3/2}$ RPES data recorded from 0.2 M NaMnO$_{4(aq.)}$ solutions in a perpendicular angle polarization configuration. **(A)** RPES map (left) and PEY-XAS spectrum (right). **(B)** As measured Mn 2p$_{3/2}$ → 2e resonant spectrum (red). **(C)** As measured Mn 2p$_{3/2}$ → 5t$_2$ resonant spectrum (blue). A spectrum recorded at an off-resonant photon energy (black), and devoid of resonantly enhanced signals is shown in panels B and C. Participator Auger signals are labelled with numbers and spectator Auger signals are labelled with letters. The BE scale is suitable for the identification of participator Auger process and a comparison with the direct XPS results reported in Section 4.1.1. For the assignment of spectator Auger signals, a KE scale is more appropriate – as will be implemented in the resonant-off-resonant difference data presented in Figure 4.8.

Based on the energetics extracted from the UV-visible absorption spectra (Figure 2.3) and assignments of similar features reported by Reinert *et al.* from similar experiments with solid phase MnO_4^- ions [174], the aforementioned resonances were assigned as Mn $2p_{3/2} \rightarrow 2e$ and Mn $2p_{3/2} \rightarrow 5t_2$, respectively. Panels B and C show higher-signal-to-noise ratio spectra recorded over an extended BE range at the Resonance I (panel B, red) and II (panel C, blue) photon energies. Numbers are used to label participator Auger signals, while spectator Auger signals are labelled using letters. A spectrum recorded at an off-resonant photon energy of 638 eV (which is devoid of resonantly-enhanced signals) is shown on each panel for comparison. In order to precisely extract the energetics of each of the resonantly-enhanced processes, the off-resonant spectrum was subtracted from the resonant data shown in panels B and C (see Section 3.4.2 for details). The resonant-off-resonant difference spectra are shown in Figure 4.8.

Figure 4.8. Mn $2p_{3/2}$ resonantly-enhanced signals from 0.2 M MnO_4^- (aq.) solutions

Resonance I (Mn $2p_{3/2} \rightarrow 2e$) and II (Mn $2p_{3/2} \rightarrow 5t_2$) RPES difference spectra produced from the raw data shown in Figure 4.7 (panels B and C, respectively). Participator Auger signals are labelled with numbers and spectator Auger signals are labelled with letters.

Two participator Auger signals were identified in the spectra shown in Figures 4.7 and 4.8, labelled as **3-a** and **5**. The numbers used to identify these signals refer to the labels shown in Table 4.1. While peak **3-a** dominates the Resonance II spectrum (and the RPES map shown in Figure 4.7 as a whole), it is either too weak to be identified or not present in Resonance I. In contrast, peak **5** is present following excitation at both Resonances I and II.

Cumulative fits to the data shown in Figure 4.8 (see Figure AI.3 and Table AI.2 in Appendix I) allowed an electron KE of 633.0 ± 0.1 eV – which corresponds to a BE of 12.66 ± 0.04 eV – to be extracted for the participator peak **3-a**. With the MO diagram shown in Figure 4.1 and the direct XPS results reported in Table 4.1 in mind, this feature was assigned to a L_{III}-$(1e/3t_2)5t_2$ participator Auger process involving the photoexcited $5t_2$ virtual valence and one *or* both of the 1e and $3t_2$ outer valence molecular orbitals. That is, a resonantly enhanced signal of the $(1e)^{-1}$ or $(3t_2)^{-1}$ ionizing transitions.

This spectral feature correspondingly highlights the Mn-character of the 1e and/or $3t_2$ orbitals. Upon comparison of the $FWHM_G$ value extracted for peak **3-a** (0.83 ± 0.04 eV) with that reported for feature **3** in Table 4.1 (1.9 ± 0.2 eV), the broader peak width of the direct XPS results suggests that a single ionization channel is enhanced at Resonance II (confirming that peak **3** in the direct XPS data is indeed formed by two underlying components, as stated in Section 4.1.1). Information from the O 1s RPES data that will be presented in Section 4.2.3 was required to identify the specific MO involved in this participator Auger process, as will be discussed in Section 4.2.3. In addition, the 0.77 ± 0.03 eV FWHM Lorentzian component (of a 1.32 ± 0.01 eV total FWHM peak width) extracted from a Voigt profile fit to peak **3-a** in the Resonance II data reveals a significant lifetime broadening contribution to the total peak width. This broadening is likely the result of constructive interference between the direct $1e^{-1}$ or $3t_2^{-1}$ ionization channels and the respective L_{III}-$1e,5t_2$ or L_{III}-$3t_2,5t2$ participator Auger channels. Given that channel interference occurs during the average ~1.8 fs Mn $2p_{3/2}$ core-hole lifetime, spectral broadenings of ~0.4 eV [237] are expected to be reflected on the (coherently) resonantly enhanced L_{III}-pre-edge peak widths. The greater (0.77 ± 0.03 eV) lifetime broadening contribution observed here suggests a shorter than average Mn $2p_{3/2}$ core-hole lifetime in $MnO_4^-{}_{(aq.)}$. Similar peak width results have been reported in RPES experiments carried out in the crystalline phase [174].

The second participator Auger feature, peak **5**, occurs at KEs of 583.9 ± 0.1 eV (Resonance I) and 585.6 ± 0.1 eV (Resonance II), with associated BEs of 59.5 ± 0.1 eV and 60.1 ± 0.1 eV, respectively. Considering the $MnO_4^-{}_{(aq.)}$ BE reported for peak **5** from the direct XPS experiments (see Table 4.1) this signal is assigned as a resonant enhancement of the $1t_2$ (Mn 3p) inner valence ionization feature, *i.e.* L_{III}-$2t_2,2e$ (Resonance I) and L_{III}-$2t_2,5t_2$ (Resonance II) participator Auger processes.

Finally, the absence of any $1t_1$ or $4t_2$ orbital participator Auger features in the $9.0 - 10.5$ eV BE region confirms the predominant O-character of these signals and the assigned molecular orbitals.

The spectator Auger signals (labelled as **a − d** in Figures 4.7 and 4.8) are observed both in the Resonance I and Resonance II data, with relatively constant KEs at both resonances (as explained in Section 2.3.3, the KE of equivalent spectator Auger processes remains constant and independent on the resonant photon energy). The assignment of each of these spectator Auger features was made by considering the BEs determined from the direct XPS experiments presented in Table 4.1. Features **a** and **b** are both made up of two or more peaks. The main features show average KEs of 627.1 ± 0.4 eV (peak **a**) and 576 ± 1 eV (peak **b**). While peak **a** was attributed a L_{III}-V,V spectator Auger process, peak **b** was assigned as a L_{III}-$2t_2$,V process involving the $MnO_4^-{}_{(aq.)}$ $2t_2$ (Mn 3p) electrons. The relatively weak **c** and **d** spectator Auger signals occur at KEs of 565.7 ± 0.8 eV and 544.2 ± 0.1 eV, respectively. Peak **c** was tentatively assigned to a L_{III}-$2t_2,5a_1$ spectator Auger involving $MnO_4^-{}_{(aq.)}$ $2t_2$ and $5a_1$ inner valence electrons. Peak **d** was assigned as a L_{III}-$4a_1$,V process, involving $4a_1$ (Mn 3s) inner valence electrons and outer valence electrons (V).

Regarding the origin of the valence electrons involved in the spectator Auger processes associated with features **a** and **b**, the energetics suggest involvement of any of the Mn-O bonding $6a_1$, 1e, and/or $3t_2$ outer valence orbitals (which show Mn-character, as explained in Section 2.1.2). In addition, given that the $6a_1$ orbital is predicted to have significant Mn 3p character [104] – unlike the 1e and $3t_2$ orbitals – peak **b** may be attributed to a L_{III}-$2t_2,6a_1$ spectator Auger process.

The assignment of feature **c** suggests electronic coupling between the inner valence $2t_2$ (Mn 3p) and $5a_1$ (O 2s) orbitals and the 2e and $5t_2$ virtual valence orbitals, highlighting that the Mn-based $2t_2$ and

O-ligand-based $5a_1$ orbitals are hybridized. Together with feature **b**, peak **c** is indicative of outer-inner valence electronic coupling. Similarly, peak **d** highlights electronic coupling and hybridization of the Mn 3s orbital with the valence manifold. Furthermore, taking into account the $MnO_4^-{}_{(aq.)}$ $4a_1$ (Mn 3s) BE from Table 4.1 and neglecting electron correlation effects, a BE of ~12.5 eV is expected for the valence orbital involved in the L_{III}-$4a_1$,V process. This BE value is consistent with those extracted from peaks **3** (direct XPS, Table 4.1) and **3-a** (participator peak), suggesting a L_{III}-$4a_1$,1e and/or L_{III}-$4a_1$,$3t_2$ process occurs, thus highlighting the Mn-character of all the involved orbitals.

The results extracted from the Mn $2p_{3/2}$ RPES data are summarized in Table 4.4. Average BE and $FWHM_G$ values of the participator Auger peaks determined from the Resonance I and II data presented here are shown in the top panel of the table. Similarly, average KEs of the spectator Auger peaks are listed in the bottom panel. (See Figure AI.3 and Table AI.2 in Appendix I).

Table 4.4. $MnO_4^-{}_{(aq.)}$ Mn $2p_{3/2}$ RPES participator and spectator Auger signals

Assignments of the Mn $2p_{3/2}$ RPES participator and spectator Auger signals associated with data shown in Figures 4.5 and 4.6. The reported values correspond to the main features' average KEs (and reported BEs) extracted at both resonances where such enhancement was observed.

Participator Auger			
Label	Assignment	BE / eV	$FWHM_G$ / eV
3-a	$(1e$ or $3t_2)^{-1}$	12.66 ± 0.04	0.83 ± 0.04
5	$(2t_2)^{-1}$	59.8 ± 0.4	2.6 ± 0.6
Spectator Auger			
Signal	Assignment		KE / eV
a	L_{III}-V,V		627.1 ± 0.4
b	L_{III}-$2t_2$,V		576 ± 1
c	L_{III}-$2t_2$,$5a_1$		565.7 ± 0.8
d	L_{III}-$4a_1$,V		544.6 ± 0.1

4.2.2 Mn $2p_{1/2}$ intramolecular Auger processes

Figure 4.9 shows a Mn $2p_{1/2}$ RPES map (panel A, left) and the associated PEY-XAS spectrum (panel A, right) recorded at the U49/2 PGM-1 beamline at BESSY II. Similar to Figure 4.7 in the previous section, Mn $2p_{1/2} \rightarrow 2e$ and Mn $2p_{1/2} \rightarrow 5t_2$ resonant spectra are shown in panels B and C, respectively. Resonant photon energies of 654.2 ± 0.2 eV (Resonance III, pink dashed lines) and 656.0 ± 0.2 eV (Resonance IV, light-green dashed lines) were extracted from a cumulative Gaussian fit to the PEY-XAS spectrum (see Figure AI.1, left panel in Appendix I). An off-resonant spectrum recorded at a lower photon energy of 638 eV (*i.e.* a spectrum devoid of resonant signal enhancements) is plotted in panels A and B for comparison. The associated Resonance III and IV difference spectra are shown in Figure 4.10.

Figure 4.9. Mn 2p$_{1/2}$ RPES spectra from MnO$_4^-$$_{(aq.)}$ solutions
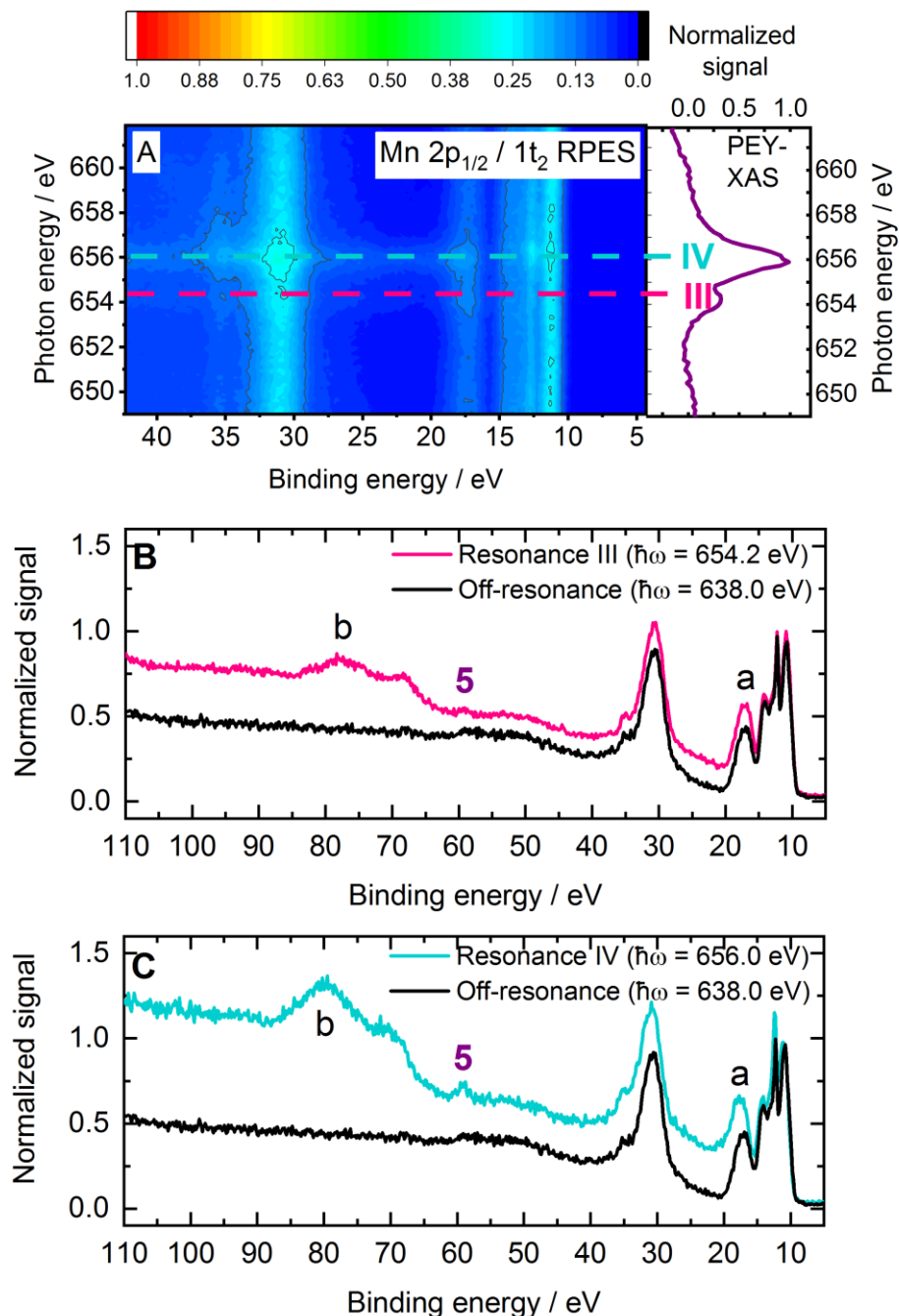
Mn 2p$_{1/2}$ RPES data recorded from 0.2 M NaMnO$_{4(aq.)}$ solutions in a perpendicular angle polarization configuration. **(A)** RPES map (left) and PEY-XAS spectrum (right). **(B)** As measured Mn 2p$_{1/2}$ → 2e resonant spectrum (pink). **(C)** As measured Mn 2p$_{1/2}$ → 5t$_2$ resonant spectrum (light green). A spectrum recorded at an off-resonant photon energy of 638.0 eV (black), devoid of resonantly enhanced signals, is shown in panels B and C. Participator Auger signals are labelled with numbers, and spectator Auger signals are labelled with letters. The BE scale is suitable for the identification of participator Auger process and a comparison with the direct XPS results reported in Section 4.1.1. For the assignment of spectator Auger signals, a KE scale is more appropriate, as will be implemented in the resonant-off-resonant data presented in Figure 4.10.

Figure 4.10. Mn 2p$_{1/2}$ resonantly-enhanced signals from MnO$_4^-$ $_{(aq.)}$ solutions

Resonance III (Mn 2p$_{1/2}$ → 2e) and IV (Mn 2p$_{1/2}$ → 5t$_2$) RPES difference spectra produced from the raw data shown in Figure 4.9 (panels B and C, respectively). Participator Auger signals are labelled with numbers and spectator Auger signals are labelled with letters. The 640 – 650 eV KE region highlighted in yellow indicates an area where over- and under-subtraction of the off-resonant spectrum from the resonant spectra resulted in sharp features that oscillate around zero in intensity, thus preventing the isolation of resonantly-enhanced MnO$_4^-$ $_{(aq.)}$ Auger features within this KE range.

In contrast to the Mn 2p$_{3/2}$ resonant data, only a participator peak associated with an enhancement of the MnO$_4^-$ $_{(aq)}$ 2t$_2$ electron ionization signal (peak **5**, with a KE of 596.1 ± 0.2 eV and a BE of 59.9 ± 0.2 eV) could be extracted from the Mn 2p$_{1/2}$ RPES data (in particular, from Resonance IV). In this case, the assignment of other participator Auger signals was generally impeded by over- and under-subtraction in the 640-650 eV electron KE region of the difference spectra, where valence participator signals might be expected (see the yellow overlay in Figure 4.10).

Two spectator Auger features – similar to those observed in the Mn 2p$_{3/2}$ resonant data and labelled as **a** and **b** in Figures 4.7 and 4.8 – are present. The spectral signatures are broader at Resonance III and IV compared to Resonance I and II. This observation is explained by a shorter average core-hole lifetime for Mn 2p$_{1/2}$ with respect to Mn 2p$_{3/2}$ (~0.7 fs versus ~1.8 fs, respectively [237]). In addition, at the higher photon energies associated with Resonances III and IV, Coster-Kronig processes [238] – L$_{II}$-L$_{III}$V in relation to feature **a** and L$_{II}$-L$_{III}$,2t$_2$ in relation to feature **b** – become accessible. These signals are observed as lower KE tails in the spectra and are spectrally shifted to lower KEs by the 1t$_2$ spin-orbit splitting energy, ~10.9 eV. The 15 – 30 eV span of feature **a** suggests a significant delocalization of the virtual valence electrons within the sub-fs core-hole lifetime. The assignment of feature **b** shows the hybridized nature of the Mn 2p (2t$_2$) atomic (inner valence molecular) orbital.

The participator and spectator Auger peak assignments associated with Figures 4.9 and 4.10 are summarized in Table 4.5 (See Figure AI.3 and Table AI.2 in Appendix I for details).

Table 4.5. MnO$_4^-$ $_{(aq.)}$ Mn 2p$_{1/2}$ RPES participator and spectator Auger signals

Assignments of the Mn 2p$_{1/2}$ RPES participator and spectator Auger signals associated with data shown in Figures 4.9 and 4.10. The reported values correspond to the main features' average KEs (and reported BEs) extracted at both resonances.

Participator Auger			
Label	Assignment	BE / eV	FWHM$_G$ / eV
5	$(2t_2)^{-1}$	59.9 ± 0.2	4.1 ± 0.4
Spectator Auger			
Label	Assignment 1	Assignment 2	KE / eV
a	L$_{II}$-V,V	-	636.6 ± 0.2
	L$_{II}$-L$_{III}$,V	-	631.0 ± 0.4
	L$_{II}$-5a$_1$,V	-	622.6 ± 0.2
b	L$_{II}$-2t$_2$,V	-	585.2 ± 0.3
	L$_{II}$-L$_{III}$,2t$_2$	L$_{II}$-2t$_2$, 5a$_1$	576.5 ± 0.2

4.2.3 O 1s intramolecular Auger processes

Panel A in Figure 4.11 shows a O 1s RPES map (left) and the associated PEY-XAS spectrum (right) recorded at the U49/2 PGM-1 beamline at BESSY II. Resonant photon energies of 528.5 ± 0.1 eV (Resonance V, orange dashed lights) and 530.0 ± 0.1 eV (Resonance VI, olive green dashed lines) were extracted from the latter (see Figure AI.1, right panel in Appendix I). Panels B and C show high-signal-to-noise resonant spectra recorded at Resonance V and VI, respectively, as well as off-resonant spectra plotted for comparison. The resonant-off-resonant difference spectra are shown in Figure 4.12.

The Auger signals present in the Resonance V and VI RPES data originate from photo-excitation from the O-centered core ligand orbitals into unoccupied metal-ligand antibonding orbitals – O 1s → 2e and O 1s → 5t$_2$, respectively. Given the non-bonding, predominant O 2p character of the 1t$_1$ and 4t$_2$ orbitals [104, 105] participator Auger signals are expected in the 9–11 eV BE range (see Table 4.1). However, photoelectron features in this spectral region likely overlap with beamline second harmonic artefact signals (peaks marked by '*' in Figures 4.11 and 4.12). In the Resonance V data, the participator Auger decay channel associated with the 1t$_1$ MO (K-2e,1t$_1$ process) is expected to be superimposed on the beamline second harmonic artefact. However, this signal can be discerned from the O 1s RPES map shown in Figure 4.11, where a 9.2 ± 0.1 eV feature is highlighted over a ~1 eV photon energy region in the vicinity of Resonance V.

In the Resonance VI data, the lower KE shoulder to the second harmonic artefact signal (labelled as peak **2-a** in Figures 4.11 and 4.12) was resolved at a KE of 520.1 ± 0.1 eV (corresponding to a BE of 9.85 ± 0.08 eV) and assigned as a K-4t$_2$,5t$_2$ participator Auger process. The identification of this participator Auger signal allowed the determination of a 9.85 ± 0.08 eV BE for the 4t$_2^{-1}$ ionization channel. It is important to note this BE may be biased by over-subtraction of the off-resonant data, and the BE value reported here represents a lower limit of the true value. The relatively narrow width (0.7 ± 0.2 eV) of peak **2-a** in comparison to the peak **2** feature extracted from the direct XPS results (1.2 ± 0.1 eV at FWHM, see Table 4.1) leads to the conclusion that peak **2** indeed consists of two overlapping components, as mentioned in Section 4.1.1. This inference is further supported by the solid-phase KMnO$_4$ experiments reported by Reinert *et al.* in Reference [167].
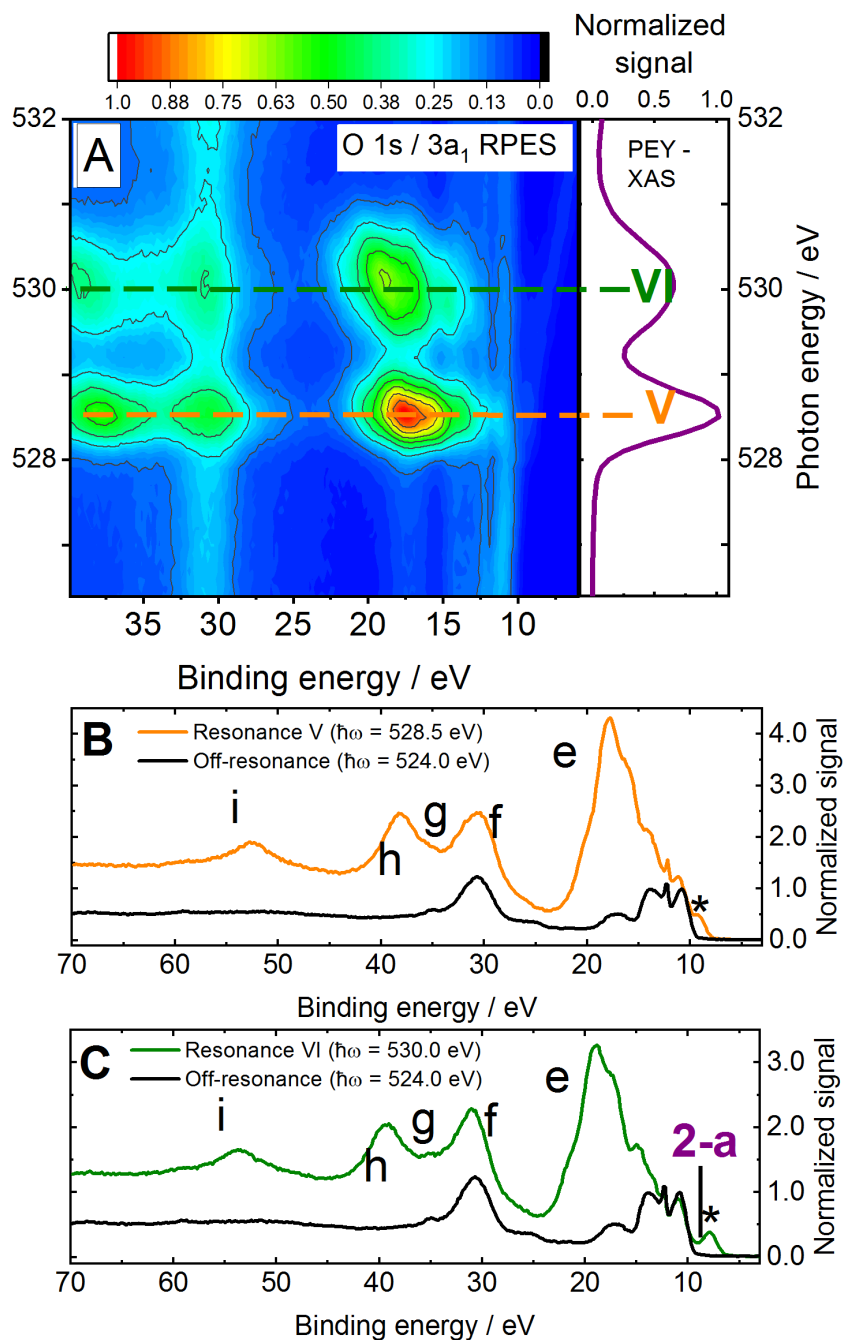
Figure 4.11. O 1s RPES data from MnO$_4^-$ (aq.)

(A) RPES map (left) and PEY-XAS spectrum (right). **(B)** As measured O 1s → 2e resonant spectrum (orange).
(C) As measured Mn 2p$_{3/1}$ → 5t$_2$ resonant spectrum (olive green). A spectrum recorded at an off-resonant photon energy (black), devoid of resonantly enhanced signals, is shown in panels B and C. Participator Auger signals are labelled with numbers, and spectator Auger signals are labelled with letters. The asterisk indicates a signal arising from ionization with the unfiltered second harmonic of the beamline. The BE scale is suitable for the identification of participator Auger process and a comparison with the direct XPS results reported in Section 4.1.1. For the assignment of spectator Auger signals, a KE scale is more appropriate, as will be implemented in the resonant-off-resonant data presented in Figure 4.12. The data was recorded in a perpendicular polarization configuration
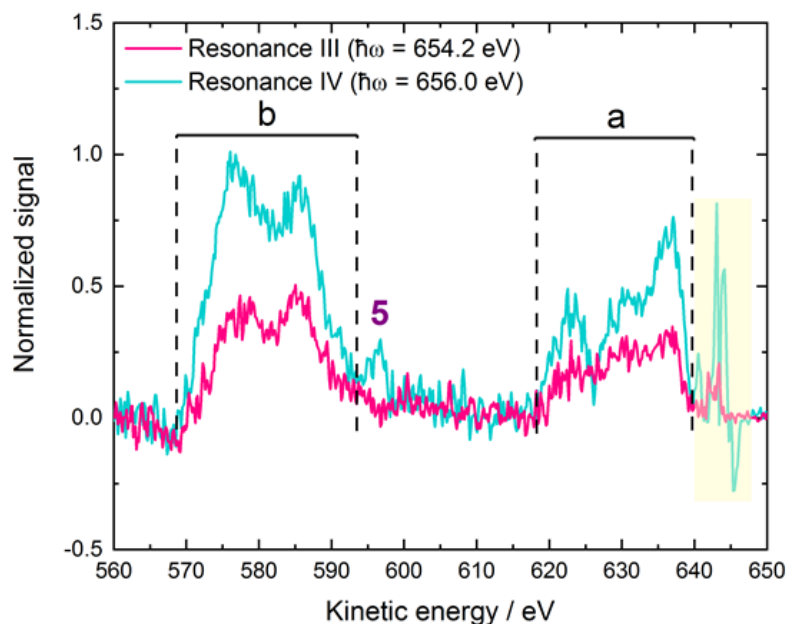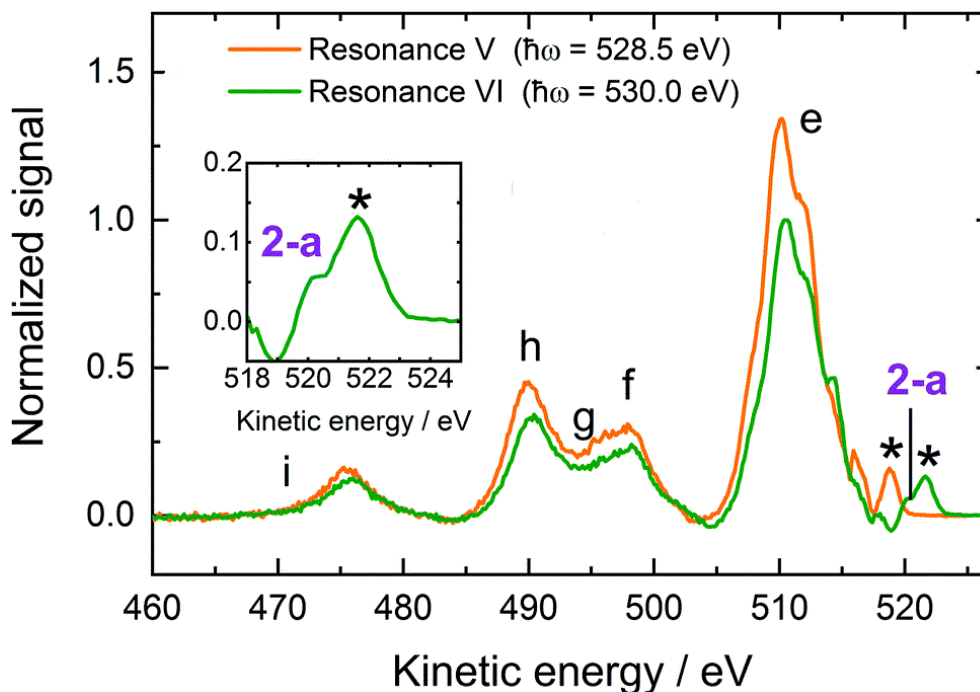
Figure 4.12. O 1s resonantly enhanced signals from MnO$_4^-$(aq.) solutions

Resonance V (O 1s → 2e) and VI (O 1s → 5t$_2$) RPES difference spectra produced from the raw data shown in Figure 4.11 (panels B and C, respectively). Participator Auger signals are labelled with numbers and spectator Auger signals are labelled with letters. The asterisk indicates signals arising from ionization with the unfiltered second harmonic of the beamline.

Finally, two additional potential participator Auger features are observed at 516.3 ± 0.1 eV KE in the Resonance V data and close to 518 eV KE in the Resonance VI data. In the first case, the stated KE corresponds to a BE of 12.18 ± 0.05 eV. With the assignments of peak **3** and peak **3-a** in mind, this feature could potentially be assigned as a selective K-1e,5t$_2$ process, with peak **3-a** correspondingly being attributed to a selective L$_{III}$-3t$_2$5t$_2$ participator Auger process. Hence, a 1e BE value of 12.18 ± 0.05 eV and a 3t$_2$ BE value of 12.66 ± 0.04 eV (peak **3-a**) can be tentatively inferred. In the second case, the ~518 eV KE feature may be linked to a L$_{III}$-5t$_2$,6a$_1$ participator channel. However, the KE and width of this peak could not be reliably extracted due to the low signal intensity and the over-subtraction of the off-resonant spectrum in this region. Given that the ~518 eV and 516.3 ± 0.1 eV potential participator peaks mentioned in this paragraph could be alternatively attributed to spectator Auger processes, the individual 1e and 3t$_2$ BEs cannot be determined unambiguously.

Regarding the spectator Auger signals, labelled as **e – i** in Figures 4.11 and 4.12, similar features are observed in both the Resonance V and VI data. Peak **e** spans the KEs of 505 – 519 eV and constitutes a manifold/convolution of four or more components with ~2.1 eV sub-structure separations. This multi-component feature was assigned to multiple K-VV spectator Auger processes. A similar result has been reported from solid state KMnO$_4$ RPES data [174]. Signals **f – i** are significantly broadened with respect to the sub-components of signal **e**. KEs of 498.3 ± 0.5 eV, 495 ± 1 eV, 490.1 ± 0.2 eV,

and 475.7 ± 0.2 eV were respectively determined for peaks **f**, **g**, **h** and **i** (see Figure AI.3 and Table AI.2 in Appendix I). Considering the $5a_1$ BE determined from the direct XPS experiments (see Table 4.1), such KEs would seem to be indicative of K-$5a_1$,V spectator Auger processes involving the $MnO_4^-{}_{(aq.)}$ non-bonding inner valence $5a_1$ (O 2s) electrons. As a result, BEs of 10.9 ± 0.5 eV, 14 ± 1 eV, 19.1 ± 0.2 eV, and 33.5 ± 0.2 eV are estimated for peaks **f**, **g**, **h** and **i**, respectively (neglecting electron correlation). These estimations would lead to possible assignments of peaks **f** and **g** as K-$5a_1$,($4t_2$/$6a_1$) and K-$5a_1$,($1e$/$3t_2$) intramolecular solute spectator Auger processes, respectively. However, the assignment of peaks **h** and **i**, based on similar considerations, is more challenging. For peak **h**, there are no solute BEs within ±6 eV of the expected ∼19 eV nominal BE of a $5a_1$ spectator Auger partner electron. For peak **i**, the closest match to its energetics is a K-$5a_1$,$5a_1$ process that would be shifted by more than 6 eV to higher KE in comparison to single-reference electronic structure expectations. These assignment challenges led to the consideration of alternative, non-local core-hole relaxation mechanisms involving secondary electron emission from solute-neighboring water molecules (*i.e.* ICD) to explain the energetics of peaks **f − i**. Such secondary electron emission channels are discussed in the following sub-section.

The results extracted from the O 1s RPES data, specifically those attributable to intramolecular solute processes, are summarized in Table 4.6. Average BE and FWHM$_G$ values of the participator Auger peaks determined from the Resonance I and II data presented here are shown in the top panel of the table. Similarly, average KEs of the spectator Auger peaks are listed in the bottom panel. (See Figure AI.3 and Table AI.2 in Appendix I).

Table 4.6. MnO$_4^-{}_{(aq.)}$ O 1s RPES participator and spectator Auger signals

Assignments of the O 1s RPES participator and spectator Auger signals associated with data shown in Figures 4.11 and 4.12. The reported values correspond to the main features' average KEs extracted at both resonances where such enhancement was observed.

Participator Auger			
Label	Assignment	BE / eV	FWHM$_G$
2-a	$(4t_2)^{-1}$	9.85 ± 0.08	0.7 ± 0.2
3-a	$(1e$ or $3t_2)^{-1}$	12.66 ± 0.04	0.83 ± 0.04
Spectator Auger			
Label	Assignment		KE / eV
e (main feature)	K-VV		510.2 ± 0.2

4.2.4 O 1s non-local autoionization processes

Participator-like resonant ICD signals have previously been identified in OH$^-{}_{(aq.)}$ solutions via the presence of a series of peaks with energetic spacings matching those of the water valence band features [75]. Such mirroring of the liquid water spectral features, specifically at explainable KE offsets, can be used to identify intermolecular autoionization processes, as discussed in the following. For features **f - i**, the energetic separation between neighbouring peaks were found to be 3 ± 1 eV, 5 ± 1 eV, and 14.4 ± 0.3 eV. Within the error bounds, these peak separations match the energy gaps between the valence BEs of liquid water (when average, 13.74 ± 0.08 eV, $3a_{1(l)}$ BEs are considered, see Table 4.2). This is illustrated in Figure 4.13, where the off-resonant spectrum recorded at 524.0 ± 0.1 eV was offset by the difference in the photon energies used to record the off-resonant and Resonance V and VI data (+4.5 ± 0.1 eV and +6.0 ± 0.1 eV, respectively) and the $5a_1$ BE (-26.82 ± 0.04 eV). This leads to overall off-resonant KE shifts of −22.3 ± 0.1 eV and −20.8 ± 0.1 eV for the Resonance V and VI data, respectively. As a result, the water valence feature peak centres overlap with the spectrally broadened **f - i** features, keeping in mind the additional differential peak shifting

associated with electron correlation effects. Considering the absolute KE positions of these photoelectron features, they are found to be in agreement with those expected for K-$5a_1V_{(w)}$ MnO_4^- $_{(aq.)}$-water ICD processes involving secondary emission of electrons from the $1b_1$, $3a_1$, $1b_2$, and $2a_1$ valence MOs of water molecules forming the first hydration shell of the solute (as indicated by the (w) sub-script).

Hence, based on the overall energetics discussed here and the lack of alternative spectator peak explanations for peaks **h** and **i**, the predominant electronic relaxation pathways associated with features **f**, **g**, **h**, and **i** are assigned as K-$5a_1,1b_{1(w)}$, K-$5a_1,3a_{1(w)}$, K-$5a_1,1b_{1(w)}$, and K-$5a_1,1b_{1(w)}$ resonant, *spectator-like* ICD processes, respectively. These results are summarized in Table 4.7.

Using similar arguments to those presented above, the presence of *participator-like* ICD relaxation can also be considered. For water $1b_1$, $3a_1$, $1b_2$, and $2a_1$ electron ejection, respective KEs of 517.2 ± 0.1 eV, 514.8 ± 0.1 eV, 511.1 ± 0.1 eV, and 497.5 ± 0.1 eV and 518.7 ± 0.1 eV, 516.3 ± 0.1 eV, 512.6 ± 0.1 eV, and 499.0 ± 0.1 eV would be expected at Resonances V and VI, respectively. These KEs span the range of feature **e** in Figure 4.12. However, the sharpness of the ionization features in these spectral regions and the occurrence of a similar spectral profile in crystalline $KMnO_4$ RPES data [174] imply that intramolecular spectator Auger decay processes dominate in the feature **e** spectral region.
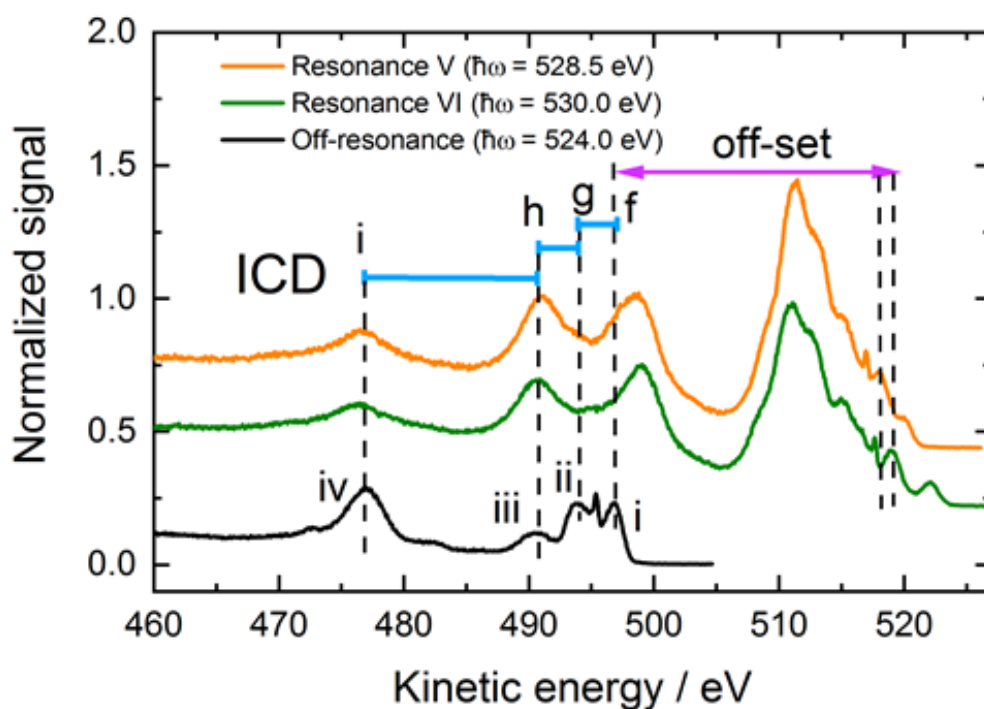
Figure 4.13. ICD signatures from MnO_4^- $_{(aq.)}$ solutions

Resonance V, Resonance VI, and off-resonant spectra (raw data, without baseline correction) showing the common energy gaps between peaks **f**, **g**, **h** and **i** in the resonant data and the water valence orbitals in the energetically shifted off-resonant spectrum. The off-resonant spectrum was offset in order to account for the resonant-non-resonant photon energy difference, the $5a_1$ binding energy, and electron correlation effects, as explained in more detail in the text.

Table 4.7. MnO$_4^-$$_{(aq.)}$ ICD signals

Assignments of the ICD signals. The reported values correspond to the main features' average KEs extracted at both resonances.

Label	Assignment	KE / eV
f	K-5a$_1$,1b$_{1(w)}$	498.3 ± 0.5
g	K-5a$_1$,3a$_{1(w)}$	495 ± 1
h	K-5a$_1$,1b$_{2(w)}$	490.1 ± 0.2
i	K-5a$_1$,2a$_{1(w)}$	475.7 ± 0.2

Overall, the occurrence of ICD processes in MnO$_4^-$$_{(aq.)}$ solutions is evidenced by the mirroring in peak separation between the resonantly-enhanced photoelectron features present in the MnO$_4^-$$_{(aq.)}$ spectra and the water photoelectron peaks in the off-resonant spectrum, highlighting matching energetics of the solvent photoelectrons involved in the ICD relaxation channel in both data sets. Further confirmation could be obtained from similar MnO$_4^-$ experiments using deuterated water as the solvent, where the lack of hydrogen bonding should render the occurrence of intramolecular relaxation of the photo-excited solute involving solvent molecules unfeasible.

4.3 Summary of key findings of Chapter 4

The electronic structure and molecular bonding of MnO$_4^-$$_{(aq.)}$, as well as MnO$_4^-$$_{(aq.)}$-water interactions, were probed by performing liquid jet XPS and RPES experiments with NaMnO$_{4(aq.)}$ and KMnO$_{4(aq.)}$ solutions:

1. An experimentally-determined, near-complete, BE-scaled MO diagram was produced for the fully hydrated MnO$_4^-$$_{(aq.)}$ ion;

2. At 0.2 M concentration, the outer and inner valence, O 1s and Mn 2p$_{3/2}$ / 2p$_{1/2}$ electron BEs proved to be independent of counter ion and liquid jet probing depth – the latter confirming similar electronic energetics in the aqueous bulk and at the gas-solution interface;

3. Depth profiling experiments performed with NaMnO$_{4(aq.)}$ solutions at 0.2 M and 1.0 M concentrations revealed a preference for MnO$_4^-$$_{(aq.)}$ to remain in the bulk of the solution and away from the gas-solution interface, potentially highlighting non-linear accumulation behavior in solution for the higher concentration case;

4. The BEs of MnO$_4^-$ in aqueous solution (MnO$_4^-$$_{(aq.)}$) and as part of a crystalline solid (KMnO$_{4(s)}$) were found to be similar, with the aqueous phase BEs shifted to lower values by up to a few-hundred meV compared to their solid state counterparts. The aqueous phase results also highlight an increase of the lowest-energy ionizing transition BEs by more than 4 eV upon hydration, *i.e.* in moving from the gas to the aqueous phase;

5. The Mn 2p$_{3/2}$ RPES experiments revealed a selective enhancement of the 3t$_2^{-1}$ feature at the Mn 2p$_{3/2}$ → 5t$_2$ resonant photon energy. This participator Auger peak allowed the 3t$_2^{-1}$ BE to be determined, which was not possible from the direct XPS data, where the Mn-O bonding 1e^{-1} and 3t$_2^{-1}$ features overlap in a single, convoluted feature;

6. Similar to the above, the O 1s RPES experiments allowed the 4t$_2^{-1}$ BE to be determined and disentangled from the convoluted 4t$_2^{-1}$ / 6a$_1^{-1}$ feature observed in the direct XPS data;

7. Overall, the Mn 2p$_{3/2}$, Mn 2p$_{1/2}$, and O 1s RPES experiments revealed hybridization of the solute constituents' atomic orbitals, including the inner valence Mn 3p and O 2s. In addition, the O 1s RPES experiments showed the presence of ICD relaxation processes, highlighting

valence $MnO_4^-{}_{(aq.)}$–$H_2O_{(l)}$ electronic couplings between $MnO_4^-{}_{(aq.)}$ O 2s electrons and the valence electronic manifold of water molecules in the first solvation shell;

The energetic information on the electronic structure, molecular bonding and solute-solvent interactions reported in this chapter constitute photoelectron spectroscopy fingerprints of the tetra-oxo Mn(VII+) charge state in aqueous solution. The determined BEs may act as experimental benchmarks for emerging multi-configurational electronic structure calculation methods focused on the explicit treatment of hydration and its effects on this TMC ion [105, 111]. In addition, the experimentally-determined BEs will be used to infer thermodynamic and redox parameters relevant for electron transfer events involving this ion, as will be presented in Chapter 6.

5 Electronic structure of manganate ions in aqueous solution ($MnO_4^{2-}_{(aq.)}$)

This chapter presents results obtained from XPS and RPES experiments performed with $MnO_4^{2-}_{(aq.)}$ solutions.

As described in Section 1.2.3, performing liquid jet-based experiments with solutions of this transient ionic species is particularly challenging. $MnO_4^{2-}_{(aq.)}$ ions are unstable towards disproportionation, converting to $MnO_4^{-}_{(aq.)}$ and $MnO_{2(s)}$ over time, with pH-, temperature- and concentration-dependent kinetics [54]. The data presented here was recorded using the micro-mixing scheme described in Section 3.2.3, which facilitated the generation of relatively stable, ~0.2 M $MnO_4^{2-}_{(aq.)}$ solutions at pH~13.5 – close to the minimum equilibrium pH in the Mn-water Pourbaix diagram (see Figure 1.2). The data reported here, in combination with the results presented in Chapter 4, allowed for a direct comparison of the electronic structure of two tetra-oxo Mn TMCs with different oxidation states in the aqueous phase: $MnO_4^{-}_{(aq.)}$ (Mn VII+ charge state, see Chapter 4) and $MnO_4^{2-}_{(aq.)}$ (Mn VI+ charge state, presented in this chapter). The spectra reported here were recorded with the electron analyzer either perpendicular or at magic angle with respect to the soft X-ray beam polarization, yielding equivalent energetic results.

This chapter is organized in four sections. Section 5.1 presents results obtained from direct XPS experiments, showing characteristic spectroscopic signatures of $MnO_4^{2-}_{(aq.)}$ (Mn VI+ oxidation state) in the valence band and core level spectral regions, including a comparison between data recorded with solution-bulk and gas-solution-interface spectral sensitivities. Section 5.2 describes the results obtained from Mn $2p_{3/2}$ / $2p_{1/2}$ and O 1s RPES experiments, from which Mn(VI)-O molecular bonding properties, $MnO_4^{2-}_{(aq.)}$-water solute-solvent interactions, and more general, intramolecular Auger processes, were investigated. In addition, as will be shown here, the RPES results provided bulk-sensitive spectroscopic information not accessible from the direct XPS measurements, which is essential for the inference of redox energetic information pertaining to the $MnO_4^{2-}_{(aq.)}$ ion (see Chapter 6). A comparison of the MnO_4^{2-} system energetics with respect to those of MnO_4^{-} in the aqueous and solid phases and the MnO_4^{2-} ion in the solid phase is presented in Section 5.3. A summary of the key findings described throughout this chapter is presented in Section 5.4.

Figure 5.1 shows a MO diagram for the $MnO_4^{2-}_{(aq.)}$ solutions studied here, based on the MnO_4^{2-} electronic and molecular structure description presented in Section 2.1.2. This diagram will be used as a reference to describe and discuss the results reported here. The energy scale summarizes the aqueous BEs determined from (bulk-sensitive) XPS and RPES experiments. The BE appended to the virtual valence MO (4.9 ± 0.04 eV, labelled as $5t_2$ in the figure) was estimated by considering the experimentally determined BE for the $(2e)^{-1}$ ionizing transition and the excitation energy extracted from a Gaussian fit to the first optical transition band in the $MnO_4^{2-}_{(aq.)}$ UV-visible absorption spectra (see Figure 2.3 and Section 2.1.2 for details), *i.e.* neglecting electron correlation effects. Spectral features associated with the different MOs will be labelled as follows: (**0**) 2e, (**1**) $1t_1$, (**2**) $4t_2/6a_1$, (**3**) $1e/3t_2$, (**4**) $5a_1$, (**5**) $2t_2$, (**6**) $4a_1$, (**7**) $3a_1$, and (**8, 9**) $1t_2$, to achieve consistency with the labelling scheme

presented in Chapter 4 for $MnO_4^-{}_{(aq.)}$. The MO diagram of the liquid water, $OH^-{}_{(aq.)}$ ion and $Na^+{}_{(aq.)}$ ion solution components are also shown for comparison.
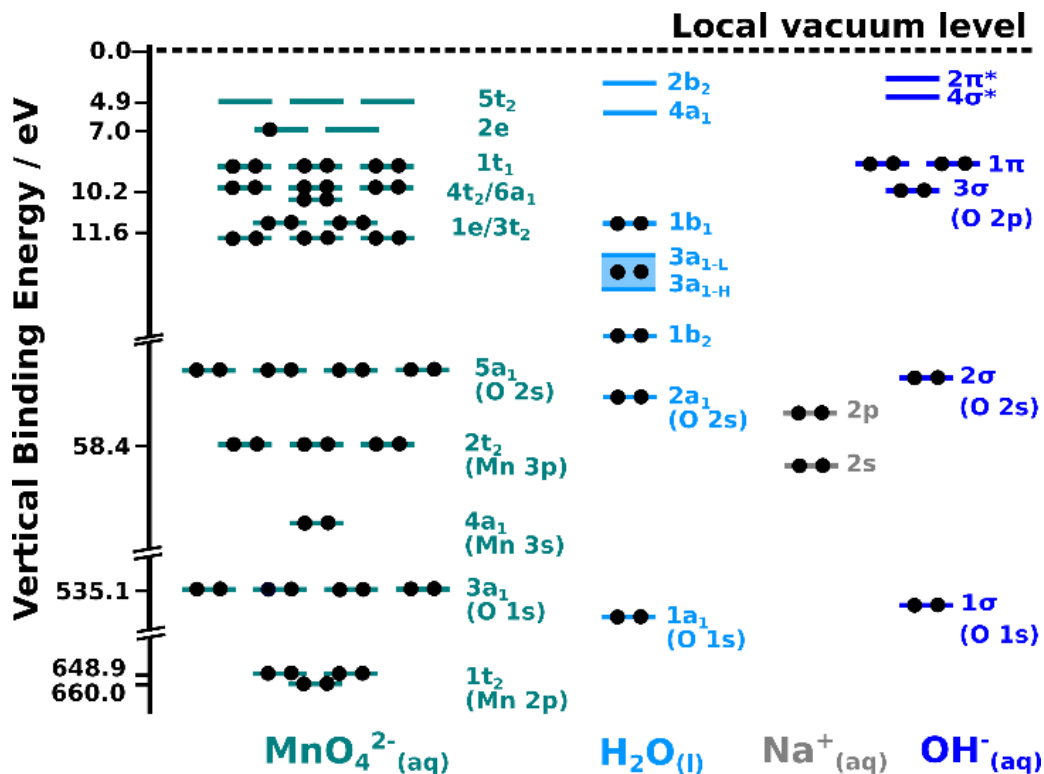
Figure 5.1. MO diagram of $MnO_4^{2-}{}_{(aq.)}$ solutions

MO diagram of MnO_4^{2-} and additional solution components in the aqueous phase. The energy scale shows BE information extracted from the bulk-sensitive liquid jet XPS and RPES bulk-sensitive experiments performed with ~0.2 M $MnO_4^{2-}{}_{(aq.)}$ in ~0.3 M $NaOH_{(aq.)}$ (pH~13.5) solutions and from UV-visible absorption measurements, as explained in the text. The $MnO_4^{2-}{}_{(aq.)}$ MO diagram was adapted from the isolated molecule diagram presented in Reference [109] (see Section 2.1.2 for details). Spectral features associated with the different MOs were labelled as discussed in the main body of the text. MO diagrams for $H_2O_{(l)}$, $Na^+{}_{(aq.)}$ and $OH^-{}_{(aq.)}$ ions are shown for comparison, based on the data reported in this chapter and in References [21, 92, 94, 239-241]. The energetic information is necessarily referenced to the local vacuum level. The numbers on the y-scale correspond to the solute BEs in the aforementioned aqueous solution, as determined from the experimental results reported here.

5.1 Direct (non-resonant) photoelectron spectroscopy

5.1.1 Bulk-sensitive spectra

Figure 5.2 shows bulk-sensitive outer valence (panel A), O 1s (panel B) and Mn $2p_{3/2}$ / $2p_{1/2}$ (panel C) spectra recorded from ~0.2 M $MnO_4^{2-}{}_{(aq.)}$ solutions (green curves). $MnO_4^{2-}{}_{(aq.)}$ ions were generated by mixing a *$MnO_4^-{}_{(aq)}$ reagent stream* (0.4 M $NaMnO_{4(aq.)}$ in 0.5 M $NaOH_{(aq.)}$) with an *$I^-{}_{(aq)}$ reagent stream* (0.066 M $NaI_{(aq.)}$ in 0.5 M $NaOH_{(aq.)}$). As a result, a ~0.2 M $MnO_4^{2-}{}_{(aq.)}$ in 0.3 M $NaOH_{(aq.)}$ (and
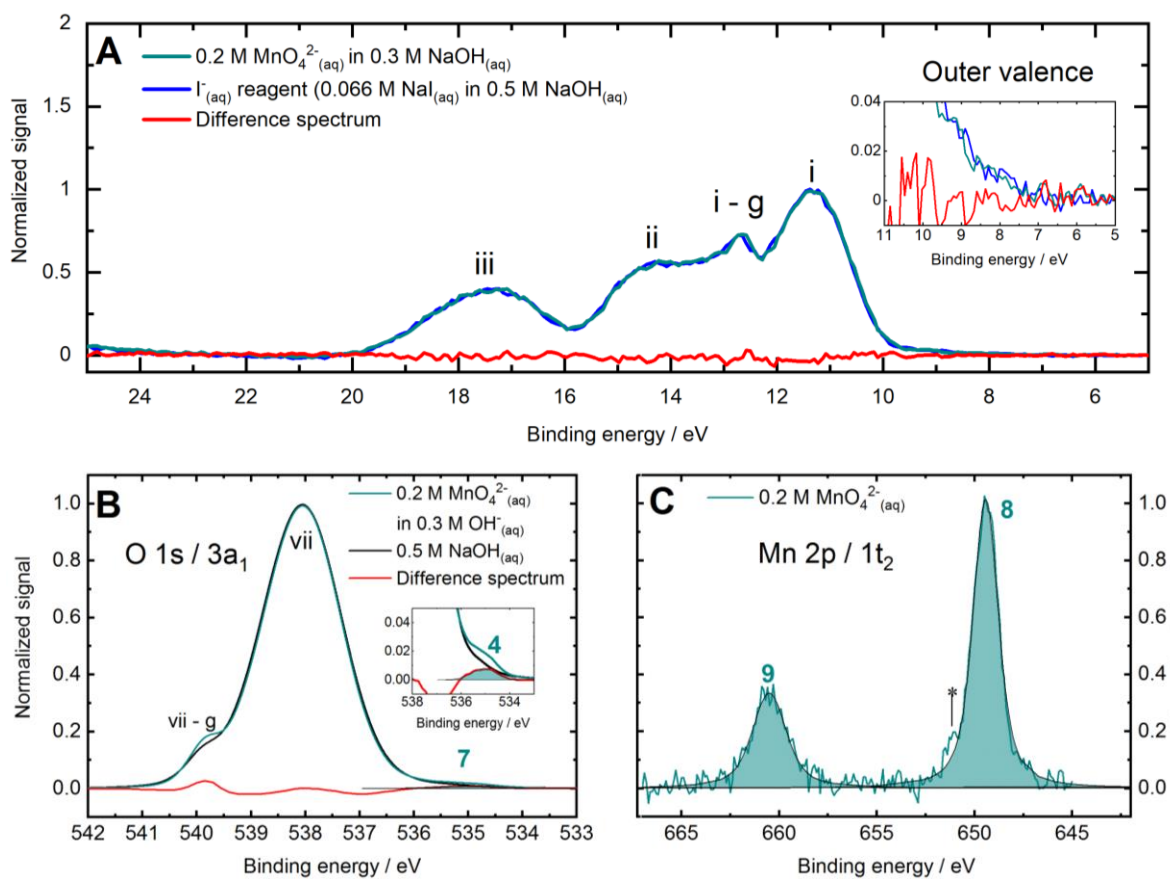
Figure 5.2. Solution bulk-sensitive spectra of MnO$_4^{2-}$$_{(aq.)}$

Bulk-sensitive XPS spectra recorded from ~0.2 M MnO$_4^{2-}$$_{(aq.)}$ in 0.3 M NaOH$_{(aq.)}$ (and reactively-produced ~0.03 M NaIO$_{3(aq.)}$) solutions (see the main body of the text for details) in a magic angle polarization configuration. **(A)** Outer valence spectrum recorded at a photon energy of 635 eV (green curve). A spectrum recorded from the $I^-_{(aq.)}$ *reagent stream* only (*i.e.* without adding the MnO$_4^-$$_{(aq.)}$ reagent to produce MnO$_4^{2-}$$_{(aq.)}$ in the mixing scheme) is shown as reference (blue curve). Importantly, signatures of the valence electronic structure of MnO$_4^{2-}$$_{(aq.)}$ could not be identified in the bulk-sensitive, direct XPS measurements. **(B)** O 1s spectra of MnO$_4^{2-}$$_{(aq.)}$ (green) and NaOH$_{(aq.)}$ reference (black curve, see the text for details) solutions recorded at a photon energy of 1135 eV. The solution-reference spectrum is shown in red. The inset highlights the Voigt profile fit to the MnO$_4^{2-}$$_{(aq.)}$ O 1s ionization feature. **(C)** Mn 2p$_{3/2}$ / 2p$_{1/2}$ spectrum recorded at a photon energy of 1251 eV. The asterisk denotes a signature potentially belonging to MnO$_4^-$$_{(aq.)}$ present as a result of less than ideal mixing conditions. MnO$_4^{2-}$$_{(aq.)}$ features are labelled with numbers, and Roman numerals are used to label ionization signatures from the water solvent molecules.

0.03 M IO$_3^-$$_{(aq.)}$) sample stream (pH~13.5) was produced and delivered into the experimental end-stations as a liquid jet with a regulated temperature of 278 K. The data shown in panel A was recorded at a photon energy of 635 eV at the U49/2 PGM-1 beamline at BESSY II. The spectra shown in panels B and C were recorded at photon energies of 1135 eV and 1251 eV, respectively, at the P04 beamline at PETRA III. MnO$_4^{2-}$$_{(aq.)}$ features have been labelled with numbers according to the labelling scheme used in Chapter 4 for the MnO$_4^-$$_{(aq.)}$ data. Similarly, water features have been labelled using Roman numerals.

Valence band features of MnO$_4^{2-}$$_{(aq.)}$ could not be isolated from spectra recorded under bulk-sensitive conditions (for example, the data shown in panel A). However, such MnO$_4^{2-}$$_{(aq.)}$ signatures were

identified in the surface-sensitive spectra (for example, during the optimization of the micro-mixing scheme described in Section 3.2.3, as shown in Figure 3.6). A difference in the relative ionization cross sections of the solute and solvent in the bulk of the solution with respect to the gas-solution interface, or potential surface-active behavior of $MnO_4^{2-}{}_{(aq.)}$ ions are possible explanations for this result. A depth profiling study – such as that described in Section 4.1.3 for $MnO_4^-{}_{(aq.)}$ – could not be performed due to the highly challenging nature of maintaining the unstable $MnO_4^{2-}{}_{(aq.)}$ liquid jet during the required data acquisition period, primarily due to solute disproportionation and $MnO_{2(s)}$ accumulation that results in blockage of the liquid jet capillary nozzle. Bulk-sensitive data for the $MnO_4^{2-}{}_{(aq.)}$ valence spectral region was extracted from RPES data, specifically from resonantly-enhanced participator Auger signals, as will be reported in Section 5.2.

The $MnO_4^{2-}{}_{(aq.)}$ O 1s data shown in panel B is plotted along with a 0.5 M $NaOH_{(aq.)}$ reference spectrum (black curve), and the associated solution-reference difference spectrum (red curve). In contrast to the valence band experiments mentioned above, using a $I_{(aq.)}$ *reagent stream* spectrum as reference (*i.e.* for background signal comparison or subtraction) was not necessary here, giving that $I^-{}_{(aq.)}$ does not produce any photoelectron contributions in the O 1s spectral region (any contribution from $IO_3^-{}_{(aq.)}$ would be below the detection limit, given the relatively low concentration of the ion in the sample stream). A 0.5 M concentration $NaOH_{(aq.)}$ reference solution was utilized for practical reasons only, given that 0.5 M $NaOH_{(aq.)}$ were utilized as part of the inter-measurement cleaning procedure required to perform experiments with the micro-mixing scheme (see Section 3.2.3).

A $MnO_4^{2-}{}_{(aq.)}$ O 1s ($3a_1$) spectroscopic signature with a BE of 535.1 ± 0.1 eV was extracted from a cumulative Voigt profile fit to the difference spectrum, highlighted by a green fill (see the inset in the figure) and labelled as peak **7**. The reported BE is a lower limit value due to over subtraction above BEs of ~536 eV, as highlighted by the BE region with negative intensity in the difference spectrum. The liquid water O 1s feature (peak vii) in the $MnO_4^{2-}{}_{(aq.)}$ spectrum was found to be narrower in comparison to the $NaOH_{(aq.)}$ reference spectrum (1.56 ± 0.03 eV versus 1.61 ± 0.01 eV, respectively), which could lead to the above-mentioned over subtraction when producing the solution-reference difference spectrum. Any O 1s spectral contribution from $MnO_4^-{}_{(aq.)}$ (resulting from incomplete mixing) or from $OH^-{}_{(aq.)}$ ions (present to ensure a pH of ~13.5 as explained previously) would occur, in both cases, at a BE of 536 eV (see Table 4.1 in Chapter 4 for $MnO_4^-{}_{(aq.)}$ and Reference [240] for $OH^-{}_{(aq.)}$).

Cumulative Voigt profile fits to the Mn $2p_{3/2}/2p_{1/2}$ ($1t_2$) spectrum of $MnO_4^{2-}{}_{(aq.)}$ shown in panel C (fit components highlighted by green fills) revealed Mn $2p_{3/2}$ and $2p_{1/2}$ BEs of 648.9 ± 0.1 eV and 660.0 ± 0.1 eV, respectively. The weak feature (highlighted by an asterisk in the figure) close to 651 eV BE is likely a signature of $MnO_4^-{}_{(aq.)}$ resulting from less than complete (ideal) mixing and reaction conditions.

The (nearly sole) presence of $MnO_4^{2-}{}_{(aq.)}$ in the O 1s and Mn 2p spectra (at least within the experimental detection limits) was tested and confirmed by recording PEY-XAS data before and after the measurements (see Section 3.2.3 and Figure 3.6 for details). In addition, a Mn $2p_{3/2}/2p_{1/2}$ spectrum recoded under partial mixing conditions – *i.e.* with both $MnO_4^{2-}{}_{(aq.)}$ and $MnO_4^-{}_{(aq.)}$ present in solution (see Figure 3.6, panel C) – provided further confirmation of the distinct $MnO_4^{2-}{}_{(aq.)}$ and $MnO_4^-{}_{(aq.)}$ Mn $2p_{3/2}/2p_{1/2}$ BE values and oxidation-state-dependent chemical shifts, as will be discussed in Chapter 6.

Table 5.1 summarizes the bulk-sensitive O1s and Mn $2p_{3/2}$/$2p_{1/2}$ BEs and Gaussian peak width components, $FWHM_G$, extracted from the data presented in this section.

Table 5.1. MnO_4^{2-} (aq.) bulk-sensitive BEs and and FWHM peak widths

0.2 M MnO_4^{2-} (aq.) bulk-sensitive BEs and Gaussian peak width components, $FWHM_G$, extracted from Voigt profile fits to the data presented in Figure 5.2. The errors represent the uncertainty on the BE scale calibration procedure (see Section 3.4.1 for details).

Label	Peak Origin	BE / eV	$FWHM_G$ / eV
7	$(3a_1)^{-1}$	535.1 ± 0.1	1.21 ± 0.04
8	$(1t_2)^{-1}$	648.9 ± 0.1	1.01 ± 0.07
9	$(1t_2)^{-1}$	660.0 ± 0.1	1.3 ± 0.3

5.1.2 Solution-gas interface spectra

Figure 5.3 shows a surface-sensitive outer valence spectrum (green curve) recorded from a ~0.2 M MnO_4^{2-} (aq.) in 0.3 M $NaOH$ (aq.) solution using a photon energy of 150 eV at the U49/2 PGM-1 beamline at BESSY II. A reference spectrum (blue curve), and the associated solution-reference difference spectrum (red curve) are also shown in the figure. The reference data corresponds to a spectrum recorded from the I^- (aq.) *reagent stream* only (see the previous section and Section 3.2.3 for details). Gaussian fits to the difference spectrum are highlighted by green fills and labelled as peaks **0**, **1**, and **2** (a detailed view is shown in the inset of the figure). The peak center extracted from each of these fits allowed the MnO_4^{2-} (aq.) BEs associated with ionizing transitions involving the HOMO (2e), HOMO-1 ($1t_1$), and HOMO- 2 ($4t_2$) MOs to be determined, as will be discussed below.
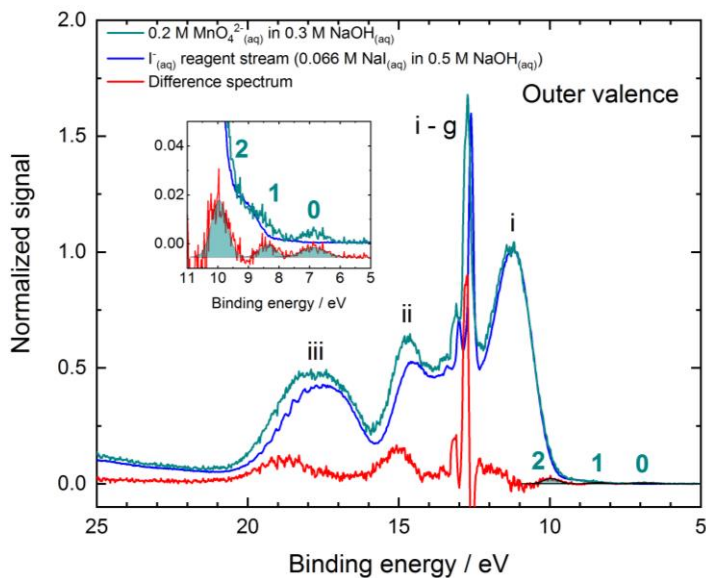
Figure 5.3. Surface-sensitive spectra of MnO_4^{2-} (aq.)

~0.2 M MnO_4^{2-} (aq.) in 0.3 M $NaOH$ (aq.) (and ~0.03 M $NaIO_3$ (aq.), see the text for details) spectrum recorded at a photon energy of 150 eV (green curve) in a perpendicular angle polarization configuration. A spectrum recorded from the I^- (aq.) *reagent stream* only (*i.e.* without adding the MnO_4^- (aq.) reagent to produce MnO_4^{2-} (aq.) in the mixing scheme) is shown as a reference spectrum (blue curve). The associated solution-reference difference spectrum is shown in red, highlighting Gaussian fits to the extracted MnO_4^{2-} (aq.) signals (green fills, see the inset on the left).

With the MO diagram presented in Figure 5.1 in mind, peaks **0 – 2** were ascribed to $(2e)^{-1}$, $(1t_1)^{-1}$, and $4t_2)^{-1}$ ionizing transitions, respectively. A value of 6.89 ± 0.04 eV was extracted for peak **1**, corresponding to the lowest VIE in $MnO_4^{2-}{}_{(aq.)}$. Similarly, BEs of 8.47 ± 0.08 eV and 9.99 ± 0.04 eV were respectively determined for peaks **1** and **2**. Notably, the HOMO ionization features from $MnO_4^{-}{}_{(aq.)}$ (which would only be present under partial mixing and reaction conditions) and $OH^{-}{}_{(aq.)}$ would have been expected at a BE of ~9.2 eV (see Section 4.1 for the $MnO_4^{-}{}_{(aq.)}$ energetics and Reference [239] for the $OH^{-}{}_{(aq.)}$ ionization energetics), and are seemingly absent here.

Valence photoelectron signatures with BEs in the 11 – 13 eV spectral region could not be extracted, as they overlapped with the intense $1b_1$ peaks of liquid and gas phase water (peaks i and i-g, respectively). Particularly in the difference spectrum, the differential shift in the position of the $1b_1$ peak of gas phase water in the solution and reference spectra lead to the signals with intensities oscillating around zero that are observed in the figure.

Table 5.2 summarizes the $MnO_4^{2-}{}_{(aq.)}$ outer valence BEs and Gaussian peak width components, $FWHM_G$, extracted from surface-sensitive data similar to the spectra presented in Figure 5.3.

Table 5.2. MnO$_4^{2-}$$_{(aq.)}$ surface-sensitive BEs and and FWHM peak widths

0.2 M $MnO_4^{2-}{}_{(aq.)}$ solution BEs and Gaussian peak width components, $FWHM_G$, extracted from Gaussian or Voigt profile fits to several surface-sensitive data sets, similar to those shown in Figure 5.3. Average BEs are shown with the error bounds defining the standard deviations of the cumulative results.

Label	Peak Origin	BE / eV	FWHM$_G$ / eV
0	$(2e)^{-1}$	6.89 ± 0.04	0.84 ± 0.04
1	$(1t_1)^{-1}$	8.47 ± 0.08	0.66 ± 0.05
2	$(4t_2)^{-1}$	9.99 ± 0.04	0.61 ± 0.01

A comparison between the surface-sensitive valence spectral information presented here and their bulk-solution-sensitive counterparts will be discussed in the next section, using information extracted from the RPES experiments.

5.2 Resonantly-enhanced photoelectron spectroscopy

This section presents results from Mn $2p_{3/2}$, $2p_{1/2}$ and O 1s RPES experiments performed with ~0.2 M $MnO_4^{2-}{}_{(aq.)}$ in 0.3 M $NaOH_{(aq.)}$ solutions generated using the micro-mixing scheme at the U49/2 PGM-1 beamline at BESSY II. The data was recorded at a liquid jet temperature of 278 K. These experiments allowed the identification of intramolecular (participator and spectator) Auger processes and provided bulk-sensitive electronic structure information that could not be extracted otherwise from direct XPS experiments. Hence, a comparison between the bulk-sensitive data presented in this section and the surface-sensitive data reported in the previous section is also presented here, to explore potential solution-gas interface effects on the energetics and electronic structure of $MnO_4^{2-}{}_{(aq.)}$.

5.2.1 Mn $2p_{3/2}$ intramolecular Auger processes

Figure 5.4 shows an overview of the Mn $2p_{3/2}$ RPES data recorded from $MnO_4^{2-}{}_{(aq.)}$ solutions. A Mn $2p_{3/2}$ RPES map (left) and the associated PEY-XAS spectrum (right) are shown in panel A. Cumulative Gaussian fits to the PEY-XAS data (see Figure AII.1, panel A in Appendix II) allowed resonance excitation energies of 642.4 ± 0.1 eV (Resonance I, red dashed lines in the RPES map) and 644.7 ± 0.1 eV (Resonance II, blue dashed lines in the RPES map) to be extracted. These resonances

were respectively assigned as Mn $2p_{3/2} \rightarrow 2e$ and Mn $2p_{3/2} \rightarrow 5t_2$ excitations, based on the information extracted from the UV-visible absorption spectra, (see Figure 2.3 and Section 2.1.2 for details) and the assignments of similar RPES data recorded from $MnO_4^{-}{}_{(aq.)}$ solutions, as reported in Section 4.2. Given that MnO_4^{2-} has a nominal d^1 electronic configuration, the aforementioned Mn $2p_{3/2} \rightarrow 2e$ transition corresponds to a core-to-HOMO resonance, while the Mn $2p_{3/2} \rightarrow 5t_2$ transition corresponds to a core-to-virtual-valence (LUMO) transition (the latter is similar to the transition described in Section 4.2 for $MnO_4^{-}{}_{(aq.)}$).

Panels B and C in Figure 5.4 show higher-signal-to-noise ratio RPES spectra recorded at Resonances I (panel B, red) and II (panel C, blue) over an extended BE range. Participator Auger signals are labelled using numbers and spectator Auger signals are labelled using letters. A spectrum recorded at an off-resonant photon energy of 635.0 eV (that is, devoid of resonant signal enhancements) is shown as reference data in each panel. The signatures observed close to 55 eV BE in the off-resonant spectra correspond to $I^{-}{}_{(aq.)}$ [21] or $IO_3^{-}{}_{(aq.)}$ 4d peaks and, in the former case, would be indicative of sub-optimal mixing conditions.

In order to precisely extract the KEs (or effective BEs in the case of participator Auger peaks) associated with each resonant Auger process, the off-resonant spectrum was subtracted from the resonant data shown in panels B and C in Figure 5.4 (see Section 3.4.2 for details). Resonance I and II difference spectra produced in such a way are shown in Figure 5.5.

Four participator Auger processes were identified from the data presented in Figures 5.4 and 5.5, labelled as peaks **0**, **2**, **3** and **5**. Based on the direct XPS results presented in Section 5.1.2, and the results reported for $MnO_4^{-}{}_{(aq.)}$ in Chapter 4, these features were assigned as resonant enhancements of $MnO_4^{2-}{}_{(aq.)}$ $2e^{-1}$, $4t_2^{-1}$ (or $6a_1^{-1}$), $3t_2^{-1}$ (or $1e^{-1}$), and $2t_2^{-1}$ (Mn 3p) photoelectron signals, respectively.

Starting with peak **0**, this resonantly-enhanced feature is present both in the Resonance I and Resonance II data. Cumulative Gaussian fits to the difference spectra shown in Figure 5.5 (see Figure 2 and Table AII in Appendix II) allowed an average BE of 7.0 ± 0.1 eV to be extracted for this feature. Within the error bars, this value is equivalent to the BE determined for the $MnO_4^{2-}{}_{(aq.)}$ $(2e)^{-1}$ ionizing transition from the surface-sensitive, direct XPS valence data presented in Section 5.1 (6.89 ± 0.04 eV, see Table 5.2). Therefore, peak **1** was assigned as a L_{III}-2e,2e participator peak in the Resonance I data and, correspondingly, a L_{III}-2e,5t_2 process in the Resonance II data. As previously mentioned, this result is of paramount importance for the estimation of redox parameters related to the $MnO_4^{2-}{}_{(aq.)}$ / $MnO_4^{-}{}_{(aq.)}$ redox pair, which will be discussed in Chapter 6.

The participator Auger feature labelled as peak **2** is seemingly present only in the Resonance I data, with a KE of 631.9 ± 0.1 eV, corresponding to an effective BE of 10.51 ± 0.04 eV. As reported in Section 5.2, a valence feature with a BE of 9.99 ± 0.04 eV was observed in the surface-sensitive, direct XPS data and ascribed to a $4t_2^{-1}$ ionization process. With this result and the MO diagram of MnO_4^{2-} presented in Figure 5.1 in mind, peak **2** can be potentially assigned as a resonant enhancement of the $4t_2$ or $6a_1$ ionization features. As described in Section 2.1.2, the $6a_1$ orbital is a bonding orbital with Mn 4s and Mn 3p atomic contributions from the metal center and O 2p contributions from the ligands. On the contrary, the $4t_2$ orbital is a non-bonding, ligand-centered MO. The predominant Mn-character expected for the $6a_1$ MO would suggest that peak **2** corresponds to a signature of L_{III}-6a_1,2e participator Auger process. However, assignment of this feature to a L_{III}-4t_2,2e participator Auger is also plausible, as will be discussed below.

Figure 5.4. Mn 2p$_{3/2}$ RPES spectra from MnO$_4^{2-}$$_{(aq.)}$ solutions
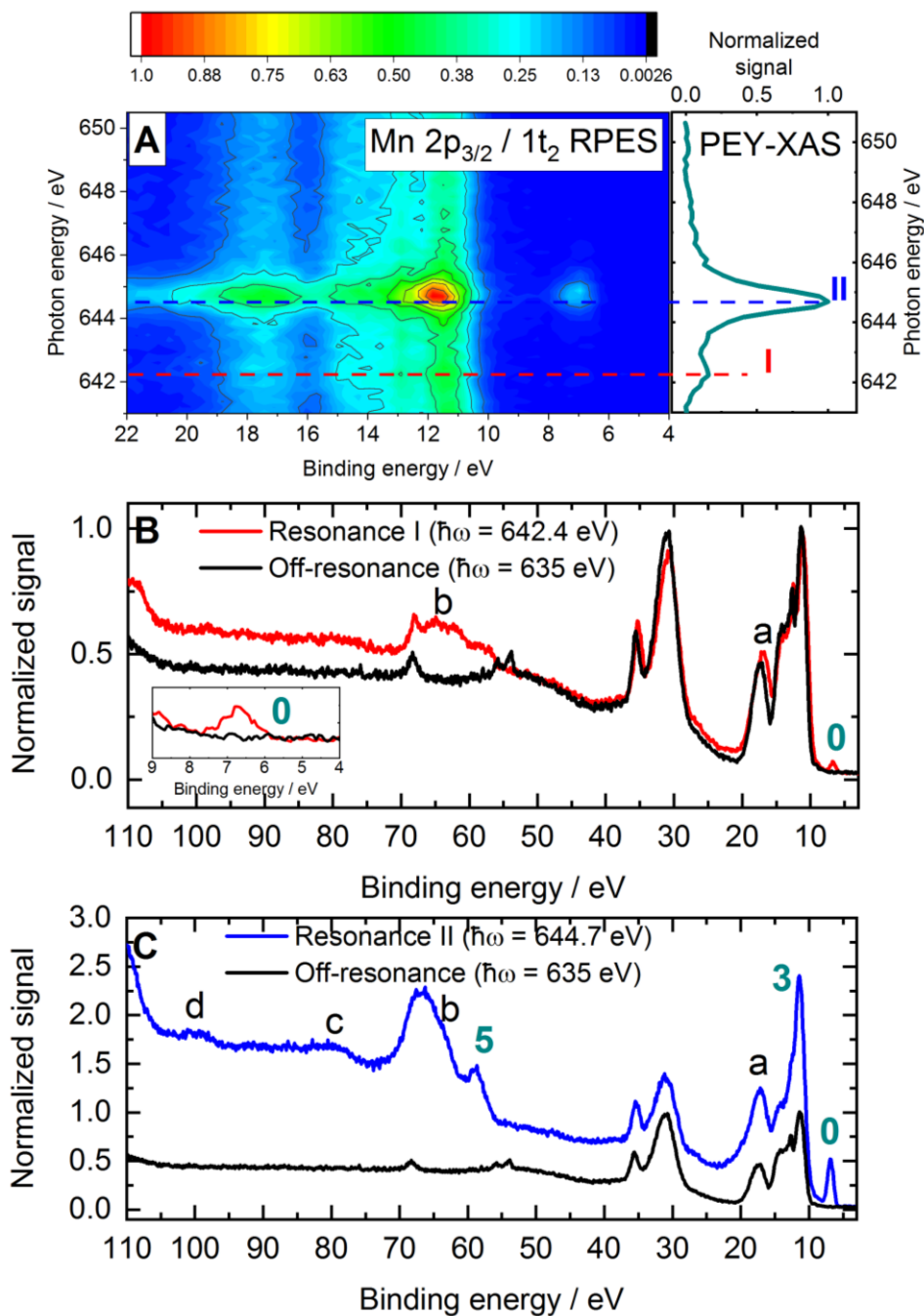
Mn 2p$_{2/3}$ RPES data recorded from ~0.2 M MnO$_4^{2-}$$_{(aq.)}$ solutions produced using the micro-mixing scheme at a regulated liquid jet temperature of 278 K in a perpendicular angle polarization configuration. **(A)** RPES map (left) and PEY-XAS spectrum (right). **(B)** As measured Mn 2p$_{3/2}$ → 2e resonant spectrum (red). (C) As measured Mn 2p$_{3/2}$ → 5t$_2$ resonant spectrum (blue). A spectrum recorded at an off-resonant photon energy (635.0 eV, black), devoid of resonantly enhanced signals, is shown in panels B and C. Participator Auger signals are labelled with numbers and spectator Auger signals are labelled with letters. The BE scale is suitable for the identification of participator Auger process and a comparison with the direct XPS results reported in Section 5.1. For the assignment of spectator Auger signals a KE scale is more appropriate, as will be implemented in the resonant-off-resonant data presented in Figure 5.5.

Figure 5.5. Mn 2p$_{3/2}$ resonantly-enhanced signals from MnO$_4^{2-}$$_{(aq.)}$ solutions
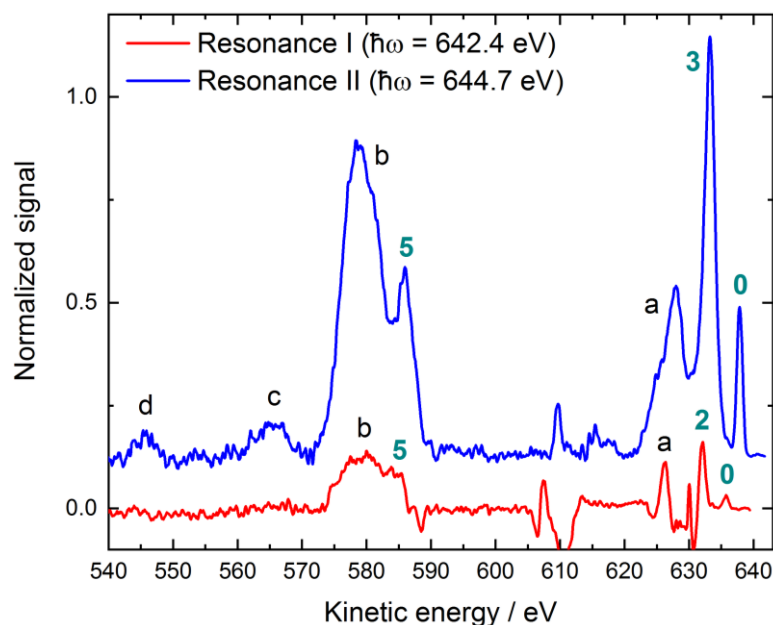
Resonance I (Mn 2p$_{3/2}$ → 2e) and II (Mn 2p$_{3/2}$ → 5t$_2$) RPES difference spectra extracted from the raw data shown in Figure 5.4 (panels B and C, respectively). Participator Auger signals are labelled with numbers and spectator Auger signals are labelled with letters.

Given the bulk-sensitivity afforded by the RPES experiments presented here, the BE of the aforementioned participator Auger signals provide the bulk-sensitive counterparts to those extracted from surface-sensitive measurements and reported in Table 5.2. For the (2e)$^{-1}$ ionizing transition, the (average) bulk-sensitive value extracted from the Resonance I and II data is 0.1 eV higher than that reported in Table 5.2. However, the increment in BE is within the experimental error associated with the determination of the average Resonance I and Resonance II peak **0** BE (± 0.1 eV). Such an error reflects mostly the uncertainty in the photon energy calibration. On the other hand, the BE associated with the peak **2** feature described above is 0.18 ± 0.04 eV higher than the value reported in Table 5.2. These results suggest that, overall, the MnO$_4^{2-}$$_{(aq.)}$ valence BEs are higher when sampling photoelectrons from the bulk of the solution in comparison with the gas-solution interface. Hence, the discrepancy between the peak **2** BE extracted from Figure 5.5 and that reported in Table 2 could be explained as a *surface versus bulk* BE shift.

The existence of *surface versus bulk* BE shifts in the outer valence MnO$_4^{2-}$$_{(aq.)}$ signals potentially highlights changes in molecular structure in the different regions of the aqueous solution. The differential shifts in BE energy may be explained by different interfacial phenomena altering the solution-phase energetics, such as changes in the hydrogen bonding environment [242], solute geometrical structural changes, and / or different solute-solvent intermolecular interactions occurring at the gas-solution interface. Overall, these results indicate a higher stability of MnO$_4^{2-}$$_{(aq.)}$ in the bulk of the solution.

The participator peak labelled as **3** was found to be present only in the Resonance II data, with a KE of 633.0 ± 0.1 eV, corresponding to a BE of 11.70 ± 0.04 eV, and assigned to either a L$_{III}$-3t$_2$,5t$_2$ or

L_{III}-1e,5t$_2$ process. The associated Gaussian peak width (1.12 ± 0.06 eV) suggests a single contribution, supporting the interpretation that a single ionization channel is selectively enhanced at Resonance II. A similar feature – assigned as a L_{III}-3t$_2$,5t$_2$ participator Auger – was observed in the MnO_4^-(aq.) Resonance II data (see Section 4.2.1). Furthermore, the observation of a L_{III}-1e,5t$_2$ participator Auger process in the MnO_4^{2-}(aq.) O 1s RPES data (which will be presented in Section 5.2.3) leads to the assignment of peak **3** as a L_{III}-3t$_2$,5t$_2$ process. This result allows the determination of the BE associated with the MnO_4^{2-} (aq.) $(3t_2)^{-1}$ ionizing transition in the bulk of the solution. Notably, peak **3** additionally shows a significant Lorentzian component (FWHM$_L$, 0.66 ± 0.06 eV) of the total feature width (FWHM, 1.97 ± 0.02 eV), as extracted via the multi-peak fitting analysis (see Table AII.1 in Appendix II). The FWHM$_L$ is smaller than the value reported for a similar RPES feature in MnO_4^-(aq.) data (0.77 ± 0.03 eV FWHM$_L$, Resonance II, peak **3-a**). As explained in Section 4.2.1, the lifetime broadening of these features are indicative of constructive interference between direct and participator Auger channels and the peak widths suggest shorter than average Mn 2p$_{3/2}$ core-hole lifetimes. Slightly different core-hole excited state lifetimes are correspondingly inferred for the MnO_4^-(aq.) and MnO_4^{2-}(aq.) ions, potentially highlighting the effect of the associated differences in formal oxidation states.

The fourth participator Auger feature, peak **5**, occurs at an average BE of 58.4 ± 0.7 eV, in both the Resonance I and II data. With the results reported from MnO_4^-(aq.) in mind (see Section 4.2.1) this feature is assigned as a resonant enhancement of the 2t$_2$ (Mn 3p) inner valence ionization feature – that is, a L_{III}-2t$_2$,5t$_2$ participator Auger process – and provides the BE for the $(2t_2)^{-1}$ ionizing transition in the bulk of the solution.

The spectral features labelled as **a – d** in Figures 5.4 and 5.5 were found to be similar to those in the MnO_4^-(aq) data. Hence, the following assignments were made: L-V,V (peak **a**, 627 ± 1 eV average KE), L_{III}-2t$_2$,V (peak **b,** 577 ± 1 eV average KE), L_{III}-2t$_2$,5a$_1$ (peak **c,** 565.1 ± 0.1 eV), and L_{III}-4a$_1$,V (peak **d,** 545.5 ± 0.1 eV). Ignoring electron correlation effects, the KEs associated with signals **c** and **d** can be used to estimate the BEs of the 5a$_1$ (from peak **c**) and 4a$_1$ (from peak **d**) MO electrons that could not be determined from the direct XPS experiments. Hence, from peak **c**, considering the 58.4 ± 0.7 eV BE extracted for the 2t$_2$ orbitals, a BE of ~25.4 eV can be estimated for the $(5a_1)^{-1}$ ionizing transition. Similarly, assuming a L_{III}-4a$_1$3t$_2$ process for peak **d** (as in Chapter 4 for MnO_4^-(aq.)) and using the 3t$_2$ BE (peak **3**) extracted from the participator Auger data, a BE of ~91.7 eV can be estimated for the $(4a_1)^{-1}$ ionizing transition.

Table 5.3 summarizes the results extracted from the Mn 2p$_{3/2}$ RPES data presented in this section. Average KEs, BEs and FWHM$_G$ of the participator Auger peaks determined from the Resonance I and II data presented here are shown in the top panel of the table. Similarly, average KEs of the spectator Auger peaks are listed in the bottom panel.

Table 5.3. $MnO_4^{2-}{}_{(aq.)}$ Mn $2p_{3/2}$ RPES participator and spectator Auger signals

Assignments of the Mn $2p_{1/2}$ RPES participator and spectator Auger signals associated with data shown in Figures 5.4 and 5.5. The reported values correspond to the main features' average KEs (and determined BEs) extracted at both resonances.

Participator Auger Label	Assignment	BE / eV	$FWHM_G$ / eV
0	2e	7.0 ± 0.1	1.0 ± 0.1
2	$(4t_2$ or $6a_1)^{-1}$	10.51 ± 0.04	0.98 ± 0.02
3	$(1e$ or $3t_2)^{-1}$	11.70 ± 0.04	1.58 ± 0.04
5	$(2t_2)^{-1}$	58.4 ± 0.7	2.9 ± 0.7
Spectator Auger Label	Assignment		KE / eV
a	L_{III}-V,V		627 ± 1
b	L_{III}-$2t_2$,V		577 ± 1
c	L_{III}-$2t_2$,$5a_1$		565.1 ± 0.1
d	L_{III}-$4a_1$,V		545.5 ± 0.1

5.2.2 Mn $2p_{1/2}$ intramolecular Auger processes

Figure 5.6 shows similar data to that presented in Figure 5.3 but for the Mn $2p_{1/2}$ spin-orbit component. Panel A shows an RPES map (left) and associated PEY-XAS spectrum (right). From a cumulative Gaussian fit to the PEY-XAS data (see Figure AII.1, panel A in Appendix II), the following resonant photon energies were extracted using a two-Gaussian-component fit, despite the considerable broadening of the resonance(s) in the Mn $2p_{1/2}$ excitation case: 653.0 eV (Mn $2p_{1/2} \rightarrow$ 2e, Resonance III) and 655.2 eV (Mn $2p_{1/2} \rightarrow 5t_2$, Resonance IV). Panel B shows a higher-signal-to-noise ratio spectrum recorded at the determined Resonance IV photon energy, over an extended BE range. An off-resonant spectrum is shown for comparison. Panel C shows the resonant-off-resonant difference spectrum. Such data collection was not possible at Resonance III, due to the challenges associated with the mixing scheme, limited signal strength and the beam time available.

In contrast to the Mn $2p_{3/2}$ Resonance II data (Mn $2p_{3/2} \rightarrow 5t_2$), only two participator Auger peaks are observed in the Resonance IV data, labelled as peaks **0** and **5**. These resonantly-enhanced features correspond to L_{II}-2e,$5t_2$ and L_{II}-$2t_2$,$5t_2$ processes, respectively. Accordingly, respective BEs of 7.10 ± 0.04 eV ($2e^{-1}$) and 58.76 ± 0.06 eV ($2t_2^{-1}$) were extracted. The results are in agreement, within the error bounds, with those reported for the Mn $2p_{3/2}$ excitation case and reported in the previous section (see Table 5.3). As was the case for the Resonance IV data recorded from $MnO_4^-{}_{(aq.)}$ solutions (Section 4.2.2), over- and under-subtraction in the 640 – 645 eV electron KE region of the difference spectra impeded the isolation of other participator Auger features (see yellow overlay in panel C of Figure 5.6).

The spectator Auger features **a** and **b** show similar characteristics to those observed in Resonance IV data from $MnO_4^-{}_{(aq.)}$ solutions. These features are broader at Resonance IV compared to Resonance I and II, as expected due to a shorter average core-hole lifetime for Mn $2p_{1/2}$ with respect to Mn $2p_{3/2}$ (~0.7 fs versus ~1.8 fs, respectively [237]). In addition, L_{II}-L_{III}V (feature **a)** and L_{II}-L_{III},$2t_2$ (feature **b)** Coster-Kronig processes [238] are present. The results are summarized in Table 5.4

Figure 5.6. Mn 2p$_{1/2}$ RPES data from MnO$_4^{2-}$$_{(aq.)}$ solutions
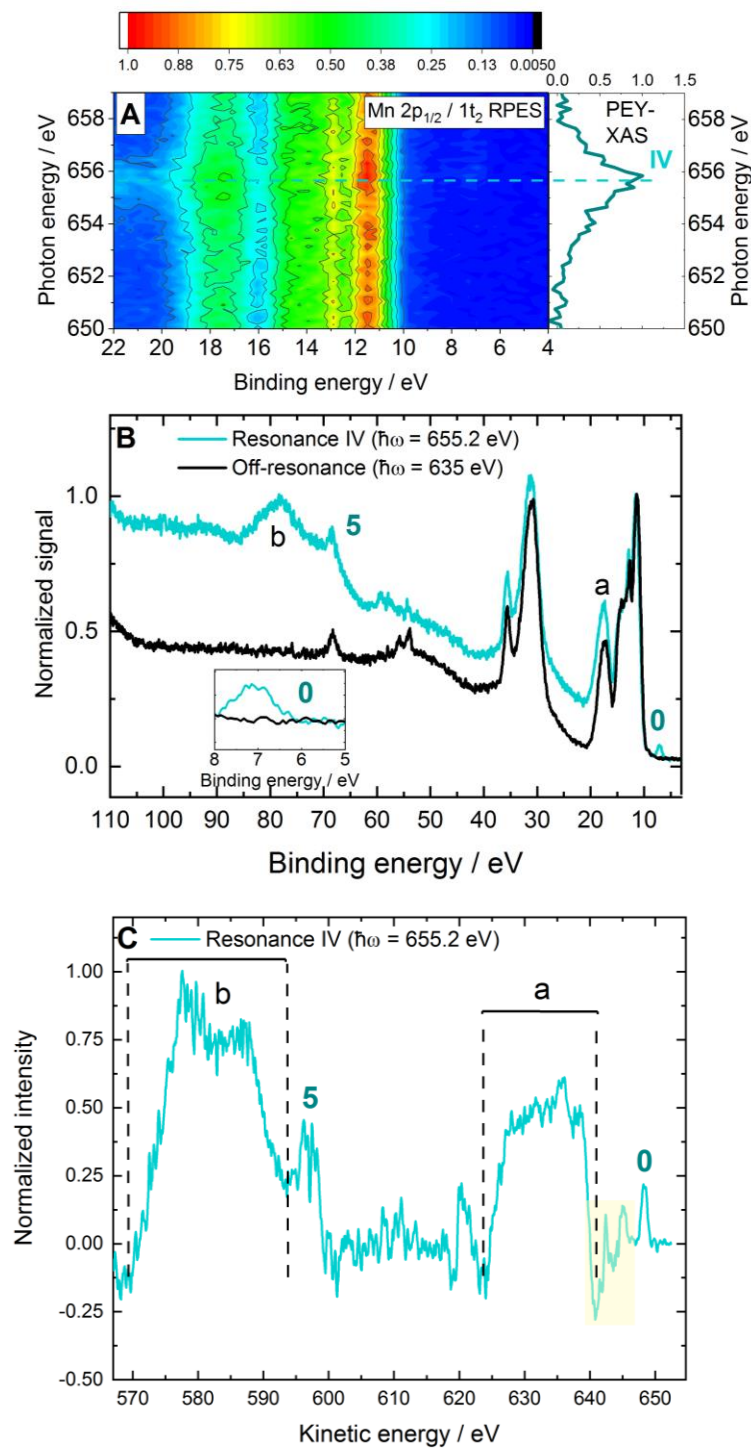
Mn 2p$_{1/2}$ RPES data from MnO$_4^{2-}$$_{(aq.)}$ solutions produced using the micro-mixing scheme at a regulated liquid jet temperature of 278 K in a perpendicular angle polarization configuration. (A) RPES map (left) and PEY-XAS spectrum (right). The BE scale is suitable for the identification of participator Auger processes and a comparison with the direct XPS results reported in Section 5.1. For the assignment of the spectator Auger signals, KEs are more appropriate and are implemented in Panel C.

Table 5.4. MnO_4^{2-} (aq.) Mn $2p_{1/2}$ RPES participator and spectator Auger signals

Assignments of the Mn $2p_{1/2}$ RPES participator and spectator Auger signals associated with data shown in Figures 5.6.

Participator Auger			
Label	Assignment	BE / eV	$FWHM_G$ / eV
0	L_{II}-2e,5t$_2$	648.1 ± 0.1	7.10 ± 0.04
5	L_{II}-2t$_2$,5t$_2$	596.4 ± 0.1	58.76 ± 0.06
Spectator Auger			
Label	Assignment 1	Assignment 2	KE / eV
a	L_{II}-V,V		638.5 ± 0.1
	L_{II}-L_{III},V		635.7 ± 0.1
	L_{II}-5a$_1$,V		629.8 ± 0.2
b	L_{II}-2t$_2$,V	L_{II}-2t$_2$, 5a$_1$	585.9 ± 0.1
	L_{II}-L_{III},2t$_2$		577.4 ± 0.1

5.2.3 O 1s intramolecular Auger and ICD processes

Figure 5.7 shows O 1s RPES data recorded from MnO_4^{2-} (aq.) solutions, highlighting resonant excitation and de-excitation associated with transitions involving MnO_4^{2-} (aq.) O 1s electrons and 2e (HOMO) and 5t$_2$ (LUMO) electrons. An RPES map and PEY-XAS spectrum are shown in panel A (left and right, respectively). Cumulative Gaussian fits to the PEY-XAS spectrum (shown in Figure AII.1, panel B in Appendix II) allowed the following resonant photon energies to be determined: 528.3 ± 0.1 eV (labelled as Resonance V), 529.2 ± 0.1 eV (labelled as Resonance VI-a), and 529.9 ± 0.1 eV (labelled as Resonance VI-b). Any resonant excitation process involving OH^- (aq.) ions is expected to occur at 532.8 eV photon energy [75], and thus does not overlap with the MnO_4^- (aq.) resonances. Considering the MO picture presented in Figure 5.1, the UV-visible absorption spectrum discussed in Section 2.1.2 (see Figure 2.3) and the O 1s resonant processes observed in MnO_4^- (aq.) solutions (as reported in Section 4.2.3 and in the solid-phase literature [174]), the aforementioned resonances were attributed to O 1s → 2e (Resonance V) and O 1s → 5t$_2$ (Resonance VI, a and b) transitions. In contrast to MnO_4^- (aq.), the PEY-XAS data shows two components to the O 1s → 5t$_2$ resonances. Here, the two resonant photon energies associated with O 1s → 5t$_2$ electron excitation (Resonance VI-a and b) may tentatively be attributed to valence interactions between the 2e HOMO and 5t$_2$ excited electrons with similar or opposite spins. The Resonance VI-a and b photon energy values are split by 0.7 ± 0.1 eV.

Such a splitting was seemingly unresolved in the Mn 2p RPES data (likely due to increased lifetime broadening effects at the Mn 2p resonances, see the PEY-XAS spectrum in Figure AII.1, panel A, in Appendix II) and is only observed in the O 1s data. Spectra recorded at each resonant photon energy – as well as an off-resonant spectrum – under higher-signal-to-noise ratio acquisition conditions over an extended BE range are shown in panels B (Resonance V), C (Resonance VI-a) and D (Resonance VI-b). In addition, the difference spectra produced by subtracting the off-resonant spectrum from the resonant data are shown in Figure 5.8.
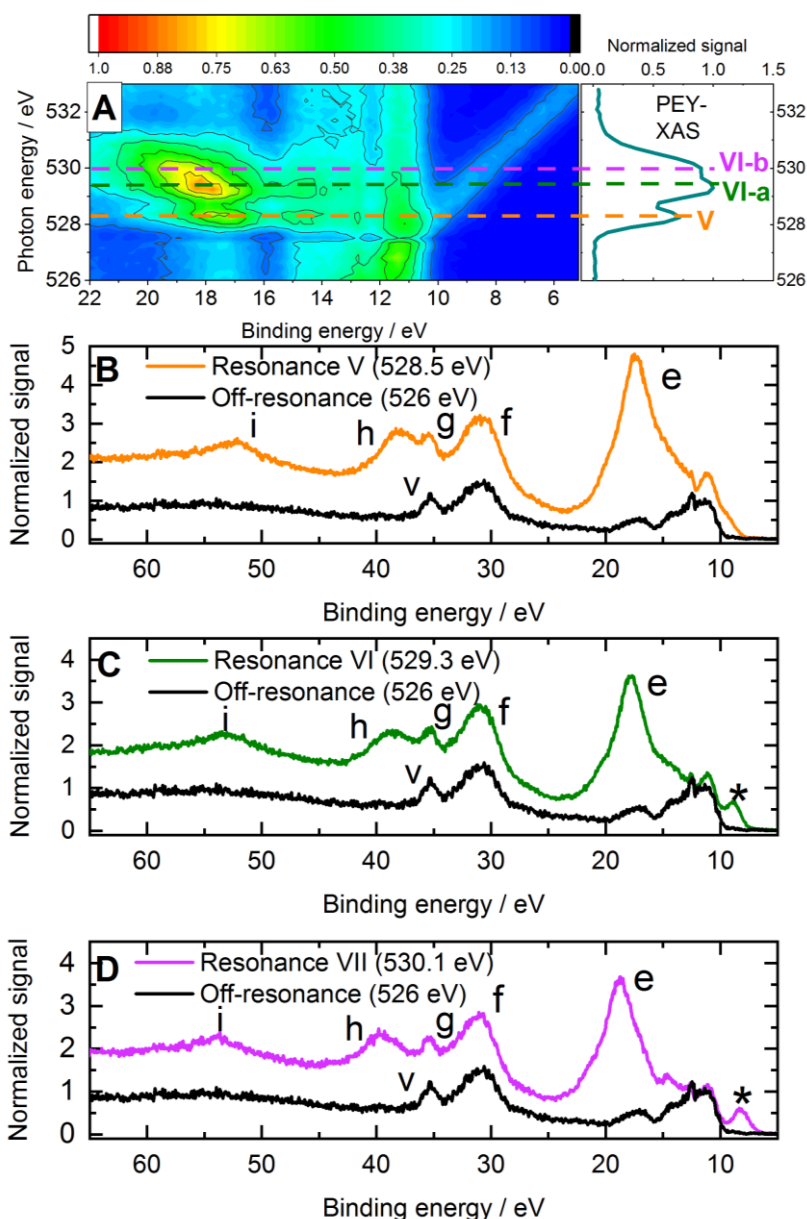
Figure 5.7. O 1s RPES data from MnO$_4^{2-}$(aq.) solutions

O 1s RPES data recorded from MnO$_4^{2-}$(aq.) solutions produced using the micro-mixing scheme at a regulated liquid jet temperature of 278 K in a perpendicular angle polarization configuration. (A) RPES map (left) and PEY-XAS spectrum (right). (B) As measured O 1s – 2e resonant spectrum (orange). (C) As measured Mn 2p$_{3/2}$ – 5t$_2$ resonant spectrum (green, Resonance VI-a). (D) As measured Mn 2p$_{3/2}$ – 5t$_2$ resonant spectrum (pink, Resonance VI-b). A spectrum recorded at an off-resonant photon energy (black), devoid of resonantly enhanced signals, is shown in panels B, C, and D. Participator Auger signals are labelled with numbers, and spectator Auger signals are labelled with letters. The asterisk indicates a signal arising from ionization with the unfiltered second harmonic of the beamline. The feature labelled as peak 'v' corresponds to the Na$^+$(aq.) 2p^{-1} ionization peak. The BE scale is suitable for the identification of participator Auger process and a comparison with the direct XPS results reported in Section 5.1. For the assignment of spectator Auger signals, KEs are more appropriate – as will be implemented in the resonant-off-resonant data presented in Figure 5.8.
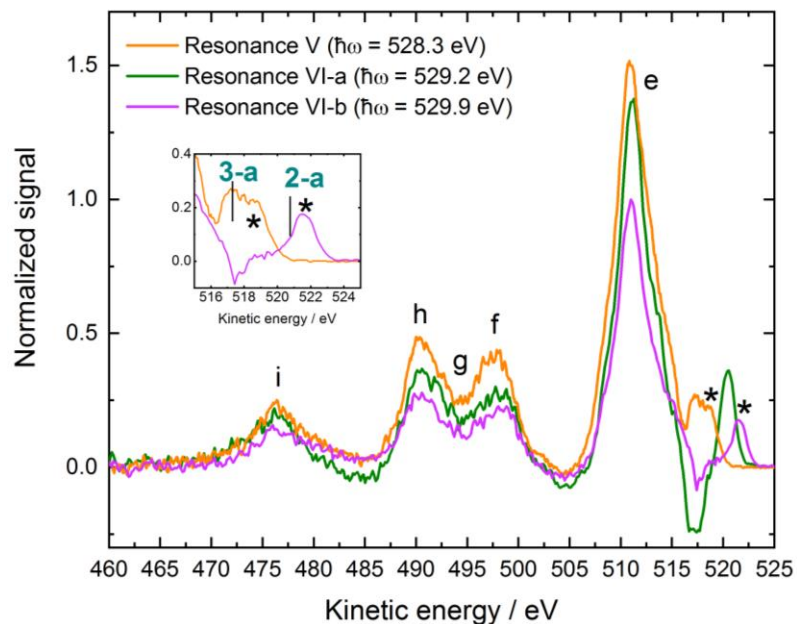
Figure 5.8. O 1s resonantly-enhanced signals from MnO_4^{2-}(aq.) solutions

Resonance V (O 1s → 2e) and VI (O 1s → $5t_2$) RPES difference spectra produced from the raw data shown in Figure 6.6. Participator Auger signals are labelled with numbers and spectator Auger / ICD signals are labelled with letters. The asterisk indicates signals arising from ionization with the unfiltered second harmonic of the beamline.

In both Figure 5.7 and 5.8, signals originating from ionization of O 1s electrons from liquid water with the unfiltered second harmonic of the beamline were labelled with asterisks, and spectator Auger / ICD peaks (as will be explained later) were labelled using letters. In Figure 5.8, identifiable participator Auger peaks were additionally labelled with numbers (specifically in the Figure inset).

Two participator Auger processes were identified in the difference spectra shown in Figure 5.8 (peaks **3-a** and **2-a**, according to the Figure). Peak **3-a** is present in the Resonance V data, with a KE of 517.0 $\pm$ 0.1 eV and associated 11.28 $\pm$ 0.04 eV effective BE. Peak **2** is evident in the Resonance VI-b data, at a KE of 519.6 $\pm$ 0.2 eV, with an associated effective BE of 10.2 $\pm$ 0.2 eV. The presence of the second harmonic signal prevented the identification of other resonantly-enhanced solute signals in the highest KE side of the resonant data.

Starting with peak **3-a** in the Resonance V data, the MO diagram shown in Figure 5.1 suggests that this signal could be attributed to a participator Auger peak involving the MnO_4^{2-}(aq.) $(1e)^{-1}$ ionizing transition – *i.e.* a K-1e,2e process. Peak **2** in the Resonance VI-b data was assigned as a K-$4t_2$,$5t_2$ process, as similarly observed and assigned for the MnO_4^-(aq.) data. Hence, a bulk-sensitive BE of 10.2 $\pm$ 0.2 eV is determined for the $(4t_2)^{-1}$ ionizing transition in MnO_4^{2-}(aq.). A comparison of this value with the surface-sensitive $4t_2^{-1}$ BE reported in Section 5.1.2 shows a negligible (+0.2 eV) positive shift when moving from the gas-solution interface to the solution bulk, with the same magnitude as the experimental error. This result follows a similar trend observed for other outer valence BEs, as described in the previous section, which highlighted higher stability of MnO_4^{2-}(aq.) in the bulk of the solution – *i.e.* as a fully hydrated ion. The observation of a K-$4t_2$,$5t_2$ Auger process highlights electron coupling between the Mn-O non-bonding $4t_2$ MO and the $5t_2$ anti-bonding MO.

Regarding the spectator Auger signals, labelled as **e – i** in Figures 5.7 and 5.8, similar features occur at nearly constant KE in the Resonance V, VI-a and VI-b data. Peak **e** shows up as a broad feature spanning the 505 – 517 eV KE range, with a maximum at a KE of 510.8 ± 0.2 eV. This peak is assigned to multiple K-V,V spectator Auger processes. The assignment was made based on the observations described in Section 4.2.3 for MnO_4^- (aq.) solutions. In contrast with the results presented there, however, the peak **e** feature in the MnO_4^{2-} (aq.) data does not show four distinct components as reported for MnO_4^- (aq.). A possible explanation for the loss of structure in the MnO_4^{2-} (aq.) case compared with that of MnO_4^- (aq.) would be additional electronic coupling between the HOMO (2e) and spectator (2e or 5t$_2$) electrons in the MnO_4^{2-} (aq.) excited state, resulting in a greater degree of spectral broadening.

Average KEs of 498.3 ± 0.7 eV, 495 ± 2 eV, 490.4 ± 0.1 eV, and 476.4 ± 0.8 eV were respectively determined for peaks **f**, **g**, **h** and **i** (see Figure 2 and Table AII in Appendix II). Considering the 5a$_1$ BE estimate reported in Section 5.2.1 (~25.4 eV), the aforementioned KEs suggest peaks **f – i** are K-5a$_1$,V spectator Auger processes involving the MnO_4^{2-}(aq.) non-bonding inner valence 5a$_1$ (O 2s) electrons. Neglecting electron correlation, BEs of ~11.3 eV, ~14.6 eV, ~19.2 eV and ~33.2 eV are estimated for the partner electrons emitted in the spectator Auger process, *i.e.* after a 5a$_1$ electron has refilled the core-hole. Given the absence of any matches with the MnO_4^{2-}(aq.) outer valence BEs reported throughout this chapter, ICD processes were considered to assign these features, following a similar approach to that applied for the MnO_4^- (aq.) data, (see Section 4.2.3 and 4.2.4).
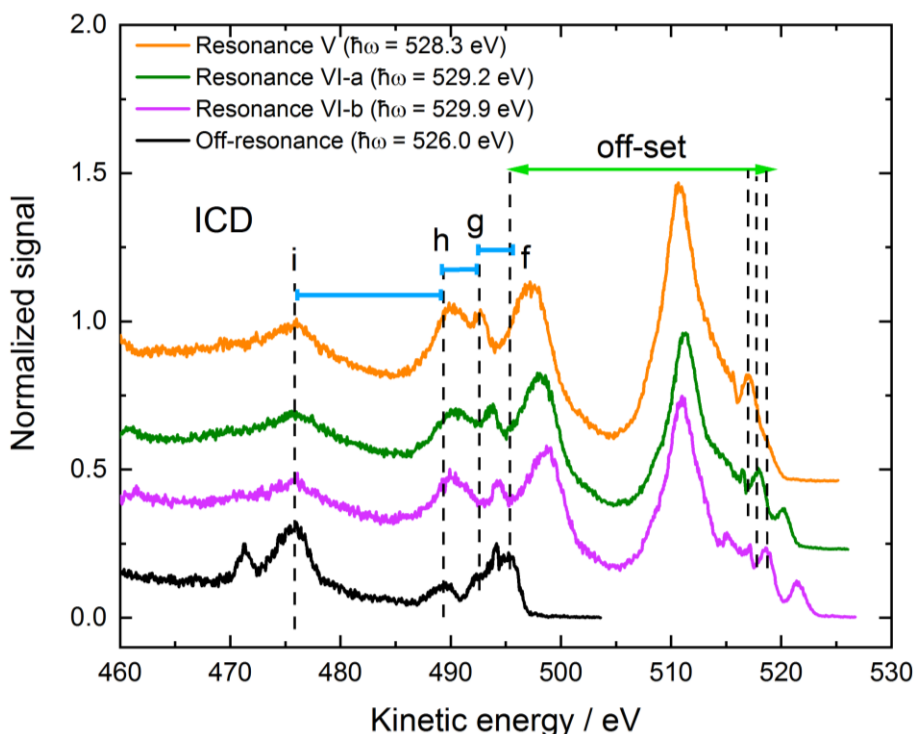
Figure 5.9. Signatures of ICD in MnO_4^{2-}(aq.) solutions

Resonance V, Resonance VI-a, Resonance VI-b spectra (raw data, without baseline correction) showing the energy gaps between peaks **f**, **g**, **h** and **i**. The off-resonant data shows the separation between the water valence ionization features. The off-resonant spectrum was offset to account for the resonant-non-resonant photon energy difference, the 5a$_1$ BE, and electron correlation effects.

The energetic separation between neighboring peaks were found to be 3 ± 2 eV (**f-g**), 5 ± 2 eV (**g-h**), and 14.0 ± 0.8 eV (**h-i**). Within the error bounds, these peak separations match the energy gaps between the valence BEs of liquid water. The KE positions of features **i-h** are all in agreement with those expected for K-$5a_1,1b_{1(w)}$, K-$5a_1,3a_{1(w)}$, K-$5a_1,1b_{2(w)}$, and K-$5a_1,2a_{1(w)}$ resonant, *spectator-like* ICD processes, respectively. The KEs and energy gaps of the ICD peaks are found to be equivalent, within the experimental uncertainties, to those reported in Section 4.2.4 for $MnO_4^-_{(aq.)}$. This is likely a reflection of the significant error bounds and the similar solvated molecular structure for both ions – *i.e.* bonding interactions between the ligand O 2s electrons and the water valence electrons are common to both ions and present similar energetics – despite the difference in formal oxidation state of the Mn metal center. Table 5.5 summarizes the O 1s RPES results reported in this section.

Table 5.5. $MnO_4^{2-}_{(aq.)}$ O 1s Auger and ICD signals

Participator Auger Signal	Assignment	BE / eV	FWHM$_G$
2-a	$(4t_2$ or $6a_1)^{-1}$	10.2 ± 0.2	1.6 ± 0.4

Spectator Auger Signal	Assignment 1	Assignment 2	KE / eV
e (main feature)	K-VV		510.8 ± 0.2
f	K-$5a_1,1b_{1(w)}$	K-$5a_1$,V	498.3 ± 0.7
g	K-$5a_1,3a_{1(w)}$	K-$5a_1$,V	495 ± 2
h	K-$5a_1,1b_{2(w)}$	K-$5a_1$,V	490.4 ± 0.1
i	K-$5a_1,2a_{1(w)}$	K-$5a_1$,V	476.4 ± 0.8

As mentioned in Chapter 4 regarding ICD in $MnO_4^-_{(aq.)}$ solutions, a mirroring in peak separation between the $MnO_4^{2-}_{(aq.)}$ resonantly-enhanced photoelectron features in the resonant data and the water valence photoelectron peaks in the off-resonant spectrum form the basis of the evidence for the occurrence of ICD in the MnO_4^{2-} aqueous system. Further confirmation for the assignment of the observed spectral features could be obtained from similar MnO_4^{2-} experiments using deuterated water.

5.3 Comparison of oxidation states across phases

Finally, a comparison of the electronic structure of MnO_4^- and MnO_4^{2-} ions in different condensed phase environments is presented. The aqueous phase BEs reported in Chapters 4 ($MnO_4^-_{(aq.)}$) and 5 ($MnO_4^{2-}_{(aq.)}$) will be compared with those reported for crystalline samples ($KMnO_{4(s)}$ and $K_2MnO_{4(s)}$) [167, 168]. As previously mentioned, in $MnO_4^-_{(aq.)}$ (and $KMnO_{4(s)}$), the Mn metal-center has a VII+ formal oxidation state. In $MnO_4^{2-}_{(aq.)}$ (and $K_2MnO_{4(s)}$), the formal oxidation state of Mn is VI+. In both complexes, the O ligands have the same formal charge (II-). In this Section, the BE shifts associated with a change in the formal oxidation state of the Mn metal center in the aqueous phase (and in the bulk of the solution) are compared to those in a crystalline environment.

Table 5.6 summarizes the $MnO_4^-_{(aq.)}$ and $MnO_4^{2-}_{(aq.)}$ bulk-sensitive BEs reported in Chapter 4 and 5, respectively, as referenced to the local vacuum level. Similar solid phase data reported in References [167, 168] is reproduced in Table 5.7, as referenced to the Fermi level. The BE differences between the two different oxidation states are indicated as $\Delta BE_{(aq.)}$ (Table 5.6) and $\Delta BE_{(s)}$ (Table 5.7).

Table 5.6. Aqueous phase (solution bulk) BEs of MnO$_4^-$ and MnO$_4^{2-}$

The values correspond to those reported in Chapters 4 and 5, respectively. The * indicate BE estimated from spectator Auger processes. The ** indicates a value extracted through combination of UV-visible and XPS spectral data.

Peak origin	MnO$_4^-$ (aq.) BE / eV	MnO$_4^{2-}$ (aq.) BE / eV	ΔBE$_{(aq.)}$ / eV
$(2e)^{-1}$	6.88 ± 0.08**	6.98 ± 0.06	
$(4t_2)^{-1}$	9.85 ± 0.08	10.2 ± 0.2	0.4 ± 0.2
$(3t_2)^{-1}$	12.66 ± 0.04*	11.70 ± 0.04	0.96 ± 0.04
$(5a_1)^{-1}$	26.82 ± 0.04	25.4*	~1.4
$(2t_2)^{-1}$	59.6 ± 0.1	58.4 ± 0.7	1.2 ± 0.7
$(4a_1)^{-1}$	94.1 ± 0.1	~91.7*	~2.4
$(3a_1)^{-1}$	536.0 ± 0.1	535.0 ± 0.1	1.0 ± 0.1
$(1t_2)^{-1}$	650.9 ± 0.1	648.9 ± 0.1	2.0 ± 0.1
$(1t_2)^{-1}$	661.9 ± 0.1	660.0 ± 0.1	1.9 ± 0.1

Table 5.7. MnO$_4^-$ and MnO$_4^{2-}$ solid phase BEs

Values taken from References [167, 168].

Peak origin	KMnO$_{4(s)}$ BE / eV	K$_2$MnO$_{4(s)}$ BE / eV	ΔBE$_{(s)}$ / eV
$(2e)^{-1}$		1.9 [168]	
$(4t_2)^{-1}$	5.4 [167]	3.9 [168]	0.5
$(3t_2)^{-1}$	7.5 [167]		
$(5a_1)^{-1}$	21.8 [168]	21.1 [168]	0.7
$(2t_2)^{-1}$	54.5 [168]	52.7 [168]	1.8
$(4a_1)^{-1}$	88.9 [168]	87.6 [168]	1.3
$(3a_1)^{-1}$	530.8 [168]	530 [168]	0.8
$(1t_2)^{-1}$	645.6 [168]	644.2 [168]	1.4
$(1t_2)^{-1}$	656.7 [168]	655.3 [168]	1.4

Overall, MnO$_4^-$ BEs are higher in comparison to those of MnO$_4^{2-}$, both in the aqueous and solid phases. This reflects the higher positive charge on the Mn-metal center in MnO$_4^-$ with respect to MnO$_4^{2-}$. Starting with the outer valence BEs ($4t_2^{-1}$ and $3t_2^{-1}$), the shift associated with the $4t_2^{-1}$ value is similar in both phases (~0.5 eV). For the $3t_2^{-1}$ BE, the chemical shift in the aqueous phase is more than twice that observed for the $4t_2^{-1}$ orbital (0.96 ± 0.04 eV). An explanation for this observation can be found in the atomic-parentage / hybridized nature of the two MOs. The $4t_2$ MO is an O-centered, non-bonding orbital, while the $3t_2$ is a Mn-O bonding orbital. This and the predominant Mn-character of the latter (as confirmed by the Mn $2p_{3/2}$ RPES experiments presented in Sections 4.2.1 and 5.2.1) are supportive of a higher sensitivity of the $3t_2$ electrons to a change in the Mn formal oxidation state.

The inner valence features ($5a_1^{-1}$ / O 2s, Mn 3p / $2t_2^{-1}$, Mn 3s, / $4a_1^{-1}$) show similar chemical shifts in both phases (~1 – 2 eV), within the experimental uncertainties.

A comparison of the O 1s and Mn $2p_{3/2}$ / $2p_{1/2}$ BEs should highlight the largest energetic shifts due to changes in the formal oxidation state, given the less hybridized nature of the core-levels with respect to the valence. The MnO$_4^{2-}$ (aq.) Mn $2p_{3/2}$ / $2p_{1/2}$ BEs were found to be 2 ± 0.1 eV lower in MnO$_4^{2-}$ (aq.) with respect to MnO$_4^-$ (aq.). The O 1s BEs are shifted to a lesser degree, by 0.9 ± 0.1 eV in the same direction. Similar shifts are observed from the solid phase values, however, the chemical shift associated with the Mn $2p_{3/2}$ / $2p_{1/2}$ BEs is ~0.5 eV higher in aqueous solution with respect to the crystalline environment. This likely results from more effective charge screening by the aqueous dielectric environment [243].

5.4 Summary of key findings of Chapter 5

The combination of liquid jet direct XPS and RPES – in conjunction with the micro-mixing sample source development – allowed the electronic structure of the MnO$_4^{2-}$ ion to be probed in the aqueous

phase, including the study of molecular bonding and MnO_4^{2-}(aq.)-water interactions. Experiments were performed with ~0.2 M MnO_4^{2-}(aq.) solutions at pH~13.5 and yielded the following results:

1. A partial experimentally-determined BE-scaled MO diagram was produced for the fully hydrated MnO_4^{2-}(aq.) ion;

2. A comparison between outer valence spectra recorded at different probing depths generally revealed ~0.2 eV larger BEs in the solution-bulk with respect to the gas-solution interface, suggesting higher stability of the ion in the bulk of the solution – *i.e.* as a fully hydrated ion. These results highlight the effect of changes in the hydrogen bonding environment, solute geometrical structural changes and / or different solute-solvent intermolecular interactions occurring at the gas-solution interface and affecting the valence energetics of MnO_4^{2-}(aq.);

3. Bulk-sensitive valence BEs could only be extracted from the RPES experiments. The $2e^{-1}$ (HOMO), $4t_2^{-1}$ (HOMO-2), $3t_2^{-1}$ (HOMO-5), and $2t_2^{-1}$ (Mn 3p) BEs were determined from participator Auger electron emission signatures.

4. The Mn $2p_{3/2}$ and $2p_{1/2}$ RPES experiments highlighted the predominant Mn-character of the $2e^{-1}$ (HOMO) ionizing transition;

5. Overall, the RPES experiments revealed similar participator and spectator Auger features, as well as spectator-like ICD processes, to those observed in the MnO_4^-(aq.) data presented in Chapter 4 (although the associated features were generally shifted towards lower BEs with respect to their MnO_4^-(aq.) counterparts). This includes the observation of a selective enhancement of the $3t_2^{-1}$ feature at the Mn $2p_{3/2} \rightarrow 5t_2$ resonance, hybridization of the inner valence Mn 3p and O 2s MOs, Koster-Cronig processes at the Mn $2p_{1/2} \rightarrow 5t_2$ resonance and ICD involving MnO_4^{2-}(aq.) O 2s electrons and the water solvent valence band in the first solvation shell.

6. A comparison between the electronic structure of both ions highlighted valence and core-level chemical shifts associated with the difference in formal oxidation state of the Mn-metal center between the two TMCs (VII+ in MnO_4^-(aq.) and VI+ in MnO_4^{2-}(aq.)). Overall, BEs are higher in MnO_4^-(aq.) with respect to MnO_4^{2-}(aq.). The magnitude of the chemical shifts were larger (~2 eV) for the Mn $2p_{3/2}$ / $2p_{1/2}$ BEs. Similar shifts of ~1 eV were observed for the O 1s and inner valence (Mn 3s, Mn 3p, O 2s) BEs. For the outer valence, ~ 1 eV shifts were observed for the $3t_2^{-1}$ (Mn-O bonding MO) BE, while a ~0.5 eV shift was observed for the $4t_2^{-1}$ (ligand-centered non-bonding MO) BE. The higher Mn 2p chemical shifts in the aqueous phase with respect to a crystalline environment highlighted the screening effect of the aqueous solvent on the charge on the Mn-center.

The electronic structure, molecular bonding, solute-solvent interactions and energetic information reported in this chapter constitute photoelectron spectroscopy fingerprints of the tetra-oxo Mn(VI+) charge state in aqueous solution. The electronic structure information will be used to infer thermodynamic parameters of the MnO_4^{2-}(aq.) / MnO_4^-(aq.) redox half reaction in the following chapter.

6 Redox energetics of MnO_4^- (aq.) and MnO_4^{2-} (aq.) solutions

In this chapter, the bulk-sensitive electronic structure information extracted from the XPS and RPES experiments performed with MnO_4^- (aq.) and MnO_4^{2-} (aq.) solutions reported in Chapters 4 and 5 will be applied to infer aqueous phase energetic parameters that underpin the redox chemistry of those ions. As discussed in Section 2.2, within the limits of the linear response approximation (LRA) – which has been proven to be appropriate when polar solvents are present, such as liquid water [244] – experimentally determined BEs and peak widths can be used to determine reorganization energies (λ), AIEs(aq.), and VEAs(aq.) [83, 126-129].

The results presented here focus on oxidation half reactions, given their parallels to the ionization processes that take place during an XPS experiment, as discussed in Sections 1.2.2 and 2.2. This approach has been previously applied in liquid jet XPS-based determinations of redox parameters for a number of aqueous redox transition metal complex systems [127, 182], including $[Mn(H_2O)_6]^{2+}$ (aq.) / $[Mn(H_2O)_6]^{3+}$ (aq.) [83]. For the later, experimental information on the $[Mn(H_2O)_6]^{3+}$ (aq.) ion was not reported. The tendency of these species to disproportionate [245] has thus far prevented the realization of associated liquid jet XPS experiments. As explained in Sections 1.2.3 and 3.2.3, a similar experimental challenge needed to be overcome for the realization of experiments with MnO_4^{2-} (aq.) ions, allowing the redox energetics of the MnO_4^{2-} (aq.) / MnO_4^- (aq.) redox pair – which have been previously investigated using theoretical methods [85] – to be reported purely from experimental data.

The chapter is divided into three sections. Section 6.1 is dedicated to the thermodynamic description of the MnO_4^- (aq.) / $MnO_4^{\bullet}$ (aq.) redox half reaction, including the derivation of the oxidative reorganization energy (λ_{ox}) and VEA of $MnO_4^{\bullet}$ (aq.) and AIE of MnO_4^- (aq.). The MnO_4^- (aq.) / $MnO_4^{\bullet}$ (aq.) redox half reaction is an exemplary case where thermodynamic information from electrochemistry-based experiments is not available due to the unstable nature of one of the components of the redox pair ($MnO_4^{\bullet}$ (aq.) in this case). Thus, the results presented here demonstrate a generic approach to study redox energetics by means of photoelectron spectroscopy where standard electrochemical methods cannot be implemented. In addition, comparison of the AIEs reported for MnO_4 (g.) [175] and the AIEs inferred for MnO_4^- (aq.) allowed the Gibbs free energy of hydration (ΔG_{hyd}) of the ion to be determined. Section 6.2 presents similar information but for the MnO_4^{2-} (aq.) / MnO_4^- (aq.) redox pair, ubiquitous in chemical and energy transfer processes involving MnO_4^- (aq.) in alkaline media. In addition, the MnO_4^{2-} (aq.) / MnO_4^- (aq.) redox energetics are of relevance for the development of redox flow batteries with electrolytes formed by these ions [40]. The photoelectron-spectroscopy-based results presented here are compared with existing

theoretical calculations [85] and Gibbs free energy values reported from electrochemistry. Finally, Section 6.3 implements the determined AIEs to construct electronic state energy diagrams for $MnO_4^-{}_{(aq.)}$ / $MnO_4^{\bullet}{}_{(aq.)}$ and $MnO_4^{2-}{}_{(aq.)}$ / $MnO_4^-{}_{(aq.)}$.

6.1 Permanganate aqueous solutions

With chemical reactions – including redox processes – primarily governed by the energetics of the most readily liberated electrons, the lowest energy vertical ionizing transition of $MnO_4^-{}_{(aq.)}$, $(1t_1)^{-1}$, can be considered to be of primary relevance to oxidative permanganate processes. This ionizing transition results in the production of the $(1)^2T_1$ state of $MnO_4^{\bullet}{}_{(aq.)}$ (permanganate radical). The process is related to the following redox half reaction:

$$MnO_{4(aq.)}^- \rightarrow MnO_{4(aq.)}^{\bullet} + e^-$$
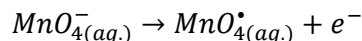
The chemical cycles associated with this redox process in the aqueous and gas phase are depicted in Figure 6.1 (panel A and B, respectively). The schematic quadratic potential energy curves highlight the free energetic relationships between the VIE and AIE of MnO_4^-, the VEA of $MnO_4^{\bullet}$ and, for the aqueous phase case, the associated reorganization free energies of oxidation (λ_{ox}) and reduction (λ_{red}). Using the lowest energy ionizing transition feature of $MnO_4^-{}_{(aq.)}$ reported in Chapter 4 (see peak **1** in Figure 4.2 and Table 4.1) and Expressions (1) and (4) in Section 2.2, it is possible to estimate λ_{ox} and the AIE of $MnO_4^-{}_{(aq.)}$.

The estimation of λ_{ox} requires knowledge of the (Gaussian) inhomogeneous broadening contribution to the photoelectron peak width (here referred to as FWHM$_{IB}$). As explained in Section 3.4, the peak widths reported throughout this thesis (and referred to as FWHM$_G$) reflect inhomogeneous broadening due to the aqueous environment and the combined beamline / analyzer instrumental resolution, excluding lifetime broadening effects (which can be ocassionally determined via Voigt profile fits and associated Lorentzian peak width conributions, particularly in core-level excitation cases). Expression (5) in Section 2.2 allows estimation of FWHM$_{IB}$ by considering and disentangling the Gaussian width of the ionization feature (FWHM$_G$, as reported in Table 4.1) and the broadening contribution from the overall instrumental resolution (FWHM$_{IR}$).

By adopting the ~635 eV photon energy FWHM$_{IR}$ value of 0.41 ± 0.01 eV (as determined via rare-gas XPS measurements under the same conditions adopted for the aqueous phase work, see Section 3.3) and the FWHM$_G$ value reported for peak **1** (Table 4.1), a FWHM$_{IB}$ value of 0.7 ± 0.1 eV was determined. Considering this result and a 278 K liquid jet temperature, a λ_{ox} value of 1.8 ± 0.2 eV or 170 ± 20 kJ mol^{-1} is determined for the $(1t_1)^{-1}$ ionizing transition using Expression (4). The λ_{ox} estimate and the lowest VIE of $MnO_4^-{}_{(aq.)}$ (9.22 ± 0.08 eV, see Table 4.1) correspondingly yields an $MnO_4^-{}_{(aq.)}$ AIE and ΔG_{ox} value of 7.4 ± 0.2 eV or 720 ± 20 kJ mol^{-1}, under the assumptions described in Section 2.2.

In addition, by using Expression (6) in Section 2.2 and the direct XPS results, the VEA$_{(aq.)}$ of $MnO_4^{\bullet}{}_{(aq.)}$ is estimated to be 5.7 ± 0.2 eV or 550 ± 20 kJ mol^{-1}. Gutsev *et al.* [175] reported an *adiabatic* EA of 4.8 eV for isolated $MnO_4^{\bullet}$ (*i.e.* in the gas phase). Their results highlighted the super-halogen character of $MnO_4^{\bullet}$ and the relatively high stability of MnO_4^- due to the existence of the metal center in the VII+ oxidation state [175]. As shown in Figure 6.1, in the aqueous phase, the *adiabatic* EA can be approximated by adding λ_{red} to VEA$_{(aq.)}$. Within the LRA, assuming $\lambda_{red} = \lambda_{ox}$ [19] and using $\lambda_{ox} = 1.8 \pm 0.2$ eV (as reported in Table 6.1), the adiabatic EA for $MnO_4^{\bullet}{}_{(aq.)}$ can be estimated to be

94

7.5 ± 0.2 eV. Here, the larger value for the aqueous phase ion compared to the gas phase highlights the effect of solvation in stabilizing the ion, as discussed when comparing the VIEs across phases in Section 4.1.4.

Finally, by comparing the MnO_4^- $AIE_{(aq.)}$ value with its gas phase counterpart, the associated value of ΔG_{hyd} can be estimated. In Figure 6.1 (panel B) the AIE value of gas phase MnO_4^- has been energetically aligned to the aqueous phase value, assuming vacuum level equivalence in liquid and gas phase PES experiments (by aligning the ground rovibronic states of $MnO_4^\bullet$ at the same energy in both phases). With such an alignment, the figure highlights that the difference between $AIE_{(aq.)}$ and $AIE_{(g)}$ is equal to ΔG_{hyd}. Using the gas phase MnO_4^- AIE of 4.80 ± 0.1 eV, as determined in Reference [175], and the $AIE_{(aq.)}$ value reported here, an estimate of 7.4 ± 0.2 eV $- 4.8 \pm 0.1$ eV $= 2.6 \pm 0.2$ eV, or 260 ± 20 kJ mol^{-1}, is obtained for ΔG_{hyd}. With fully solvated MnO_4^- $_{(aq.)}$ ions expected to form an average of 3.7 hydrogen bonds in solution [246], average MnO_4^- $_{(aq.)}$ hydrogen-bonding energies of 0.7 ± 0.1 eV can be inferred. The vertical axes in the figure show energetic information expressed as free energy (left) and potential energy (right). A parallel is thus stablished between the enthalpic and entropic (free energy) changes taking place upon removal of an electron from the solvated species in solution and the equivalent, respective potential energy changes experienced by the aqueous solute in its ground state configuration upon ionization in the condensed phase aqueous medium.
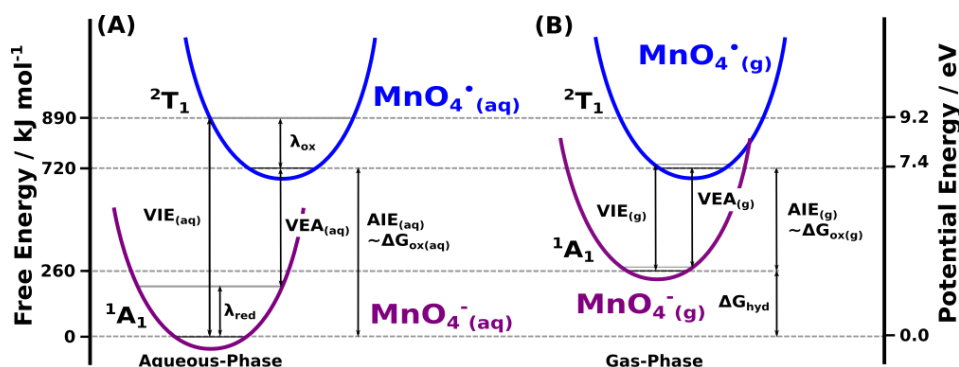
Figure 6.1. Redox energetics of MnO$_4^-$$_{(aq.)}$ / MnO$_4^\bullet$$_{(aq.)}$ and MnO$_4^-$$_{(g)}$ / MnO$_4^\bullet$$_{(g)}$

(A) Schematic potential energy curves for MnO$_4^-$$_{(aq.)}$ and MnO$_4^\bullet$$_{(aq.)}$, depicting the definition and relation between VIE$_{(aq.)}$, λ_{ox}, λ_{red}, VEA$_{(aq.)}$ and AIE$_{(aq.)}$. **(B)** As shown in panel A, but for MnO$_4^-$$_{(g)}$ and MnO$_4^\bullet$$_{(g)}$, using the energetic information reported in Reference [175]. The ground rovibronic state of MnO$_4^\bullet$ was commonly aligned between the aqueous and the gas phase.

Based on the MnO_4^- $_{(aq.)}$ $1t_1^{-1}$ ionizing transition analysis above and the $4t_2$ BE and peak width extracted from the RPES data presented in Section 4.2, the λ_{ox} and AIE values for the first electronically excited state of $MnO_4^\bullet$$_{(aq.)}$ can also be estimated. In this case, the RPES results correspond to a 283 K liquid jet temperature but are still comparable with the 277–278 K $MnO_4^\bullet$$_{(aq.)}$ ground state results (such a temperature variation leads to a less than 40 meV difference in λ_{ox} and AIE values, below the reported experimental uncertainties). The results of such an analysis, as well as the aforementioned findings reported in this section, are summarized in Table 6.1. The energetics are presented along with the electronic state symmetries of the produced $MnO_4^\bullet$$_{(aq.)}$ radicals (assuming a retention of T_d symmetry

upon ionization), with the assigned dominant molecular orbital symmetry of the removed electron given in parenthesis.

Table 6.1. MnO$_4^-$(aq.) energetic and thermodynamic parameters from PES data

Summary of the valence state energetic and thermodynamic parameters extracted from the MnO$_4^-$(aq.) liquid jet XPS and RPES data. Photo-oxidized radical state labels are appended to the table, with the dominant molecular orbital configuration changes with respect to the MnO$_4^-$(aq.) ground state shown in parenthesis. The valence BE values, VIE$_{(aq.)}$, and associated peak widths (see Table 4.1) were used to extract the FWHM$_{IB}$ terms. The oxidative reorganization energies, λ_{ox}, and adiabatic ionization energies, AIE$_{(aq.)}$, were extracted using the latter values. The extracted Gibbs free energy of hydration, ΔG_{hyd}, determined by comparison of the lowest aqueous phase AIEs to corresponding gas phase data [175], is also shown.

Radical state	VIE$_{(aq.)}$/eV	FWHM$_{IB}$/eV	λ_{ox}/eV	AIE$_{(aq.)}$/eV	ΔG_{hyd}/eV
(1)^{2}T$_1$ (1t$_1^{-1}$)	9.22 ± 0.08	0.7 ± 0.1	1.8 ± 0.2	7.4 ± 0.2	2.6 ± 0.3
(1)^{2}T$_2$ (4t$_2^{-1}$)	9.85 ± 0.08	0.6 ± 0.2	1.5 ± 0.5	8.4 ± 0.5	2.3 ± 0.5

6.2 Manganate aqueous solutions

Following a similar analysis to that presented in Section 6.1.1 for MnO$_4^-$(aq.) solutions, this section will use the bulk-sensitive data presented in Chapter 5 to estimate redox parameters associated with the MnO$_4^{2-}$(aq.) / MnO$_4^-$(aq.) redox pair.

Upon ionization, the removal of the most readily liberated electron from MnO$_4^{2-}$(aq.) corresponds to a (2e)$^{-1}$ ionizing transition, which can be related to the following redox half reaction:

$$MnO_{4(aq.)}^{2-} \rightarrow MnO_{4(aq.)}^{-} + e^{-}$$
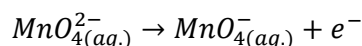
The chemical cycle associated with this redox process and redox information derived in this chapter is shown in Figure 6.2. Expressions (1) and (4) in Section 2.2, and the 2e^{-1} BE of MnO$_4^{2-}$(aq.) reported in Chapter 5 (see peak **0** in Figure 5.5 and Table 5.3), were used to estimate λ_{ox} and AIE values for MnO$_4^{2-}$(aq.).
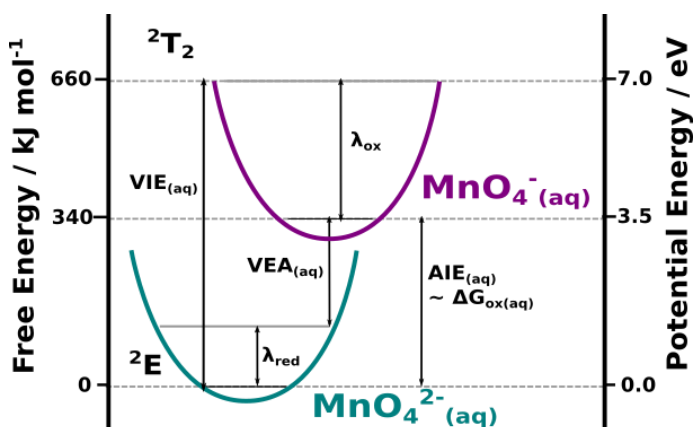
Figure 6.2. Redox energetics of MnO$_4^{2-}$(aq.) / MnO$_4^-$(aq.)

Schematic quadratic potential energy curves for MnO$_4^{2-}$(aq.) and MnO$_4^-$(aq.), highlighting the relationship between VIE$_{(aq.)}$, λ_{ox}, λ_{red}, VEA$_{(aq.)}$ and AIE$_{(aq.)}$. The system energetics have been scaled in accordance with the parameter values determined in this Chapter.

As described for MnO_4^-(aq.) in Section 6.1.1, Expression (5) was used to estimate FWHM$_{IB}$, the inhomogeneous broadening contribution to the width of the MnO_4^{2-}(aq.) photoelectron peak required for the determination of λ_{ox}. The Gaussian peak width, FWHM$_G$, reported in Table 5.3 corresponds to an average extracted from RPES spectra recorded at Resonance I and II, which provided bulk-sensitive data otherwise unavailable from direct XPS measurements (see Section 5.2.1 for details) at the U49/2 PGM-1 beamline (see Section 3.1.2). At those photon energies, under the experimental conditions adopted during the measurements, a beamline energy resolution of ~330 meV is expected. The electron analyzer was operated under conditions for which a resolution of ~200 meV was calculated. The latter was determined based on the experimentally-determined instrumental resolution (beamline and electron analyzer) values reported in Section 3.3 and the aforementioned beamline resolution. These estimates are fully consistent with the energy resolution determinations using Ar gas described in Section 3.3. As a result, a FWHM$_{IRF}$ value of 0.3 ± 0.1 eV was determined. The FWHM$_{IB}$ for peak **0** in Table 5.3 was found to be 1.0 ± 0.1 eV. Considering this result and a 278 K liquid jet temperature, and implementing Expression (4), yields a λ_{ox} value of 3.4 ± 0.1 eV or 330 ± 10 kJ mol^{-1} for the lowest vertical ionizing transition $(2e)^{-1}$. The λ_{ox} value and the $(2e)^{-1}$ VIE of MnO_4^{2-}(aq.) (7.0 ± 0.1 eV, see Table 5.3) results in a MnO_4^{2-}(aq.) AIE and ΔG_{ox} value of 3.6 ± 0.1 eV or 350 ± 10 kJ mol^{-1}.

The ΔG_{ox} determined from spectroscopic data can be compared with that known from electrochemistry. The redox potential of the MnO_4^{2-}(aq.) / MnO_4^-(aq.) half reaction introduced at the beginning of this section is $E^0 = -0.558$ V at 298 K [247] as referenced to SHE (with the minus sign denoting it is an oxidation reaction) or, equivalently, -53.8 kJ mol^{-1}. The redox potential corresponding to oxidation of MnO_4^{2-}(aq.) into MnO_4^-(aq.) is independent of the pH (see the Pourbaix diagram in Figure 1.2). For electron transfer reactions with coupled protonation processes [129, 248], consideration of the redox potential and Gibbs free energy referenced to the RHE becomes relevant (see Expression 3 in Section 2.2).

The results inferred here are similar to the electrochemical values: -0.8 ± 0.1 eV / 77 ± 10 kJ mol^{-1} versus SHE (albeit extracted at 278 K). To achieve consistency between the ΔG_{ox} value determined from the RPES data and that determined from electrochemistry, the experimental VIEs should be referenced to the vacuum level at infinity and entropic contributions to the Gibbs free energy should be considered (see Figure 2.5 and Sections 2.2 and 2.3 for details).

A density functional molecular dynamics study of the MnO_4^{2-}(aq.) / MnO_4^-(aq.) redox half reaction [85] reported a λ_{ox} value of 0.8 eV. The theoretical studies reported by those authors included electronic structure calculations for the MnO_4^{2-}(aq.) and MnO_4^-(aq.) ions, which showed insignificant mixing between the MOs involved in the transfer electron process and those of the water solvent. The opposite has been highlighted by the experimental results presented in Sections 4.2 and 5.2, specifically the observation of resonant ICD processes. This could potentially explain the discrepancy between the λ_{ox} value calculated in Reference [85] (0.8 eV) with the one estimated using the LRA and spectroscopic information here (3.4 ± 0.1 eV, determined from RPES data), given the sensitivity of λ_{ox} to polarizing interactions between solute and solvent molecules [19].

Finally, by using Expression (6) in Section 2.2, the VEA(aq.) of MnO_4^-(aq.) is estimated to be 0.2 ± 0.1 eV. In general, lower electron affinities are indicative of the associated species behaving as an electron acceptor and negative electron affinities are commonly observed for ions such as MnO_4^-(aq.) [249, 250]. Notably, Farrokhpour *et al* [250] reported an adiabatic EA of -2 eV for MnO_4^-(aq.). By

taking into account the reductive reorganization energy (approximating it to be equal to the oxidative reorganization energy), the adiabatic EA can be estimated to be -3.4 ± 0.1 eV from the results presented here. The AEA value estimated here is of the same order of magnitude as the calculated value, and highlights the strong oxidizing capabilities of MnO_4^- (aq.), as introduced in Section 1.1 (the discrepancies between both results can be attributed to insufficient treatment of the solute-solvent geometries). The spontaneous oxidation of MnO_4^-(aq.) in air is thermodynamically favorable, although the process displays slow kinetics and MnO_4^-(aq.) solutions are known to slowly oxidize to $MnO_{2(s)}$ (IV+ oxidation state) at neutral pH, MnO_4^{2-}(aq.) (VI+ oxidation state) at alkaline pH, or $[Mn(H_2O)_6]^{2+}$(aq.) (II+ oxidation state) at acidic pH (see Figure 1.1). Cumulatively, this highlights the properties of MnO_4^-(aq.) as a versatile, strong oxidizing agent and effective electron acceptor.

6.3 Electronic state energy level diagrams

In this Section, the valence band spectroscopic results reported in Chapters 4 and 5 and the redox energetics estimated in the previous section will be presented as electronic state energy level diagrams of MnO_4^-(aq.) / $MnO_4^•$(aq.) and MnO_4^{2-}(aq.) / MnO_4^-(aq.), as shown in Figure 6.3 (left and right, respectively). The diagrams are energetically referenced to the rovibronic ground state of MnO_4^-(aq.) (left panel) or MnO_4^{2-}(aq.) (right panel). Vertical excitation energies for the electronically excited anion states were determined from the UV-visible absorption spectra and associated literature presented in Section 2.1.2 (see Figure 2.3). The VIE values extracted directly from the direct XPS and RPES results are labelled as *vertical*, while the AIE values determined from the associated BEs and peak widths in the previous section are labelled as *adiabatic*.
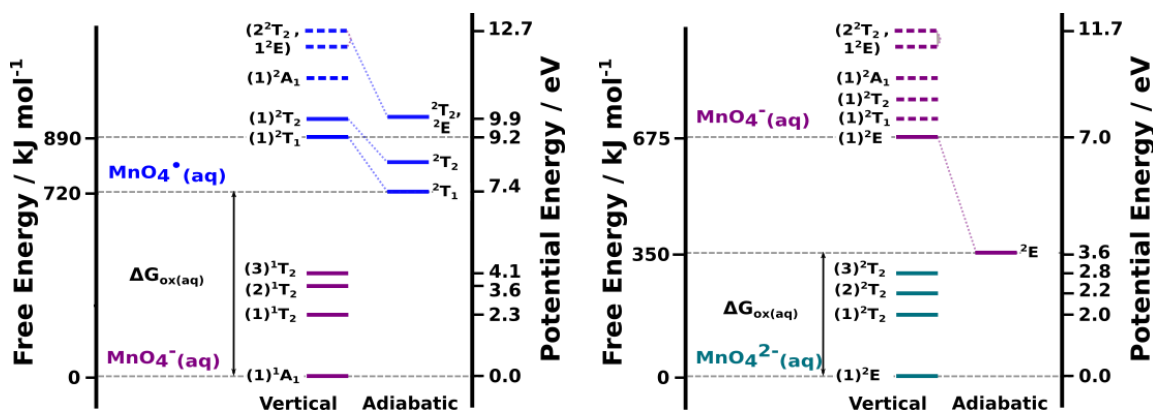
Figure 6.3. Electronic energy state diagrams of MnO$_4^-$(aq.) / MnO$_4^\bullet$(aq.) and MnO$_4^{2-}$(aq.) / MnO$_4^-$(aq.)

(Left) Electronic energy level diagram of MnO$_4^-$ (aq.) and MnO$_4^\bullet$(aq.) extracted from the spectroscopic results reported in Chapter 4 and potential energy referenced to the MnO$_4^-$(aq.) electronic ground state. On the left of the diagram, vertical excitation energies and associated state energy levels of the optically active excited states of MnO$_4^-$(aq.) (see Figure 2.3) and valence electronically excited states of the MnO$_4^\bullet$(aq.) radical are shown. Solid lines are used to denote the precisely determined MnO$_4^-$(aq.) and MnO$_4^\bullet$(aq.) state energies, with dashed lines denoting the equivocally inferred (1)^{2}A$_1$ (6a$_1^{-1}$), (1)^{2}E (1e^{-1}), and (2)^{2}T$_2$ (3t$_2^{-1}$) MnO$_4^\bullet$(aq.) state energetics at the equilibrium geometry of the MnO$_4^-$(aq.) ground state. For the two lowest VIEs, corresponding adiabatic MnO$_4^\bullet$(aq.) radical state energy levels (^{2}T$_1$ and ^{2}T$_2$), as extracted using the direct XPS and RPES peak BEs/widths and the LRA and reported in Sections 6.1 and 6.2, are shown to the right. **(Right)** Electronic energy level diagram of MnO$_4^{2-}$ (aq.) and MnO$_4^-$(aq.) based on the RPES results reported in Chapter 5. The energy scale has been referenced to the MnO$_4^{2-}$ (aq.) electronic ground state. Vertical excitation energies and state energy levels of the optically active excited states of MnO$_4^{2-}$ (aq.) (see Figure 2.3) and valence electronically excited states of MnO$_4^-$(aq.) are shown on the scale on the left. Solid lines denote precisely determined MnO$_4^{2-}$ (aq.) and MnO$_4^-$(aq.) state energies. Dashed lines denote the equivocally inferred (1)^{2}T$_1$ (1t$_1^{-1}$), (1)^{2}T$_2$ (4t$_2^{-1}$), (1)^{2}A$_1$ (6a$_1^{-1}$), (1)^{2}E (1e^{-1}), and (2)^{2}T$_2$ (3t$_2^{-1}$) MnO$_4^{2-}$ (aq.) state energetics at the equilibrium geometry of the MnO$_4^{2-}$ (aq.) ground state. The AIE of MnO$_4^{2-}$ (aq.), as reported in Section 6.2, is also shown to the right of the panel.

Overall, the results presented in this chapter highlight how redox energetics in aqueous solution can be studied using photoemission spectroscopy and by applying thermodynamics, linear response treatments and Marcus theory. Such a methodology can facilitate the determination of a range of thermodynamic quantities, related to the stability of redox pairs, that often cannot be obtained from regular electrochemical methods [83], such as cyclic voltammetry [251]. This combined photoelectron spectroscopy and thermodynamic approach becomes especially relevant for the study of redox reactions involving transient intermediates or unstable species, which quickly react or decompose upon formation. More generally, this approach expands the information content that can be extracted from liquid-phase XPS experiments [83, 126, 127] and provides a means to connect that data to thermodynamic quantities extracted using complementary techniques [124, 125].

7 Summary, conclusions and outlook

The work presented in this thesis described the application of liquid jet soft X-ray photoelectron spectroscopy to the study of the electronic structure and electron transfer energetics of redox reactants in aqueous solution. Two tetra-oxo, Mn-based TMCs were studied: the aqueous permanganate ($MnO_4^-{}_{(aq.)}$) and manganate ($MnO_4^{2-}{}_{(aq.)}$) ions. This chapter summarizes the main findings and conclusions derived from the experiments performed with $NaMnO_{4(aq.)}$, $KMnO_{4(aq.)}$, and chemically and electrochemically generated $MnO_4^{2-}{}_{(aq.)}$ solutions. An outlook for future work is presented in addition, along with more general perspectives.

7.1 Summary and conclusions

The combined application of micro-fluidic-based sample sources, the liquid microjet technique, direct XPS, and RPES provided the required spectroscopic information to map the electronic structure, molecular bonding and solute-solvent interactions in $MnO_4^-{}_{(aq.)}$ and $MnO_4^{2-}{}_{(aq.)}$ solutions. Spectroscopic data was used to infer redox energetics, thus exploring the electronic structure-redox function relationship in those transition metal complexes. As proposed in Section 1.3, the following points have been addressed:

1. Aqueous phase electronic structure of permanganate ($MnO_4^-{}_{(aq.)}$) and manganate ($MnO_4^{2-}{}_{(aq.)}$): A combination of the results from direct XPS and RPES experiments provided the necessary information to map the electronic structure of $MnO_4^-{}_{(aq.)}$ and $MnO_4^{2-}{}_{(aq.)}$. Outer and inner valence, O 1s and Mn $2p_{3/2}$ / $2p_{1/2}$ electron BEs were determined and used to produce MO and valence electronic state energy level diagrams for both ions.

The $MnO_4^-{}_{(aq.)}$ BEs reported here were compared with those reported for $KMnO_{4(s)}$ and $MnO_4^-{}_{(g)}$ in the literature. Aqueous and solid phase BEs were found to be similar, with the former being up to a few-hundred meV lower compared to their solid state counterparts. An increase of more than 4 eV was found for the lowest-energy ionizing transition BEs in $MnO_4^-{}_{(aq.)}$ with respect to $MnO_4^-{}_{(g)}$, highlighting the effect of hydration on the energetics of the isolated ion.

The $MnO_4^-{}_{(aq.)}$ / $MnO_4^{2-}{}_{(aq.)}$ chemical shifts (due to the different formal oxidation state of the Mn metal center, VII+ and VI+, respectively) were found to be similar in the aqueous and solid phases for valence and O 1s BEs. For the Mn $2p_{3/2}$ / $2p_{1/2}$ BEs, however, the chemical shift is ~0.5 eV larger for the aqueous solvated ions (with respect to a crystalline environment). In addition, orbital-specific chemical shifts highlighted a larger sensitivity to changes in oxidation state for Mn-based valence MOs, and for those with Mn-O bonding character (in comparison to the non-bonding or O-centered orbitals).

2. Comparison of energetics in two different hydration environments: Experiments performed at different liquid jet probing depths – *i.e.* at the gas-solution interface and in the solution bulk – provided insight into solute distributions in the bulk of the solution and interfacial effects on the electronic structure.

For MnO_4^-(aq.), at 0.2 M concentration, valence and core-level BEs were found to be equivalent both at the interface and in the solution bulk, independently of the nature of the counter ion in solution (Na^+(aq.) or K^+(aq.)). Depth profiling studies performed with 0.2 M and 1.0 M $NaMnO_4$(aq.) solutions revealed a preference for MnO_4^-(aq.) to remain in the bulk of the solution and away from the gas-solution interface, with non-linear accumulation behavior potentially taking place only for the higher concentration case. These results can potentially offer insight into the (concentration-dependent) effect of MnO_4^-(aq.) on the surface tension of water.

For MnO_4^{2-}(aq.), at 0.2 M concentration, BEs were generally found to be ~0.2 eV larger in the bulk of the solution with respect to the gas-solution interface. This result suggests a higher stability of MnO_4^{2-}(aq.) in the bulk of the solution, i.e. as a fully hydrated ion, and highlights the effect of different interfacial phenomena in the solution phase energetics. These BE shifts may be related to changes in the hydrogen bonding environment, solute geometrical structural changes, and / or different solute-solvent intermolecular interactions occurring at the gas-solution interface.

3. Intramolecular and intermolecular interactions: Mn $2p_{3/2}$ / $2p_{1/2}$ and O 1s RPES experiments provided insight into intramolecular (between the Mn center and the O ligands) and intermolecular (between the O ligands and water molecules) electronic charge distributions. Intramolecular Auger processes assigned in these experiments facilitated the identification of valence photoelectron signatures that were not accessible in the (non-resonant) XPS experiments. The O 1s RPES experiments additionally revealed spectator-like, ICD features corresponding to interaction between O 2s ligand-based (hybridized) electrons and valence electrons from water molecules in the first hydration shell.

4. Inference of redox energetics from spectroscopic information: The bulk-sensitive BEs and peak widths extracted from the XPS and RPES experiments, thermodynamic cycles and the LRA were used to infer aqueous phase energetic parameters that underpin the redox chemistry of MnO_4^-(aq.) and MnO_4^{2-}(aq.) ions. Aqueous phase reorganization energies (λ), AIEs (aq.) and VEAs (aq.) were estimated, providing a thermodynamic description of the MnO_4^-(aq.) / $MnO_4^{\bullet}$(aq.) and MnO_4^{2-}(aq.) / MnO_4^-(aq.) oxidation half reactions.

Gibbs free energies of oxidation were also calculated for oxidation half reactions with the aforementioned redox pairs. For MnO_4^{2-}(aq.) / MnO_4^-(aq.), the results were similar to those extracted from electrochemical measurements. For MnO_4^-(aq.) / $MnO_4^{\bullet}$(aq.), the information reported here demonstrates the application of a generally applicable, combined photoelectron spectroscopy and thermodynamics approach to study the redox energetics of highly unstable species, such as $MnO_4^{\bullet}$(aq.).

5. Sample source developments for the generation of MnO_4^{2-}(aq.) transient ions: Flowing chemical mixing and electrolysis-based MnO_4^{2-}(aq.) generation routes were explored to produce stable liquid jets. A micro-mixing scheme and an electrolysis cell were successfully interfaced with the liquid micro jet technique. The micro-mixing scheme facilitated the generation of 0.2 M MnO_4^{2-}(aq.) solutions at a pH of ~13.5. The setup was used to record the XPS and RPES data presented here. To achieve maximum conversion efficiency, mixing lengths and flow rates were optimized by observing the MnO_4^{2-}(aq.) / MnO_4^-(aq.) signal ratio in PEY-XAS spectra. In addition, Mn 2p and PEX-XAS data

recorded under partial and full mixing conditions provided experimental proof of distinct spectroscopic signatures of MnO_4^{2-} (aq.) (Mn VI+) and MnO_4^- (aq.) (Mn VII+) ions.

The capabilities of the electrolysis cell liquid jet were tested in a number of proof-of-principle experiments, applying the device to the electrolysis of MnO_4^- (aq.) at pH~14.6. This route for the electrolytic generation of MnO_4^{2-} (aq.) ions was tested as a function of flow rate and applied voltage. Currently, the conversion efficiencies of the electrolysis cell are limited to 10% by the flow rate range needed for stable jet formation and the working and counter electrode areas. Further developments are required to engineer near-complete electrochemical conversion. Specifically, the working and counter electrode surface areas must be increased while maintaining an in-vacuum cell form factor that can be accommodated within the experimental chamber and sample-soft-X-ray-beam interaction region.

7.2   Future work and outlook

Aqueous manganese species, such as the MnO_4^- (aq.) (Mn, VII+) and MnO_4^{2-} (aq.) (Mn, VI+) species studied here, form versatile redox pairs suitable for green chemistry and energy conversion applications. However, the investigation of the overall electronic structures and solute behaviors of the aqueous Mn-species with alternative oxidation states has yet to be performed and would allow the complete characterization of their electronic structure-redox behavior. These species include MnO_4^- (aq.), MnO_4^{2-} (aq.), MnO_4^{3-} (aq.), $[Mn(H_2O)_6]^{3+}$ (aq.), and $[Mn(H_2O)_6]^{2+}$ (aq.). While $[Mn(H_2O)_6]^{2+}$ (aq.) (Mn, II+) form stable solutions, MnO_4^{3-} (aq.) (Mn, V+) and $[Mn(H_2O)_6]^{3+}$ (aq.) (Mn, III+) are transient species [52, 56, 245] and hence require the implementation of alternative sample sources. Examples of such soruces are the micro-mixing scheme or the electrolysis liquid jet implemented to generate MnO_4^{2-} (aq.) during the course of this work.

With all of the above in mind, and considering each of the aforementioned Mn species, future work would include:

1. Further concentration-dependence experiments with MnO_4^- (aq.) and depth profiling study of MnO_4^{2-} (aq.): As a follow-up to the depth profiling experiments reported in Section 4.1.3, valence band spectra recorded at different concentrations and at different probing depths could provide insight into solute and solvent electronic structure changes associated with the (non-linear) accumulation behavior of the bulk-active MnO_4^- (aq.) ions reported here. As a comparison with the data reported here for MnO_4^- (aq.), a depth profiling study of MnO_4^{2-} (aq.) would potentially clarify the reason for the difficulties in observing MnO_4^{2-} (aq.) valence band signatures in direct XPS experiments performed at probing depths that are predominantly sensitive to the aqueous bulk environment, as reported in Chapter 5. We have performed initial experiments with $NaMnO_4$ (aq.) solutions with the aim of determining water orbital-specific shifts as a function of concentration. Further associated data analysis and interpretation are still required.

2. Characterization of the electronic structure, molecular bonding, solute-solvent interactions and redox properties of $[Mn(H_2O)_6]^{2+}$ (aq.): Surface-sensitive, valence band spectra of $[Mn(H_2O)_6]^{2+}$ (aq.) in the presence of NO_3^- (aq.) and Cl^- (aq.) counter ions have already been published in the literature, including the estimation of oxidative reorganization energies [83, 100]. We have collected a more expansive $[Mn(H_2O)_6]^{2+}$ (aq.) data set including both direct XPS (outer and inner valence and core-level spectra) and RPES/PEY-XAS spectra, that still needs to be understood and interpreted. The experiments were performed from solutions with Cl^- (aq.) and SO_4^{2-} (aq.) counter ions with both gas-solution interface and

solution-bulk spectral sensitivities. The former would provide insight into the energetics of interfacial redox chemistry in the ocean [30], while the latter would inform about the energetics associated with the $[Mn(H_2O)_6]^{2+}_{(aq.)}$, / $[Mn(H_2O)_6]^{3+}_{(aq.)}$ redox pairs, as implemented in redox flow batteries [41].

3. Tailoring of the sample source developments presented here to the generation of $[Mn(H_2O)_6]^{3+}_{(aq.)}$ and $MnO_4^{3-}_{(aq.)}$ transient ions: The implementation of an electrolysis-based sample source device such as the electrolysis cell liquid jet described here provides a route to the realization of liquid jet XPS and RPES experiments with these two Mn TMCs.

0.2 M $[Mn(H_2O)_6]^{3+}_{(aq.)}$ solutions can be stabilized with respect to disproportionation on a minute time scale at acidic pH, requiring relatively high concentrations of stabilizing agents (~4 M $H_2SO_{4(aq.)}$, 0.5 M $[Mn(H_2O)_6]^{2+}_{(aq.)}$ [252]. This approach has been tested with the micro-mixing scheme described here. The outcome of those experiments highlighted the challenges of working in extremely corrosive and acidic environments with regard to the chemical compatibility of the materials employed in the delivery system. In addition, spectroscopic signatures of $[Mn(H_2O)_6]^{3+}_{(aq.)}$ were buried under those of the stabilizing agents. Similarly – and even more challenging – is the generation of $MnO_4^{3-}_{(aq.)}$ liquid jet samples. $MnO_4^{3-}_{(aq.)}$ ions are stable on a microsecond time scale in extremely alkaline environments [215] (and references therein). Hence, an electrolysis device capable of achieving high redox conversion efficiencies in millisecond (for $[Mn(H_2O)_6]^{3+}_{(aq.)}$) or microsecond (for $MnO_4^{3-}_{(aq.)}$) residence time scales would be required. Large electrode areas and small reaction volumes need to be combined in the right form factor (as discussed in the previous section) while maintaining laminar flow conditions so as to enable the formation of stable liquid jet samples.

Implementation of an electrolytic cell device with the aforementioned characteristics would enable the study of the electronic structure, molecular bonding, and solute-solvent interactions of $[Mn(H_2O)_6]^{3+}_{(aq.)}$ and $MnO_4^{3-}_{(aq.)}$ transient ions. The combined photoelectron spectroscopy and thermodynamics approach presented in this work would then allow the energetics of redox processes involving $MnO_4^{3-}_{(aq.)}$ and $[Mn(H_2O)_6]^{3+}_{(aq.)}$ to be investigated.

Furthermore, by performing RPES experiments as a function of applied voltage and pH, the interaction between valence and conduction band states in solution can be probed by probing participator and spectator Auger and (potentially) ICD processes. These experiments would provide further insight into the electron transfer processes between different Mn TMCs redox pairs and between species in their various oxidation states (as illustrated in Figure 1.1). Such information could be applied to the realization of Mn-based redox flow batteries [40, 41]. This methodology would also be generally applicable to any other chemical species [24, 253].

Combinatorially, the liquid jet direct XPS and RPES and chemically- and electrochemically-based sample sources for the generation of transient species directly provide electronic structure information and a microscopic description of aqueous redox systems. The application of such data with thermodynamics provides the means for directly correlating molecular information with macroscopic (electron transfer) behavior, offering unique insights into the structure-function relationship of environmentally-relevant aqueous redox species.

Appendix I

This appendix presents the complementary content referred to in Chapter 4, addressing the following points: (**1**) BEs extracted from surface-sensitive XPS spectra; (**2**) Analysis of the $NaMnO_{4(aq.)}$ PEY-XAS spectra; (**3**) Bulk-sensitive (RPES) data recorded from $KMnO_{4(aq.)}$ solutions; (**4**) Multi-peak fitting analysis of the (a) $NaMnO_{4(aq.)}$ and (b) $KMnO_{4(aq.)}$ RPES data.

1. BEs extracted from surface-sensitive XPS spectra

Table AI.1 summarizes the $MnO_4^-{}_{(aq)}$ BEs extracted from fits to the surface-sensitive data shown in Figure 4.4 in **Section 4.1.2**. The top panel summarizes the inner and outer valence BEs extracted from data sets recorded at 150 eV and 225 eV photon energies. The bottom panel displays the $3a_1^{-1}$ and $1t_2^{-1}$ solute BEs extracted from spectra recorded at 688 eV and 800 eV photon energies, respectively. Signal assignments are explained in the text in **Section 4.1.2**.

Table AI.1. $MnO_4^-{}_{(aq)}$ BEs extracted from Gaussian (top) and Voigt profile (bottom) fits to the surface-sensitive spectra

Label	Peak Origin	$\hbar\omega$ = 150 eV		$\hbar\omega$ = 225 eV	
		BE / eV	$FWHM_G$ / eV	BE / eV	$FWHM_G$ / eV
1	$(1t_1)^{-1}$	9.27 ± 0.04	0.69 ± 0.06	9.22 ± 0.08	0.6 ± 0.2
2	$(4t_2)^{-1}$	10.59 ± 0.04	1.34 ± 0.05	10.71 ± 0.06	1.5 ± 0.2
4	$(2a_1)^{-1}$	-	-	26.9 ± 0.1	3.6 ± 0.3
5	$(2t_2)^{-1}$	-	-	59.7 ± 0.3	2.0 ± 0.3
Label	Peak Origin	$\hbar\omega$ = 688 eV		$\hbar\omega$ = 800 eV	
		BE / eV	$FWHM_G$ / eV	BE / eV	$FWHM_G$ / eV
7	$(3a_1)^{-1}$	536.2 ± 0.1	1.59 ± 0.01	-	-
†	?	538.3 ± 0.2	1.0 ± 0.1	-	-
8	$(1t_2)^{-1}$	-	-	650.8 ± 0.1	1.11 ± 0.04

2. Analysis of the $NaMnO_{4(aq.)}$ PEY-XAS spectra

Figure 1 shows Mn $L_{II,III}$-pre-edge and O K-pre-edge PEY-XAS spectra produced from the RPES data recorded from 0.2 M $NaMnO_{4(aq.)}$ solutions presented in **Section 4.2**. The photon energy scale was calibrated as described in Section 3.4.2.
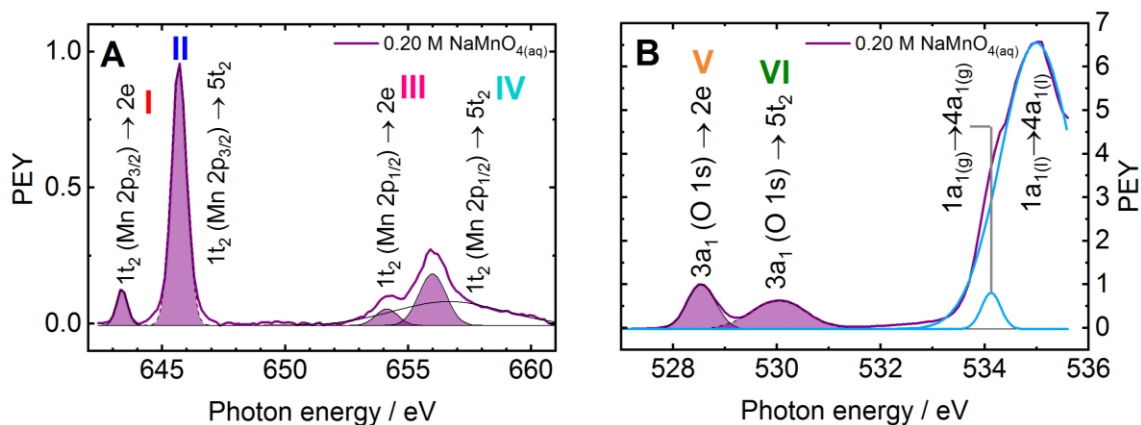
Figure AI.1

(A) Baseline-corrected Mn L-pre-edge PEY-XAS spectrum and cumulative Gaussian fits (purple) used to determine the $1t_2$ (Mn $2p_{3/2}$) $\rightarrow$ 2e, $1t_2$ (Mn $2p_{3/2}$) $\rightarrow$ $5t_2$, $1t_2$ (Mn $2p_{1/2}$) $\rightarrow$ 2e, and $1t_2$ (Mn $2p_{1/2}$) $\rightarrow$ $5t_2$ resonant photon energies. The broad Gaussian in the $652 - 661$ eV range was added to account for the remaining background after the baseline correction procedure. **(B)** O K-pre-edge PEY-XAS spectrum and cumulative Gaussian fits (purple) used to determine the $3a_1$ (O 1s) $\rightarrow$ 2e and $3a_1 \rightarrow 5t_2$ resonant photon energies. The light blue curves close to 534 eV and 535 eV correspond to the O 1s $-$ $4a_1$ transitions from gas phase [254] and liquid phase [255] water, respectively.

3. Bulk-sensitive (RPES) data recorded from KMnO$_{4(aq.)}$ solutions

Figure 2 shows Mn $2p_{3/2}$ and O 1s RPES data recorded from 0.15 M KMnO$_{4(aq.)}$ solutions similar to the data recorded from 0.20 M NaMnO$_{4(aq.)}$ solutions and presented in **Section 4.2**. The high photon energies associated with the core-to-virtual valence energy gaps in the Mn 2p and O1s RPES experiments ensure bulk-solution sensitivity. Hence, bulk-sensitive RPES results from 0.15 M KMnO$_{4(aq.)}$ solutions can be compared to the NaMnO$_{4(aq.)}$ results (presented in **Section 4.1.1**) to assess the effects of the counter-ion on the bulk electron energetics. The resonant-off-resonant difference spectra and associated fit results are shown in Section 4 (b) of this appendix. At ~0.2 M concentration, intramolecular Auger relaxation mechanisms and non-local autoionization processes in MnO$_4^-{}_{(aq.)}$ solutions are similar both in the presence of Na$^+{}_{(aq.)}$ or K$^+{}_{(aq.)}$ counter ions.
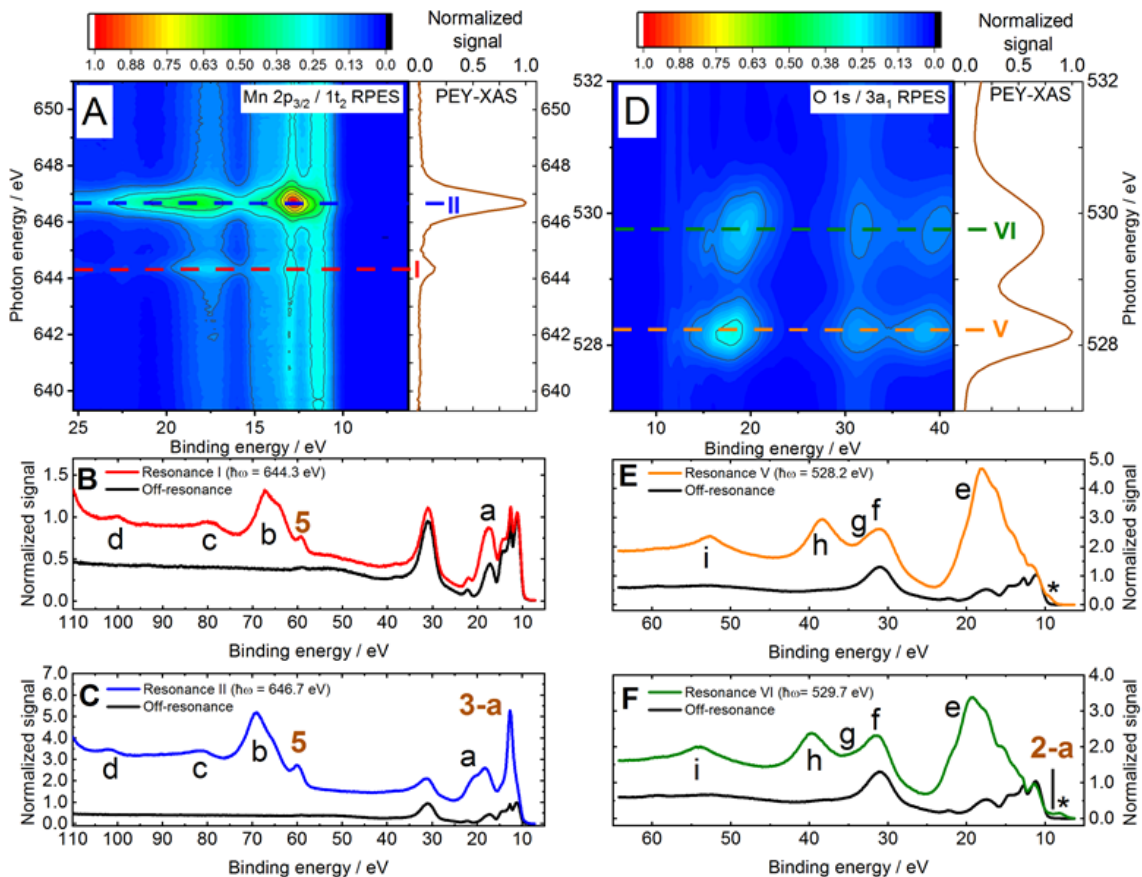
Figure AI.2

(A) Mn 2p$_{3/2}$ RPES map (left) and PEY-XAS spectrum (right) recorded from 0.15 M KMnO$_{4(aq.)}$ solutions. **(B)** As measured Mn 2p$_{3/2}$ → 2e resonant spectrum (red). **(C)** As measured Mn 2p$_{3/2}$ → 5t$_2$ resonant spectrum (blue). **(D)** O 1s RPES map (left) and PEY-XAS spectrum (right) recorded from 0.15 M KMnO$_{4(aq.)}$ solutions. **(E)** As measured O 1s → 2e resonant spectrum (orange). **(F)** As measured O 1s → 5t$_2$ resonant spectrum (green). An off-resonant spectrum (black curve, without resonant signal enhancements) is added for comparison in panels B, C, E and F. Features labelled with an asterisk in panels E and F correspond to signals resulting from ionization with the unfiltered second harmonic of the beamline. Participator Auger signals are labelled with numbers and spectator Auger signals are labelled with letters. The BE scale is suitable for the identification of participator Auger process and a comparison with the direct XPS results reported in Section 4.1.1.

4. Multi-peak fitting analysis and results of the NaMnO$_{4(aq.)}$ and KMnO$_{4(aq.)}$ RPES data

(a) Cumulative fits to NaMnO$_{4(aq.)}$ resonant spectra

Figure 3 shows cumulative fits to the resonant-off-resonant difference spectra recorded from 0.2 M NaMnO$_{4(aq.)}$ solutions presented in Figures 4.8, 4.10 and 4.12. The results obtained from these fits were used to report the KEs presented in **Section 4.2**. The fitting results and peak assignments are summarized in Table 2.
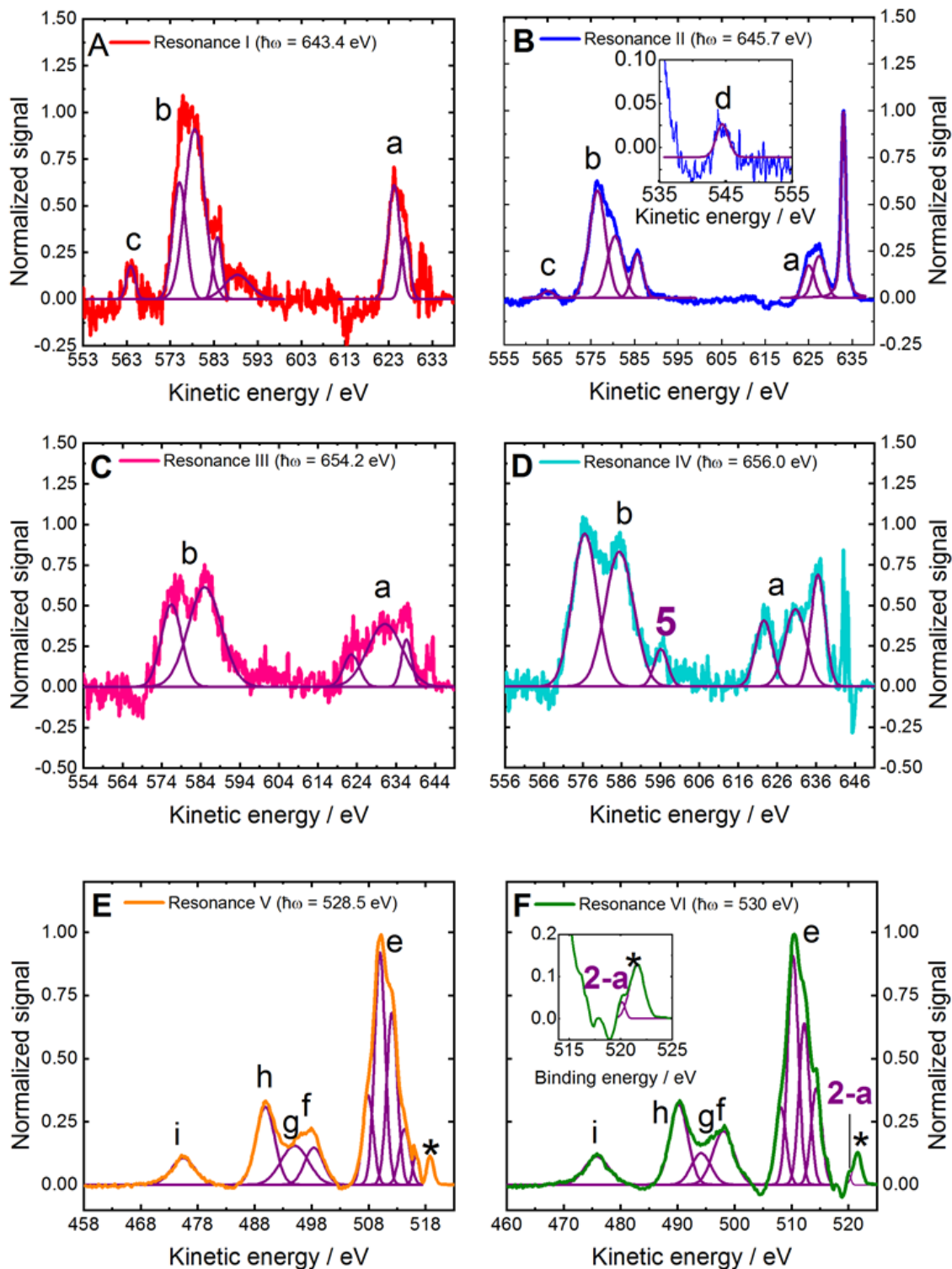
Figure AI.3

Cumulative fits corresponding to the RPES difference spectra recorded at Resonances I (panel A), II (panel B), III (panel C), IV (panel D), V (panel E), and VI (panel F). Participator Auger and spectator Auger / ICD signals are labelled and assigned in accordance with those discussed throughout Chapter 4 and are detailed in Table AI.2 below. Features labelled with an asterisk in panels E and F correspond to signals resulting from ionization with the unfiltered second harmonic of the beamline.

Table AI.2. 0.2 M NaMnO$_{4(aq.)}$ Auger and ICD signal cumulative fit results and assignments from the RPES spectra shown in Figure AI.3. FWHM$_G$ (Gaussian widths) are reported where results were extracted from cumulative Gaussian fits. FWHM$_L$ (Lorentzian widths) are additionally reported where results were extracted from cumulative Voigt profile fits.

Peak	Assignment	KE / eV	(Nominal) BE / eV	FWHM$_G$ / eV	FWHM$_L$ / eV
Resonance I					
a	L$_{III}$-V,V / L$_{III}$-5a$_1$,V	626.8 ± 0.3	16.6 ± 0.3	2.4 ± 0.4	-
		624.3 ± 0.2	19.1 ± 0.2	3.2 ± 0.3	-
5	L$_{III}$-2t$_2$2e	583.9 ± 0.1	59.5 ± 0.1	2.2 ± 0.3	-
b	L$_{III}$-2t$_2$,V	578.8 ± 0.4	64.8 ± 0.5	5.3 ± 0.8	-
		575.2 ± 0.3	68.3 ± 0.3	3.6 ± 0.4	-
c	L$_{III}$-2t$_2$,5a$_1$	566.3 ± 0.1	79.4 ± 0.1	2.3 ± 0.3	-
Resonance II					
3-a	L$_{III}$-1e5t$_2$ / L$_{III}$-3t$_2$5t$_2$	633.0 ± 0.1	12.66 ± 0.04	0.83 ± 0.04	0.77 ± 0.03
a	L$_{III}$-V,V / L$_{III}$-5a$_1$,V	627.4 ± 0.3	18.3 ± 0.3	3.3 ± 0.3	-
		625.1 ± 0.3	20.6 ± 0.3	3.0 ± 0.3	-
5	L$_{III}$-2t$_2$5t$_2$	585.6 ± 0.1	60.05 ± 0.04	3.02 ± 0.05	-
b	L$_{III}$-2t$_2$,V	580.7 ± 0.1	65.15 ± 0.08	4.2 ± 0.1	-
		576.6 ± 0.1	69.23 ± 0.05	4.45 ± 0.06	-
c	L$_{III}$-2t$_2$,5a$_1$	565.1 ± 0.1	80.6 ± 0.1	3.0 ± 0.2	-
d	L$_{III}$-4a$_1$,V	544.6 ± 0.1	101.1 ± 0.1	2.8 ± 0.2	-
Resonance III					
a	L$_{II}$-V,V	636.7 ± 0.2	17.5 ± 0.2	3.1 ± 0.4	-
	L$_{II}$-L$_{III}$,V	631.2 ± 0.4	23.0 ± 0.3	10.4 ± 0.9	-
	L$_{II}$-5a$_1$,V	622.6 ± 0.2	31.6 ± 0.2	4.8 ± 0.6	-
b	L$_{II}$-2t$_2$,V	585.0 ± 0.2	69.2 ± 0.2	10.0 ± 0.5	-
	L$_{II}$-L$_{III}$,2t$_2$ / L$_{II}$-2t$_2$, 5a$_1$	576.5 ± 0.2	77.7 ± 0.2	6.2 ± 0.4	-
Resonance IV					
a	L$_{II}$-V,V	636.5 ± 0.2	19.5 ± 0.2	4.3 ± 0.2	-
	L$_{II}$-L$_{III}$,V	630.7 ± 0.2	25.3 ± 0.2	6.4 ± 0.6	-
	L$_{II}$-5a$_1$,V	622.6 ± 0.2	33.4 ± 0.2	5.1 ± 0.3	-
5		596.1 ± 0.2	59.9 ± 0.2	4.1 ± 0.4	-
b	L$_{II}$-2t$_2$,V	585.4 ± 0.2	70.6 ± 0.2	8.6 ± 0.3	-
	L$_{II}$-L$_{III}$,2t$_2$ / L$_{II}$-2t$_2$, 5a$_1$	576.5 ± 0.2	79.5 ± 0.2	7.5 ± 0.2	-
Resonance V					
e	K-V,V	516.3 ± 0.1	12.18 ± 0.05	1.23 ± 0.09	-
		514.3 ± 0.2	14.2 ± 0.2	2.2 ± 0.4	-
		512.1 ± 0.1	16.39 ± 0.05	2.2 ± 0.2	-
		510.0 ± 0.1	18.51 ± 0.04	2.2 ± 0.1	-
		507.9 ± 0.1	20.6 ± 0.1	2.2 ± 0.1	-
f	K-5a$_1$,1b$_{1(w)}$ / K-5a$_1$,V	498.4 ± 0.4	30.1 ± 0.4	3.8 ± 0.7	-
g	K-5a$_1$,3a$_{1(w)}$ / K-5a$_1$,V	496 ± 1	33 ± 1	6 ± 3	-
h	K-5a$_1$,1b$_{2(w)}$ / K-5a$_1$,V	489.9 ± 0.1	38.6 ± 0.1	3.9 ± 0.1	-
i	K-5a$_1$,2a$_{1(w)}$ / K-5a$_1$,V	475.5 ± 0.1	53.04 ± 0.05	4.9 ± 0.1	-
Resonance VI					
2-a	K-4t$_2$,5t$_2$	520.1 ± 0.1	9.85 ± 0.08	0.7 ± 0.2	-
e	K-V,V	514.4 ± 0.1	15.6 ± 0.1	2.2 ± 0.1	-
		512.2 ± 0.1	17.8 ± 0.1	2.2 ± 0.3	-
		510.3 ± 0.1	19.73 ± 0.09	2.2 ± 0.2	-
		508.1 ± 0.2	21.9 ± 0.2	2.2 ± 0.2	-
f	K-5a1,1b1(w) / K-5a1,V	498.1 ± 0.3	31.9 ± 0.3	4.3 ± 0.3	-
g	K-5a1,3a1(w) / K-5a1,V	494.1 ± 0.3	35.9 ± 0.3	4 ± 1	-
h	K-5a1,1b2(w) / K-5a1,V	490.2 ± 0.1	39.8 ± 0.1	3.8 ± 0.1	-
i	K-5a1,2a1(w) / K-5a1,V	475.8 ± 0.1	54.19 ± 0.06	5.0 ± 0.1	-

(b) Cumulative fits to KMnO$_{4(aq.)}$ resonant spectra

Figure AI.4 shows cumulative fits to the resonant-off-resonant difference spectra recorded from 0.15 M KMnO$_{4(aq.)}$ solutions (shown in Figure AI.3 of this appendix). The fitting results and peak assignments are summarized in Table AI.3.
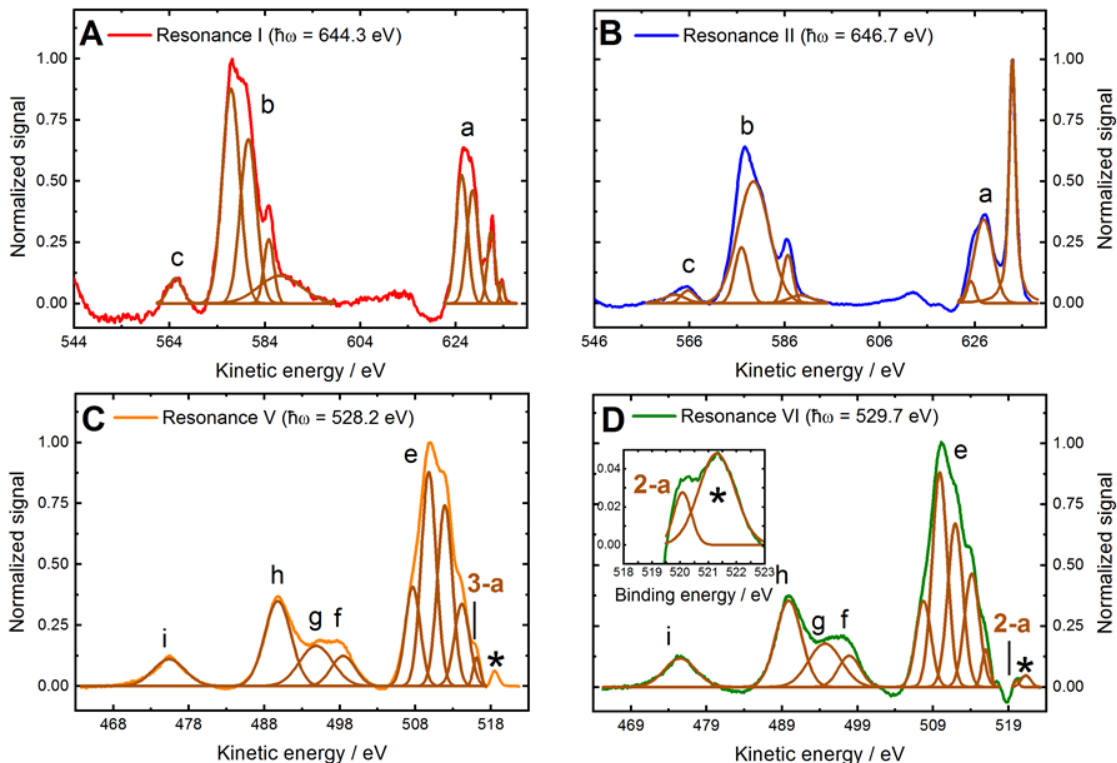
Figure AI.4

Cumulative fits corresponding to the 0.15 M KMnO$_{4(aq.)}$ solution resonant-off-resonant RPES difference spectra recorded at Resonances I (panel A), II (panel B), V (panel C) and VI (panel D). Participator Auger and spectator Auger / ICD signals are detailed in Table AI.3 below. Features labelled with an asterisk in panels C and D correspond to signals resulting from ionization with the unfiltered second harmonic of the beamline.

Participator Auger and spectator Auger / ICD signals were found to be in accordance with the assignments discussed in Section 4.2 for NaMnO$_{4(aq.)}$ solutions. Regarding peak **3-a**, a BE of 12.66 ± 0.04 eV was determined from NaMnO$_{4(aq.)}$ solutions, with a consistent BE of 12.80 ± 0.1 eV being extracted from KMnO$_{4(aq.)}$. While the Gaussian component of the width (FWHM$_G$) is equivalent between NaMnO$_{4(aq.)}$ and KMnO$_{4(aq.)}$ samples, the Lorentzian component, 1.20 ± 0.04 eV at FWHM, is slightly larger in the latter case. (The total Voigt feature FWHM was determined to be 1.64 ± 0.02 eV). This discrepancy is attributed to resonant excitation at slightly different photon energies, resulting in differing core-hole lifetime extractions, between the measurements.

For peak **2-a**, BEs of 9.85 ± 0.08 eV and 9.61 ± 0.1 eV were respectively extracted from the NaMnO$_{4(aq.)}$ and KMnO$_{4(aq.)}$ samples. The observed nominal BE difference are attributed to uncertainties associated with the photon energy calibration procedure and to a differential effect of the over-subtraction on the fit procedure used to determine the BEs. Finally, two additional BEs – 12.87 ± 0.04 eV and 10.57 ± 0.08 eV – could be extracted from the Resonance I KMnO$_{4(aq.)}$ data with

respect to similar data from NaMnO$_{4(aq.)}$ (see panels A in Figures AI.3 and AI.4, respectively). The 12.87 ± 0.04 eV BE feature corresponds to the resonantly-enhanced signal labelled peak **3-a** (similar to that observed in the Resonance II spectrum in panel B). The second extracted BE may be a signature of a L$_{III}$-6a1,2e process. A similar ~10.5 ± 0.1 eV feature was observed in some of the NaMnO$_{4(aq.)}$ Resonance I, III, and IV data sets but could not be reproducibly extracted. Hence, the latter assignment cannot be confirmed without further experimental investigation.

Table AI.3. 0.15 M KMnO$_{4(aq.)}$ Auger and ICD signals cumulative fit results and assignments from the RPES spectra shown in Figure AI.4. FWHM$_G$ (Gaussian widths) are reported where results were extracted from cumulative Gaussian fits. FWHM$_L$ (Lorentzian widths) are additionally reported where results were extracted from cumulative Voigt profile fits.

Peak	Assignment	KE / eV	Nominal BE / eV	FWHM$_G$ / eV	FWHM$_L$ / eV
Resonance I					
a	L$_{III}$-V,V / L$_{III}$-5a$_1$,V	626.8 ± 0.1	16.7 ± 0.2	2.9 ± 0.3	-
		624.4 ± 0.1	19.1 ± 0.2	2.9 ± 0.2	-
5	L$_{III}$-2t$_2$2e	584.0 ± 0.1	59.5 ± 0.1	2.5 ± 0.1	-
b	L$_{III}$-2t$_2$,V	579.7 ± 0.1	63.8 ± 0.1	4.0 ± 0.2	-
		576.1 ± 0.1	67.4 ± 0.1	4.3 ± 0.1	-
c	L$_{III}$-2t$_2$,5a$_1$	564.4 ± 0.1	79.1 ± 0.1	3.5 ± 0.2	-
Resonance II					
3-a	L$_{III}$-1e,5t$_2$ / L$_{III}$-3t$_2$,5t$_2$	633.0 ± 0.1	12.8 ± 0.1	0.83 ± 0.05	1.20 ± 0.04
a	L$_{III}$-V,V / L$_{III}$-5a$_1$,V	627.0 ± 0.1	18.8 ± 0.1	4.7 ± 0.2	-
		624.3 ± 0.1	21.5 ± 0.1	2.0 ± 0.3	-
5	L$_{III}$-2t$_2$5t$_2$	585.8 ± 0.1	60.0 ± 0.1	2.52 ± 0.07	-
b	L$_{III}$-2t$_2$,V	578.6 ± 0.1	67.2 ± 0.1	7.81 ± 0.05	-
		576.1 ± 0.1	69.8 ± 0.1	3.39 ± 0.06	-
c	L$_{III}$-2t$_2$,5a$_1$	564.8 ± 0.1	81.0 ± 0.2	3.5 ± 0.5	-
Resonance V					
e	K-V,V	516.1 ± 0.2	12.1 ± 0.1	1.06 ± 0.05	-
		514.2 ± 0.2	14.0 ± 0.2	2.3 ± 0.2	-
		511.9 ± 0.2	16.3 ± 0.1	2.3 ± 0.2	-
		509.8 ± 0.1	18.4 ± 0.1	2.3 ± 0.1	-
		507.7 ± 0.1	20.6 ± 0.1	2.34 ± 0.07	-
f	K-5a$_1$,1b$_{1(w)}$ / K-5a$_1$,V	498.5 ± 0.2	29.7 ± 0.2	3.7 ± 0.2	-
g	K-5a$_1$,3a$_{1(w)}$ / K-5a$_1$,V	494.9 ± 0.3	33.3 ± 0.3	5.2 ± 0.8	-
h	K-5a$_1$,1b$_{2(w)}$ / K-5a$_1$,V	489.8 ± 0.2	38.4 ± 0.1	4.13 ± 0.06	-
i	K-5a$_1$,2a$_{1(w)}$ / K-5a$_1$,V	475.4 ± 0.2	52.8 ± 0.1	4.97 ± 0.06	-
Resonance VI					
2-a	K-4t$_2$,5t$_2$	520.1 ± 0.2	9.6 ± 0.1	0.73 ± 0.03	-
e	K-V,V	516.0 ± 0.2	13.7 ± 0.1	1.20 ± 0.08	-
		514.1 ± 0.2	15.6 ± 0.2	2.4 ± 0.3	-
		512.0 ± 0.2	17.8 ± 0.1	2.4 ± 0.4	-
		509.9 ± 0.2	19.8 ± 0.2	2.4 ± 0.2	-
		507.7 ± 0.2	22.0 ± 0.2	2.4 ± 0.1	-
f	K-5a$_1$,1b$_{1(w)}$ / K-5a$_1$,V	497.7 ± 0.2	31.8 ± 0.2	3.4 ± 0.4	-
g	K-5a$_1$,3a$_{1(w)}$ / K-5a$_1$,V	494.7 ± 0.4	35.0 ± 0.4	5 ± 1	-
h	K-5a$_1$,1b$_{2(w)}$ / K-5a$_1$,V	489.9 ± 0.2	39.8 ± 0.1	4 ± 1	-
i	K-5a$_1$,2a$_{1(w)}$ / K-5a$_1$,V	475.5 ± 0.2	54.2 ± 0.1	4.9 ± 0.3	-

Appendix II

This appendix presents the complementary content referred to in Chapter 5, addressing the following points: (**1**) Analysis of the $MnO_4^{2-}_{(aq.)}$ PEY-XAS spectra; (**2**) Multi-peak fitting analysis and results of the $MnO_4^{2-}_{(aq.)}$ RPES data processing.

1. Analysis of the $MnO_4^{2-}_{(aq.)}$ PEY-XAS spectra

Figure AII.1 shows Mn $L_{II,III}$-pre-edge and O K-pre-edge PEY-XAS spectra produced from the RPES data recorded from the ~0.2 M $MnO_4^{2-}_{(aq.)}$ in 0.3 M $NaOH_{(aq.)}$ solutions described in **Section 5.2**. The photon energy scale was calibrated as described in Section 3.4.2.
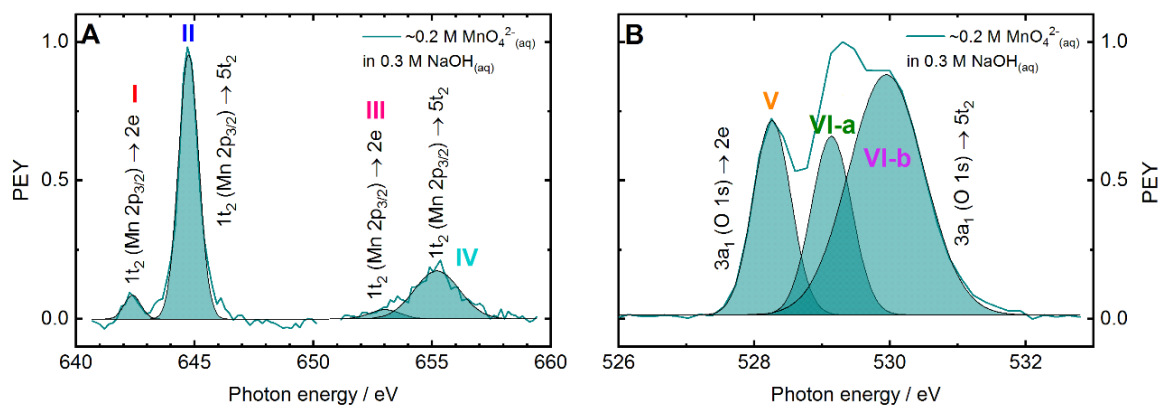
Figure AII.1

(A) Baseline-corrected Mn L_{III}- (640 – 650 eV photon energy range) and L_{II}- (652 – 660 eV photon energy range) pre-edge PEY-XAS spectra, including the cumulative Gaussian fits used to determine the 1t$_2$ (Mn 2p$_{3/2}$) → 2e, 1t$_2$ (Mn 2p$_{3/2}$) → 5t$_2$, 1t$_2$ (Mn 2p$_{1/2}$) → 2e, and 1t$_2$ (Mn 2p$_{1/2}$) → 5t$_2$ resonant photon energies. **(B)** O K-pre-edge PEY-XAS spectrum and cumulative Gaussian fits used to determine the 3a$_1$ (O 1s) → 2e and 3a$_1$ → 5t$_2$ resonant photon energies.

2. Multi-peak fitting analysis and results of the $MnO_4^{2-}_{(aq.)}$ RPES data

Figure AII.2 shows cumulative fits to the resonant-off-resonant difference spectra recorded from ~0.2 M $MnO_4^{2-}_{(aq.)}$ in 0.3 M $NaOH_{(aq.)}$ solutions associated with the data presented in Figures 5.5, 5.6 and 5.8. The results obtained from these fits were used to report the KEs presented in **Section 5.2**. The fit results and peak assignments are summarized in Table AII.1.
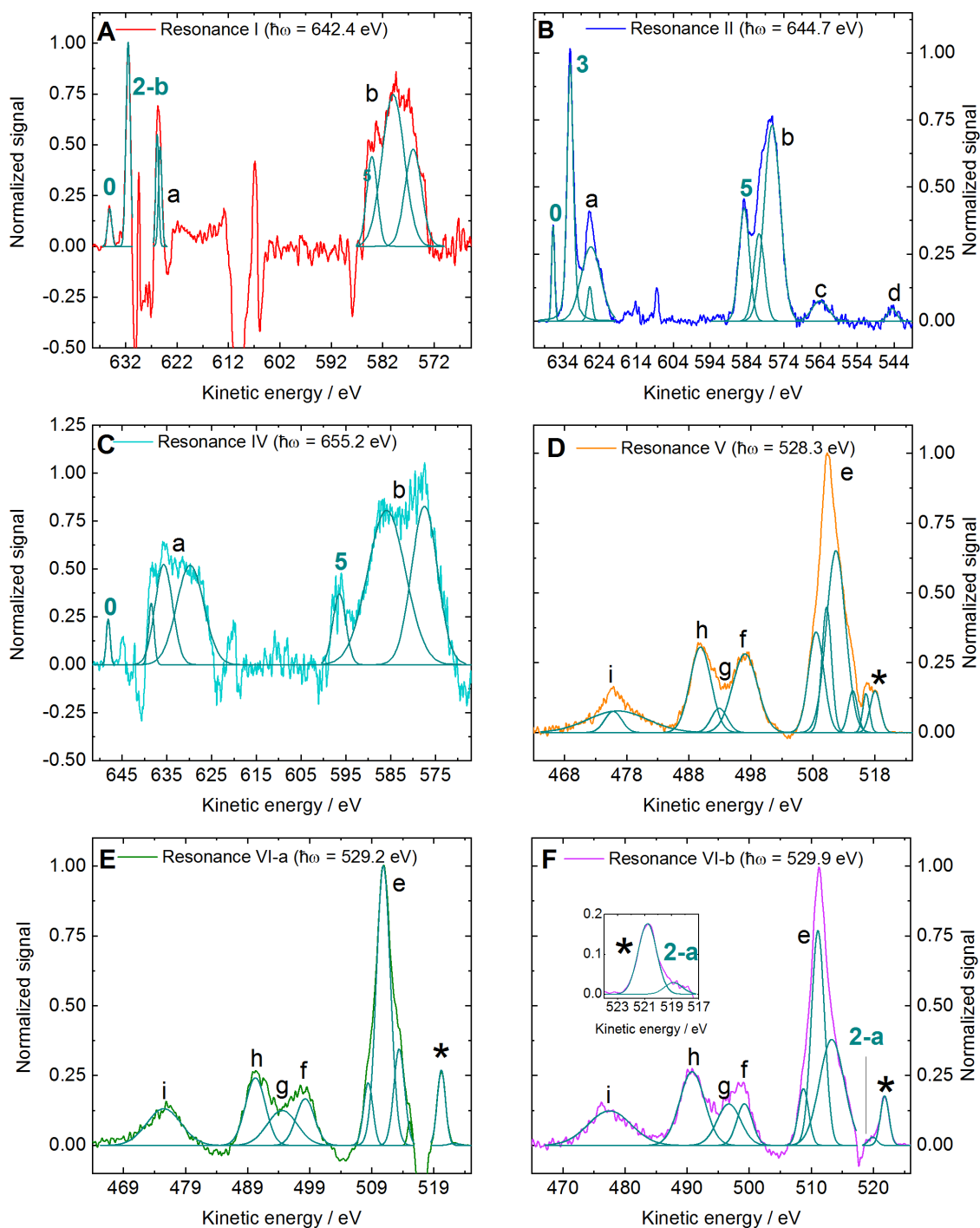
Figure AII.2

Cumulative fits to the 0.2 M MnO$_4^{2-}$$_{(aq.)}$ in 0.3 M OH$^-$$_{(aq.)}$ resonant-off-resonant difference spectra recorded at Resonances I (panel A), II (panel B), IV (panel C), V (panel D), VI-a (panel E) and VI-b (panel F). Participator Auger and spectator Auger / ICD signals are labelled and assigned in accordance with those discussed throughout Chapter 5 and detailed in Table AII.1 below. Features labelled with an asterisk in panels D, E and F correspond to signals resulting from ionization with the unfiltered second harmonic of the beamline.

Table AII.1. ~0.2 M $MnO_4^{2-}{}_{(aq.)}$ in 0.3 M $OH^-{}_{(aq.)}$ Auger and ICD signals cumulative fit results and assignments from the RPES spectra shown in Figure AII.2. $FWHM_G$ (Gaussian widths) are reported where results were extracted from cumulative Gaussian fits. $FWHM_L$ (Lorentzian widths) are additionally reported where results were extracted from cumulative Voigt profile fits.

Peak	Assignment	KE / eV	(Nominal) BE / eV	$FWHM_G$ / eV	$FWHM_L$ / eV
Resonance I					
0	L_{III}-2e,2e	635.5 ± 0.1	6.91 ± 0.04	1.0 ± 0.1	-
a	L_{II}-V,V	626.2 ± 0.1	16.2 ± 0.1	0.7 ± 0.1	-
		625.7 ± 0.2	16.7 ± 0.2	0.8 ± 0.2	-
5	L_{III}-2t$_2$,2e	584.5 ± 0.1	57.91 ± 0.08	2.4 ± 0.2	-
b	L_{III}-2t$_2$,V	580.4 ± 0.3	62.0 ± 0.3	5 ± 1	-
		576.4 ± 0.4	66.0 ± 0.4	3.8 ± 0.4	-
Resonance II					
0	L_{III}-2e,5t$_2$	637.6 ± 0.1	7.06 ± 0.04	0.97 ± 0.02	-
3	L_{III}-1e5t$_2$ / L_{III}-3t$_2$5t$_2$	633.0 ± 0.1	11.70 ± 0.04	1.58 ± 0.04	0.66 ± 0.06
a	L_{III}-V,V	627.7 ± 0.1	17.03 ± 0.05	1.5 ± 0.1	1E-23
		627.4 ± 0.1	17.33 ± 0.04	6.3 ± 0.1	1E-19
5	L_{III}-2t$_2$,5t$_2$	585.7 ± 0.1	58.97 ± 0.07	3.36 ± 0.05	-
b	L_{III}-2t$_2$,V	581.7 ± 0.1	63.05 ± 0.05	3.5 ± 0.1	-
		578.1 ± 0.2	66.6 ± 0.2	5.16 ± 0.08	-
c	L_{III}-2t$_2$,5a$_1$	565.1 ± 0.1	79.62 ± 0.07	5.2 ± 0.2	-
d	L_{III}-4a$_1$,V	545.5 ± 0.1	99.24 ± 0.08	2.8 ± 0.2	-
Resonance IV					
0	L_{II}-2e,5t$_2$	648.1 ± 0.1	7.10 ± 0.04	1.02 ± 0.02	-
a	L_{II}-V,V	638.5 ± 0.1	16.72 ± 0.04	1.4 ± 0.1	-
	L_{II}-L_{III},V	635.7 ± 0.1	19.53 ± 0.08	4.6 ± 0.3	-
	L_{II}-5a$_1$,V	629.8 ± 0.2	25.4 ± 0.2	7.1 ± 03	-
5	L_{II}-2t$_2$,5t$_2$	596.4 ± 0.1	58.76 ± 0.06	3.4 ± 0.1	-
b	L_{II}-2t$_2$,V	585.9 ± 0.1	69.1 ± 0.1	10.0 ± 0.3	-
	L_{II}-L_{III},2t$_2$ / L_{II}-2t$_2$, 5a$_1$	577.4 ± 0.1	77.79 ± 0.09	6.8 ± 0.2	-
Resonance V					
e	K-V,V	514.9 ± 0.1	13.40 ± 0.07	1.7 ± 0.3	-
		512.2 ± 0.6	16.1 ± 0.6	4 ± 1	-
		510.7 ± 0.1	17.62 ± 0.04	1.8 ± 0.2	-
		509.0 ± 0.4	19.3 ± 0.4	2.9 ± 0.2	-
f	K-5a1,1b1(w) / K-5a1,V	497.5 ± 0.1	30.76 ± 0.04	4.68 ± 0.05	-
g	K-5a1,3a1(w) / K-5a1,V	493.4 ± 0.1	34.91 ± 0.1	3.0 ± 0.2	-
h	K-5a1,1b2(w) / K-5a1,V	490.4 ± 0.1	37.93 ± 0.06	3.97 ± 0.08	-
i	K-5a1,2a1(w) / K-5a1,V	476.3 ± 0.1	51.99 ± 0.04	3.2 ± 0.1	-
Resonance VI-a					
e	K-V,V	515.2 ± 0.1	14.06 ± 0.06	0.7 ± 0.2	-
		513.6 ± 0.1	15.7 ± 0.1	2.0 ± 0.2	-
		511.0 ± 0.1	18.23 ± 0.04	2.6 ± 0.2	-
		508.5 ± 0.1	20.7 ± 0.1	1.8 ± 0.2	-
f	K-5a1,1b1(w) / K-5a1,V	498.4 ± 0.5	30.8 ± 0.5	3 ± 1	-
g	K-5a1,3a1(w) / K-5a1,V	495 ± 1	35 ± 1	6 ± 10	-
h	K-5a1,1b2(w) / K-5a1,V	490.4 ± 0.4	38.8 ± 0.4	3.8 ± 0.5	-
i	K-5a1,2a1(w) / K-5a1,V	475.6 ± 0.1	53.6 ± 0.1	6.5 ± 0.2	-
Resonance VI-b					
2-a	K-4t$_2$,5t$_2$	519.6 ± 0.2	10.2 ± 0.2	1.6 ± 0.4	-
e	K-V,V	513.0 ± 0.3	16.8 ± 0.3	4.7 ± 0.4	-
		510.8 ± 0.1	19.03 ± 0.04	2.5 ± 0.1	-
		508.5 ± 0.1	21.4 ± 0.1	1.9 ± 0.1	-
f	K-5a$_1$,1b$_{1(w)}$ / K-5a$_1$,V	498.9 ± 0.3	30.9 ± 0.3	2.9 ± 0.7	-
g	K-5a$_1$,3a$_{1(w)}$ / K-5a$_1$,V	497 ± 1	33 ± 1	4 ± 2	-
h	K-5a$_1$,1b$_{2(w)}$ / K-5a$_1$,V	490.5 ± 0.1	39.3 ± 0.1	4.7 ± 0.2	-
i	K-5a$_1$,2a$_{1(w)}$ / K-5a$_1$,V	477.2 ± 0.1	52.6 ± 0.1	8.2 ± 0.2	-

References

1. Kennepohl, P. and E.I. Solomon, *Electronic Structure Contributions to Electron-Transfer Reactivity in Iron−Sulfur Active Sites: 1. Photoelectron Spectroscopic Determination of Electronic Relaxation.* Inorganic Chemistry, 2003. **42**(3): p. 679-688.

2. Kirchhoff, H., *Structure-Function Relationships in Photosynthetic Membranes: Challenges and Emerging Fields.* Plant Sci, 2018. **266**: p. 76-82.

3. Tundo, P., et al., *Synthetic Pathways and Processes in Green Chemistry. Introductory Overview.* Pure and Applied Chemistry, 2000. **72**(7): p. 1207-1228.

4. Li, X., et al., *Microenvironment Modulation of Single-Atom Catalysts and Their Roles in Electrochemical Energy Conversion.* Science Advances, 2020. **6**(39): p. eabb6833.

5. Tian, H., Boschloo, G., Hagfeldt, A., *Molecular Devices for Solar Energy Conversion and Storage*. Green Chemistry and Sustainable Technology. 2018, Singapore: Springer.

6. Björn, L.O., *The Nature of Light and Its Interaction with Matter*, in *Photobiology: The Science of Life and Light*, L.O. Björn, Editor. 2008, Springer New York: New York, NY. p. 1-39.

7. Nan, Z., et al., *Exploring Structure-function Relationship of Two-dimensional Electrocatalysts with Synchrotron Radiation X-ray Absorption Spectrum.* Current Chinese Science, 2020. **1**: p. 1-22.

8. Seidel, R., B. Winter, and S.E. Bradforth, *Valence Electronic Structure of Aqueous Solutions: Insights from Photoelectron Spectroscopy.* Annual Review of Physical Chemistry, 2016. **67**(1): p. 283-305.

9. Jinich, A., et al., *Quantum Chemistry Reveals Thermodynamic Principles of Redox Biochemistry.* PLOS Computational Biology, 2018. **14**(10): p. e1006471.

10. Krylov, A.I., *From Orbitals to Observables and Back.* The Journal of Chemical Physics, 2020. **153**(8): p. 080901.

11. Schärtl, W., *Statistical Thermodynamics and Spectroscopy: How Classical Thermodynamics Relates to Quantum Chemistry*. First ed. 2015: 2015 Wolfgang Schärtl & bookboon.com.

12. Bronowska, A.K., *Thermodynamics of Ligand-Protein Interactions: Implications for Molecular Design*, in *Thermodynamics - Interaction Studies - Solids, Liquids, and Gases*, J.C. Moreno-Pirajan, Editor. 2011, IntechOpen.

13. Abriata, L.A., et al., *Alternative Ground States Enable Pathway Switching in Biological Electron Transfer.* Proceedings of the National Academy of Sciences, 2012. **109**(43): p. 17348.

14. Zakem, E.J., M.F. Polz, and M.J. Follows, *Redox-Informed Models of Global Biogeochemical Cycles.* Nature Communications, 2020. **11**(1): p. 5680.

15. R. Chen, S.K., Z. Chang, *Redox Flow Batteries: Fundamentals and Applications*. 2017, CRC Press Taylor & Francis Group.

16. Crisenza, G.E.M. and P. Melchiorre, *Chemistry Glows Green with Photoredox Catalysis.* Nature Communications, 2020. **11**(1): p. 803.

17. Adriaanse, C., et al., *Aqueous Redox Chemistry and the Electronic Band Structure of Liquid Water.* The Journal of Physical Chemistry Letters, 2012. **3**(23): p. 3411-3415.

18. Yamazaki, T., H. Sato, and F. Hirata, *A Quantum Solute–Solvent Interaction Using Spectral Representation Technique applied to the Electronic Structure Theory in Solution.* The Journal of Chemical Physics, 2003. **119**(13): p. 6663-6670.

19. Marcus, R.A., *Electron transfer reactions in chemistry. Theory and experiment.* Reviews of Modern Physics, 1993. **65**(3): p. 599-610.

20. Marcus, Y., *Effect of Ions on the Structure of Water: Structure Making and Breaking.* Chemical Reviews, 2009. **109**(3): p. 1346-1370.

21. Winter, B. and M. Faubel, *Photoemission from Liquid Aqueous Solutions.* Chemical Reviews, 2006. **106**(4): p. 1176-1211.

22. Seidel, R., S. Thürmer, and B. Winter, *Photoelectron Spectroscopy Meets Aqueous Solution: Studies from a Vacuum Liquid Microjet.* The Journal of Physical Chemistry Letters, 2011. **2**(6): p. 633-641.

23. Armstrong, F.A., *Why did Nature Choose Manganese to Make Oxygen?* Philosophical Transactions of the Royal Society B: Biological Sciences, 2008. **363**(1494): p. 1263-1270.

24. Pan, F. and Q. Wang, *Redox Species of Redox Flow Batteries: A Review.* Molecules (Basel, Switzerland), 2015. **20**(11): p. 20499-20517.

25. Yam, V.W.-W., A.K.-W. Chan, and E.Y.-H. Hong, *Charge-Transfer Processes in Metal Complexes Enable Luminescence and Memory Functions.* Nature Reviews Chemistry, 2020. **4**(10): p. 528-541.

26. Dursch, T.J., *Transition-Metal Complexes: Simple(r) Solutions to Complex Chemistry.* Trends in Chemistry, 2019. **1**(5): p. 455-456.

27. Vol'pin, M.E., et al., *Transition Metal Complexes as Catalysts in Biochemical Systems. Interaction with Electron Transfer Processes.* Inorganica Chimica Acta, 1981. **50**: p. 21-31.

28. P. W. Atkins, T.L.O., J.P. Rourke, M. T. Weller and F. A. Armstrong, *Shriver and Atkins' Inorganic Chemistry*. Fifth Edition ed. 2010, Great Britain: Oxxford University Press.

29. Zhang, H.-C., et al., *Synergistic Effect of Permanganate and in Situ Synthesized Hydrated Manganese Oxide for Removing Antibiotic Resistance Genes from Wastewater Treatment Plant Effluent.* Environmental Science & Technology, 2019. **53**(22): p. 13374-13381.

30. van Hulten, M., et al., *Manganese in the World Ocean: a First Global Model.* Biogeosciences Discussions, 2016: p. 1-38.

31. Cannon, W.F., B.E. Kimball, and L.A. Corathers, *Manganese*. Professional Paper 1802-L, ed. K.J. Schulz, et al. 2017: U. S. Geological Survey.

32. Post, J.E., *Manganese oxide minerals: Crystal structures and economic and environmental significance.* Proceedings of the National Academy of Sciences, 1999. **96**(7): p. 3447.

33. Shule, L., et al., *Risk Identification and Evaluation of the Long-term Supply of Manganese Mines in China Based on the VW-BGR Method.* Sustainability, 2019. **11**: p. 2683.

34. Bal, B., S. Ghosh, and A.P. Das, *Microbial Recovery and Recycling of Manganese Waste and Their Future Application: a Review.* Geomicrobiology Journal, 2019. **36**(1): p. 85-96.

35. Rothwell, R.G., *Micronodules (Fe-Mn Oxides and Hydroxides)*, in *Minerals and Mineraloids in Marine Sediments: An Optical Identification Guide*, R.G. Rothwell, Editor. 1989, Springer Netherlands: Dordrecht. p. 151-155.

36. Boytsova, O., T. Shekunova, and A. Baranchikov, *Nanocrystalline Manganese Dioxide Synthesis by Microwave-Hydrothermal Treatment.* Russian Journal of Inorganic Chemistry, 2015. **60**: p. 546-551.

37. Zhao, Y., Y. Zhu, and X. Zhang, *Challenges and perspectives for manganese-based oxides for advanced aqueous zinc-ion batteries.* InfoMat, 2020. **2**(2): p. 237-260.

38. Glauber, J.R., 1691. **Prosperitas Germanice**.

39. Singh, N. and D.G. Lee, *Permanganate: A Green and Versatile Industrial Oxidant.* Organic Process Research & Development, 2001. **5**(6): p. 599-603.

40. Colli, A.N., P. Peljo, and H.H. Girault, *High Energy Density MnO_4^-/MnO_4^{2-} Redox Couple for Alkaline Redox Flow Batteries.* Chemical Communications, 2016. **52**(97): p. 14039-14042.

41. Xue, F.-Q., et al., *Investigation on the Electrode Process of the Mn(II)/Mn(III) Couple in Redox Flow Battery.* Electrochimica Acta, 2008. **53**(22): p. 6636-6642.

42. Николайчук, П., *The potential - pH diagram for Mn - H2O system.* 2015.

43. Shaabani, A., et al., *Green oxidations. The Use of Potassium Permanganate Supported on Manganese Dioxide.* Tetrahedron, 2004. **60**(50): p. 11415-11420.

44. Roderick, M.S., et al., *Chemiluminescence Evidence Supporting the Selective Role of Ligands in the Permanganate Oxidation of Micropollutants.* The Journal of Physical Chemistry A, 2013. **117**(40): p. 10286-10293.

45. Adcock, J.L., et al., *Advances in the Use of Acidic Potassium Permanganate as a Chemiluminescence Reagent: A Review.* Analytica Chimica Acta, 2014. **807**: p. 9-28.

46. Chang, Y., Y. Bai, and J. Qu, *Does KMnO4 Preoxidation Reduce the Genotoxicity of Disinfection By-Products?* Chemosphere, 2016. **163**: p. 73-80.

47. Liu, B., et al., *Microcystis aeruginosa-laden water treatment using enhanced coagulation by persulfate/Fe(II), ozone and permanganate: Comparison of the simultaneous and successive oxidant dosing strategy.* Water Research, 2017. **125**: p. 72-80.

48. Xie, P., et al., *Comparison of Permanganate Preoxidation and Preozonation on Algae Containing Water: Cell Integrity, Characteristics, and Chlorinated Disinfection Byproduct Formation.* Environmental Science & Technology, 2013. **47**(24): p. 14051-14061.

49. You, S., et al., *A Microbial Fuel Cell Using Permanganate as the Cathodic Electron Acceptor.* Journal of Power Sources, 2006. **162**(2): p. 1409-1415.

50. Ellis, R., et al., *Development of Manganese(VI) Oxidising Agents Soluble in Organic Solvents.* Synlett, 2012. **23**(09): p. 1371-1373.

51. Vepřek-šiška, J. and V. Ettel, *The Mechanism of the Decomposition of Alkaline Permanganate Solutions.* Journal of Inorganic and Nuclear Chemistry, 1969. **31**(3): p. 789-798.

52. Simándi, L. and É. Záhonyi-Budó, *Relative Reactivities of Hydroxy Compounds with Short-Lived Manganese(V).* Inorganica Chimica Acta, 1998. **281**(2): p. 235-238.

53. Jáky, M., Z. Szeverényi, and L.I. Simándi, *Formation of manganate(V) in oxidations by permanganate ion in strongly alkaline solutions.* Inorganica Chimica Acta, 1991. **186**(1): p. 33-37.

54. Duke, F.R., *The Disproportionation of Manganate Ion. Managanese Dioxide as Heterogeneous Catalyst.* The Journal of Physical Chemistry, 1952. **56**(7): p. 882-884.

55. Pode, J.S.F. and W.A. Waters, *144. Stages in oxidations of organic compounds by potassium permanganate. Part VII. Characteristic features of oxidations involving the manganate, MnO_4^{2-}, and hypomanganate, MnO_4^{3-}, anions.* Journal of the Chemical Society (Resumed), 1956(0): p. 717-725.

56. Ahmed, G.A., A. Fawzy, and R.M. Hassan, *Spectrophotometric Evidence for the Formation of Short-Lived Hypomanganate(V) and Manganate(VI) Transient Species During the Oxidation of K-Carrageenan by Alkaline Permanganate.* Carbohydrate Research, 2007. **342**(10): p. 1382-1386.

57. Lee, D.G. and T. Chen, *Reduction of manganate(VI) by mandelic acid and its significance for development of a general mechanism of oxidation of organic compounds by high-valent transition metal oxides.* Journal of the American Chemical Society, 1993. **115**(24): p. 11231-11236.

58. Chang, H.-S., G.V. Korshin, and J.F. Ferguson, *Investigation of Mechanisms of Oxidation of EDTA and NTA by Permanganate at High pH.* Environmental Science & Technology, 2006. **40**(16): p. 5089-5094.

59. Nordling, C., E. Sokolowski, and K. Siegbahn, *Precision Method for Obtaining Absolute Values of Atomic Binding Energies.* Physical Review, 1957. **105**(5): p. 1676-1677.

60. Siegbahn, K., *ESCA Applied to Free Molecules*. 1970: North-Holland Pub. Co.

61. Siegbahn, K. and K.V.-s.i. Uppsala, *ESCA; Atomic, Molecular and Solid State Structure Studied by Means of Electron Spectroscopy*. 1967: Almqvist & Wiksells.

62. Hüfner, S., *Photoelectron spectroscopy: principles and applications*. 3rd ed. 2003: Springer.

63. Reinert, F. and S. Hüfner, *Photoemission Spectroscopy—from Early Days to Recent Applications.* New Journal of Physics, 2005. **7**: p. 97-97.

64. Fadley, C.S., *X-Ray Photoelectron Spectroscopy: From Origins to Future Directions.* Nuclear Instruments and Methods in Physics Research Section A: Accelerators, Spectrometers, Detectors and Associated Equipment, 2009. **601**(1): p. 8-31.

65. Greczynski, G. and L. Hultman, *X-ray photoelectron spectroscopy: Towards reliable binding energy referencing.* Progress in Materials Science, 2020. **107**: p. 100591.

66. Faubel, M., B. Steiner, and J.P. Toennies, *Photoelectron Spectroscopy of Liquid Water, Some Alcohols, and Pure Nonane in Free Micro Jets.* The Journal of Chemical Physics, 1997. **106**(22): p. 9013-9031.

67. Weber, R., *Photoelectron Spectroscopy of Liquid Water and Aqueous Solutions in Free Microjets Using Synchrotron Radiation*, in *PhD thesis, Department of Physics*. 2003, Freie Universität Berlin.

68. Siegbahn, H. and K. Siegbahn, *ESCA Applied to Liquids.* Journal of Electron Spectroscopy and Related Phenomena, 1973. **2**(3): p. 319-325.

69. Faubel, M., S. Schlemmer, and J.P. Toennies, *A Molecular Beam Study of the Evaporation of Water from a Liquid Jet.* Zeitschrift für Physik D Atoms, Molecules and Clusters, 1988. **10**(2): p. 269-277.

70. Watanabe, I., J.B. Flanagan, and P. Delahay, *Vacuum Ultraviolet Photoelectron Emission Spectroscopy of Water and Aqueous Solutions.* The Journal of Chemical Physics, 1980. **73**(5): p. 2057-2062.

71. Faubel, M., *Photoelectron Spectroscopy at Liquid Surfaces*, in *Photoionization and Photodetachment*. 1994, Springer, Boston, MA. p. 634-690.

72. Winter, B., *Liquid Microjet for Photoelectron Spectroscopy.* Nuclear Instruments and Methods in Physics Research Section A: Accelerators, Spectrometers, Detectors and Associated Equipment, 2009. **601**(1): p. 139-150.

73. Ottosson, N., et al., *Photoelectron spectroscopy of liquid water and aqueous solution: Electron effective attenuation lengths and emission-angle anisotropy.* Journal of Electron Spectroscopy and Related Phenomena, 2010. **177**(2-3): p. 60-70.

74. Suzuki, Y.-I., et al., *Effective attenuation length of an electron in liquid water between 10 and 600 eV.* Physical Review E, 2014. **90**(1): p. 010302.

75. Aziz, E.F., et al., *Interaction Between Liquid Water and Hydroxide Revealed by Core-Hole De-Excitation.* Nature, 2008. **455**(7209): p. 89-91.

76. Ali, H., et al., *Molecular species forming at the α-Fe2O3 nanoparticle–aqueous solution interface.* Chemical Science, 2018. **9**(19): p. 4511-4523.

77. Giacomo, F.D., *Introduction to Marcus Theory of Electron Transfer Reactions*. 2020: World Scientific Publishing Co. Pte. Ltd.

78. Kubin, M., et al., *Probing the oxidation state of transition metal complexes: a case study on how charge and spin densities determine Mn L-edge X-ray absorption energies.* Chemical Science, 2018. **9**(33): p. 6813-6829.

79. Aullón, G. and S. Alvarez, *Oxidation States, Atomic Charges and Orbital Populations in Transition Metal Complexes.* Theoretical Chemistry Accounts, 2009. **123**(1): p. 67-73.

80. Orr-Ewing, A.J., *Taking the plunge: chemical reaction dynamics in liquids.* Chemical Society Reviews, 2017. **46**(24): p. 7597-7614.

81. Jiao, Y., et al., *Ultrafast X-ray absorption study of longitudinal–transverse phonon coupling in electrolyte aqueous solution.* Physical Chemistry Chemical Physics, 2017. **19**(40): p. 27266-27274.

82. Nalewajski, R., *Electronic Structure and Chemical Reactivity.* Advances in Quantum Chemistry, 2003.

83.   Moens, J., et al., *Energy Levels and Redox Properties of Aqueous Mn²⁺/³⁺ from Photoemission Spectroscopy and Density Functional Molecular Dynamics Simulation.* The Journal of Physical Chemistry B, 2010. **114**(28): p. 9173-9182.

84.   Wernet, P., *Electronic Structure in Real Time: Mapping Valence Electron Rearrangements during Chemical Reactions.* Physical Chemistry Chemical Physics, 2011. **13**(38): p. 16941-16954.

85.   Tateyama, Y., et al., *Density-Functional Molecular-Dynamics Study of the Redox Reactions of Two Anionic, Aqueous Transition-Metal Complexes.* The Journal of Chemical Physics, 2005. **122**(23): p. 234505.

86.   Delahay, P., *Correlation between thermal electron transfer in solution and photoelectron emission.* Chemical Physics Letters, 1982. **87**(6): p. 607-611.

87.   R., S., *Electronic-structure interactions in aqueous solutions: a liquid-jet photoelectron-spectroscopy study.* PhD Thesis, Faculty of Mathematics and Natural Sciences II, 2011.

88.   Zhang, J., et al., *Design and Scaling Up of Microchemical Systems: A Review.* Annual Review of Chemical and Biomolecular Engineering, 2017. **8**(1): p. 285-305.

89.   Modestino, M.A., et al., *The potential for microfluidics in electrochemical energy systems.* Energy & Environmental Science, 2016. **9**(11): p. 3381-3391.

90.   Lee, C.-Y., et al., *Passive mixers in microfluidic systems: A review.* Chemical Engineering Journal, 2016. **288**: p. 146-160.

91.   H. Eyring, J.W., G. E. Kimball, *Quantum Chemistry.* 1944: John Wiley & Sons, Inc.

92.   Winter, B., et al., *Full Valence Band Photoemission from Liquid Water Using EUV Synchrotron Radiation.* The Journal of Physical Chemistry A, 2004. **108**(14): p. 2625-2632.

93.   Banna, M.S., et al., *The Photoelectron Spectrum of Water in the 30 to 140 eV Photon Energy Range.* The Journal of Chemical Physics, 1986. **84**(9): p. 4739-4744.

94.   Kurahashi, N., et al., *Photoelectron spectroscopy of aqueous solutions: Streaming potentials of NaX (X = Cl, Br, and I) solutions and electron binding energies of liquid water and X⁻.* The Journal of Chemical Physics, 2014. **140**(17): p. 174506.

95.   Pohl, M.N., et al., *Do water's electrons care about electrolytes?* Chemical Science, 2019. **10**(3): p. 848-865.

96.   Kathmann, S.M., I.F.W. Kuo, and C.J. Mundy, *Electronic Effects on the Surface Potential at the Vapor−Liquid Interface of Water.* Journal of the American Chemical Society, 2008. **130**(49): p. 16556-16561.

97.   Gerig, J.T., *Solute−Solvent Interactions Probed by Intermolecular NOEs.* The Journal of Organic Chemistry, 2003. **68**(13): p. 5244-5248.

98.   Mennucci, B., J.M. Martínez, and J. Tomasi, *Solvent Effects on Nuclear Shieldings: Continuum or Discrete Solvation Models To Treat Hydrogen Bond and Polarity Effects?* The Journal of Physical Chemistry A, 2001. **105**(30): p. 7287-7296.

99.   Hindman, J.C., *Nuclear Magnetic Resonance Effects in Aqueous Solutions of 1–1 Electrolytes.* The Journal of Chemical Physics, 1962. **36**(4): p. 1000-1016.

100.   Yepes, D., et al., *Photoemission Spectra and Density Functional Theory Calculations of 3d Transition Metal–Aqua Complexes (Ti–Cu) in Aqueous Solution.* The Journal of Physical Chemistry B, 2014. **118**(24): p. 6850-6863.

101.   Pham, T., et al., *Electronic structure of aqueous solutions: Bridging the gap between theory and experiments.* Science Advances, 2017. **3**: p. e1603210.

102.   Barth, S., et al., *Valence Ionization of Water Clusters: From Isolated Molecules to Bulk.* The Journal of Physical Chemistry A, 2009. **113**(48): p. 13519-13527.

103.   Hunt, P., M. Sprik, and R. Vuilleumier, *Thermal versus electronic broadening in the density of states of liquid water.* Chemical Physics Letters, 2003. **376**(1): p. 68-74.

104.   Jose, L., M. Seth, and T. Ziegler, *Molecular and Vibrational Structure of Tetroxo d⁰ Metal Complexes in their Excited States. A Study Based on Time-Dependent Density Functional Calculations and Franck–Condon Theory.* The Journal of Physical Chemistry A, 2012. **116**(7): p. 1864-1876.

105.   Sharma, P., D.G. Truhlar, and L. Gagliardi, *Multiconfiguration Pair-Density Functional Theory Investigation of the Electronic Spectrum of MnO_4^-.* The Journal of Chemical Physics, 2018. **148**(12): p. 124305.

106.   Schmidt, M.W., E.A. Hull, and T.L. Windus, *Valence Virtual Orbitals: An Unambiguous ab Initio Quantification of the LUMO Concept.* The Journal of Physical Chemistry A, 2015. **119**(41): p. 10408-10427.

107.   Ziegler, T., *A Chronicle About the Development of Electronic Structure Theories for Transition Metal Complexes*, in *Molecular Electronic Structures of Transition Metal Complexes II*, D.M.P. Mingos, P. Day, and J.P. Dahl, Editors. 2012, Springer Berlin Heidelberg: Berlin, Heidelberg. p. 1-38.

108.   Almeida, N.M.S., R.G. McKinlay, and M.J. Paterson, *Excited Electronic States of MnO4−: Challenges for Wavefunction and Density Functional Response Theories.* Chemical Physics, 2015. **446**: p. 86-91.

109.   Jasinski, J.P. and S.L. Holt, *Calculation of the electronic structure for the manganate and hypomanganate ions by the self consistent field X-Scattered Wave Method.* Journal of the Chemical Society, Faraday Transactions 2: Molecular and Chemical Physics, 1976. **72**(0): p. 1304-1312.

110.   Ziegler, T., A. Rauk, and E.J. Baerends, *The Electronic Structures of Tetrahedral Oxo-Complexes. The Nature of the "Charge Transfer" Transitions.* Chemical Physics, 1976. **16**(2): p. 209-217.

111.   Olsen, J.M. and E. Hedegård, *Modeling the absorption spectrum of the permanganate ion in vacuum and in aqueous solution.* Physical Chemistry Chemical Physics, 2017. **19**(24): p. 15870-15875.

112.   Olsen, J.M., *Aarhus University, Department of Chemistry. Personal Communication*. 2019.

113.   Sham, T.K. and B.S. Brunschwig, *X-Ray Absorption Spectra of Permanganate(1-) and Permanganate(2-) Ions with Synchrotron Radiation: a Study of Structure and Bonding Properties of Transition-Metal Complexes in Solution.* Journal of the American Chemical Society, 1981. **103**(6): p. 1590-1591.

114.   Kiefer, W. and H.J. Bernstein, *The resonance Raman effect of the permanganate and chromate ions.* Molecular Physics, 1972. **23**(5): p. 835-851.

115.   Palenik, G.J., *Crystal structure of potassium manganate.* Inorganic Chemistry, 1967. **6**(3): p. 507-511.

116.   Fenske, R.F. and C.C. Sweeney, *Semiempirical Molecular Orbital Theory. I. Permanganate and Related Anions.* Inorganic Chemistry, 1964. **3**(8): p. 1105-1113.

117.   Carrington, A. and D.S. Schonland, *The Absorption Spectra of Permanganate, Manganate and Related Oxyions.* Molecular Physics, 1960. **3**(4): p. 331-338.

118.   Wegner, B., et al., *Predicting the Yield of Ion Pair Formation in Molecular Electrical Doping: Redox-Potentials versus Ionization Energy/Electron Affinity.* Journal of Materials Chemistry C, 2019. **7**(44): p. 13839-13848.

119.   Conradie, J., *A Frontier Orbital Energy Approach to Redox Potentials.* Journal of Physics: Conference Series, 2015. **633**: p. 012045.

120.   Paddon-Row, M.N., *Orbital interactions and long-range electron transfer*, in *Advances in Physical Organic Chemistry*. 2003, Academic Press. p. 1-85.

121.   Piela, L., *Chapter 8 - Orbital Model of Electronic Motion in Atoms and Molecules*, in *Ideas of Quantum Chemistry (Second Edition)*, L. Piela, Editor. 2014, Elsevier: Oxford. p. 389-504.

122. Blumberger, J. and M. Sprik, *Ab Initio Molecular Dynamics Simulation of the Aqueous Ru2+/Ru3+ Redox Reaction: The Marcus Perspective.* The Journal of Physical Chemistry B, 2005. **109**(14): p. 6793-6804.

123. Blumberger, J., *Cuaq+/Cuaq2+ Redox Reaction Exhibits Strong Nonlinear Solvent Response Due to Change in Coordination Number.* Journal of the American Chemical Society, 2008. **130**(47): p. 16065-16068.

124. Blumberger, J. and M. Sprik, *Quantum versus classical electron transfer energy as reaction coordinate for the aqueous Ru2+/Ru3+ redox reaction.* Theoretical Chemistry Accounts, 2006. **115**(2): p. 113-126.

125. Zeng, X., et al., *Ab initio quantum mechanical/molecular mechanical simulation of electron transfer process: fractional electron approach.* The Journal of chemical physics, 2008. **128**(12): p. 124510-124510.

126. Seidel, R., et al., *Valence Photoemission Spectra of Aqueous $Fe^{2+/3+}$ and $[Fe(CN)_6]^{4-/3-}$ and Their Interpretation by DFT Calculations.* The Journal of Physical Chemistry B, 2011. **115**(40): p. 11671-11677.

127. Seidel, R., et al., *Single-Ion Reorganization Free Energy of Aqueous Ru(bpy)32+/3+ and Ru(H2O)62+/3+ from Photoemission Spectroscopy and Density Functional Molecular Dynamics Simulation.* Journal of the American Chemical Society, 2009. **131**(44): p. 16127-16137.

128. Ghosh, D., et al., *First-Principle Protocol for Calculating Ionization Energies and Redox Potentials of Solvated Molecules and Ions: Theory and Application to Aqueous Phenol and Phenolate.* The Journal of Physical Chemistry B, 2012. **116**(24): p. 7269-7280.

129. Schroeder, C.A., et al., *Oxidation Half-Reaction of Aqueous Nucleosides and Nucleotides via Photoelectron Spectroscopy Augmented by ab Initio Calculations.* Journal of the American Chemical Society, 2015. **137**(1): p. 201-209.

130. Seeber, R., C. Zanardi, and G. Inzelt, *Links between Electrochemical Thermodynamics and Kinetics.* ChemTexts, 2015. **1**(4): p. 18.

131. Cheng, J. and M. Sprik, *Alignment of electronic energy levels at electrochemical interfaces.* Physical Chemistry Chemical Physics, 2012. **14**(32): p. 11245-11267.

132. Trasatti, S., *The Absolute Electrode Potential: an Explanatory Note (Recommendations 1986).* Pure and Applied Chemistry, 1986. **58**(7): p. 955-966.

133. Jerkiewicz, G., *Standard and Reversible Hydrogen Electrodes: Theory, Design, Operation, and Applications.* ACS Catalysis, 2020. **10**(15): p. 8409-8417.

134. Winget, P., et al., *Computational electrochemistry: aqueous one-electron oxidation potentials for substituted anilines.* Physical Chemistry Chemical Physics, 2000. **2**(6): p. 1231-1239.

135. Guerard, J.J., et al., *Explicit solvent simulations of the aqueous oxidation potential and reorganization energy for neutral molecules: gas phase, linear solvent response, and non-linear response contributions.* Physical Chemistry Chemical Physics, 2015. **17**(22): p. 14811-14826.

136. Cahen, D. and A. Kahn, *Cahen, D. & Kahn, A. Electron energetics at surfaces and interfaces: Concepts and experiments. Adv. Mater. 15, 271-277.* Advanced Materials, 2003. **15**: p. 271-277.

137. Broughton, J.Q. and D.L. Perry, *Electron Binding Energies in The Study of Adsorption by Photoelectron Spectroscopy: The Reference Level Problem.* Surface Science, 1978. **74**(1): p. 307-317.

138. Helander, M.G., et al., *Pitfalls in measuring work function using photoelectron spectroscopy.* Applied Surface Science, 2010. **256**(8): p. 2602-2605.

139. Gabovich, A., *Image Forces in Physics and Chemistry.* Chemistry, Physics and Technology of Surface, 2010. **1**: p. 72-86.

140. Kahn, A., *Fermi level, work function and vacuum level.* Materials Horizons, 2016. **3**(1): p. 7-10.

141. Cahen, D. and A. Kahn, *Electron Energetics at Surfaces and Interfaces: Concepts and Experiments.* Advanced Materials, 2003. **15**(4): p. 271-277.

142. Egelhoff, W.F., *Core-level Binding-Energy Shifts at Surfaces and in Solids.* Surface Science Reports, 1987. **6**(6): p. 253-415.

143. Tissot, H., et al., *The Electronic Structure of Saturated NaCl and NaI Solutions in Contact with a Gold Substrate.* Topics in Catalysis, 2016. **59**(5): p. 605-620.

144. Olivieri, G., et al., *Quantitative ionization energies and work functions of aqueous solutions.* Physical Chemistry Chemical Physics, 2016. **18**(42): p. 29506-29515.

145. Colón Santana, J.A., *Brief Theory of Photoemission Spectroscopy*, in *Quantitative Core Level Photoelectron Spectroscopy*. 2015, Morgan & Claypool Publishers. p. 1-1-1-33.

146. A., D., *Probing the Electronic Structure of Complex Systms by ARPES.* Physica Scripta, 2004. **T109**: p. 61-74.

147. Delahay, P., *Photoelectron Emission Spectroscopy of Solutions: An Interpretation.* The Journal of Chemical Physics, 1971. **55**(9): p. 4188-4197.

148. Delahay, P., *Photoelectron Emission Spectroscopy of Aqueous Solutions.* Accounts of Chemical Research, 1982. **15**(2): p. 40-45.

149. Spicer, W.E., *Photoemissive, Photoconductive, and Optical Absorption Studies of Alkali-Antimony Compounds.* Physical Review, 1958. **112**(1): p. 114-122.

150. Thürmer, S., et al., *Photoelectron Angular Distributions from Liquid Water: Effects of Electron Scattering.* Physical Review Letters, 2013. **111**(17): p. 173005.

151. Mudryk, K.D., et al., *The electronic structure of the aqueous permanganate ion: aqueous-phase energetics and molecular bonding studied using liquid jet photoelectron spectroscopy.* Physical Chemistry Chemical Physics, 2020.

152. Jungwirth, P. and D.J. Tobias, *Ions at the Air/Water Interface.* The Journal of Physical Chemistry B, 2002. **106**(25): p. 6361-6373.

153. Kathmann, S.M., et al., *Understanding the Surface Potential of Water.* The Journal of Physical Chemistry B, 2011. **115**(15): p. 4369-4377.

154. Bergmann, U. and P. Glatzel, *X-Ray Emission Spectroscopy.* Photosynthesis Research, 2009. **102**(2): p. 255.

155. Holzmeier, F., et al., *Normal and resonant Auger spectroscopy of isocyanic acid, HNCO.* The Journal of Chemical Physics, 2018. **149**(3): p. 034308.

156. Wernet, P., *Chemical Interactions and Dynamics with Femtosecond X-Ray Spectroscopy and the role of X-Ray Free-Electron Lasers.* Philosophical Transactions of the Royal Society A: Mathematical, Physical and Engineering Sciences, 2019. **377**(2145): p. 20170464.

157. Barthés-Labrousse, M.-G., *The Auger Effect.* Microsc. Microanal. Microstruct., 1995. **6**(3): p. 253-262.

158. Erbudak, M. *Physics and Chemistry at Surfaces. An Electronic Course offered at the Physics Department of the Boˇgazi̧ci University to 4th year and Master-Degree students*. 2012; Available from: http://www.phys.boun.edu.tr/~phys48w/papers/manus.pdf.

159. Auger, P., *Sur l'effet photoélectrique composé.* Journal de Physique et le Radium, 1925. **6**(6): p. 205-208.

160. Meitner, L., *Über dieb-Strahl-Spektra und ihren Zusammenhang mit derg-Strahlung.* Zeitschrift für Physik, 1922. **11**(1): p. 35-54.

161. Svensson, S., *Soft X-Ray Photoionization of Atoms and Molecules.* Journal of Physics B: Atomic, Molecular and Optical Physics, 2005. **38**(9): p. S821-S838.

162.   Jahnke, T., et al., *Interatomic and Intermolecular Coulombic Decay.* Chemical Reviews, 2020. **120**(20): p. 11295-11369.

163.   Unger, I., et al., *Observation of Electron-Transfer-Mediated Decay in Aqueous Solution.* Nature Chemistry, 2017. **9**(7): p. 708-714.

164.   Miteva, T., et al., *The All-Seeing Eye of Resonant Auger Electron Spectroscopy: A Study on Aqueous Solution Using Tender X-rays.* The Journal of Physical Chemistry Letters, 2018. **9**(15): p. 4457-4462.

165.   Thürmer, S., et al., *Relaxation of Electronically Excited Hydrogen Peroxide in Liquid Water: Insights from Auger-Electron Emission.* The Journal of Physical Chemistry C, 2013. **117**(43): p. 22268-22275.

166.   Golnak, R., et al., *Undistorted X-ray Absorption Spectroscopy Using s-Core-Orbital Emissions.* The Journal of Physical Chemistry A, 2016. **120**(18): p. 2808-2814.

167.   Reinert, F., et al., *The Electronic Structure of $KMnO_4$ Investigated by Photoemission and Electron-Energy-Loss Spectroscopy.* Zeitschrift für Physik B Condensed Matter, 1994. **94**(4): p. 431-438.

168.   Oku, M., *X-ray photoelectron spectra of $KMnO_4$ and K_2MnO_4 fractured in situ.* Journal of Electron Spectroscopy and Related Phenomena, 1995. **74**(2): p. 135–148.

169.   Connor, J.A., et al., *Ab Initio Molecular Orbital Calculations of Transition Metal Complexes.* Molecular Physics, 1972. **24**(3): p. 497-509.

170.   Oku, M., T. Shishido, and S. Kohiki, *Potassium Permanganate by XPS.* Surface Science Spectra, 2004. **11**(1): p. 59-65.

171.   Oku, M., K. Wagatsuma, and T. Konishi, *Transition metal 2p x-ray photoelectron and high-resolution Kα x-ray emission spectra of K_2CrO_4 and $KMnO_4$.* X-Ray Spectrometry, 1999. **28**(6): p. 464-469.

172.   Biesinger, M.C., et al., *Resolving Surface Chemical States in XPS Analysis of First Row Transition Metals, Oxides and Hydroxides: Cr, Mn, Fe, Co and Ni.* Applied Surface Science, 2011. **257**(7): p. 2717-2730.

173.   Reinert, F., P. Steiner, and S. Hüfner, *Electron Spectroscopy on $KMnO_4$.* Journal of Magnetism and Magnetic Materials, 1995. **140-144**: p. 177-178.

174.   Reinert, F., et al., *The Electronic Structure of KMnO4 Investigated by Resonant Photoemission.* Zeitschrift für Physik B Condensed Matter, 1995. **99**: p. 229-234.

175.   Gutsev, G., et al., *Origin of the unusual stability of MnO_4^-.* Chemical Physics Letters, 1999. **312**(5): p. 598-605.

176.   Mehadji, C., et al., *X-ray absorption of tetraoxomanganates (MnO_4^{n-}: Experimental and MS LSD computational studies.* Chemical Physics, 1990. **148**(1): p. 95-102.

177.   Energie, H.-Z.B.f.M.u., *The Plane Grating Monochromator Beamline U49/2 PGM1 at BESSY II.* Journal of large-scale research facilities, 2016. **2**(A72).

178.   Seidel, R., et al., *Advances in Liquid Phase Soft-X-Ray Photoemission Spectroscopy: A new Experimental Setup at BESSY II.* Review of Scientific Instruments, 2017. **88**(7): p. 073107.

179.   Viefhaus, J., et al., *The Variable Polarization XUV Beamline P04 at PETRA III: Optics, mechanics and their performance.* Nuclear Instruments and Methods in Physics Research Section A: Accelerators, Spectrometers, Detectors and Associated Equipment, 2013. **710**: p. 151-154.

180.   http://www.fhi-berlin.mpg.de/mp/winter/Main/ExperimentalMethods. 2020 [cited 2020 11.08].

181.   P. Rullhusen, X.A., P. Dhez, *Novel radiation sources using relativistic electrons; from infrared to X-rays.* 1998: World Scientific Publishing Co. Pte. Ltd.

182.   Smith, N., *Science with Soft X Rays.* Physics Today, 2001. **54**(1): p. 29-34.

183.   Kramar, U., *X-Ray Fluorescence Spectrometers*, in *Encyclopedia of Spectroscopy and Spectrometry (Second Edition)*, J.C. Lindon, Editor. 1999, Academic Press: Oxford. p. 2989-2999.

184. Hemberg, O., M. Otendal, and H.M. Hertz, *Liquid-metal-jet anode electron-impact X-ray source.* Applied Physics Letters, 2003. **83**(7): p. 1483-1485.

185. Hudson, L.T. and J.F. Seely, *Laser-produced X-ray sources.* Radiation Physics and Chemistry, 2010. **79**(2): p. 132-138.

186. Bartzsch, S. and U. Oelfke, *Line Focus X-Ray Tubes—a New Concept to Produce High Brilliance X-Rays.* Physics in Medicine & Biology, 2017. **62**(22): p. 8600-8615.

187. Stein, G.J., et al., *Water-Window Soft X-Ray High-Harmonic Generation up to the Nitrogen K-edge driven by a kHz, 2.1μm OPCPA Source.* Journal of Physics B: Atomic, Molecular and Optical Physics, 2016. **49**(15): p. 155601.

188. Nakajima, K., *Towards a table-top free-electron laser.* Nature Physics, 2008. **4**(2): p. 92-93.

189. Mobilio, S. and A. Balerna, *Introduction to the main properties of Synchrotron Radiation.* 2021.

190. Shintake, T., *Review of the Worldwide SASE FEL Development*, in *Particle Accelerator Conference (PAC 07)*, C. Petit-Jean-Genaz, Editor. 2007. p. 89-93.

191. Wansleben, M., et al., *Photon Flux Determination of a Liquid-Metal Jet X-Ray Source by means of Photon Scattering.* Journal of Analytical Atomic Spectrometry, 2019. **34**(7): p. 1497-1502.

192. Deitrick, K.E., et al., *High-brilliance, high-flux compact inverse Compton light source.* Physical Review Accelerators and Beams, 2018. **21**(8): p. 080703.

193. Krämer, J.M., et al., *Making spectral shape measurements in inverse Compton scattering a tool for advanced diagnostic applications.* Scientific Reports, 2018. **8**(1): p. 1398.

194. Helk, T., M. Zuerch, and C. Spielmann, *Perspective: Towards single shot time-resolved microscopy using short wavelength table-top light sources.* Structural Dynamics, 2019. **6**: p. 010902.

195. Popmintchev, D., et al., *Near- and Extended-Edge X-Ray-Absorption Fine-Structure Spectroscopy Using Ultrafast Coherent High-Order Harmonic Supercontinua.* Physical Review Letters, 2018. **120**(9): p. 093002.

196. A. Bharti, N.G., *Fundamentals of Synchrotron Radiations*, in *Synchrotron Radiation - Useful and Interesting Applications*, D. Joseph, Editor. 2019, IntechOpen.

197. Patterson, B.D., *A simplified approach to synchrotron radiation.* American Journal of Physics, 2011. **79**(10): p. 1046-1052.

198. Shenoy, G., *Basic Characteristics of Synchrotron Radiation.* Structural Chemistry, 2003. **14**(1): p. 3-14.

199. Ansaldo, E.J., *Uses of Synchrotron Radiation.* Contemporary Physics, 1977. **18**(6): p. 527-546.

200. Rowe, E.M. and J.H. Weaver, *The Uses of Synchrotron Radiation.* Scientific American, 1977. **236**(6): p. 32-41.

201. Khan, S., *Ultrashort Pulses from Synchrotron Radiation Sources*, in *Synchrotron Light Sources and Free-Electron Lasers*, K.S. Jaeschke E., Schneider J., Hastings J., Editor. 2020, Springer: Cham. p. 51-81.

202. Berlin, H.-Z. *Operandi Modi BESSY II*. 2020 [cited 2020 04.11.2020]; Available from: https://www.helmholtz-berlin.de/forschung/oe/np/betrieb-beschleuniger/betriebsmodi_en.html.

203. M. Bieler, I.A., H. Ehrlichmann, J. Keil, G. Sahoo, R. Wanzenberg. *PETRA III operation*. in *IPAC2017*. 2017. Copenhagen, Denmark.

204. Wiedemann, H., *Overview of Synchrotron Radiation*, in *Particle Accelerator Physics*. 2015, Springer International Publishing: Cham. p. 815-855.

205. A. Jankowiak, J.K., P. Goslawski, N. Neumann, *Technical Design Study BESSY VSR*. 2015: Helmholtz-Zentrum Berlin.

206. K. Balewski, W.B., W. Decking, H. Franz, R. Rohlsberger et al, *PETRA III: A low emittance synchrotron radiation source. Technical design report*. 2004-035: DESY.

207. Franz, H., et al., *Technical Report: PETRA III: DESY's New High Brilliance Third Generation Synchrotron Radiation Source.* Synchrotron Radiation News, 2006. **19**: p. 25-29.

208. Follath, R., *The Versatility of Collimated Plane Grating Monochromators.* Nuclear Instruments and Methods in Physics Research Section A: Accelerators, Spectrometers, Detectors and Associated Equipment, 2001. **467-468**: p. 418-425.

209. Hellmann, S., et al., *Time-Resolved X-ray Photoelectron Spectroscopy at FLASH.* New Journal of Physics, 2012. **14**(1): p. 013062.

210. Zimmerman, G., *Photochemical Decomposition of Aqueous Permanganate Ion.* The Journal of Chemical Physics, 1955. **23**(5): p. 825-832.

211. Wilson, K.R., et al., *Investigation of Volatile Liquid Surfaces by Synchrotron X-Ray Spectroscopy of Liquid Microjets.* Review of Scientific Instruments, 2004. **75**(3): p. 725-736.

212. Sutter, J.H., K. Colquitt, and J.R. Sutter, *Kinetics of the Disproportionation of Manganate in Acid Solution.* Inorganic Chemistry, 1974. **13**(6): p. 1444-1446.

213. Zhao, X., et al., *Kinetic and Mechanistic Aspects of the Reactions of Iodide and Hypoiodous Acid with Permanganate: Oxidation and Disproportionation.* Environ Sci Technol, 2016. **50**(8): p. 4358-65.

214. March, J.G., F. Maya, and V. Cerdà, *Kinetic-Photometric Monitoring of the Formation of MnO_2 Nanoparticles and their Application to the Determination of Iodide.* Microchimica Acta, 2016. **183**(12): p. 3127-3134.

215. Simandi, L.I., et al., *Kinetics and Mechanism of the Permanganate Ion Oxidation of Sulfite in Alkaline Solutions. The Nature of Short-Lived Intermediates.* Journal of the American Chemical Society, 1985. **107**(14): p. 4220-4224.

216. Hallen, R. and A. Gauger, *Individual Reactions of Permanganate & Various Reductants - Student Report to the DOE ERULF Program for Work Conducted May to July 2000*. 2012: United States.

217. Kim, D., I.H. Lee, and T. Kwon, *A barrier embedded Kenics micromixer.* Journal of Micromechanics and Microengineering, 2004. **14**: p. 1294.

218. Green, R.A., R.C.D. Brown, and D. Pletcher, *Understanding the Performance of a Microfluidic Electrolysis Cell for Routine Organic Electrosynthesis.* Journal of Flow Chemistry, 2015. **5**(1): p. 31-36.

219. Kuleshova, J., et al., *The methoxylation of N-formylpyrrolidine in a microfluidic electrolysis cell for routine synthesis.* Electrochimica Acta, 2012. **69**: p. 197-202.

220. Pletcher, D., R.A. Green, and R.C.D. Brown, *Flow Electrolysis Cells for the Synthetic Organic Chemistry Laboratory.* Chemical Reviews, 2018. **118**(9): p. 4573-4591.

221. Peljo, P. and H.H. Girault, *Electrochemical potential window of battery electrolytes: the HOMO–LUMO misconception.* Energy & Environmental Science, 2018. **11**(9): p. 2306-2309.

222. Godeffroy, L., et al., *Fast and complete electrochemical conversion of solutes contained in micro-volume water droplets.* Electrochemistry Communications, 2018. **86**: p. 145-148.

223. Eriksson, S.K., et al., *A Versatile Photoelectron Spectrometer for Pressures up to 30 mbar.* Review of Scientific Instruments, 2014. **85**(7): p. 075119.

224. https://scientaomicron.com/en/components/electron-analysers. [cited 2020 10.12].

225. Trinter, F., *Fritz-Haber-Institut der Max-Planck-Gesellschaft & Deutsches Elektronen-Synchrotron. Personal Communication*. 2020.

226. Malerz, S., *Fritz-Haber-Institut der Max-Planck-Gesellschaft. Personal Communication*. 2020.

227. Winter, B., et al., *Hydrogen Bonds in Liquid Water studied by Photoelectron Spectroscopy.* The Journal of Chemical Physics, 2007. **126**(12): p. 124504.

228. Winter, B., et al., *Hydrogen Bonding in Liquid Water Probed by Resonant Auger-Electron Spectroscopy.* The Journal of Chemical Physics, 2007. **127**(9): p. 094501.

229. Ziegler, T., *A Chronicle About the Development of Electronic Structure Theories for Transition Metal Complexes*, in *Molecular Electronic Structures of Transition Metal Complexes II. Structure and Bonding*, D. Mingos, Day P., Dahl J., Editor. 2011, Springer: Berlin, Heidelberg. p. 1-38.

230. Thompson, J.K.A.C., Atwood, D. T., Gullikson E. M., Howells M. R., Kortright J. B., Liu Y., Robinson A. L., Underwood J. H., Kim K., Lindau I., Pianetta P., Winick H., Williams G. P., Scofield J. H., *X-ray Data Booklet.* 3rd ed. 2009, Berkeley, California 94720: Lawrence Berkely National Laboratory, University of California.

231. Tong, Y., I.Y. Zhang, and R.K. Campen, *Experimentally quantifying anion polarizability at the air/water interface.* Nature Communications, 2018. **9**(1): p. 1313.

232. Haynes, W., *CRC Handbook of Chemistry and Physics*. 92nd ed. 2011: CRC Press.

233. Pflüger, A., *Über die Farbe der Ionen.* Annalen der Physik, 1903. **317**(10): p. 430-438.

234. Tuckermann, R., *Surface Tension of Aqueous Solutions of Water-Soluble Organic and Inorganic Compounds.* Atmospheric Environment, 2007. **41**(29): p. 6265-6275.

235. Hsin, W.L., et al., *Surface Tension Increment due to Solute Addition.* Physical Review E, 2004. **69**(3 Pt 1): p. 031605.

236. Akyol, N.H., *Surfactant-Enhanced Permanganate Oxidation on Mass-Flux Reduction and Mass Removal (MFR-MR) Relationship for Pool-Dominated TCE Source Zones in Heterogeneous Porous Media.* Water, Air, & Soil Pollution, 2018. **229**(8): p. 285.

237. Campbell, J.L. and T. Papp, *Widths of the atomic K-N7 levels.* Atomic Data and Nuclear Data Tables, 2001. **77**(1): p. 1-56.

238. Coster, D. and R.D. L. Kronig, *New type of auger effect and its influence on the x-ray spectrum.* Physica, 1935. **2**(1): p. 13-24.

239. Winter, B., et al., *Electron Binding Energies of Hydrated H_3O^+ and OH^-: Photoelectron Spectroscopy of Aqueous Acid and Base Solutions Combined with Electronic Structure Calculations.* Journal of the American Chemical Society, 2006. **128**(12): p. 3864-3865.

240. Brown, M.A., M. Faubel, and B. Winter, *X-Ray Photo- and Resonant Auger-electron Spectroscopy Studies of Liquid Water and Aqueous Solutions.* Annual Reports Section "C" (Physical Chemistry), 2009. **105**(0): p. 174-212.

241. Luther, G., *Kinetics of the Reactions of Water, Hydroxide Ion and Sulfide Species with CO_2, OCS and CS_2: Frontier Molecular Orbital Considerations.* Aquatic Geochemistry, 2004. **10**: p. 81-97.

242. Cipcigan, F.S., et al., *Hydrogen Bonding and Molecular Orientation at the Liquid–Vapour Interface of Water.* Physical Chemistry Chemical Physics, 2015. **17**(14): p. 8660-8669.

243. Tennakone, K., *Electronic conduction in solid potassium permanganate excited by water molecules.* Journal of Solid State Chemistry, 1984. **51**(1): p. 131-132.

244. Georgievskii, Y., C.-P. Hsu, and R.A. Marcus, *Linear Response in Theory of Electron Transfer Reactions as an Alternative to the Molecular Harmonic Oscillator Model.* The Journal of Chemical Physics, 1999. **110**(11): p. 5307-5317.

245. Sisley, M.J. and R.B. Jordan, *First Hydrolysis Constants of Hexaaquacobalt(III) and -manganese(III): Longstanding Issues Resolved.* Inorganic Chemistry, 2006. **45**(26): p. 10758-10763.

246. Bühl, M., *Structure, Dynamics, and Magnetic Shieldings of Permanganate Ion in Aqueous Solution. A Density Functional Study.* The Journal of Physical Chemistry A, 2002. **106**(44): p. 10505-10509.

247. Vanýsek, P., *Electrochemical Series*, in *CRC Handbook of Chemistry and Physics*, W.M. Haynes, Editor. 2015, CRC Press/Taylor and Francis: Boca Raton, FL. p. 5-80-5-91.

248. Krishtalik, L.I., *pH-dependent redox potential: how to use it correctly in the activation energy analysis.* Biochimica et Biophysica Acta (BBA) - Bioenergetics, 2003. **1604**(1): p. 13-21.

249. Farrokhpour, H., et al., *The Role of Delocalization Energy on Superhalogen Property: The Electron Affinity of MnX^{n-}, MnX_2^{n-}, and MnX_3^{n-} (X=O, S, and Se).* ChemistrySelect, 2020. **5**(13): p. 3859-3873.

250. Farrokhpour, H., et al., *Theoretical Insights into the Electron Affinity of Manganese Superhalogen Compounds; NBO, QTAIM and Energy Decomposition Analysis.* Molecular Physics, 2020. **118**(15): p. e1718791.

251. Elgrishi, N., et al., *A Practical Beginner's Guide to Cyclic Voltammetry.* Journal of Chemical Education, 2018. **95**(2): p. 197-206.

252. Otomonga, J.P., *Stopped-Flow Kinetic Investigation of Manganese-based Chemiluminescence Oxidation Reactions*, in *Doctoral Thesis, University of Huddersfield. http://eprints.hud.ac.uk/id/eprint/18054/*. 2013.

253. Nagasaka, M., et al., *Electrochemical Reaction of Aqueous Iron Sulfate Solutions Studied by Fe L-Edge Soft X-ray Absorption Spectroscopy.* The Journal of Physical Chemistry C, 2013. **117**(32): p. 16343-16348.

254. Nilsson, A., et al., *X-Ray Absorption Spectroscopy and X-Ray Raman Scattering of Water and Ice; an Experimental View.* Journal of Electron Spectroscopy and Related Phenomena, 2010. **177**(2): p. 99-129.

255. Näslund, L.Å., et al., *X-ray Absorption Spectroscopy Measurements of Liquid Water.* The Journal of Physical Chemistry B, 2005. **109**(28): p. 13835-13839.